AVANCES EN SISTEMAS INTERACTIVOS PARA PERSONAS CON PARÁLISIS CEREBRAL

Dina Niculaes

UNIVERSITAT ROVIRA i VIRGILI

UNIVERSITÀ DEGLI STUDI DI GENOVA

Iron oxide nanocubes for magnetic hyperthermia

DINA NICULAES

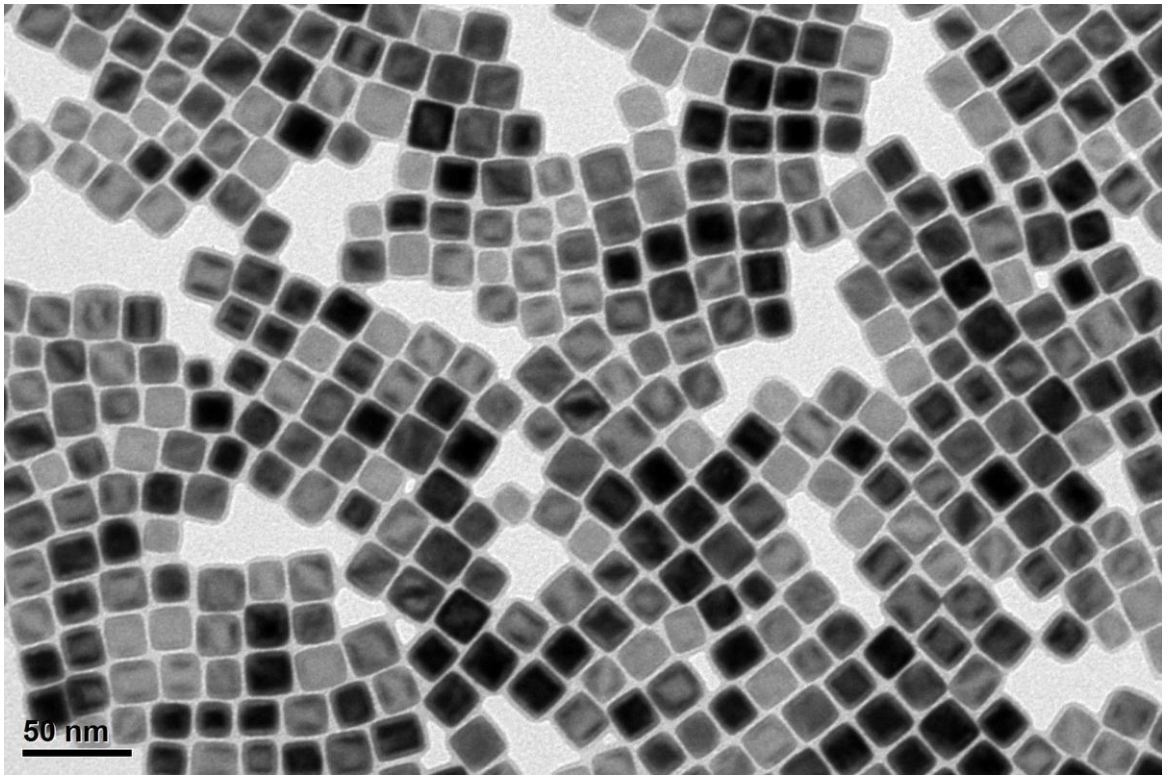

DOCTORAL THESIS

2017

UNIVERSITAT ROVIRA I VIRGILI
AVANCES EN SISTEMAS INTERACTIVOS PARA PERSONAS CON PARÁLISIS CEREBRAL
Dina Niculaes

Dina Niculaes

Iron oxide nanocubes for magnetic hyperthermia

Doctoral Thesis
supervised by:
Dr. Teresa Pellegrino
Prof. Miquel A. Pericàs

UNIVERSITÀ DEGLI STUDI DI GENOVA

Università degli Studi di Genova
Nanochemistry Department, Italian Institute of Technology (IIT), Genoa, Italy

UNIVERSITAT ROVIRA I VIRGILI

Universitat Rovira i Virgili
Institute of Chemical Research of Catalonia (ICIQ),Tarragona, Spain

February, 2017

UNIVERSITAT ROVIRA I VIRGILI
AVANCES EN SISTEMAS INTERACTIVOS PARA PERSONAS CON PARÁLISIS CEREBRAL
Dina Niculaes

Dr. TERESA PELLEGRINO and Prof. MIQUEL A. PERICÀS BRONDO,

STATE, that the present Doctoral Thesis entitled: **"IRON OXIDE NANOCUBES FOR MAGNETIC HYPERTHERMIA"**, presented by Dina Niculaes to receive the degree of Doctor, has been carried out under their supervision between the University of Genova (UniGE) and the Institute of Chemical Research of Catalonia (ICIQ).

Genova, February 17th, 2017

Tarragona, February 27th, 2017

Dr. Teresa Pellegrino

Prof. Miquel Àngel Pericàs Brondo

UNIVERSITAT ROVIRA I VIRGILI
AVANCES EN SISTEMAS INTERACTIVOS PARA PERSONAS CON PARÁLISIS CEREBRAL
Dina Niculaes

Table of contents

UNIVERSITAT ROVIRA I VIRGILI
AVANCES EN SISTEMAS INTERACTIVOS PARA PERSONAS CON PARÁLISIS CEREBRAL
Dina Niculaes

1. Introduction

1.1. Thesis abstract

During the three year doctoral course (**XXIX cycle**, 2014–2016), in the Nanochemistry department at the Italian Institute of Technology (*Genoa*, **Italy**), my research was focused on the development of new nanosystems based on iron oxide cubic-shaped nanoparticles for magnetic hyperthermia application in cancer treatment. Three main projects were conducted under the supervision of Dr. Teresa Pellegrino. The goals of each project and the main results obtained are summarized below.

The novel use of magnetic hyperthermia set-up for the mild oxidization of $Fe_{1-x}O/Fe_{3-\delta}O_4$ core-shell nanocubes to single Fe_3O_4 phase was demonstrated. The wüstite/magnetite core-shell nanocubes after synthesis *via* decomposition of iron pentacarbonyl $Fe(CO)_5$, resulting in non-interacting particles with moderate magnetization, were easily transferred into water by exchanging the short organic surfactant with a poly(ethylene glycol) based water soluble polymer. The water transferred samples had their specific absorption rate (SAR) values determined. Given that these values were lower compared to fully magnetite iron oxide nanocubes of similar cube edge length, the unstable FeO core was oxidized in two different ways: a “harsh” one, after which the SAR values increased alongside the loss of stability and a “mild” one that preserved sample stability. The latter was called magnetic hyperthermia (MH) stimulation. After a handful of MH treatments, the SAR values increased up to two times, while colloidal stability, size distribution and shape remained unaffected. The magnetically stimulated iron oxide nanocubes (IONCs) showed a significantly higher saturation magnetization M_S than the initial core-shell

ones, reflecting structural and compositional changes as confirmed by high resolution transmission electron microscopy/scanning transmission electron microscopy and superconductive quantum interference device studies. The MH treatment also opened up the possibility of attaching biologically relevant molecules to the surface of core-shell nanocubes and preserving their activity while improving the IONCs heat performance. On biotin-tagged nanoparticles, the affinity of biotin towards streptavidin ligands was preserved even after 25 hours of magnetic oxidation treatment. The method here described enabled a mild magnetic transformation of nanocubes resulting in more efficient heat mediators while preserving both the colloidal stability and molecular targeting of the heating nano-probes. These are all crucial features for optimal preparation of heat mediators for *in vivo* hyperthermia.

In continuity with the previous work, the SAR values of core-shell iron oxide nanocubes could be enhanced not only by oxidizing the FeO core, but by controlled clustering of nanocubes in chain like structures driven by anisotropic interactions. Initially the controlled clustering of the IONCs during their water transfer was developed, enabling the formation of soft colloidal clusters with average hydrodynamic sizes that could be tuned between *ca.* 30 and 100 nm. The size tuning could be achieved both by varying the ratio of the amphiphilic random copolymer, poly(styrene-*co*-maleic anhydride), cumene terminated (M_n = 1 600 g/mol), to the particle surface or by varying the initial iron concentration. With this versatile method, magnetic nanoparticles of different shapes—spherical, cubic, cubic with rounded edges—and sizes—in the range 15 to 22 nm— alongside gold nanoparticles, could be clustered in a controlled manner. By increasing the ratio of amphiphilic polymer per nm^2 of particle surface or the Fe concentration bigger nanoclusters were obtained.

The hyperthermia response of individually coated nanocubes *vs.* soft colloidal nanoclusters of different sizes, with hydrodynamic diameters below 100 nm was evaluated. These results were correlated with their magnetic properties as determined by various magnetic characterization techniques. The so called “dimers” and “trimers”, 1D and 2D structures formed with two and respectively three iron oxide nanocubes, showed higher SAR values compared both to individual IONCs or more-centro symmetrical clusters with the number of cubes per cluster higher than 4. Lastly, by implementing previous findings, the clusters could be formed with freshly synthesized core-shell nanocubes, followed by their annealing in aqueous solutions at 80 °C, that resulted in stable nanosystems with higher specific absorption rate values.

Drug loading on two nanosystems designed for heat-triggered chemotherapeutic drug release was achieved. Both systems were based on magnetite 19 nm iron oxide nanocubes coated with thermo-responsive polymers grown from the surface of the IONCs by living radical polymerization, one being reversible addition-fragmentation chain transfer (RAFT) polymerization. Doxorubicin hydrochloride (doxo) loading conditions as a function of initial doxo concentration, incubation time, cleaning method, and loading volume were studied. The two thermo-responsive polymers of choice were poly(N-isopropylacrylamide)-*co*-poly(ethylene glycol) methyl ether acrylate (PNIPAM-*co*-PEGA) and poly(diethylene glycol methyl ether methacrylate-*co*-oligo ethylene glycol methyl ether methacrylate) (P(DEGMEMA-*co*-OEGMEMA)) due to their biocompatibility and ease of lower critical solution temperatures (LCST) tuning in the range from 39 to 41 °C, by varying the polymer composition. The goal was to have stable nanocarriers at

body temperature that would release the cargo (the chemotherapeutic drug) exclusively upon the application of an alternating magnetic field, generating an increase in temperature that would be accompanied by the shrinking of the polymeric shell and release of the entrapped drug. Once individually thermo-responsive polymer coated iron oxide nanocubes with high specific absorption values were obtained, solutions of these IONCs were characterized in terms of specific absorption rate and maximum temperature reached during 3 cycles of 30 minutes of hyperthermia treatment, carried out in small volumes of 50 µL at Fe concentrations ranging from 2.5 to 4 g/L in preparation for *in vivo* studies. The heat-triggered doxorubicin release under alternating magnetic field, at biologically relevant frequency (105 kHz) and field amplitude (25 mT), was qualitatively, but not quantitatively proven.

During my ten-month mobility stay (2015–2016), in the group of Professor Miquel A. Pericàs at the Institute of Chemical Research of Catalonia (*Tarragona*, **Spain**), the selective oxidation of benzyl alcohol into benzaldehyde under mild reaction conditions, using caffeic acid coated iron oxide nanoparticles (spherical and cubic) as catalysts was investigated. The oxidation process was studied as a function of reaction time, amount, and type of catalyst. Recyclability studies were carried out once the best reaction conditions had been identified. The results are summarized in the Annex.

1.2. Overall aims and research objectives

The aim of my research stay at the Italian Institute of Technology is to study colloidal magnetic nanoparticles, specifically iron oxide core-shell nanocubes with edge length in the range from 16 to 21 nm, as nano-platforms for magnetic hyperthermia in cancer treatment.

The above aim will be accomplished by fulfilling the following research objectives:

1. Estimation of specific absorption rate values from heating profile for nanocubes of various edge lengths.
2. Improvement of specific absorption rate values of core-shell iron oxide nanocubes by oxidizing the paramagnetic core in mild conditions—at temperatures below 37 °C—by magnetic stimulation under alternating magnetic field.
3. Controlled clustering of core-shell iron oxide nanocubes in soft colloidal nanoclusters with hydrodynamic sizes below 100 nm.
4. Correlation of specific absorption rate values of soft colloidal nanoclusters of different sizes with their magnetic behavior as determined by superconducting quantum interference device measurements;
5. Chemotherapeutic drug loading on iron oxide nanocubes coated with thermo-responsive polymers having a lower critical solution temperature a few degrees above body temperature.
6. Controlled heat-triggered drug release from drug-loaded iron oxide nanocubes by applying an alternating magnetic field.

The focus of the research will shift towards catalysis applications of similar nanosystems during the ten-month mobility stay at the Institute of Chemical Research of Catalonia.

2. Monodisperse core-shell iron oxide nanocubes for magnetic hyperthermia

Parts of this chapter have been published in:

Lak, A.; Niculaes, D.; Anyfantis, G. C.; Bertoni, G.; Barthel, M. J.; Marras, S.; Cassani, M.; Nitti, S.; Athanassiou, A.; Giannini, C.; Pellegrino, T.; Facile transformation of FeO/Fe_3O_4 core-shell nanocubes to Fe_3O_4 *via* magnetic stimulation, *Sci. Rep.* **2016**, *6*, 33295

Adapted with permission from Lak, A.; Niculaes, D.; Anyfantis, G. C.; Bertoni, G.; Barthel, M. J.; Marras, S.; Cassani, M.; Nitti, S.; Athanassiou, A.; Giannini, C.; Pellegrino, T.; Facile transformation of FeO/Fe_3O_4 core-shell nanocubes to Fe_3O_4 *via* magnetic stimulation, *Sci. Rep.* **2016**, *6*, 33295

2.1. Introduction

Iron oxide nanoparticles are an indispensable candidate for varieties of nanoparticle-based therapeutics and diagnostics owing to their switchable magnetization, biocompatibility and biodegradation.[1,2] Magnetic hyperthermia (MH) is a novel non-invasive therapy, now under clinical trial on patients with brain or prostate tumors, that exploits magnetic nanoparticles as heat mediators to burn cancer mass.[3–5] The heat dissipation strongly depends on physico-chemical features of the particles. Up to now, there have been many studies aiming at the design of optimal heat mediators.[6–8] Recently, it was reported that anisotropic cubic-shaped particles revealed a superior heating performance with respect to spherical ones, yet tightly relying on their structural and compositional properties.[9,10]

The synthesis of monodisperse iron oxide nanocubes is a great challenge and hardly attainable by any other method other than high temperature colloidal syntheses. The iron pentacarbonyl and iron oleate are among the most frequently used precursors for the synthesis of iron oxide nanoparticles due to their particular decomposition profile that allows a distinctive separation between nucleation and growth steps, a vital criterion for obtaining uniform nanocrystals.[11–16] Some of the developed synthetic procedures that make use of these precursors result in the formation of initial paramagnetic FeO (wüstite structure) particles because of the reductive nature of the decomposition reaction.[17] After being exposed to ambient conditions, the outer particle surface transforms into Fe_3O_4 phase (inverse spinel structure) and eventually core-shell structures, having an antiferromagnetic core (below Néel temperature T_N of 198 K) and a ferri(o)magnetic shell (AFM-FiM), are formed.[18] The core-shell particles, depending on the composition of

the core and the shell, exhibit intriguing features such as exchange coupling between hard and soft magnets and exchange bias coupling, which have raised lots of scientific interest.[19]

The idea behind the research presented in this chapter was to work with iron oxide nanoparticles that were cubic-shaped, with a paramagnetic core and a ferri(o)magnetic shell, thus non-interacting at RT. These types of nanoparticles can be easily manipulated and thus functionalized with targeting molecules while by post-treating them in mild oxidation conditions under magnetic hyperthermia set-up (Figure 1a) their magnetic properties could be improved thus resulting in better targeted hyperthermia agents. In this chapter, the research carried out on metastable core-shell iron oxide nanocubes[20,21] under different conditions—in order to evaluate their heating performances in magnetic hyperthermia—is reported.

The research is divided into several parts: after the colloidal synthesis and water transfer of 2 batches of core-shell IONCs of different sizes, their specific absorption rate (SAR) values were measured at different frequencies and field amplitudes in section 2.3. As the SAR values were considerably smaller compared to SAR values of magnetite IONCs with a 19 nm cube edge length[22], we attempted to improve their heating performance by oxidizing the wüstite core in two ways: at elevated temperatures in organic solvents (harsh treatment) or by magnetic stimulation under hyperthermia at temperatures below body temperature (mild treatment, Figure 1a). Both methods provided an increase in SAR values: the mild one from 50 up to 100 % increase in SAR values and the harsh one up to a 6 fold increase (section 2.4.). Next, on a freshly synthesized sample, 25 cycles of mild treatment under MH stimulation were carried out (Figure 1b) and the sample was fully characterized from a

structural and magnetic point of view before the treatment and after 10 and 25 cycles of MH (section 2.5). Lastly, the nanocubes were functionalized with biotin and the activity of biotin was assessed prior and after exposure to 25 MH cycles. The biotin activity was preserved as streptavidin could bind to biotin molecules both before and after 25 MH cycles (section 2.6.).

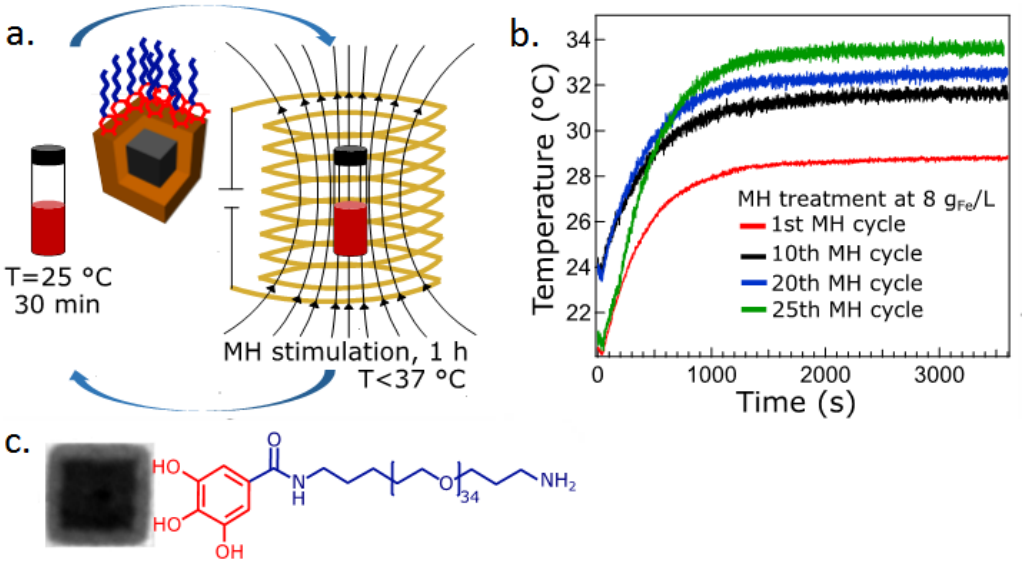

Figure 1: (a) Schematic representation of core oxidation under mild treatment by magnetic hyperthermia (MH) stimulation, (b) heating profiles of poly(ethylene glycol) coated nanocubes *vs.* MH cycle number, particles concentration fixed at 8 g/L of Fe, (c) scheme of a gallic-PEG coated core-shell nanocube.[23]

2.2. Iron oxide nanocubes synthesis and water transfer

Initially, the goal was to study two batches of core-shell iron oxide nanocubes of different sizes: 15.8 ± 1.4 nm and 21.1 nm ± 1.8 nm cube edge length, that will be referred to as 16 and 21 nm IONCs, respectively. We were curious to measure their SAR values and find out how they compared between

each other. A typical synthesis of the 16 nm core-shell iron oxide nanocubes can be found below.

To a 50 mL three-necked flask connected to a reflux cooler and pumped to vacuum for 30 minutes at 120 °C, oleic acid (1.6 g, 5.7 mmol), sodium oleate (0.939 g, 3 mmol) and 1-octadecene (4 mL) were added. Afterwards the solution was cooled down to room temperature (RT) and put under N_2 flux. Then the iron precursor solution, $Fe(CO)_5$ (0.597 g, 3 mmol) dissolved in 2 mL of 1-ODE, was injected and the mixture was heated from RT to 320 °C, at the heating rate of 20 °C/min. The solution reaction was stirred vigorously at 320 °C for 1.5 hours, then cooled down and exposed to air for 30 minutes at 130 °C. Lastly, it was left to cool down to RT. The nanoparticles (NPs) were collected by centrifugation and washed in a mixture of 2-propanol and acetone (1:2 v%). The purification process was carried out three times and the NPs were stored in chloroform.

The IONCs were characterized by dynamic light scattering (DLS) and transmission electron microscopy (TEM). The DLS results are summarized in Table 1 and the corresponding TEM micrographs are presented in Figure 2. The average hydrodynamic size by volume in $CHCl_3$ was 47 ± 7 (PDI 0.21) and 57 ± 15 (PDI 0.16) for the 16 and the 21 nm sample, respectively (Table 1). Such low PDI values indicated a stable sample and lack of aggregates, as confirmed by TEM analysis. A well dispersed monolayer of core-shell IONCs can be seen on the TEM grid (Figure 2). It is worth mentioning that for the hyperthermia study the synthesis of the nanocubes was done 9 months prior to the water transfer and thus the initial core-shell structure might have been different after 9 months storage with respect to the freshly synthesized sample. Given that the wüstite core is unstable and tends to oxidize in air over very long periods of

time (year timescale) the core-shell structure could be better visualized for the 21 nm sample (Figure 2b), compared to the 16 nm sample (Figure 2a), on the latter indeed the oxidation proceeded at a faster speed due to its higher area to volume ratio.

Table 1: DLS data* for iron oxide nanocubes dispersed in $CHCl_3$

Sample	Z-Ave	PdI	Number mean	Intensity mean	Volume mean
	[nm]		[nm]	[nm]	[nm]
16 nm IONCs	72 ± 1	0.21 ± 0.01	27 ± 10	89 ± 7	47 ± 7
21 nm IONCs	138 ± 1	0.16 ± 0.02	26 ± 12	168 ± 5	57 ± 15

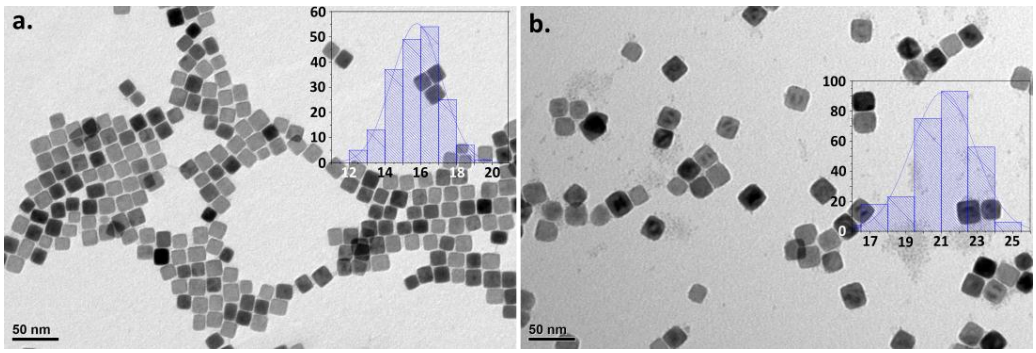

Figure 2: Representative transmission electron microscopy (TEM) micrographs of core-shell iron oxide nanocubes, dispersed in chloroform, for cube edge lengths of (a) 16 nm and (b) 21 nm (insets: corresponding size histograms (a) 15.8 ± 1.4 nm and (b) 21.1 ± 1.8 nm).

* For DLS measurements at least 3 measurements were carried out. The mean value with its standard deviation is reported.

After the synthesis, the IONPs had to be transferred into aqueous media. We decided to focus our attention on one of the two main strategies that have been developed for the water transfer of magnetic nanoparticles (MNPs) after their colloidal synthesis by thermal decomposition methods. This strategy, called ligand exchange, is based on stripping the initial stabilizing agents and replacing them with water soluble and biocompatible ligands.[24–27] The latter has to be composed of an anchoring unit—gallic acid in this study—with high affinity for the MNP's surface and a hydrophilic polymeric backbone—poly(ethylene glycol) (PEG)—which ensures water stabilization (Figure 1c). A typical water transfer procedure, by ligand exchange, with a PEG based polymer with a gallic acid anchor, is described in section 2.8.

The second strategy for achieving surface functionalization, called encapsulation, consists of enveloping the inorganic nanoparticle inside an amphiphilic copolymer[28–31]. The hydrophobic chains of the copolymer can interdigitate with the hydrophobic stabilizing agents on the particle surface and the hydrophilic blocks would provide colloidal stability in aqueous media. The water transfer by encapsulation inside the poly(maleic anhydride-*alt*-1-octadecene) polymer was also tried. The results are not reported here, as we realized that during the polymer coating with the amphiphilic polymer, there was a step involving the evaporation of solvent which would heat the sample (during polymer coating the samples were left overnight inside the oven at 65 °C)—thus the metastable core was affected by this step as the metastable phase underwent oxidation in a non-controlled way. This was a side effect that we wanted to avoid, as the oxidation had to be carried out only under controlled conditions.

When using gallic-PEG polymer, the successful exchange was confirmed by the aqueous stability of the IONCs@PEG. DLS data is summarized in Table 2. For example, for sample 16 nm IONCs the average hydrodynamic diameter d_H by number increased from 27 ± 10 nm to 37 ± 18 nm, which confirmed the successful exchange of the organic capping agents with the hydrophilic polymer that had a higher molecular mass and a larger gyration radius. TEM micrographs of the two samples in water are presented in Figure 3.

Table 2: DLS data for iron oxide nanocubes, coated with gallic-PEG, in H_2O

Sample	Z-Ave	PdI	Number mean	Intensity mean	Volume mean
	[nm]		[nm]	[nm]	[nm]
16 nm IONCs@PEG	111 ± 1	0.23 ± 0.01	37 ± 18	145 ± 2	97 ± 27
21 nm IONCs@PEG	77 ± 1	0.26 ± 0.01	33 ± 1	210 ± 25	98 ± 14

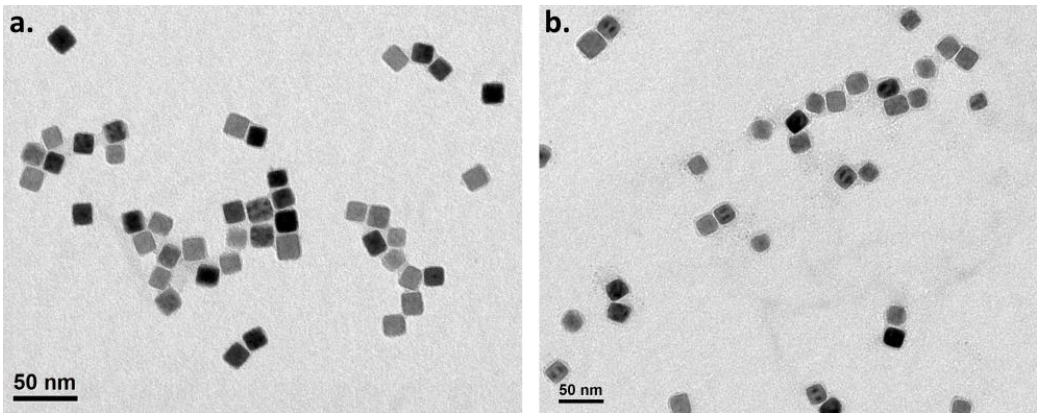

Figure 3: Representative TEM micrographs[†] of iron oxide nanocubes coated with the hydrophilic polymer poly(ethylene glycol), for cube edge lengths of (a) 16 nm and (b) 21 nm. A thin polymer shell could be observed around the IONCs and sometimes in between the nanocubes.

[†] Different scale bars on TEM micrographs

A very thin light grey shell of 1-2 nm surrounding each nanocube could be seen on the TEM micrographs that was ascribable to the polymeric PEG layer. In solution however the polymer shell was in its extended state, thus increasing the overall hydrodynamic size as confirmed by DLS data. For example the 21 nm IONCs@PEG nanocubes as seen by TEM, dispersed in H_2O, had a mean hydrodynamic diameter by number of 33 ± 1 nm.

2.3. Magnetic hyperthermia

Once both samples were transferred into water, at sufficient amount for running hyperthermia experiments, the heating capacities of the 16 and 21 nm cube edge length IONCs were determined. Typical nanocube solution had to be at *ca*. 5 g/L Fe concentrations in order to be suitable for hyperthermia measurements. For the SAR measurements, under alternating magnetic field (AMF), frequencies and magnetic field amplitudes ranging from 105 to 302 kHz and from 15 to 40 mT were chosen.

The heating capacity of magnetic nanoparticles is expressed by their specific absorption rate. SAR was calculated based on the following equation:

$$SAR\ (\frac{W}{g}) = \frac{C}{m} \times \frac{dT}{dt}$$

where C was the specific heat capacity of water per unit volume and m was the concentration (g/L of Fe) of magnetic material in solution. The calorimetric measurements were carried out in quasi-adiabatic conditions and the slope of the curve $\frac{dT}{dt}$ was measured by taking into account only the first 20-25 seconds. The measured SAR values are summarized in Table 3 and plotted in Figure 4, as a function of the amplitude and frequency of the alternating magnetic field applied for both PEG coated samples.

Table 3: SAR values obtained at various magnetic field frequencies and amplitudes for (a) 16 nm and (b) 21 nm core-shell iron oxide nanocubes

a. Sample 16 nm IONCs@PEG	Frequency [kHz]		
	105	220	302
B [mT]	SAR [W/g_{Fe}]	SAR [W/g_{Fe}]	SAR [W/g_{Fe}]
15	-	27 ± 2	37 ± 2
22	16 ± 2	38 ± 1	62 ± 1
30	22 ± 3	59 ± 2	94 ± 5
40	29 ± 3	-	-

b. Sample 21 nm IONCs@PEG	Frequency [kHz]		
	105	220	302
B [mT]	SAR [W/g_{Fe}]	SAR [W/g_{Fe}]	SAR [W/g_{Fe}]
15	-	14 ± 1	22 ± 1
22	21 ± 1	36 ± 1	44 ± 1
30	36 ± 1	70 ± 1	88 ± 3
40	71 ± 1	-	-

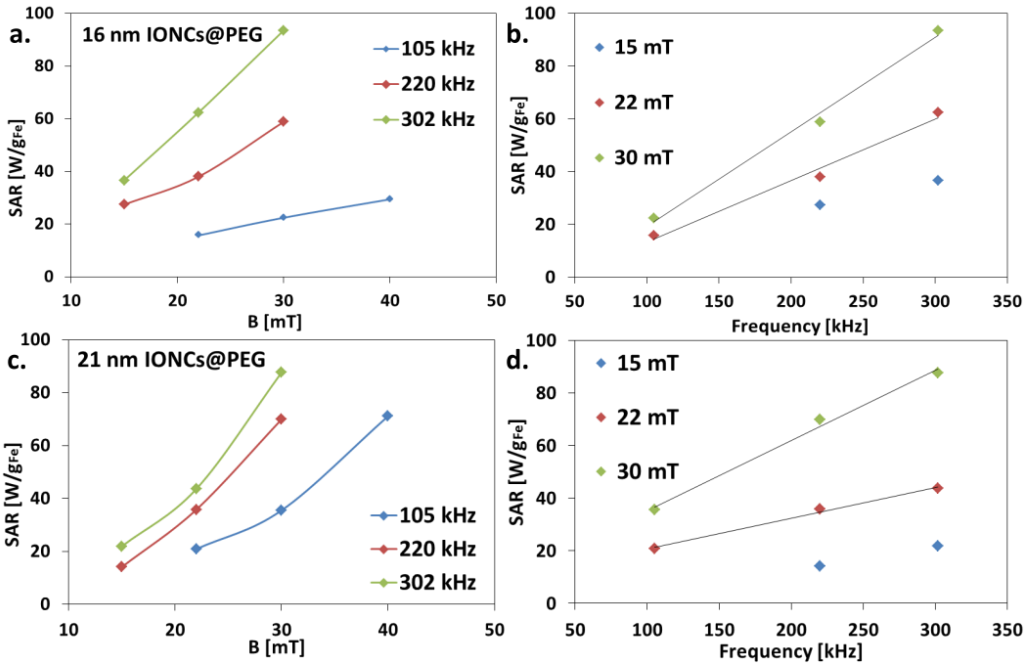

Figure 4: Specific absorption rate (SAR) values as a function of amplitude of the applied magnetic field at frequencies of 105 kHz (blue diamonds), 220 kHz (red diamonds), and 302 kHz (green diamonds) for (a) 16 nm and (c) 21 nm IONCs@PEG. (b,d) SAR values as a function of frequency at magnetic field amplitudes of 15 mT (blue diamonds), 22 mT (red diamonds), and 30 mT (green diamonds) for (b) 16 nm and (d) 21 nm IONCs. For both samples an increase in SAR values was observed by increasing the magnetic field amplitude or/and the frequency. The solid lines are guides for the eye.

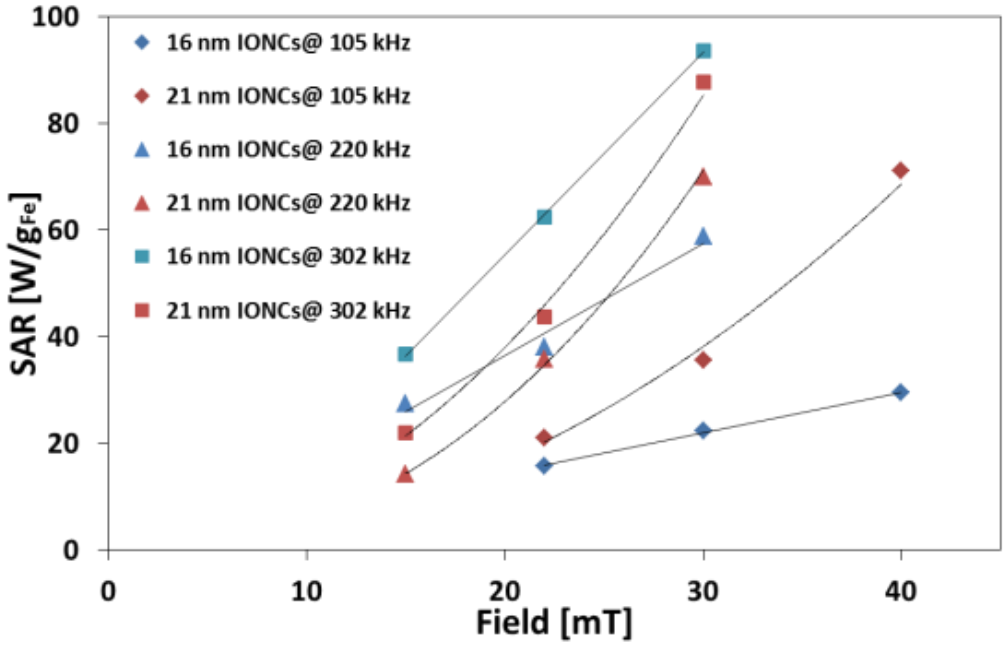

Figure 5: SAR values as a function of the applied magnetic field at frequencies of 105 kHz (blue diamonds—16 nm, red diamonds—21 nm), 220 kHz (blue triangles—16 nm, red triangles—21 nm), and 302 kHz (blue squares—16 nm, red squares—21 nm) for 16 nm and 21 nm IONCs@PEG. The solid black lines are guides for the eye.

The comparison between SAR values for 16 nm and 21 nm IONCs@PEG, as a function of the amplitude of the magnetic field applied and frequency, can be found in Figure 5 and Figure 6, respectively.

Interestingly, at lower frequency of 105 kHz the SAR values of the 16 nm IONCs@PEG were smaller than the SAR values of the 21 nm IONCs@PEG, with that trend being inversed for higher frequencies of 302 kHz (Figure 6). A possible explanation would be the switch between Brownian and Néel relaxation for the superparamagnetic 16 nm IONCs at higher frequencies (only AC Susceptibility measurements could have confirmed that fact, measurements that were, unfortunately, not carried out on these samples).

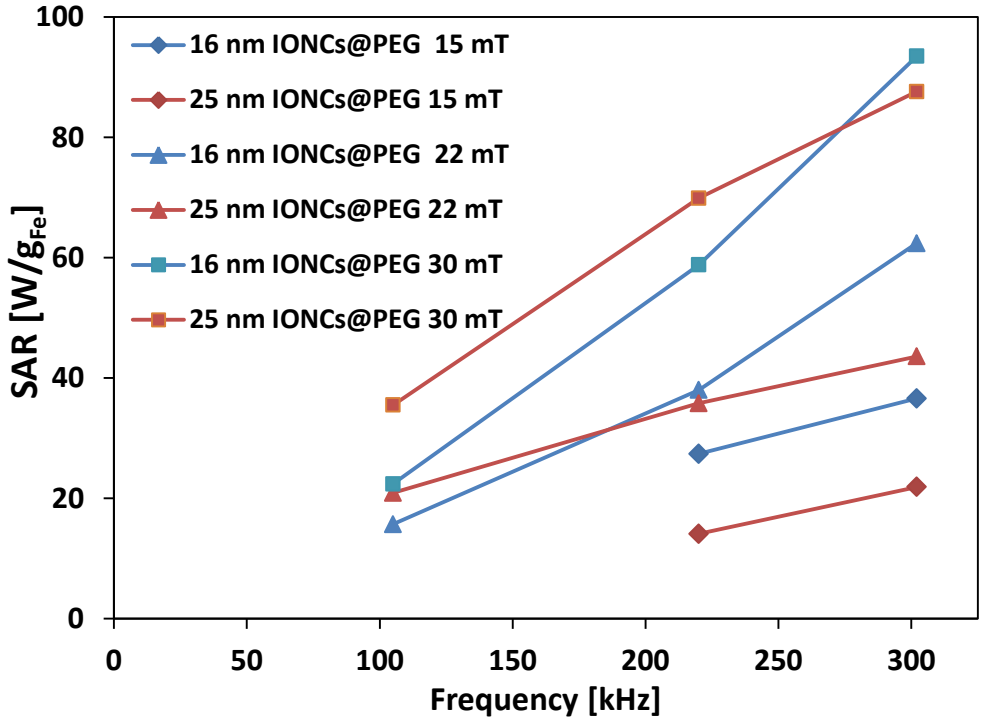

Figure 6: SAR values as a function of frequency at magnetic field amplitudes of 15 mT (blue diamonds—16 nm, red diamonds—21 nm), 22 mT (blue triangles—16 nm, red

triangles—21 nm), and 30 mT (blue squares—16 nm, red squares—21 nm). The solid lines are guides for the eye.

As mentioned earlier, our group has already synthesized fully magnetite cubic-shaped IONPs with high SAR values.[22] For 19 nm IONCs, the SAR value at f = 219 kHz and B = 25 mT (H = 20 kA/m), was *ca*. 350 W/g_{Fe}. In the case of core-shell IONCs the SAR values were in the range of 50 W/g_{Fe} at same magnetic field amplitude and frequency. The heat performance of the latter was an order of magnitude lower, but the main advantage of the core-shell nanocubes used in this work over the cubes synthesized previously by our group was the fact that at RT they were superparamagnetic and that characteristic made them easy to functionalize with any type of polymer. Instead, for the 19 nm magnetite nanocubes, being at the interface between superparamagnetic and ferri(o)magnetic regime, it was not possible to functionalize their surface with small ligand/antibody fragments because of severe precipitation of the nanocubes during functionalization (data not shown). We therefore opted here for the core-shell nanocubes. We first wondered if the low SAR values of the nanocubes employed in this study were due to their paramagnetic core and whether an annealing process would have improved their properties. To this aim we set and compared two oxidation protocols.

2.4. Oxidation of wüstite core

2.4.1. Harsh conditions

The next step was to oxidize the paramagnetic wüstite core in order to obtain a homogenous magnetite phase[21], as schematically presented in Figure 7, and supported by XRD patterns presented in Figure 9. In a first instance we thought of employing a direct approach using high temperatures in the presence of oxygen. We named this approach the "harsh" oxidation protocol. A fresh sample of core-shell iron oxide nanocubes was synthesized with cube edge length of 20.2 ± 1.8 nm (Figure 8a). The initial oxidation attempts were done on these IONCs dispersed in organic solutions (1-octadecene).

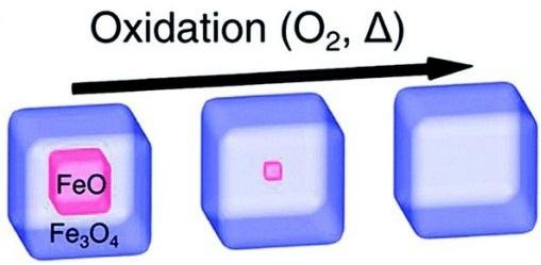

Figure 7: Schematic representation of the gradual FeO core elimination under "harsh" oxidation conditions—high temperatures for several hours, in the presence of oxygen.[21]

Several oxidation combinations by changing process temperature and time were tried. In a first attempt, at temperature of 180 °C for an oxidation time of 5 hours—the IONCs lost their cubic shape, becoming truncated octahedra as can be seen in the inset in Figure 8b. Instead, the optimal oxidation procedure, that preserved both the size and the shape of the IONCs required a lower temperature of 130 °C, and longer oxidation time of 7 hours (section 2.8).

The characteristics of the freshly synthesized 20 nm IONCs in chloroform, before and after oxidation, alongside the sample coated with gallic-PEG after oxidation in organic solvents at 130 °C for 7 hours, are presented in Table 4 and in Figure 8.

Table 4: DLS data for iron oxide nanocubes of 20.2 ± 1.8 nm cube edge length

Sample	Z-Ave	PdI	Number mean	Intensity mean	Volume mean
	[nm]		[nm]	[nm]	[nm]
20 nm IONCs in $CHCl_3$	335 ± 26	0.30 ± 0.03	26 ± 1	168 ± 16	57 ± 4
20 nm IONCs_ox in $CHCl_3$	158 ± 3	0.46 ± 0.02	28 ± 1	213 ± 8	118 ± 16
20 nm IONCS_ox@PEG in H_2O	207 ± 4	0.19 ± 0.02	154 ± 30	231 ± 17	262 ± 28

After the oxidation of the core following the harsh protocol, the DLS results of nanocubes in chloroform showed a slight increase in average hydrodynamic diameter by number from 26 ± 1 nm (PDI 0.3) to 28 ± 1 nm (PDI 0.46) corespponding to the core-shell nanocubes and the oxidized NPs in $CHCl_3$, respectively (Table 4). Once again after the particles were coated with gallic-PEG, the size of the NPs increased even further, due to an exchange of a short capping organic molecule (oleic acid) with a polymer of higher molecular weight.

TEM characterization cofirmed the core-shell structure before oxidation (Figure 8a). After oxidation, the wüstite core could no longer be observed (Figure 8b-d, some contrast on the cubes could be due to the presence of defects). Stability of the particles was maintained after oxidation process as no aggregation of particles could be observed on the TEM grid (Figure 8b). Alongside stability, the IONCs preserved their cubic shape (Figure 8 b-d).

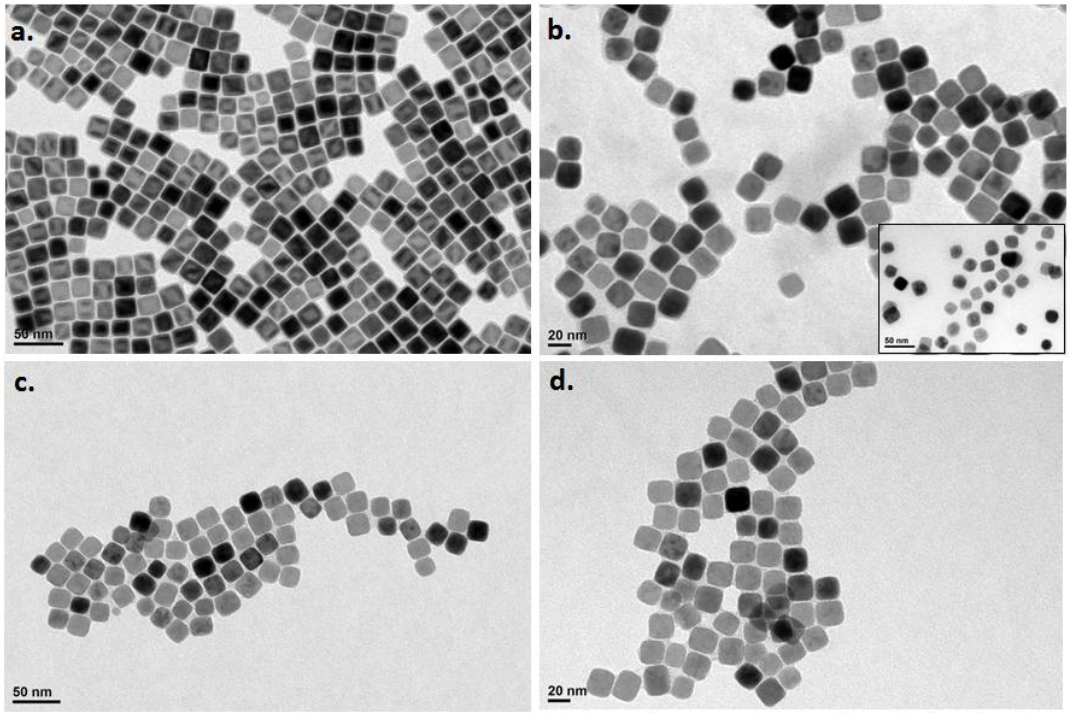

Figure 8: Representative TEM micrographs of 20 nm IONCs in $CHCl_3$ (a) before and (b) after 7 h@130 °C oxidation (inset: 5 h@180 °C); (c,d) 20 nm IONCs_ox@PEG in H_2O. Before oxidation the core-shell structure was clearly visible (a). After oxidation, the core could no longer be observed, neither in chloroform (b) nor in water (c,d).

Both the initial 20 nm core-shell sample and the oxidized sample (oxidation in organic solvents at 130 °C for 7 hours) were coated with gallic-PEG and dispersed in H_2O. The XRD data of these two samples (IONCs@PEG and IONCs_ox@PEG), before and after the harsh oxidation treatment, confirmed the oxidation and thus the disappearance of the paramagnetic core that had a wüstite crystallographic structure (Figure 9). Before oxidation, the reflections related to wüstite was clearly evident. After oxidation, the characteristic reflections of wüstite disappeared and only the reflections of magnetite were present.

After transfer to physiological media of the oxidized sample, hyperthermia measurements were carried out in order to determine the SAR values of the 20 nm IONCs_ox@PEG. When comparing the SAR values of core-shell IONCs with that of oxidized IONCs, the results were encouraging as up to a six fold increase of SAR value was observed, as summarized in Table 5. For instance, the SAR value of 20 nm core-shell sample before oxidation was 39 ± 4 W/g_{Fe}, at magnetic field amplitude of 25 mT (20 kA/m) and frequency of 220 kHz (Table 5). After oxidation in harsh conditions, at same frequency and magnetic field amplitude, the sample had a SAR of 238 ± 1 W/g_{Fe} (Table 5). The SAR values after oxidation are plotted in Figure 10.

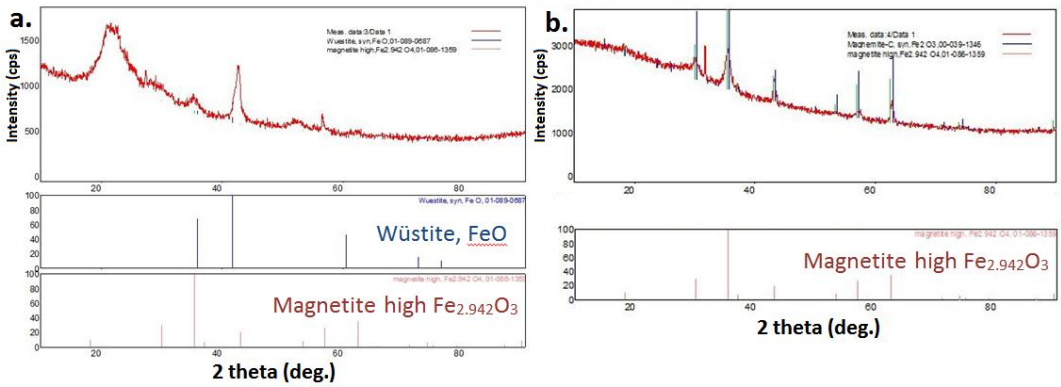

Figure 9: Crystallographic X-Ray diffraction (XRD) data for sample 20 nm IONCs@PEG (a) before and (b) after oxidation at 130 °C for 7 hours (harsh conditions). Before oxidation both wüstite and magnetite reflections were present, while after oxidation only magnetite phase was detected. The broad peak present at 22 ° (a) was due to the gallic-PEG polymer.

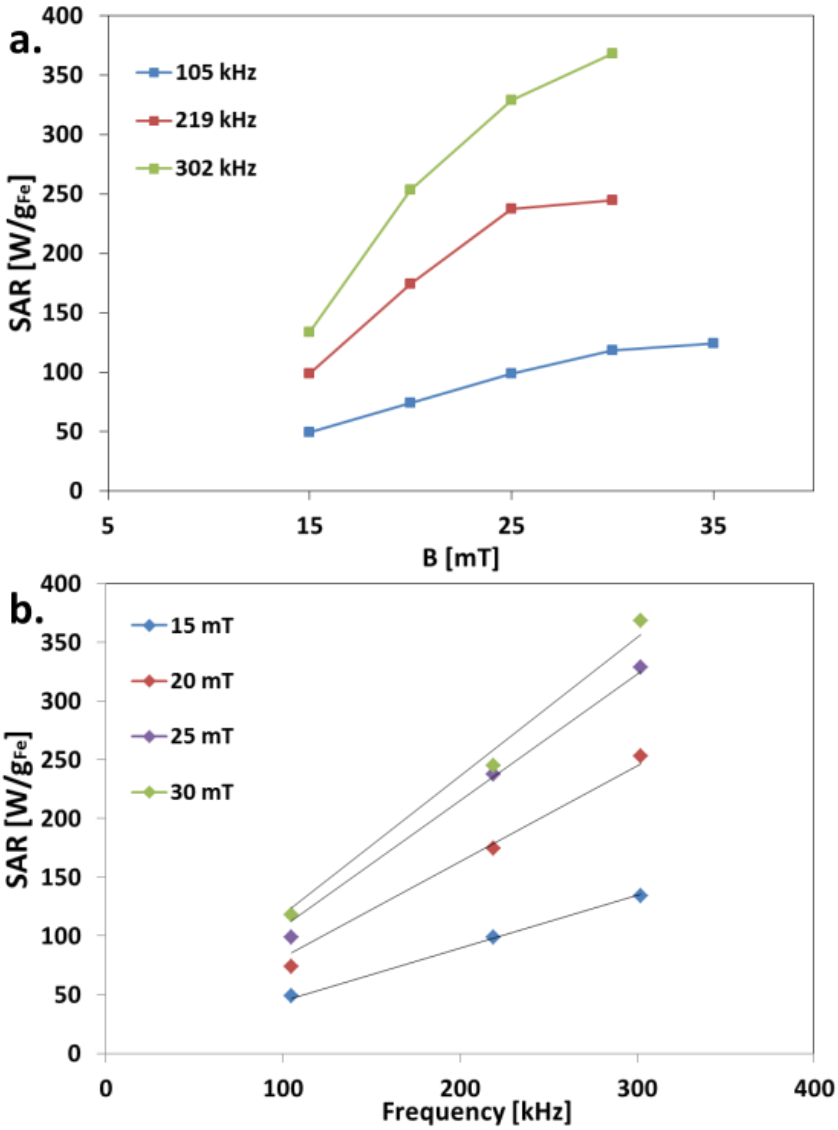

Figure 10: SAR values of 20 nm IONCs oxidized in harsh conditions, after water transfer, as a function of (a) the applied magnetic field at frequencies of 105 kHz (blue squares), 220 kHz (red squares), and 302 kHz (green squares). (b) SAR values of 20 nm IONCs oxidized in harsh conditions as a function of frequency at magnetic field amplitudes of 15 mT (blue diamonds), 20 mT (red diamonds), 25 mT (violet diamonds), and 30 mT (green diamonds) for 20 nm IONCs_ox@PEG. The solid lines are guides for the eye.

Table 5: SAR values for 20 nm iron oxide nanocubes, before and after oxidation under harsh conditions (7 hours @130 °C)

Sample 20 nm IONCs	Frequency 105 kHz		Frequency 220 kHz		Frequency 302 kHz	
B [mT]	SAR [W/g_{Fe}] **before** oxidation	SAR [W/g_{Fe}] **after** harsh oxidation	SAR [W/g_{Fe}] **before** oxidation	SAR [W/g_{Fe}] **after** harsh oxidation	SAR [W/g_{Fe}] **before** oxidation	SAR [W/g_{Fe}] **after** harsh oxidation
15	-	49 ± 4	-	99 ± 3	-	134 ± 4
20	-	74 ± 1	27 ± 2	174 ± 2	35 ± 1	253 ± 2
25	22 ± 2	99 ± 1	39 ± 4	238 ± 1	57 ± 4	329 ± 3
30	38 ± 2	118 ± 3	60 ± 3	245 ± 2	79 ± 1	368 ± 3
35	53 ± 1	124 ± 4	-	-	-	-

When oxidizing the paramagnetic core, the SAR value increased significantly. However the stability of the nanoparticles decreased as assessed by DLS. The average d_H by number increased from 28 ± 1 nm (IONCs_ox in $CHCl_3$) to 154 ± 30 nm (IONCs_ox@PEG in H_2O) (Table 4), one of the plausible reasons being the increase in dipole-dipole interactions. Therefore, these data suggested that the phase transformation of the core-shell was a good strategy to improve the SAR however stability issues needed to be solved. This has prompted us to look for an alternative strategy to high temperature oxidation.

2.4.2. Mild conditions

This alternative was envisioned by oxidation of the FeO core under so called “mild” conditions. Under an alternative magnetic field (AMF), the nanoparticles still converted magnetic energy into thermal energy, and the local heat drove the oxidation of the core. The frequency and field of the AMF were chosen in order to reach macroscopic solution temperatures that remained below body temperature. In the case of harsh oxidation conditions, the IONCs were coated with gallic-PEG after oxidation, the oxidation being

carried out in organic solvents. In the case of mild conditions, the curing occurred in aqueous media directly on water soluble and stable IONCs@PEG nanocubes (Figure 1a).

In a typical oxidation under AMF the sample was subjected to several cycles of hyperthermia each of one-hour long. The frequency was set to 331 kHz and the magnetic field to 17 mT (13.6 kA/m). Between each hyperthermia treatment, the vial was opened (as the amount of oxygen inside the vial was limited) and left on the bench for 30 min (Figure 1a). A typical temperature profile as a function of time recorded during the treatment is presented in Figure 11 for sample 21 nm IONCs@PEG.

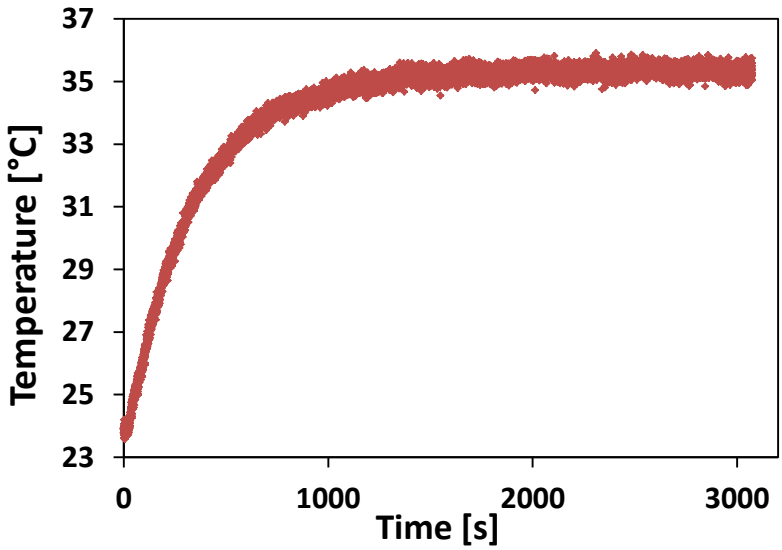

Figure 11: Oxidation of 21 nm IONCs@PEG under alternating magnetic field (f = 330.9 kHz, B = 17 mT)

After every AMF exposure, the SAR values were measured. It was noticed that no change in the temperature profile was measured for the first 8 trials. While continuing the oxidation under mild conditions for several more

trials, an increase in SAR values was obtained at that particular frequency and magnetic field amplitude. For sample 21 nm IONCs@PEG, the total amount of AMF exposure was 12 hours and 30 minutes. The macroscopic maximum temperature reached during the experiments was 36 °C. The increase in SAR values measured was up to 100% of the SAR value of the initial untreated sample.

Table 6: SAR values at various frequencies and magnetic field amplitudes for (a) 21 nm and (b) 20 nm iron oxide nanocubes, before and after (a) 12 h 30 min and (b) 15 h 30 min of MH stimulation

a. Sample 21 nm IONCs	Frequency 105 kHz		Frequency 220 kHz		Frequency 302 kHz	
B [mT]	SAR [W/g_{Fe}] **before** MH	SAR [W/g_{Fe}] **after** MH	SAR [W/g_{Fe}] **before** MH	SAR [W/g_{Fe}] **after** MH	SAR [W/g_{Fe}] **before** MH	SAR [W/g_{Fe}] **after** MH
15	-	-	14 ± 1	-	22 ± 1	44 ± 2
22	21 ± 1	-	36 ± 1	73 ± 2	44 ± 1	97 ± 1
30	36 ± 1	54 ± 2	70 ±1	123 ± 3	88 ± 3	165 ± 3

b. Sample 20 nm IONCs	Frequency 105 kHz		Frequency 220 kHz		Frequency 302 kHz	
B [mT]	SAR [W/g_{Fe}] **before** MH	SAR [W/g_{Fe}] **after** MH	SAR [W/g_{Fe}] **before** MH	SAR [W/g_{Fe}] **after** MH	SAR [W/g_{Fe}] **before** MH	SAR [W/g_{Fe}] **after** MH
20	-	-	27 ± 2	-	35 ± 1	43 ± 1
25	22 ± 2	-	39 ± 4	-	57 ± 4	81 ± 2
30	38 ± 2	46 ± 2	60 ± 3	92 ±1	79 ± 1	116 ± 1
35	53 ± 1	71 ± 1	-	-	-	-
40	73 ± 2	94 ± 1	-	-	-	-

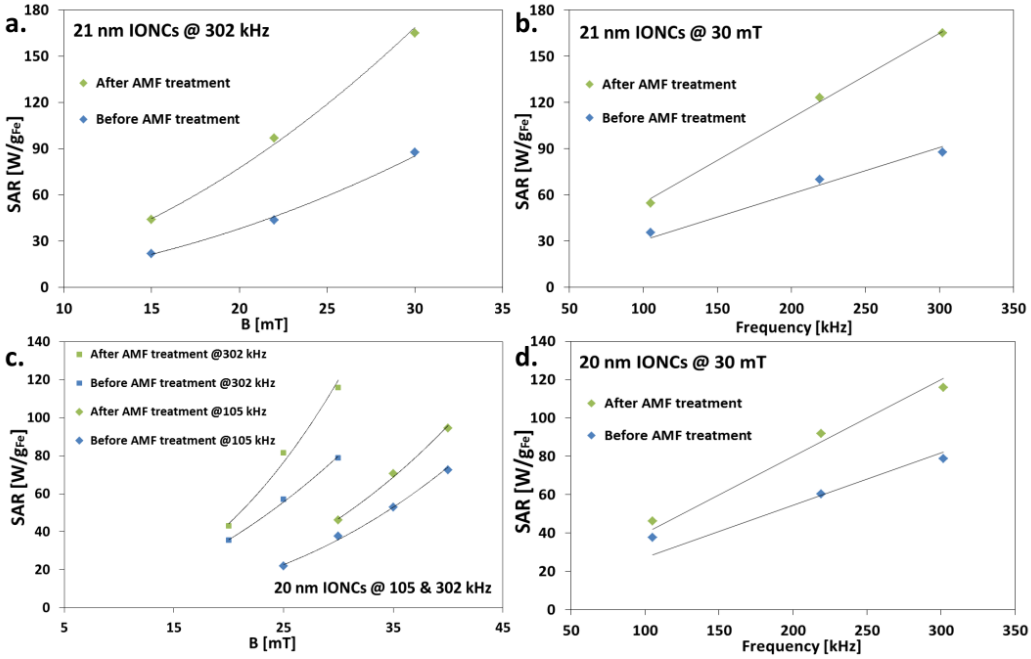

Figure 12: SAR values comparison, for 21 nm IONCs@PEG, as a function of (a) the applied magnetic field at the frequency of 302 kHz: untreated core-shell IONCs—blue diamonds, IONCs after 12 h 30 min of MH stimulation—green diamonds; (b) SAR values as a function of frequency at magnetic field amplitude of 30 mT: untreated core-shell IONCs—blue diamonds, IONCs after 12 h 30 min of MH stimulation—green diamonds. SAR values comparison, for 20 nm IONCs, as a function of (c) the applied magnetic field at the frequency of 105 kHz (untreated core-shell IONCs—blue diamonds, IONCs after 15 h 30 min of MH stimulation—green diamonds) and 302 kHz (untreated core-shell IONCs—blue squares, IONCs after 15 h 30 min of MH stimulation—green squares); (d) SAR values as a function of frequency at magnetic field amplitude of 30 mT: untreated core-shell IONCs—blue diamonds, IONCs after 15 h 30 min of MH stimulation—green diamonds. The solid black lines are guides for the eye.

For sample 20 nm IONCs@PEG, the macroscopic maximum temperature did not exceed 30 °C, therefore the MH stimulation was carried out for a longer time. After 15 hours and 30 minutes similar improvements in SAR values were obtained (up to 50% of initial SAR value). These results are plotted in Figure 12 and the data is summarized in Table 6 for both 20 and 21 nm cube edge length IONCs.

Similar to oxidation in harsh conditions, an improvement in SAR values was obtained, though more modest values were recorded. A comparison of SAR values after mild and harsh oxidation conditions *vs.* the initial SAR values for sample 21 nm IONCs@PEG is presented in Figure 13.

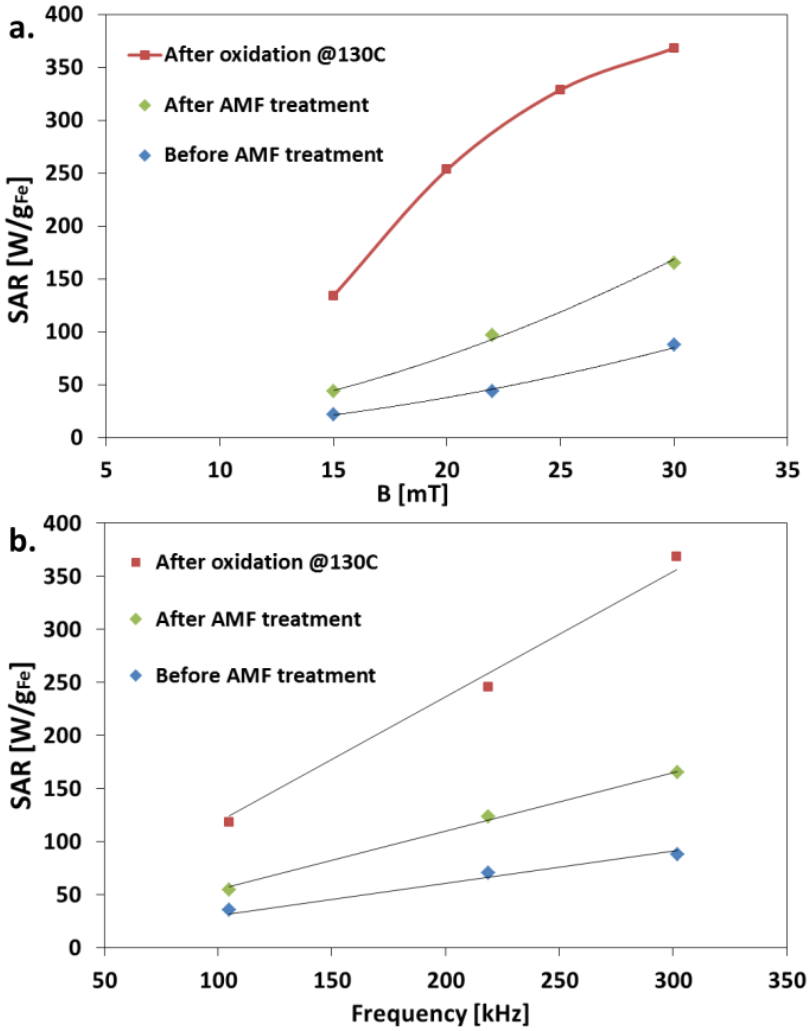

Figure 13: SAR values comparison, for 20 nm IONCs, as a function of (a) the applied magnetic field at the frequency of 302 kHz: untreated core-shell IONCs—blue diamonds, IONCs after 15 h 30 min of MH stimulation—green diamonds, and IONCs after 7 h @130 °C oxidation—red squares. (b) SAR values as a function of frequency at magnetic field amplitude of 30 mT: untreated core-shell IONCs—blue diamonds, IONCs after 15 h 30 min of MH stimulation—green diamonds, and IONCs after 7 h @130 °C oxidation—red squares. The solid black lines are guides for the eye. When curing by MH stimulation (for 15 h 30 min/**15.5 MH cycles**) a two fold increase in SAR values occurred, while maintaining the stability of the IONCs in water. Oxidation in

organic solvents at high temperatures increased the SAR values 4 fold, but after transfer in aqueous media the stability of the IONCs was lost, due to an increase in dipole-dipole interaction, similar to 'classical' 19 nm IONCs synthesized by our group[22] that were at the interface between superparamagnetic and ferromagnetic regimes at room temperature.

The highest SAR results were obtained by oxidation of the paramagnetic core in harsh conditions, but the results after mild oxidation were encouraging as well as it showed the possibility of improving the SAR values after functionalization with biologically relevant molecules. From research carried out previously by our group[32] we knew that at the surface of the IONCs the temperature was much higher compared to the macroscopic temperature measured in solution. This ΔT vanished within 4 nm from the surface. Therefore we believed that even if the mild curing was occurring without macroscopically changing the temperature, the temperature at the surface of the NP was higher, promoting a faster diffusion of oxygen and thus oxidation of the core.

To summarize, with these preliminary data (sections 2.2.-2.4.), new systems made up of iron oxide nanocubes (IONCs) with a core-shell structure—wüstite core/magnetite shell were characterized. The IONCs were transferred into physiological media by ligand exchange with a poly(ethylene glycol) based hydrophilic polymer. The suitability of these nanosystems for magnetic hyperthermia was tested. The specific absorption rate values were lower than the 'classical' Fe_3O_4 IONCs of similar size and shape, due to the paramagnetic core that did not contribute to the magnetic behavior of the IONCs. The gradual oxidation of wüstite core was studied by following the evolution of SAR values. The two distinct oxidations were: (i) the first

comprised a harsh environment of high temperatures for prolonged times and (ii) a second approach—a milder one—in which the increase in temperature was generated by the IONCs themselves when magnetically stimulated by hyperthermia. In both cases an increase in SAR values was observed. But the main difference was the stability of the IONCs in physiological media—after oxidation by magnetic stimulation the IONCs were stable in water, while the IONCs oxidized in harsh conditions showed stronger dipole-dipole interactions.

To this aim a new sample of 17 ± 2 nm cube edge length was prepared and a complete study of the SAR evolution over 25 cycles of magnetic hyperthermia stimulation was carried out. For two frequency (105 and 302 kHz), SAR values were recorded as a function of magnetic field amplitudes on the sample of untreated nanocubes and after a certain number of cycles, usually 10 and 25 MH cycles (Figure 14). Notably, at all field values, higher SAR values were recorded for the samples that underwent magnetic stimulation, consistent with previous results. By increasing the frequency from 105 to 302 kHz, as expected, the SAR values raised. For example, the SAR value at 302 KHz and 25 mT increased from 47 W/g_{Fe} to 106 W/g_{Fe} after 25 MH treatment cycles, indicating a change in structural and magnetic properties of the particles. Although the highest temperature recorded during the treatment never exceeded 34 °C, a gradual increase of the initial slope of the temperature *vs.* time curve and the maximum temperature reached at the end of the cycle was always registered as more treatment cycles were applied (Figure 1b).

To furthermore support the magnetically stimulated phase transformation hypothesis, rather than a bulk temperature effect *per se*, in a control experiment, the initial core-shell nanocubes were heated in a water bath for 25 hours (*i.e.* corresponding to 25 MH treatment cycles) applying the same heating profile as recorded in the MH treatment. For the sample heated in the water bath for 25 hours, the SAR value measured at 302 kHz and 25 mT was only 49 W/g_{Fe}, showing a marginal increase compared to the SAR of the initial sample (47 W/g_{Fe}).

Upon applying alternating magnetic fields, the particles went through multiple magnetization-demagnetization hysteresis loops, resulting in the conversion of magnetic to heat energy. It is known from previous studies that the temperature at the surface proximity of nanoparticles is substantially higher than the macroscopic temperature detected by the optic fiber sensor in the solution. Apparently, these hot spots could accelerate the oxidation and structural change in the core-shell nanocubes and consequently improved their heat performance.[32,33] It is also worth mentioning that the final SAR values recorded on the nanocubes after 25 cycles of MH treatment were higher than SAR values, measured in a comparable magnetic field amplitude and frequency, reported for iron oxide nanoparticles and nanoclusters obtained from other direct synthesis methods.[34,35]

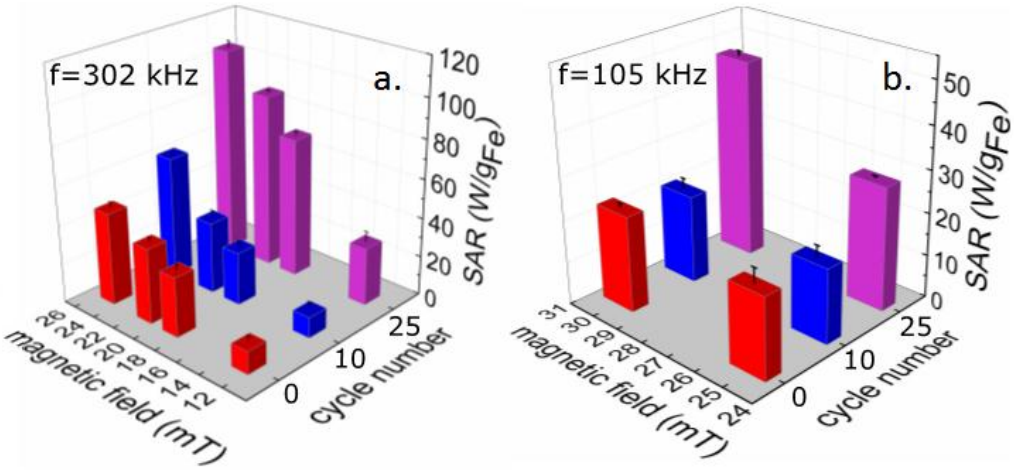

Figure 14: Temporal evolution of SAR values over 25 MH treatment cycles as a function of magnetic fields measured at two fixed frequencies of (a) 302 and (b) 105 kHz, respectively.[23]

On this 17 ± 2 nm sample a full structural and magnetic characterization was carried out: an in depth HRTEM/STEM, geometric phase analysis (GPA) and SQUID characterization to confirm the gradual core oxidation under MH stimulation (section 2.5). Finally, as a proof of concept, the attachment of biotin (able to recognize streptavidin) to the surface of the nanoparticles was carried out, followed by 25 cycles of MH treatments (section 2.6.). After magnetic stimulation by hyperthermia, the biological activity of biotin was checked by attaching streptavidin. If the proof of concept worked, biotin could potentially be replaced by any other molecular targeting moieties, making use of pairs like antibody-antigen or receptor-ligand for tumor targeting.

2.5. Structural and magnetic characterization

As previously mentioned, the in-depth structural and magnetic characterization of the core-shell structure and its gradual evolution under MH treatment was carried out on the $Fe_{1-x}O$/ $Fe_{3-\delta}O_4$ sample with an average cube edge length of 17 ± 2 nm (SAR values plotted in Figure 14). A representative TEM image is shown in Figure 15a, with the corresponding particle size histogram in Figure 15b. The nanocubes were transferred into water by the classical ligand exchange procedure with gallic-PEG. The water transfer approach allowed attaining single-core particles as shown previously from DLS and TEM studies.

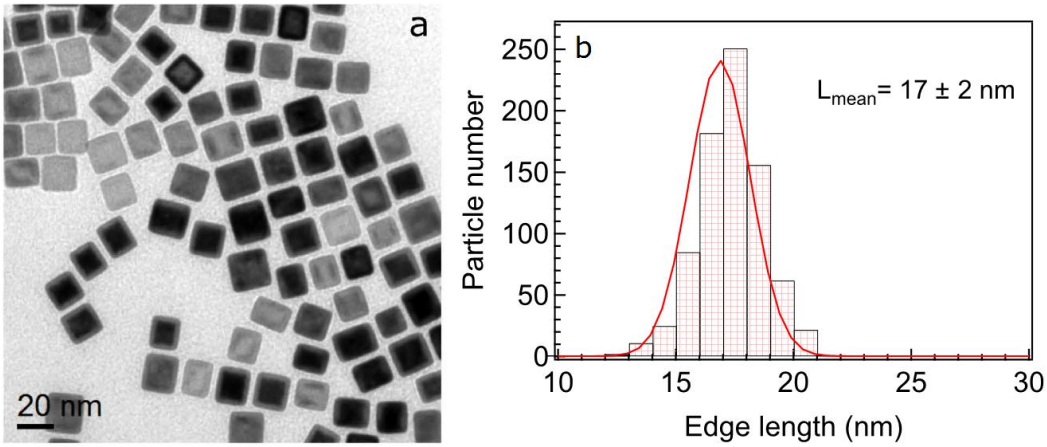

Figure 15: Representative TEM micrographs of (a) core-shell iron oxide nanocubes, dispersed in chloroform, for cube edge length of 17 nm ± 2 nm with (b) the corresponding size histogram.[23]

As briefly stated earlier, in a typical magnetic hyperthermia (MH) treatment cycle, the PEGylated nanocubes in water were sequentially exposed to 1 hour alternating magnetic fields at frequency of 331 kHz and field amplitude of 17 mT, followed by 30 minutes rest time at ambient conditions

and this cycle was repeated for a certain number of times (Figure 1a). For the structural and magnetic characterization, the gradual oxidation of the wüstite core was followed by comparison of the untreated core-shell nanocubes sample with the 10 and 25 MH cycles treated samples.

2.5.1. High resolution electron microscopy characterization

The core-shell structure of the initial nanocubes could easily be discerned by looking at HRTEM (Figure 16a), and it was even more evident in the STEM images (Figure 16c). On the same nanocube treated for 25 MH cycles, a more homogenous and ordered crystal structure was detected with no trace of the initial core-shell structure (Figure 16b and 16d).

To gain more information about the phase structure of the nanocubes, geometric phase analysis[36] was performed (see section 2.8.). The amplitude map of $\{220\}_S$, a fringe only ascribable to the $Fe_{3-\delta}O_4$ (Figure 16e) showed a significantly higher magnitude in the outer layers than in the core of the initial nanocubes. In the amplitude map, the higher intensity corresponds to a higher occurrence of the selected plane. Instead, the amplitude map of $\{220\}_S$ fringe of 25 MH cycles treated nanocubes revealed high magnitude on both the shell and the core of the particles, thus implying the growth of the $Fe_{3-\delta}O_4$ phase towards the core (Figure 16f). Based on the discontinuities observed in the amplitude map of the $\{220\}_S$ fringe, it appears that the $Fe_{3-\delta}O_4$ phase nucleates as small subdomains on the shell of nanocubes which grow larger during the oxidation. This island-like nucleation and growth has previously been observed in iron oxide core-shell nanoparticles.[18,21] Compared to the amplitude map of $\{400\}_S$-$\{200\}_{RS}$ of the initial nanocubes which is mainly brighter in the center (Figure 17a), the amplitude map of $\{400\}_S$ fringe after the MH treatment, showed a high magnitude throughout the whole nanocube (Figure 17b).

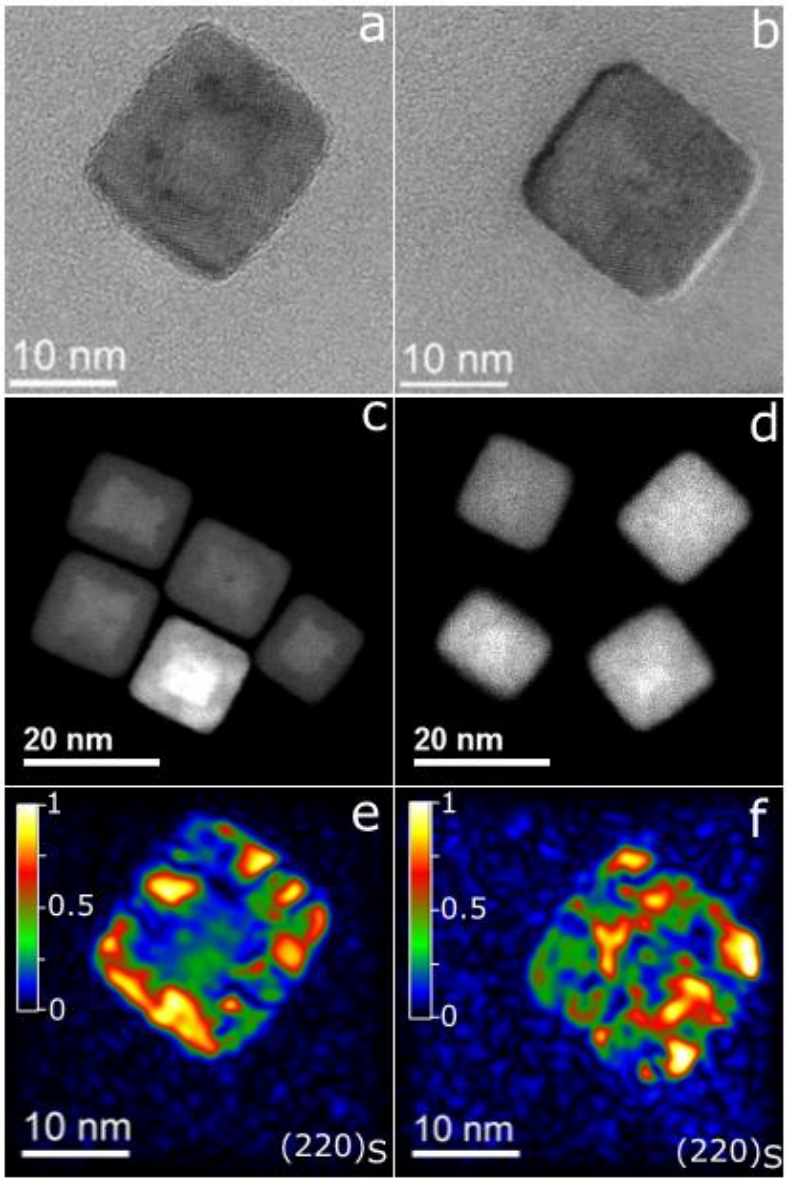

Figure 16: High resolution electron microscopy characterization. (a,b) HRTEM, (c,d) STEM micrographs of initial core-shell nanocubes and 25 MH cycles treated IONCs, and (e,f) amplitude maps of relative intensity of $\{220\}_S$ spinel-only fringe of initial core-shell and 25 MH cycles treated nanocubes, respectively, obtained from the GPA analysis. The $\{220\}_S$ fringe corresponds to the Fe_3O_4 phase. The [001] zone-axis lied parallel to the electron beam.[23]

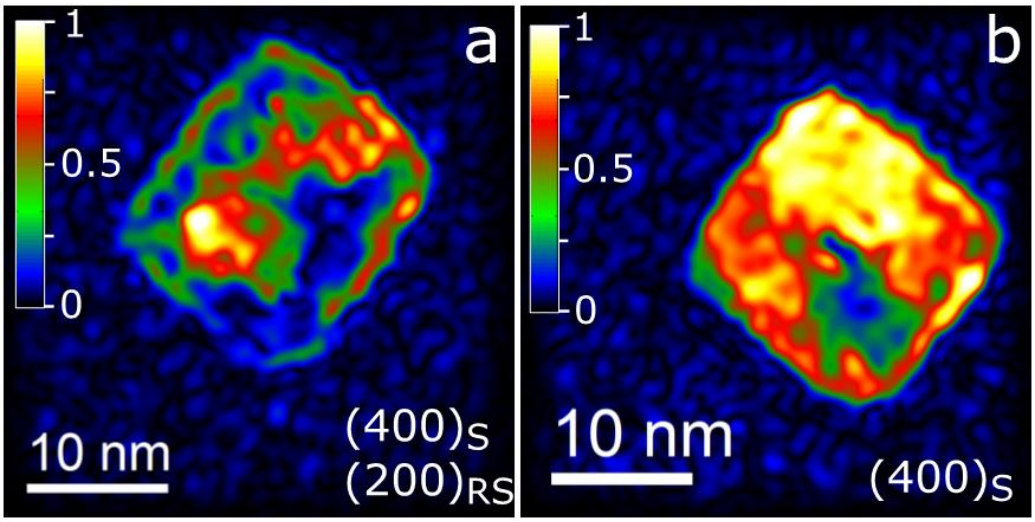

Figure 17: Amplitude map of $\{400\}_S/\{200\}_{RS}$ and $\{400\}_S$ fringe of (a) initial core-shell and (b) 25 MH cycles treated nanocubes respectively, acquired from the GPA analysis.[23]

2.5.2. Field and temperature dependence of magnetization

Since a change in the structural features of the nanocubes is reflected in their magnetic properties, the magnetization hysteresis loops were compared before and after the MH treatment. Interestingly, the superparamagnetic behavior of the initial core-shell nanocubes was not affected by the MH treatment, and samples after 10 and 25 MH cycles revealed zero coercive fields at 298 K as the initial core-shell nanocubes did. As an indicator of the change in the structure, it is important to trace the saturation magnetization (M_s). At 298 K, M_s increased from 53 emu/g_{Fe} for the initial nanocubes to 69 emu/g_{Fe} and eventually to 72 emu/g_{Fe} after 10 and 25 MH treatment cycles, respectively (Figure 18a). At 5 K, M_s value of 25 MH treated nanocubes was 94 emu/g_{Fe}—corresponding to 73 emu/g_{Fe3O4}—deviating from the bulk magnetite value[37] (Table 7). This deviation is mainly

due to the presence of a tiny fraction of FeO after full MH treatment (data not shown).

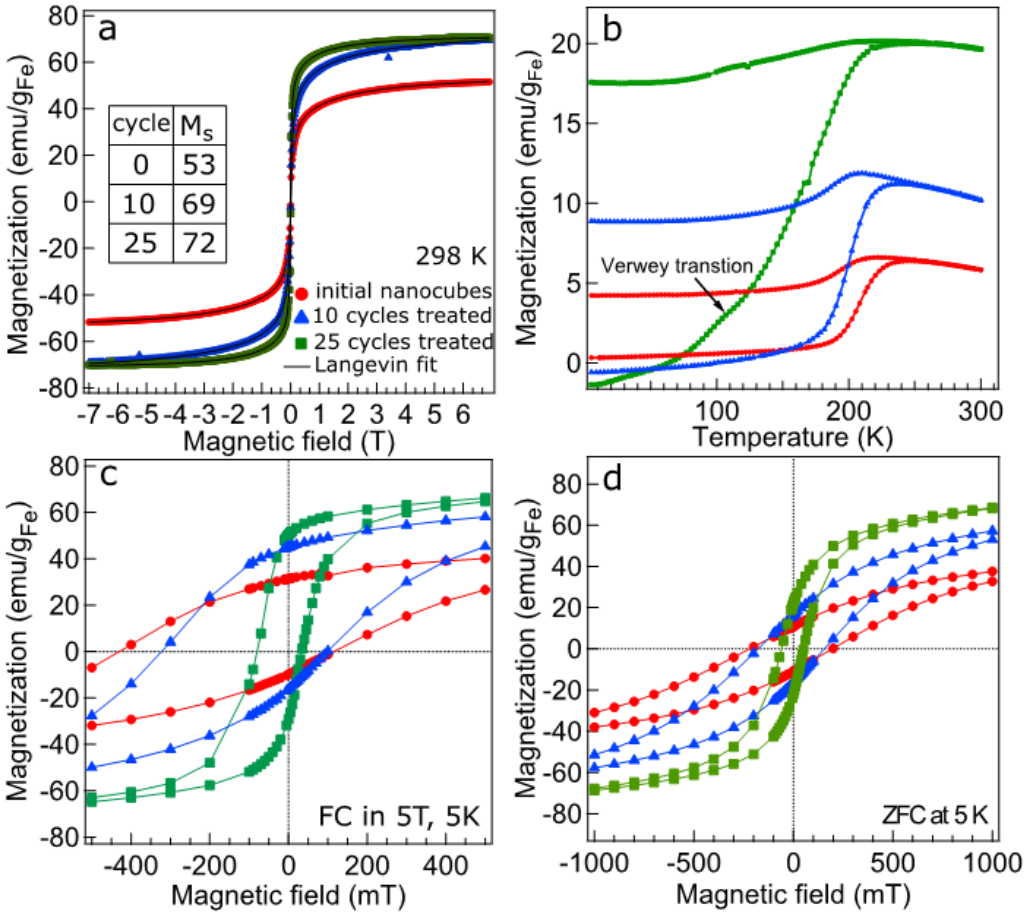

Figure 18: Field and temperature dependent magnetization. (a) M-H magnetization loops measured at room temperature (symbols) and the best fits (solid lines), (b) Temperature dependent zero-field-cooled (ZFC) and field-cooled (FC) magnetizations measured at 10 mT, (c) FC and (d) ZFC hysteresis loops of immobile particles cooled in 5 T and recorded at 5 K for the initial core-shell nanocubes (red circles), 10 (blue triangles) and 25 (green squares) MH cycles treated nanocubes.[23]

Table 7: Magnetic properties. M_s, H_C, H_{EB}, and T_b[‡] obtained from the analysis of the magnetization curves.

Sample	M_s^{298K} / M_s^{5K} [emu/g_{Fe}]	H_C [mT]	H_{EB} [mT]	T_B^{10mT} [K]
Initial IONCs@PEG	53 / 60	272	158	244
after 10 MH cycles	69 / 89	210	112	235
after 25 MH cycles	72 / 94	57	23	232
TA-130	79 / 92	20	5	226

By looking at the temperature dependent zero-field-cooled (ZFC) and field-cooled (FC) magnetizations (Figure 18b) it could be seen that the magnetization of initial core-shell and that of 10 cycles treated nanocubes rose slightly up to the Néel temperature (T_N) of FeO of 198 K. This huge rise around T_N was due to the transition from antiferromagnetic to paramagnetic spin configuration in FeO. Differently, on the nanocubes exposed to a full 25 MH treatment cycles, a clear kink at 110 K in the ZFC curve was seen which can be attributed to the Verwey transition in magnetite.[18,38] A long-range crystal structure ordering in 25 cycles treated nanocubes could be accounted for this observation. Prominently, the Verwey transition has not been observed in core-shell nanocubes which were annealed at 150 °C[21], analogous to the here studied nanocubes after thermal annealing at 130 °C (Figure 19b). This suggests that in the present $Fe_{1-x}O/Fe_{3-\delta}O_4$ nanocubes the magnetic heating triggered the phase transformation *via* different pathways than plain high temperature annealing. The superparamagnetic blocking temperatures (T_b) were estimated from the maximum peak in the ZFC curve (Table 7). As the particles undergo more cycles of MH treatment, T_b decreases.

‡ M_s (emu/g_{Fe}); T_b (K); H_C and H_{EB} (mT); TA-130: thermally annealed nanocubes for 7 h @130 °C.

The spin configuration in $Fe_{1-x}O$ was paramagnetic at room temperature and upon cooling below its T_N, the spins oriented antiferromagnetically. However, part of the spins at the $Fe_{1-x}O/Fe_{3-\delta}O_4$ interface remained uncompensated which pinned the $Fe_{3-\delta}O_4$ spins towards the cooling field. These antiferromagnetic-ferrimagnetic (AFM-FiM) interfaces generated large exchange bias fields H_{EB}, identified by shifted hysteresis loops in the opposite direction of the applied fields.[39] The measured FC magnetization curves performed on particles cooled to 5 K in 5 T, showed that as the particles were progressively oxidized, both horizontal and vertical shifts in the FC loops were reduced (Figure 18c). This is an indication of the shrinkage of $Fe_{1-x}O$ core and AFM-FiM interfacial spins. H_{EB} lowered significantly after 25 MH treatment cycles, not yet entirely vanished (Table 7). A similar trend was observed in Fe_3O_4 films and was linked to the presence of antiphase boundaries (APBs) at the interface of growing magnetic domains.[40–42] The ever existing H_{EB} field was detected in iron oxide nanocubes oxidized post synthesis up to 48 h as well as in single-phase Fe_3O_4 and γ-Fe_2O_3 nanocrystals.[34,37,43,44] It appears that on the nanocubes here studied, the exchange coupling plausibly had a structural origin. ZFC hysteresis loops revealed no asymmetric behavior. Also H_c reduced as the spinel domains grew larger.

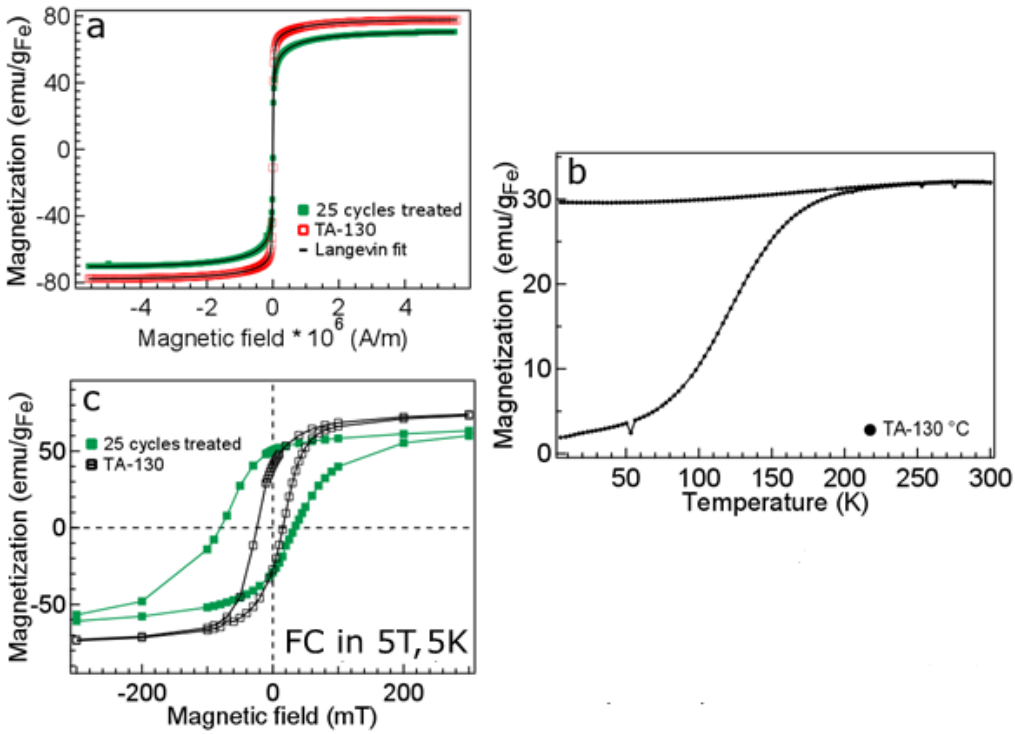

Figure 19: Structural and magnetic characterization of nanocubes thermally annealed at 130 °C (TA-130). (a) ZFC and FC temperature dependent magnetizations recorded in 10 mT, (b) magnetization hysteresis loops recorded at 298 K, (c) FC hysteresis loops of particles cooled to 5 K in 5 T.[23]

2.6. Bio-activity and colloidal stability

The main distinctive feature of the here proposed magnetically triggered oxidation compared to typical thermal annealing processes[21,38] is that the oxidation of the core-shell $Fe_{1-x}O$/ $Fe_{3-\delta}O_4$ nanocubes to $Fe_{3-\delta}O_4$ occurs under mild conditions—below 37°C as opposed to 130 °C for thermal annealing in harsh conditions. The MH treatment, being a process that is performed on core-shell nanocubes transferred in water when the inter-particle interactions are virtually absent—due to the antiferromagnetic-

ferrimagnetic structure—enables quantitative water transfer of well soluble and single core-shell particles with excellent colloidal stability. The shape and single-core nature of the nanocubes indeed remain well preserved after 25 MH treatment cycles (Figure 20).

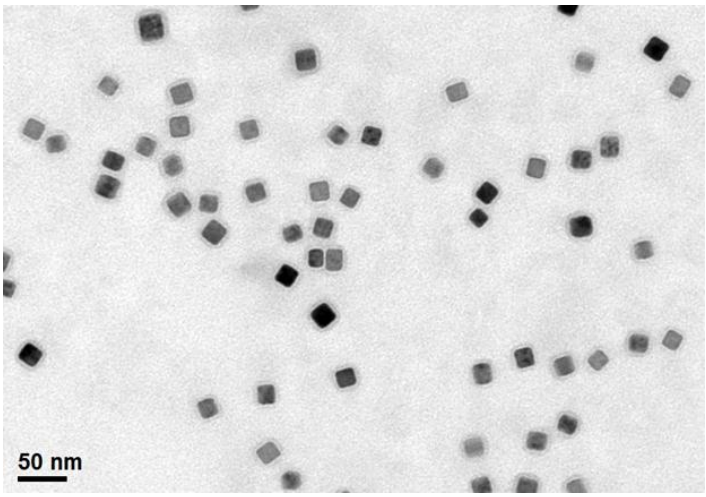

Figure 20: Representative TEM micrograph of 25 MH cycles treated PEGylated nanocubes. It can be clearly seen that the shape and single-core nature of the nanocubes remained intact after applying 25 cycles of MH treatment.[23]

Moreover, the mild temperature of the MH treatment also implies that biomolecules attached to the nanocube surface may preserve their functionality (*i.e.* targeting properties). To prove this point, the amino terminated moieties of PEG molecules on the nanocube surface were reacted with NHS carboxyl-activated biotin molecules (Figure 21). After biotin functionalization, the hydrodynamic diameter of the nanocubes increased from 30 nm to 40 nm (Figure 21d). Given the mono-modal size distribution and the absence of other peaks, the single-core nature of the biotin functionalized nanocubes was retained. In addition, the particle surface potential drops from

15 mV to 8 mV after biotin functionalization, indicating a change in the particle surface chemistry after biotin attachment.

The colloidal stability of biotin modified nanocubes after exposure to 25 MH treatment cycles obviously remained unaffected (Figure 21d). The dot blot assay was performed to evaluate the binding affinity of the biotin on the particle surface towards the FITC-streptavidin (Figure 21a-c). The nanocubes, prior and after having been exposed to the MH treatment, were spotted on the nitrocellulose membrane. After addition of the FITC-streptavidin solution, the fluorescence signals were detected on the spots, indicating that surface biotin was still able to bind streptavidin even if the nanocubes were previously exposed to the MH treatment. The spots emitted a fluorescence signal even at low nanocubes concentration of 1.8 nM which indicated a high density of biotin molecules attached per nanocube. On the contrary, the PEGylated nanocubes bearing no biotin molecules did not emit any fluorescence signal.

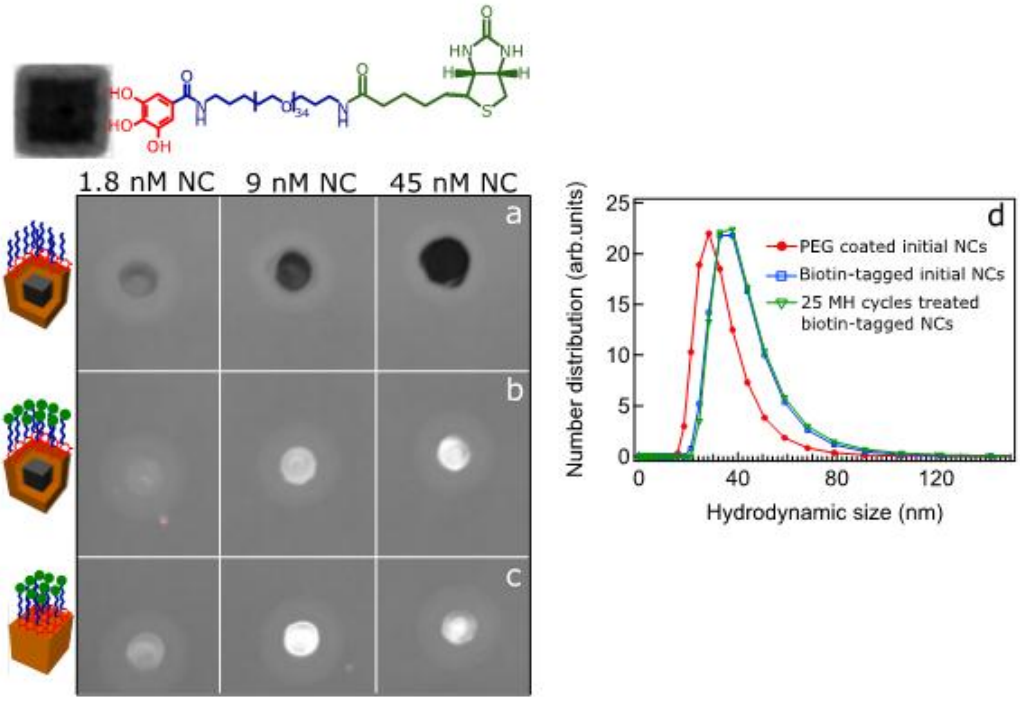

Figure 21: Functional and colloidal stability assays of biotin-modified nanocubes. Optical images taken at excitation wavelength of 488 nm from the dot blot nitrocellulose membrane of (a) PEGylated core-shell nanocubes, biotin-functionalized nanocubes (b) prior and (c) after 25 MH treatment cycles spotted at three different particle concentrations after being treated with FITC-streptavidin. The fluorescence signal indicated the presence of streptavidin bound to the biotin on the nanocubes before and after the MH treatment. (d) Hydrodynamic size distribution (number weighted) of PEG coated (red line) and biotin-tagged nanocubes prior (blue line) and after (green line) 25 MH treatment cycles. On biotin-nanocubes no change in hydrodynamic size was observed before and after the MH treatment.[23]

2.7. Conclusions

In the first chapter a nanosystem made up of core-shell iron oxide nanocubes $Fe_{1-x}O/Fe_{3-\delta}O_4$ coated with a poly(ethylene glycol) based polymer was investigated, with the main focus being the study of IONCs@PEG suitability as heating agents for magnetic hyperthermia. Afterwards, by modifying the core by different means of oxidation—either in air, at high temperatures or by magnetic stimulation under alternating magnetic fields—we could engineer IONCs with higher SAR values as compared to the initial IONCs.

The novelty of this approach is the self-oxidation of the paramagnetic wüstite core: the heat dissipated by the particles *via* hysteresis and relaxation processes was exploited to transform the $Fe_{1-x}O/Fe_{3-\delta}O_4$ core-shell nanocubes to a major $Fe_{3-\delta}O_4$ phase. The structural and magnetic characterizations confirmed the occurrence of magnetically triggered phase transformation, being responsible for the doubling of SAR values. Moreover, since this process occurred in mild conditions, we have demonstrated the possibility of conducting this treatment on nanocubes functionalized with biotin molecules without altering their binding affinity towards streptavidin and concomitantly preserving the colloidal stability of the MH treated nanocubes. The magnetically self-oxidized nanocubes possess all crucial physico-chemical features for being efficient heat mediators for *in vivo* cancer treatment by magnetic hyperthermia. These highly monodisperse and non-interacting core-shell nanocubes are potentially useful as heat mediators that upon magnetic hyperthermia stimulation at the tumor site may gradually improve their heating performance in a self-regulatory manner.

2.8. Experimental part

CHEMICALS

All reagents were obtained from commercial suppliers and used without further purification. Iron pentacarbonyl $Fe(CO)_5$ (98%), 1-octadecene (1-ODE, 99%), oleic acid (OA, 90%), triethylamine (99%), chloroform ($CHCl_3$), ethanol (EtOH), dichloromethane (DCM), dimethyl sulfoxide (DMSO), α,ω-aminopropyl-poly(ethylene glycol) (M_n = 1 500 g/mol), gallic acid, *N*-hydroxysuccinimide (NHS), *N*-(3-dimethylaminopropyl)-*N*'-ethylcarbodiimide hydrochloride (EDC), 2-(*N*-morpholino) ethanesulfonic acid hydrate (MES), phosphate buffered saline (PBS) (150 mM NaCl, pH 7.4), sodium chloride, sodium sulfate, sodium hydroxide, Tween20, NHS-activated biotin and fluorescein isothiocyanate (FITC) conjugated Streptavidin were purchased from Sigma-Aldrich. Sodium oleate (97%) was obtained from TCI. α-gallic-ω-amino-poly(ethylene glycol) (gallic-PEG) was synthesized as previously published.[23]

CHARACTERIZATION

Dynamic Light scattering (DLS)

Particle size measurements were carried out using a Malvern Zetasizer Nano series instrument, operated in the 173° backscattered mode on diluted aqueous solutions of nanoclusters. The measurements were performed at 25 °C. An equilibration time of 2 minutes was allowed before each measurement and at least three measurements were performed for each sample.

Transmission electron microscopy (TEM)

Conventional TEM images were obtained using JEOL JEM 1011 electron microscope, working with an acceleration voltage of 100 kV and equipped with a W thermionic electron source and a 11Mp Orius CCD Camera (Gatan

company, USA). Samples were prepared by placing a drop of sample onto a carbon coated copper grid which was then left to dry before imaging.

SAR measurements

The calorimetric measurements to determine the specific absorption rate value of the iron oxide nanocubes were carried out using the Nanoscale Biomagnetics instrument (DM100) operating over the range of frequencies from 105 to 302 kHz and fields up to 40 and 30 mT, for 105 and 302 kHz respectively. The SAR value was calculated using the formula:

$$SAR\ (\frac{W}{g}) = \frac{C}{m} \times \frac{dT}{dt}$$

where *C* is the specific heat capacity of dispersing medium (H_2O in most cases) per unit volume (J/K) and m is the concentration (g/L of Fe) of magnetic material in solution. The calorimetric measurements were carried out in quasi-adiabatic conditions and the slope of the curve $\frac{dT}{dt}$ was measured by taking into account only the first 20-25 seconds of measurement.

Elemental analysis

Elemental analysis was carried out via Inductively Coupled Plasma Atomic Emission Spectroscopy (ICP-AES) on a ThermoFisher iCAP 6000 series instrument. The samples were prepared by digesting 2.5-10 µL sample in 1 mL of aqua regia in a 10 mL volumetric flask, overnight. The next day, the flask was filled up to the graduation mark with milli-Q water and filtered through a 0.45 µm membrane prior to the measurement.

Magnetic characterization

Field dependent static magnetic measurements were carried out employing an ever cooled Magnetic Property Measurement System (*MPMS-XL*, Quantum Design) on immobile nanocubes. The samples were prepared by mixing 50 µL

of nanocubes dispersed in milli-Q water, at an iron concentration of 1-2 g/L, with 60 mg gypsum in the designated polycarbonate capsules and drying them thoroughly. The zero-field-cooled (ZFC) and field-cooled (FC) temperature dependent magnetization measurements were performed on samples prepared in the same way in the cooling field of 10 mT. The FC M-H hysteresis loops were recorded after cooling the samples from RT to 5 K in 5 T magnetic fields. The residual magnetic field in the SQUID magnets was nulled using the designated low field Hall sensor prior to ZFC measurements. All the presented magnetization data are corrected with respect to the diamagnetic and paramagnetic contributions of water and gypsum using the automatic background subtraction routine. The curves were normalized to the iron concentration as obtained from the elemental analysis.

Powder X-ray diffraction

Powder X-ray diffraction (XRD) analysis was conducted on a Rigaku SmartLab diffractometer machine operating at 150 mA and 40 kV. The patterns were acquired in Bragg-Brentano configuration using D-tex Ultra 1D detector in the reflection mode. The samples were prepared by drop casting concentrated particle suspensions on a zero diffraction silicon wafer.

Dot Blot assay

Dot Blot assay was carried out on pre-activated nitrocellulose membrane. Typically, 5 µL particle suspension was spotted on the membrane and left to dry thoroughly. Next, the membrane was gently shaken in 40 mL suspension of PBS-T20-dried milk powder (100:4 w/w%) for 30 minutes to block non-specific binding sites. Afterwards, the membrane was washed twice with PBS-T20 and finally soaked in 30 mL PBS-T20 containing 30 µL FITC-streptavidin. The mixture was gently shaken for 2 h in darkness and then the membrane was

rinsed 3 times with 30 mL PBS-T20 to remove unbound streptavidin counterparts. The membrane was imaged using Bio-Rad ChemiDoc MR imaging system at 488 nm wavelength.

Geometric phase analysis of high resolution TEM images

The geometric phase analysis (GPA)[36] has been performed employing the FRWRtools plugin for DigitalMicrograph (TM) (Gatan, Inc.). In summary, GPA measures the relative displacement of lattice fringes compared to a reference area from a HRTEM image to calculate the strain tensor (ε_{ij}) and the rotation (ω_{xy}). In GPA analysis, the Fourier component **g** of a particular set of fringes are selected. The intensity of these fringes is given by:

$$I_g(\boldsymbol{r}) = A_g(\boldsymbol{r})\exp(iP_g(\boldsymbol{r}))$$

with $A_g(\boldsymbol{r})$ the amplitude and $P_g(\boldsymbol{r})$ the phase.

The relative phase shift induced by a small displacement of the fringes **u**(**r**) with respect to the selected reference region is given by:

$$P_g(\boldsymbol{r}) = -2\pi \boldsymbol{g}.\boldsymbol{u}(\boldsymbol{r})$$

By taking two non-collinear **g** components into analysis, the two-dimensional displacement field holds:

$$\boldsymbol{u}(\boldsymbol{r}) = \frac{-1}{2\pi}(P_{g1}(\boldsymbol{r})\boldsymbol{a_1} + P_{g2}(\boldsymbol{r})\boldsymbol{a_2})$$

with $\mathbf{a_1}$ and $\mathbf{a_2}$ lattice vectors corresponding to $\mathbf{g_1}$ and $\mathbf{g_2}$ in the real space. The strain tensor and rotation are defined by:[45]

$$\varepsilon_{ij} = \frac{1}{2}(\frac{\partial u_i}{\partial x_j} + \frac{\partial u_j}{\partial x_i})$$

$$\omega_{xy} = \frac{1}{2}(\frac{\partial u_y}{\partial x} + \frac{\partial u_x}{\partial y})$$

Here, in a typical GPA analysis, a Fourier filtered power spectrum of an HRTEM image is used to generate amplitude and phase shift images. The phase shift of

the lattice fringes relative to a reference region (with phase fluctuations < ± 0.2) is employed to build the corresponding strain (ε_{ij}) and rotation (ω_{xy}) maps.

METHODS

Water transfer procedure by ligand exchange with gallic-PEG

Two mL of sample of IONCs ([Fe] = 6.744 g/L, 0.28 µM) were added to a 40 mL vial. Next 18 mL (50 mM) of gallic-PEG ligand were added to the vial (the amount of ligand was calculated in order to have 500 molecules ligand/nm^2) together with 1.8 mL triethylamine (TEA) (12.9 mM). The vial was closed with a cap, sealed with parafilm and left to stir overnight (*ca*.17 h) at a speed of 1 500 rotations per minute (rpm). The following morning the sample was transferred into a 500 mL separating funnel and was extracted with a mix of toluene, water and acetone (1:6:2 v%) (3x). After evaporation of the solvents (toluene, acetone, water) under reduced pressure, the sample was left under dialysis against water for at least 72 hours (50 kDa membrane). In the end, the sample was concentrated by centrifugation using Amicon 100 kDa tubes, at 1 500 rpm for 10 minutes. The final iron concentration was determined by ICP-AES.

Oxidation procedure of the IONCs in 'harsh' conditions

In a 50 mL three-neck round-bottom flask 20 mL of 1-ODE were slowly heated to 130 °C. When the temperature reached 70 °C the solution of IONCs (m_{Fe} = 10 mg) in $CHCl_3$ was added dropwise. Once all the solvent evaporated—when no more boiling of the solution was observed—the solution was kept at 130 °C for 7 hours. Afterwards the solution was left to cool to room temperature. The oxidized IONCs were collected by centrifugation and washed in a mixture of chloroform, acetone and ethanol (1:2:3 v%). The purification process was carried out three times and the NPs were stored in chloroform.

Oxidation procedure of the IONCs in 'mild' conditions

In a typical magnetic hyperthermia (MH) treatment cycle (Figure 1a), the PEGylated nanocubes in water (300 µL suspension having iron concentrations in the range between 4 to 10 g/L of Fe) were sequentially exposed to 1 h alternating magnetic fields at 331 kHz frequency and 17 mT field amplitude, followed by 30 min rest time at ambient conditions (with the lid of the vial off) and this cycle was repeated for a certain number of times. For a given frequency, SAR values were recorded as a function of magnetic fields on the sample of the untreated iron oxide nanocubes and after a certain number of cycles, usually 10 and 25 MH cycles.

Biotin functionalization of nanocubes

The EDC-NHS coupling chemistry was utilized to bind biotin to the surface of the nanocubes. First, the amino-PEG coated nanocubes were dispersed in MES buffer (0.01 M, pH 5.5) at a final particle concentration of 0.18 µM. A 180 µM solution of NHS-biotin was prepared by dissolving 0.001 g NHS-activated biotin firstly in 200 µL DMSO and then 29.8 mL MES buffer. To 1 mL nanocube MES buffer solution, 1 mL biotin solution (180 µM) was added such that the molar ratio of biotin/NC is 1 000. Subsequently, 1 mL EDC MES buffer solution (0.45 M) was poured into the mixture such that the molar ratio of EDC/NC is 250 000. The mixture was stirred vigorously at RT overnight. Afterwards, unbound and excessive biotin molecules were removed by filtering the suspension through Amicon 100 kDa filter tubes. The cleaning process was repeated five times. At the last filtering step, the particle suspension was concentrated to the desired iron concentration for further analysis and magnetic hyperthermia treatment.

3. Soft colloidal nanoclusters

3.1. Introduction

Iron oxide nanoparticles (IONPs) provide a valuable platform for a wide range of applications in biomedicine.[46] IONPs have been used for magnetic guidance in drug delivery, as contrast agents in magnetic resonance imaging and as heat mediators in magnetically induced hyperthermia[47]. The group of Dr. Teresa Pellegrino, to whom I belonged, is one of the few groups to have synthesized iron oxide nanocubes (IONCs) with high values of specific absorbance rate (SAR).[22] These 19 nm IONCs are very efficient heat mediators in hyperthermia, being at the interface between superparamagnetic and ferro(i)magnetic at room temperature (RT) and having high saturation magnetization, which accounts for their exceptional heat-ability, but on the other hand, they tend to strongly interact. This makes the coating of these nanocubes with biocompatible polymers like poly(ethylene glycol) (PEG) or thermo-responsive block copolymers more challenging than when working with smaller superparamagnetic nanoparticles. The functionalization of superparamagnetic nanoparticles, due to their non-interacting magnetic nature, is much easier to handle as achieved by many other groups, *e.g*. Prof. Wolfgang Parak[48,49], and also our group on different sizes of spherical iron oxide nanoparticles. As an alternative strategy, the idea behind the work presented in this chapter and the research presented in the previous chapter, was to work with nanoparticles that are still cubic-shape iron oxides, but they had a core-shell structure with a paramagnetic core at RT (antiferromagnetic below 198 K) and a ferri(o)magnetic shell, thus non-interacting at RT. These types of nanoparticles could be easily manipulated and thus transferred into water by different types of coatings including ligand exchange with PEG

molecules. At the same time we found that by post-treating them either by exposing them to an annealing process or to mild oxidation conditions under magnetic hyperthermia, their magnetic properties could be significantly improved thus resulting in much better post-treated hyperthermia agents. Therefore, initially, I focused my research on iron oxide core-shell nanocubes[20,21] and studied whether they were good heat mediators for magnetic hyperthermia after exposure to different oxidation processes. The results showed that we obtained IONCs with higher SAR values, as compared to the initial core-shell IONCs, by reducing the paramagnetic core by different means of oxidation: either in air, at high temperatures, or by long term exposure to an alternating magnetic field (AMF), the latter treatment in much milder conditions that meant at temperatures not surpassing body temperature.

The next objective of this part of the work was to investigate the possibility of increasing SAR value by clustering the nanoparticles in a controlled manner. Controlled or uncontrolled aggregation in centro-symmetrical 3D configuration—a beads like assembly—was expected to lower SAR values[35,50–52]. For example, Guibert *et al.*[35] studied the coupling between dynamic light scattering (DLS) and SAR measurements. They reported a correlation between the aggregation state and the heating properties of 12 ± 4 nm IONPs. Indeed, the formation of large and dense aggregates observed by DLS—when varying the ionic strength or solution pH—lead to a significant decrease of SAR values. Further information about the aggregates structure was obtained by carrying out small angle X-ray scattering (SAXS) experiments. They concluded that the compactness of aggregates played a crucial role, with

closer nanoparticles leading to a more important decrease of heating efficiency.

On the contrary, controlled aggregation in a chain like structures driven by anisotropic interactions of magnetic nanoparticles was supposed to increase SAR values. In this respect, as shown by the group of Martinez-Boubeta[53], by means of Monte Carlo simulations, they investigated the influence of dipolar interactions on the hysteresis loops in magnetic nano-assemblies. Their inspiration came from nature as indeed bacterial magnetosomes are cubic shaped iron oxide nanocubes individually coated with a lipid shell and naturally aligned in chain-like morphologies on protein filaments presenting state of the art hyperthermia performance. The computational modeling predicted an increase in the area of the hysteresis loop by increasing the chain length, though after 8 particles in a row, no noticeable heating performance gain was forecast. Alongside computational modelling, their experimental calorimetrical measurements on 44 nm magnetite nanoparticles forming μm long chains by applying a 0.12 T magnetic field, demonstrated the important role of chain alignment on the heating efficiency.[53]

As briefly mentioned before, in addition to their therapeutic effect, IONPs can act as diagnostic/imaging tools, by their use as contrast agents (CA) in magnetic resonance imaging (MRI). This imaging technique allows the investigation of diseased tissues and the blood flow around it; therefore the magnetic carriers can be tracked inside the body and imaged *in vivo*.[54]

Xiong Fei and co-workers[55] reported an assembly procedure of rubik-like structures by solvent-exchange using 10 nm oleic acid coated IONCs and dioleate-modified polyethylene glycol. The rubik-like nano-assemblies were

used for the delivery of the highly hydrophobic chemotherapeutic drug paclitaxel and their suitability as *in vivo* MRI contrast agents was assessed. The results suggested an increase in the therapeutic effect of paclitaxel delivered by the magnetic carriers in comparison with the same dose of free paclitaxel. The authors envisioned the rubik-like structures as potential multifunctional theranostic nanodevices capable to detect, diagnose, treat and monitor tumors. However, in their case, the heat efficiencies of the magnetic nanoparticles as assembled or as single nanoparticles were not compared. Inspired by this work, we explored a procedure that allowed with a similar amphiphilic polymer and playing with the reaction parameters to obtain both controlled assemblies of nanocubes and single coated nanocubes thus allowing a direct comparison of their magnetic properties and their magnetic hyperthermia performance.

Dioleate-modified polyethylene glycol[55] is one of many amphiphilic polymers used to form micellar clusters of magnetic nanoparticles. Among other diblock copolymers, poly(ϵ-caprolactone)-*b*-poly(ethylene glycol) (PCL-*b*-PEG)[56], poly(trimethylammonium ethylacrylate methyl sulfate)-*b*-poly(acrylamide)[57], poly(ethylene oxide-*b*-acrylate) (H_2N-PEO-*b*-PAA)[58], poly(lactic-*co*-glycolic acid)-*b*-poly(ethylene glycol) (PLGA-*b*-PEG)[59] and even triblock copolymers like poly(ethylene imine)-*b*-poly(ε-caprolactone)-*b*-poly(ethylene glycol) (PEI-*b*-PCL-*b*-PEG)[60], have been used to form soft colloidal nanocrystal clusters (term introduced by the group of Bakandritsos et al.[61]) as contrast agents for MRI. The reason behind the assembly of superparamagnetic nanoparticles was the enhancement of T_2 relaxation process, leading to higher r_2 relaxivity, alongside an increase in magnetic response while maintaining the superparamagnetic characteristics.

To date, these clusters have mainly been exploited for magnetic resonance imaging[55–60] and few studies have been dedicated to studying their performance for magnetic hyperthermia. The research presented in this chapter aims to deepen the knowledge on controlled clustering of iron oxide nanocubes with the specific goal of studying hyperthermia response of individual nanocubes *vs.* soft colloidal nanoclusters of different sizes, with hydrodynamic diameters below 100 nm.

3.2. Controlled clustering of various types of nanoparticles

Herein the controlled clustering of IONPs during their aqueous phase transfer is being reported. Briefly, the method consists of the following steps (Figure 1):

i) dispersion of oleic acid coated nanoparticles in THF in which the amphiphilic polymer, namely poly(styrene-*co*-maleic anhydryde) cumene terminated (M_n = 1 600 g/mol), was previously dissolved;

ii) controlled dropwise addition of water, by syringe pump, under sonication in an ice bath,

iii) slow evaporation of the organic solvent overnight, thus transfer of MNPs into aqueous phase,

iv) fast addition of $CHCl_3$ in order to induce aggregation.

To set this main protocol different parameters were investigated by changing them one by one, including the rate of THF evaporation, the ratio of water to THF, the total solution volume, and the amount of polymer. However the main parameter that actually controlled the tuning of the size and configuration of the nanoclusters, as reported in detail in section 3.2., is the ratio of amphiphilic polymer, poly(styrene-*co*-maleic anhydride) to the particle

surface (Figure 2). The method proved to be versatile as magnetic nanoparticles of different shapes (spherical, cubic, and cubic with rounded edges) and sizes (in the range from 15 to 22 nm), and even gold nanoparticles, were clustered in a controlled manner, and without the use of an external magnetic field—in the case of MNPs. The magnetic properties of the clusters were characterized by AC susceptibility measurements, which confirmed the DLS and TEM results in terms of cluster size. By increasing the ratio of molecules of polymer per nm^2 of particle surface bigger nanoclusters were obtained. The soft colloidal nanoclusters were studied as nanoheaters for magnetically induced hyperthermia in section 3.3.

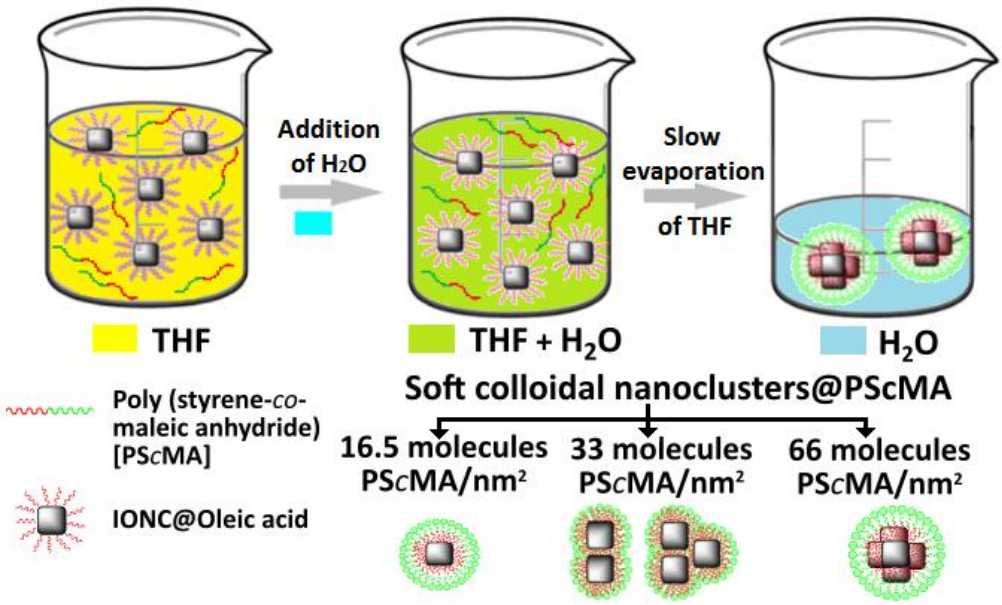

Figure 1: Schematic representation of the formation of soft colloidal nanoclusters

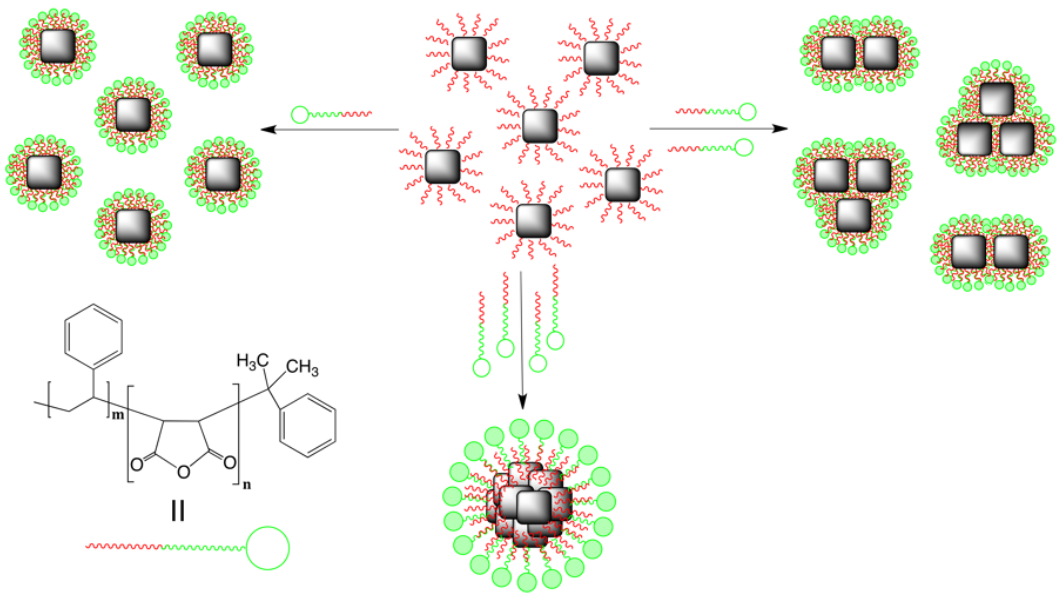

Figure 2: Schematic representation of fine-tuning the size of soft colloidal nanoclusters by varying the amount of amphiphilic polymer added during the water transfer

In an attempt to reproduce the work of Xiong and co-workers[55], 35 μL of iron oxide nanocubes solution ([Fe] = 6.09 g/L), with a core-shell structure and a cube edge length of 20.2 ± 1.5 nm (Figure 3a), were dispersed in 10 mL THF alongside the amphiphilic polymer poly(styrene-*co*-maleic anhydride) (PS*c*MA), cumene terminated (M_n = 1 600 g/mol), in a ratio of 66 polymer chains/nm^2 of nanoparticle surface. The choice of the core-shell nanocubes, made of FeO core and Fe_xO_y shell, was due to their non-interacting magnetic nature and their stability in THF—a full solubility of such nanoparticles as shown by the transparent THF solution was observed. Both parameters were considered a prerequisite for a successful clustering procedure—attempts done with non-completely soluble nanoparticles were never successful (data not shown). Afterwards, 1 mL H_2O was added dropwise by syringe pump at the

speed of 0.5 mL per minute, while sonicating the solution in an ice bath. The solution had to remain clear, if it became turbid during the addition of water that was an indication that the water transfer would not proceed as expected. To remove THF, several evaporation methods were tried for transferring the IONCs from the organic into the aqueous phase, and among them: i) evaporation under reduced pressure (for roughly one hour), ii) atmospheric pressure evaporation of THF, while stirring the solution with a magnetic stirrer in an open beaker under the fume hood (for several hours), and iii) nitrogen bubbling of the solution (for a couple of hours) were considered.

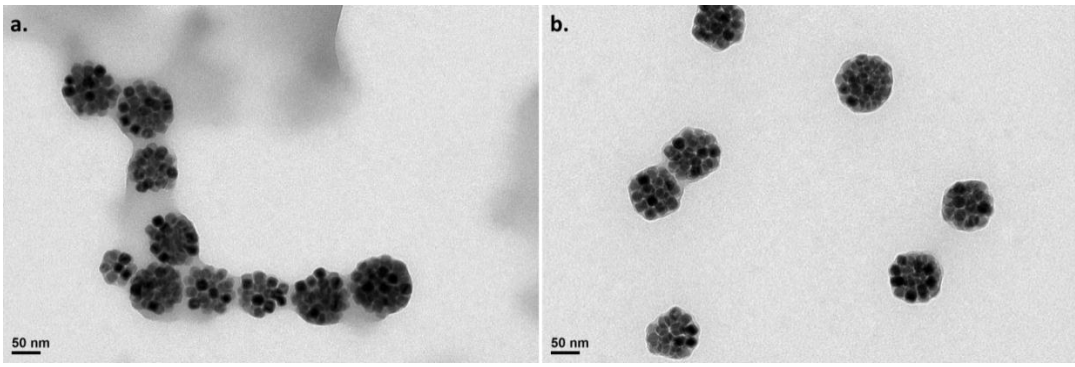

Figure 3: Impact of $CHCl_3$ addition as the last step in cluster formation process. TEM micrographs of clusters made of 19 nm core-shell IONCs (a) in H_2O/THF mixture before $CHCl_3$ addition, (b) in H_2O, after $CHCl_3$ addition. Before addition of $CHCl_3$ a polymer layer was observed on the TEM grid. After addition of $CHCl_3$ the excess of polymer was removed and it was no longer present in aqueous phase.

Though the first results were encouraging as the clusters were obtained, when using evaporation under reduced pressure and nitrogen bubbling, the reproducibility of the experiments was not good. This suggested that cluster formation in a controlled manner depended on the rate of THF evaporation, that could not be so easily controlled by the aforementioned

conditions. Therefore, a new evaporation condition was tried: slow evaporation of THF over 24 hours, when placing the 20 mL vial (without the lid) on a horizontal shaker at a speed of 125 rotations per minute (rpm). Unlikely previous evaporation conditions, in this case, the solution was usually clear after the evaporation of THF. Lastly, $CHCl_3$ was added to discard the excess of polymer. Two layers were formed, with the top layer being the aqueous phase that contained the nanoclusters.

Schematically, the overall clustering process is shown in Figure 1. The as-synthesized oleic acid coated magnetic nanoparticles after being in contact with the polymer solution in the mixture THF/water were transferred into the water phase by slowly evaporating the THF and intercalation of the amphiphilic polymer—poly(styrene-*co*-maleic anhydride)—with the surfactant shell. In a H_2O/THF mixture, the nanoparticles were already clustered (Figure 3a) and a layer of polymer was observed on the TEM grid in between clusters. After addition of $CHCl_3$ the excess of polymer was discarded by migrating to the interface between organic and aqueous phase, with only clusters remaining in aqueous phase as seen in Figure 3b.

3.2.1. Clusters of iron oxide nanocubes of different sizes

Three samples of IONCs in the range from 16 to 21 nm were used for the first clustering experiment. As seen from the DLS results in Table 1 and the TEM micrographs in Figure 4, with an increase in size of the cube edge length, while keeping the amount of polymer constant at *ca*. 70 molecules of polymer/nm^2, bigger clusters were formed—both in size and in number of particles per cluster.

The average hydrodynamic diameters d_H varied from 38 nm to 190 nm, by intensity, for clusters formed with 16, 20 and 21 nm cube edge length, respectively. The corresponding transmission electron microscopy micrographs are shown in Figure 4. As expected, the diameters as seen by TEM were smaller than the corresponding DLS values, as by TEM only the inorganic particle volume was observed, while in solution the distribution of particle hydrodynamic size was measured.

Table 1: DLS results of 16, 20 and 21 nm IONCs@PS*c*MA in H_2O

Sample	Z-Ave [nm]	PdI	Number Mean [nm]	Intensity Mean [nm]	Volume Mean [nm]
16 nm IONCs@PS*c*MA	33 ± 1	0.16 ± 0.02	21 ± 1	37 ± 1	27 ± 5
20 nm IONCs@PS*c*MA	93 ± 1	0.08 ± 0.01	67 ± 1	102 ± 1	86 ± 1
21 nm IONCs@PS*c*MA	178 ± 1	0.05 ± 0.02	154 ± 4	190 ± 4	192 ± 5

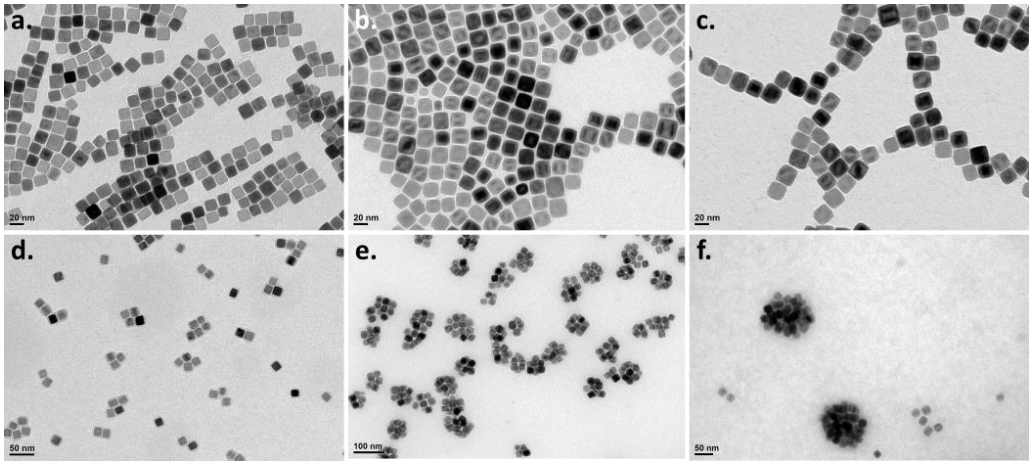

Figure 4: Soft colloidal clusters formed using IONCs with a cube edge length of 16, 20 and 21 nm. (a,b,c) TEM micrographs of as-synthesized (a) 16 nm, (b) 20 nm, and (c) 21 nm IONCs in $CHCl_3$. (d,e,f) TEM micrographs of soft colloidal clusters (IONCs@PS*c*MA) dispersed in H_2O, formed starting from: (d) 16 nm (Z-average 33 ± 1, PDI 0.16), (e) 20 nm (Z-average 93 ± 1, PDI 0.08), and (f) 21 nm IONCs (Z-average 178 ± 1, PDI 0.05).

3.2.2. Cluster size tuning by changing the amount of polymer

The further studies involved the 20.2 ± 1.5 nm IONCs (Figure 4b) that formed raspberry like clusters at a ratio of 66 molecules polymer/nm^2 of particle surface (Figure 4e). As described by Pöselt and co-workers[60] by changing the molar excess of the triblock copolymer PEI-*b*-PCL-*b*-PEG, from 5 to 1 000 fold the amount of IONPs, the size of centro-symmetrical clusters formed could be adjusted between 51 and 141 nm, starting from *ca*. 10 nm superparamagnetic IONPs. The authors reported that a high ratio favored the formation of discretely encapsulated MNPs, whereas at low ratio particle clusterization was enforced by the relative depletion of polymer. In our case, the ratio was calculated as the number of molecules of polymer per nm^2 of the surface of the nanocubes (66 molecules/nm^2 corresponding to a weight ratio 1:11 MNPs to diblock copolymer and roughly to a stoichiometric molarity). Given that the average d_H of the starting clusters was 102 ± 1 nm, by intensity, the amount of polymer was decreased in order to form smaller clusters.

Contrary to the results reported by Pöselt et al.[60], in our case with an increase of the polymer amount the degree of clustering increased as seen from the TEM micrographs in Figure 5 and the DLS results plotted in Figure 6. If we are to compare the two procedures, in both cases the solvents used were THF and H_2O. In their case the THF was removed by nitrogen bubbling, while we opted for the slow THF evaporation for a higher reproducibility of cluster formation. Most likely the major difference between the two procedures was the amphiphilic polymer itself: a triblock polymer poly(ethylene imine)-*b*-poly(ε-caprolactone)-*b*-poly(ethylene glycol) with an average M_n between 6 500 - 9 400 g/mol was used by the group in Hamburg, while we used the

copolymer poly(styrene-*co*-maleic anhydride) with an average M_n of 1 600 g/mol.

As judged from the inter-particle distance (Figure 5a), for the ratio of 16.5 molecules of polymer/nm^2, the majority of the nanocubes were individually coated, while by doubling the amount of polymer dimers and trimers were formed (Figure 5b). In this specific case, the dimers and trimers arrangement was even more evident when looking at a collection of TEM pictures in which clearly isolated groups of two or three nanocubes were seen (Figure 5E-H). The corresponding DLS volume distributions are plotted in Figure 6. The volume weighted hydrodynamic diameters were 38, 51, 68 and 99 nm for 16.5, 33, 50 and 66 PS*c*MA/nm^2, respectively. The increase of the cluster size with the increase of the polymer was probably due to a preferential interaction of the hydrophobic part of the copolymer, the poly(styrene), with sides of different nanocubes, instead of the surface of only one cube, thus decreasing the strain on the polymer chain, while preserving the hydrophobic interactions and increasing its overall gyration radius.

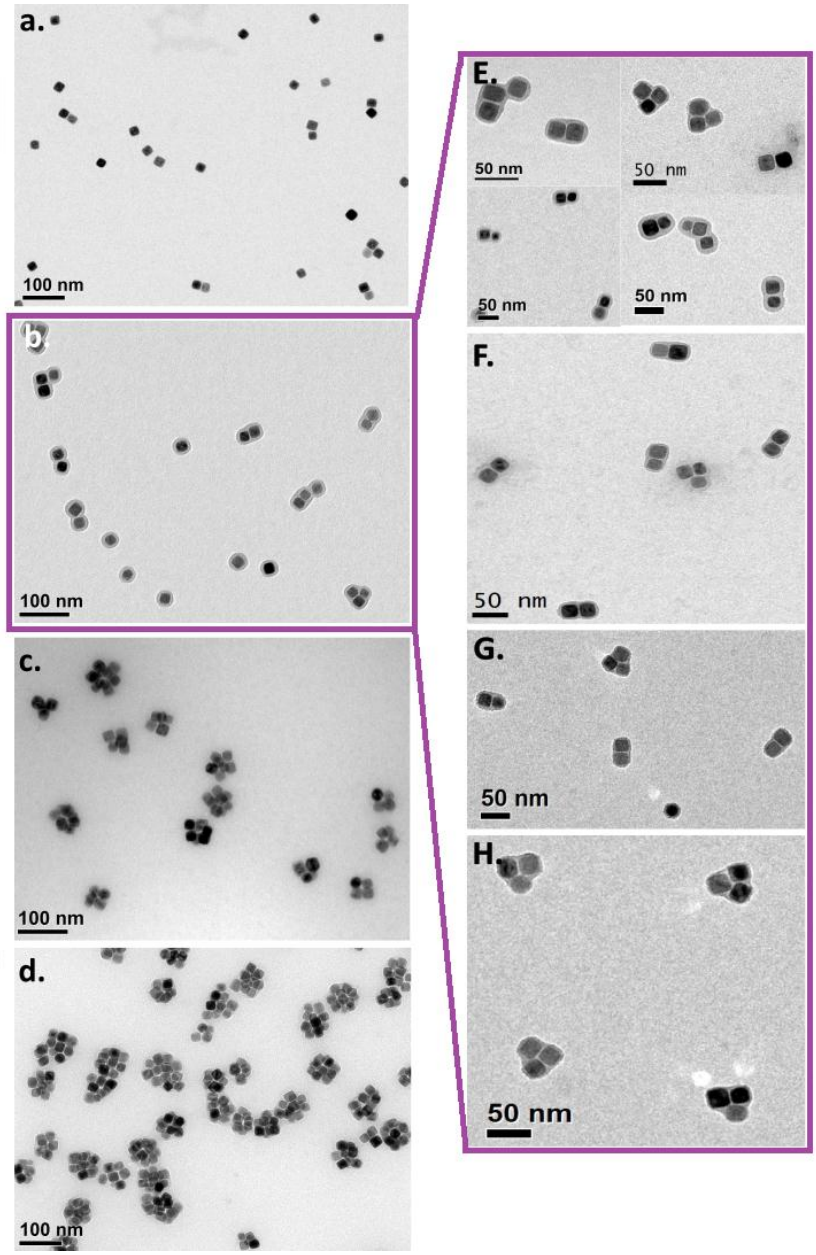

Figure 5: Clusters formed using 20 nm core-shell iron oxide nanocubes. Representative TEM micrographs of IONCs@PS*c*MA in H_2O for a ratio of (a) 16.5, (b) 33, (c) 50 and (d) 66 polymer chains/nm^2. (E-H) a collection of close ups of dimers and trimers formed for a ratio of 33 molecules PS*c*MA/nm^2.

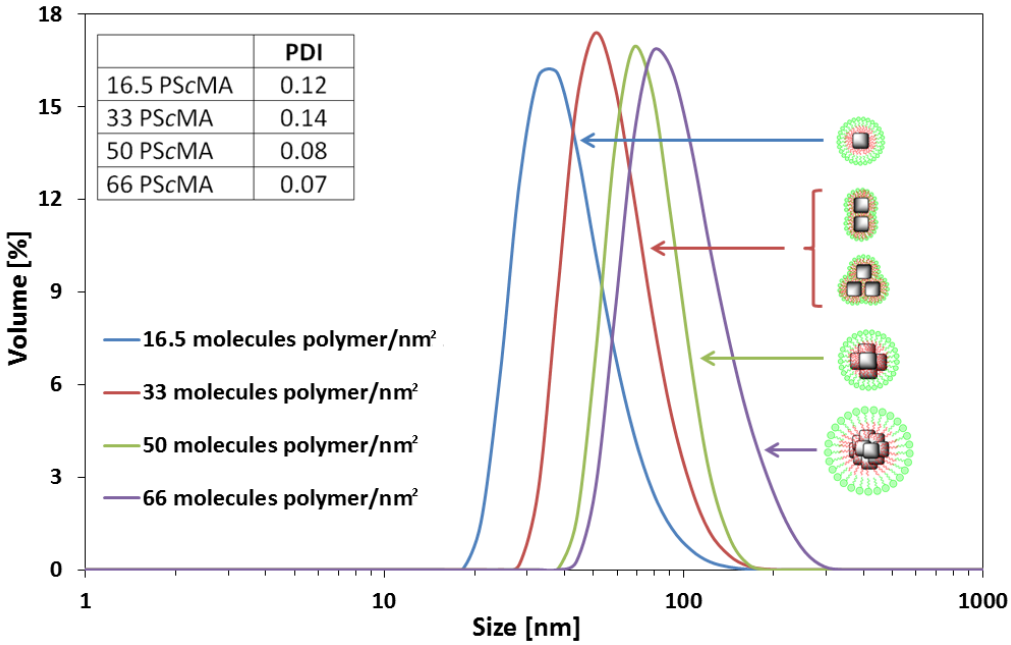

Figure 6: Tuning the mean hydrodynamic diameter of clusters by varying the polymer amount. DLS volume distributions of soft colloidal clusters in H_2O starting from 20 nm IONCs. The d_H was adjusted between 38 and 99 nm, by volume. No aggregation of clusters was detected as PDI values were between 0.07 and 0.14 (see inset).

3.2.3. Clusters of iron oxide nanoparticles of different shapes

Taking into consideration that most of the literature on controlled clustering of iron oxide nanoparticles dealt with spherical IONPs, the next step was to test the versatility of our method by changing the shape of the nanoparticles. Two shapes were tested: spherical and cubic with rounded edges. Though most of the investigations report clustering of superparamagnetic nanoparticles with sizes below 10 nm (e.g.: 6.3 nm[57], 6.6 and 9.5 nm[58], 8 nm[59], 4, 7.5, 8.7, 9.8, 11.8 and 13.1 nm[60]), we were inquisitive to find out whether 22 nm spherical IONPs (Figure 7a) would present the same clustering trend as the cubic IONCs with a similar size.

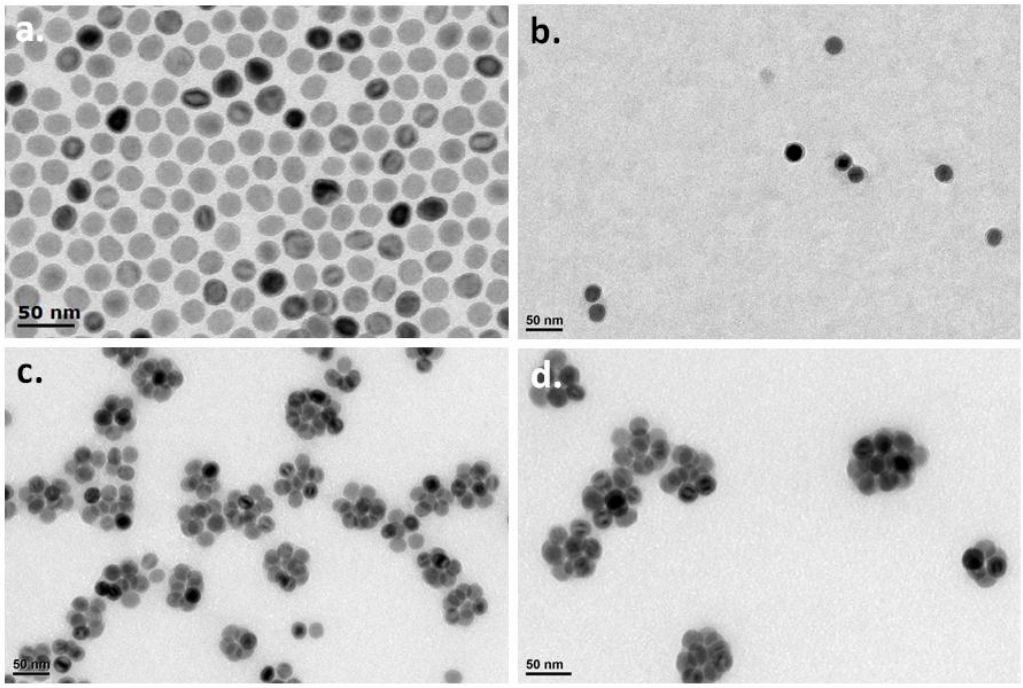

Figure 7: Soft colloidal clusters formed using spherical iron oxide nanoparticles. TEM micrographs of (a) as-synthesized 22 nm spherical IONPs in $CHCl_3$ and nanoclusters formed for a ratio of (b) 18, (c) 36 and (d) 53 PS*c*MA molecules/nm^2 particle surface, dispersed in H_2O.

The TEM micrographs presented in Figure 7 suggest that the trend of forming bigger clusters for bigger amounts of polymer persisted for spherical nanoparticles as well. For 18 molecules of polymer/nm^2, Figure 7b, one can see both individual nanoparticles and dimers, but by considering the hydrodynamic diameter distributions plotted in Figure 8, in solution d_H by volume mean was equal to 52 nm therefore we supposed that the majority of nanoparticles formed dimers.

By doubling and tripling the amount of copolymer, from 18 to 36 and 53 PS*c*MA/nm^2, the cluster size increased to 70 and 86 nm by volume mean. As

seen from TEM micrographs in Figure 7c and 7d, with spherical particles more centro-symmetrical clusters were observed.

Lastly, a sample of 19 nm core-shell iron oxide nanocubes with rounded edges was transferred into aqueous phase by the solvent-exchange method described above. The previously used core-shell nanocubes had a FeO paramagnetic core representing 40% v./v., while this new batch had a bigger FeO core, occupying 80% of the volume (data not shown here). The controlled clustering was once again achieved and the size of the clusters was tuned by changing the amount of polymer used. The average hydrodynamic diameters by volume were 30, 72 and 106 nm for 17, 35 and 71 PS*c*MA molecules/nm^2, respectively, as plotted in Figure 9. The corresponding TEM micrographs can be seen in Figure 10.

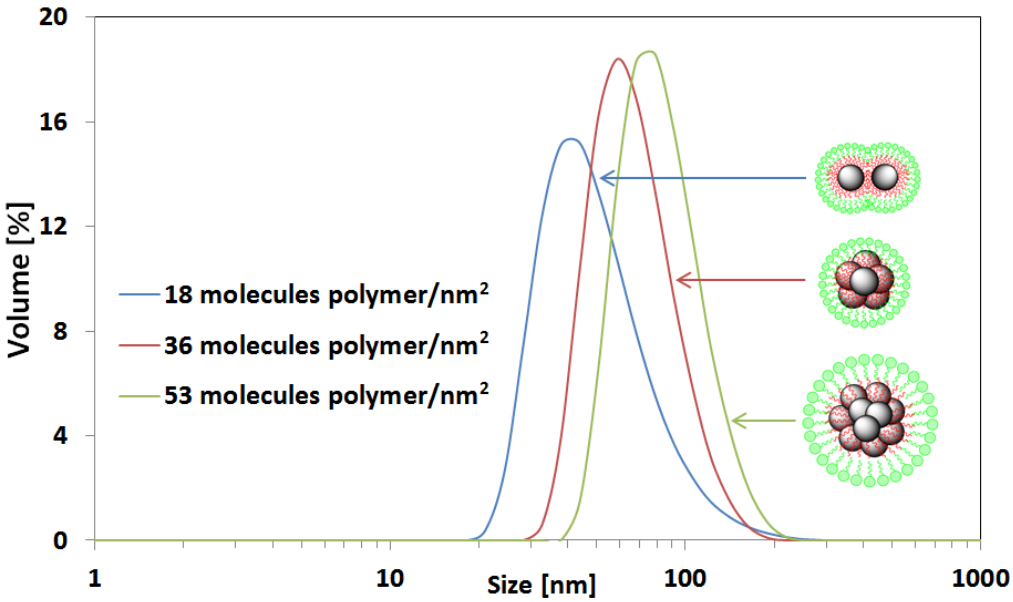

Figure 8: Tuning the mean hydrodynamic diameter of clusters by changing the polymer amount. DLS volume distributions of soft colloidal clusters in H_2O starting from 22 nm spherical IONPs. The d_H was adjusted between 52 and 86 nm, by volume.

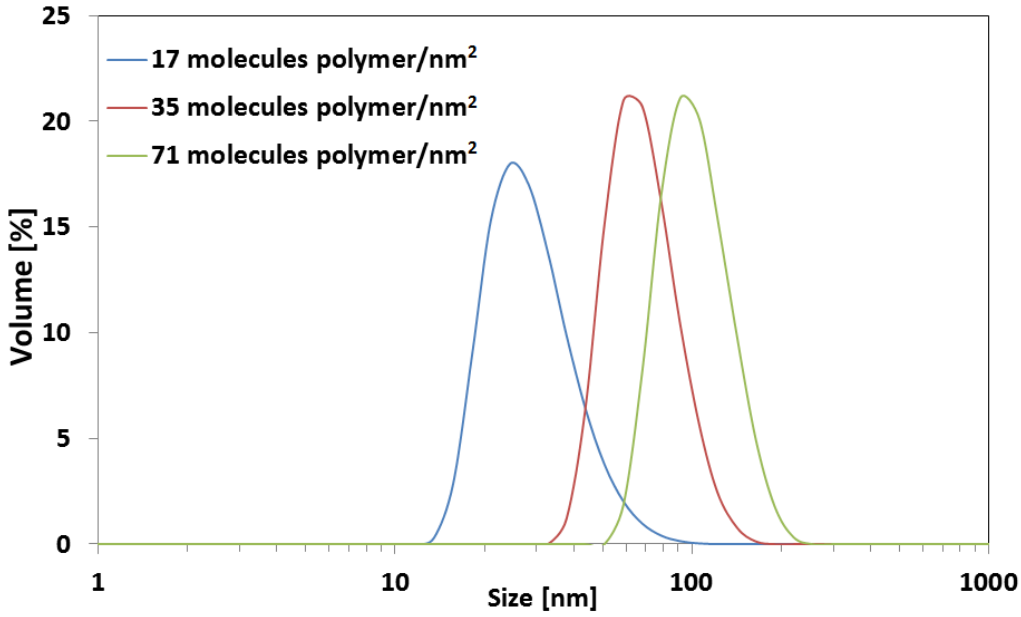

Figure 9: Tuning the mean hydrodynamic diameter of clusters by changing the polymer amount. DLS volume distributions of soft colloidal clusters in H_2O starting from 19 nm cubic IONPs with rounded edges. The d_H was adjusted between 30 and 106 nm, by volume.

For 17 molecules of polymer/nm^2 the IONCs were discretely encapsulated inside a polymeric shell (Figure 10a) as confirmed by DLS results (Figure 9—blue curve), with d_H equal to 30 nm by volume mean (24 nm by number mean). When quadrupling the amount of amphiphilic polymer the hydrodynamic diameter increased to 106 nm (Figure 9—green curve) by volume mean (91 nm by number mean). Higher amounts of polymer would have led to clusters with d_H bigger than 100 nm, but that was outside of the scope of this research, as we wanted to investigate the behavior of clusters made of few nanoparticles with sizes below 100 nm.

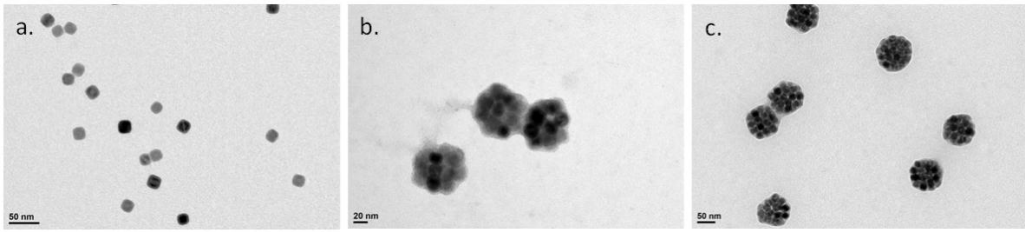

Figure 10: Soft colloidal clusters formed using 19 nm nanocubes with rounded edges. TEM micrographs of clusters for a ratio of (a) 17, (b) 35 and (c) 71 PS*c*MA molecules/nm^2, dispersed in H_2O.

3.2.4. Clusters of gold nanoparticles

The versatility of the clustering method was briefly tested on nanoparticles other than iron oxide based MNPs. The idea behind this study was to find out whether the water transfer process was specific for iron oxide nanomaterials, or whether other types of NPs could be passed into aqueous media. The test was carried out on 8 nm gold nanoparticles (Figure 11a) coated with oleylamine and dispersed in hexane.

The controlled clustering was successful with Au NPs as well. The average hydrodynamic diameter, by number, increased from 53 to 96 nm, by doubling the amount of amphiphilic polymer from 75 to 150 molecules/nm^2 particle surface, respectively (corresponding TEM images—Figure 11b and Figure 11c). These results strongly supported the fact that the polystyrene branches of the copolymer were intercalated with the surfactant shell of the nanoparticle—as the water transfer worked both with oleic acid and oleylamine—while the maleic anhydride moiety provided stability in aqueous media.

By further decreasing the polymer amount, we would expect to have obtained dimers, trimers and individually coated gold NPs. But this idea was

not pursued any further, as it was just a quick test to check the versatility of our approach.

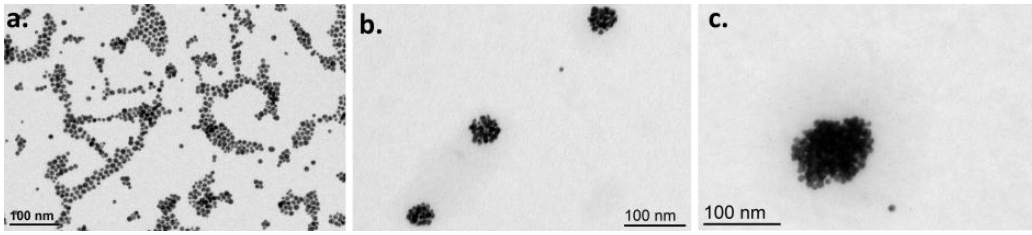

Figure 11: Soft colloidal clusters formed using 8 nm gold nanoparticles. TEM micrographs of (a) as-synthesized Au NPs in hexane, Au NPs@PS*c*MA for a ratio of (b) 75 and (c) 150 PS*c*MA molecules/nm^2, dispersed in H_2O.

3.2.5. Stability of nanoclusters in basic and acidic pH

Next, the stability of the nanoclusters was investigated. If the clusters are to be used for biomedical applications stability is of great importance. When stored at room temperature in neutral pH (milliQ H_2O), the clusters were stable for months (> 12 months). Over time the clusters tended to precipitate, but gently shaking the vial by hand was enough to disperse the clusters back in solution—no sonication was required.

In addition to colloidal stability over time, two extreme cases were studied: basic pH (8-9) and acidic pH (2-3). Upon addition of 1 µL of triethylamine (TEA) to 50 µL of nanoclusters solution the clusters broke down, and instead of nano-assemblies, individually coated nanocubes were present. In water the hydrolysis of maleic anhydride moieties occurred, the hydroxyl groups being negatively charged at basic pH, therefore the amphiphilic polymer coated nanocubes started repelling each other and disintegrating the clusters. For example, for the soft colloidal nanoclusters formed with the 19 nm core-shell IONCs at a ratio of 71 molecules polymer/nm^2 (Figure 10c), d_H by

volume mean decreased from 96 ± 1 nm, PDI 0.02 ± 0.01 (Figure 12—blue line), to 26 ± 1 nm, PDI 0.09 ± 0.02 (Figure 12—green line), upon addition of the base, the insets representing the corresponding TEM micrographs.

As the pH was lowered below the pk_a of the carboxylic acid groups found on the polymer backbone (pk_{a1} = 1.9, pk_{a2} = 6.07), they became protonated, and the polymer became positively charged. This led to an attraction between the neutral moieties of the copolymer and the positively charged ones, resulting in aggregation of the soft colloidal nanoclusters. The DLS results showed a steep increase in hydrodynamic diameter of the clusters from 99 nm to 649 nm by volume mean, from 76 to 397 nm by number mean and from 119 to 546 nm by intensity mean.

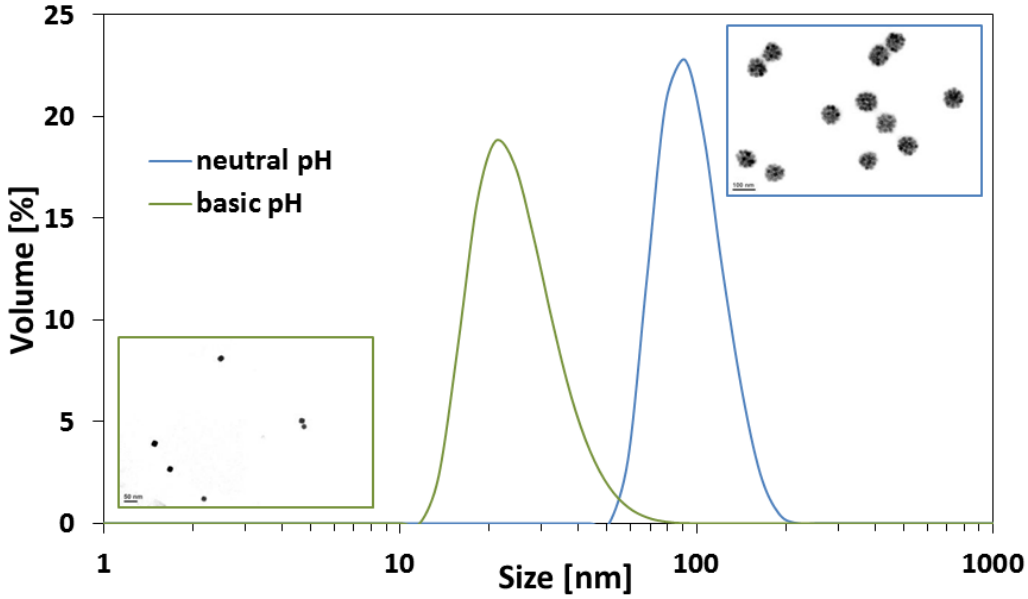

Figure 12: Stability of clusters at basic pH. DLS volume distributions of 19 nm IONCs@PS*c*MA in H_2O at neutral pH (blue line, d_H 96 ± 1 nm) and basic pH (green line, d_H 26 ± 1 nm). Upon addition of the base the negatively charged hydroxyl groups of the polymer backbone started repelling each other, thus 'breaking' the clusters.

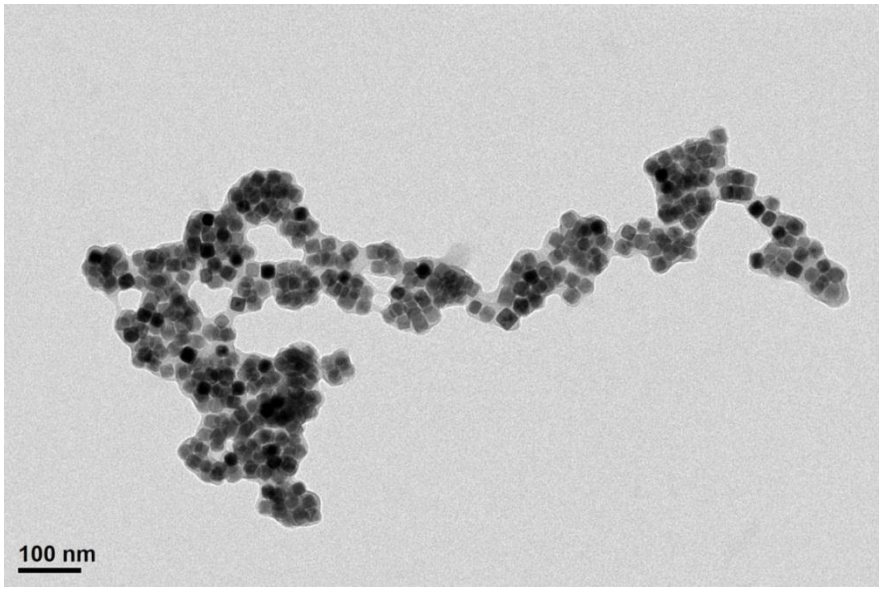

Figure 13: Stability of clusters at acidic pH. TEM micrographs of 20 nm IONCs@PS*c*MA (ratio of 66 molecules/nm^2) in H_2O at pH 2. Upon addition of the acid, the clusters started aggregating and having overlapping polymeric coronas.

A long ´polymeric-like´ chain could be seen on the TEM micrograph (Figure 13). The clusters were no longer individual and an overlap between the polymeric coronas of different clusters could be clearly observed. This feature can be potentially exploited *in vivo* as once the clusters reach the tumor microenvironment that is more acidic than the rest of the body, they will further cluster and stop circulating. But there are many more trials to be carried out before fully grasping the applicability of such systems for *in vivo* applications.

3.2.6 Cluster size determination by AC susceptibility measurements

AC magnetic susceptibility is the technique that allows a visualization of the magnetization relaxation of suspensions of nanoparticles. When measuring the complex AC susceptibility two terms are plotted as a function of frequency:

the in-phase susceptibility component χ´ and the out-of-phase susceptibility component χ´´. The alternating magnetic field frequency at which optimum phase lag occurs for a given particle type can be seen as a peak in the out-of-phase susceptibility component.[62] For magnetically blocked nanoparticles that are freely moving in solvents, the peak position—that happens at $\omega * \tau_B = 1$ (with ω the angular frequency)—reveals the Brownian relaxation time (the Néel relaxation time would be visible if measured up to MHz regime) and can be used to calculate the hydrodynamic size of the particles according to the following equation:

$$\tau_B = \frac{3\eta v_H}{k_B T} \quad \text{(Eq. 1)}$$

with v_H the hydrodynamic volume of the particle, η the dynamic viscosity of the fluid, k_B the Boltzmann's constant and T the temperature.

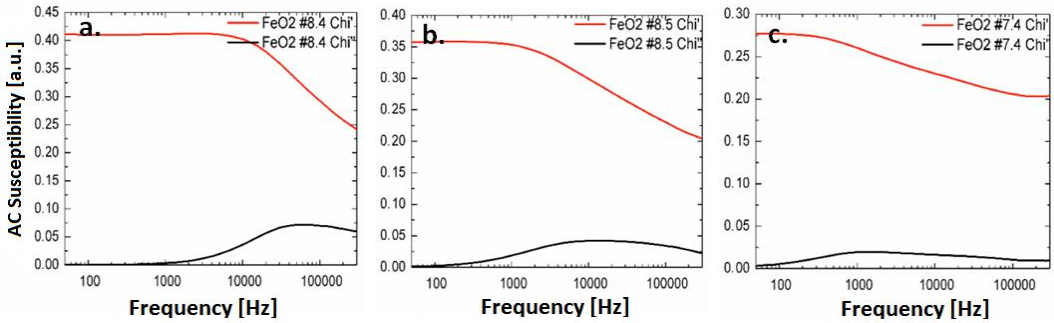

Figure 14: Hydrodynamic size determination by AC Susceptibility measurements. AC susceptibility curves for the 19 nm IONCs@PS*c*MA clusters in H_2O for a ratio of (a) 17, (b) 35 and (c) 71 PS*c*MA molecules/nm^2.

The AC susceptibility provides a direct method for determining the effect of the micro-environment on the magnetization relaxation of nanoparticles, and conversely, an indirect method for probing the micro-environment of the particles.

The nanoclusters formed starting with 19 nm core-shell nanocubes with rounded edges were subjected to AC susceptibility measurements. Our colleague at Keele University, Dalibor Soukup-Croy, carried out these experiments. The results that interested us were determining hydrodynamic sizes of clusters in solution, d_H being calculated based on the equation for the Brownian relaxation (Eq. 1) from the AC susceptibility Brownian peaks. The AC susceptibility curves are plotted in Figure 13 and the corresponding calculated hydrodynamic diameters are 26 (Figure 14a), 39 (Figure 14b) and 94 nm (Figure 14c) for 17, 35 and 71 PS*c*MA polymer molecules/nm^2, respectively. These results are summarized in Table 2. They were in agreement with the sizes obtained by DLS (Figure 9) and observed by transmission electron microscopy (Figure 10).

Table 2: Volume comparison between DLS and AC susceptibility results for 19 nm IONCs@PS*c*MA (in H_2O) at various ratios of polymer/nm^2 of particle surface

Sample	Volume mean by DLS [nm]	Volume by AC susceptibility [nm]
17 PS*c*MA molecules/nm^2	30 ± 1	26
35 PS*c*MA molecules/nm^2	61 ± 2	39
71 PS*c*MA molecules/nm^2	96 ± 1	94

To summarize, in section 3.2., a nanosystems made up of iron oxide nanoparticles coated with the amphiphilic polymer poly(styrene-*co*-maleic anhydride), cumene terminated, was investigated. The main focus was the formation of soft colloidal nanoclusters that could be used as nanoheaters for magnetically induced hyperthermia. Nanoclusters of different sizes were obtained by changing the polymer to nanoparticle surface ratio. When increasing the ratio bigger clusters were obtained, with sizes up to 100 nm.

The method proved to be versatile as nanoparticles of different shapes, sizes, and types could be clustered in a controlled manner. The cluster size was confirmed by DLS and TEM (for all samples), and AC susceptibility measurements (for the sample of 19 nm IONCs with rounded edges).

Regarding the study of soft colloidal nanoclusters, the steps that were subsequently taken and that are presented in the section 3.3. were:

i) scaling-up of the cluster formation in order to obtain a concentrated sample for hyperthermia,

ii) comparing the SAR values between individually coated nanocubes and soft colloidal nanoclusters.

3.3. Specific absorption rate value comparison of the nanoclusters

The research presented in this section deals with the characterization of nanoclusters made of iron oxide nanocubes having a core-shell structure (wüstite core/magnetite shell). The main focus was to correlate SAR values of these nanoclusters to their size, composition and magnetic features. This was achieved by exploiting a variety of characterization techniques like X-ray diffraction (XRD), SQUID magnetometer, as well as high frequency alternating magnetic field magnetometer.

Three IONCs samples with an identical edge size, (i) sample A: L_c = 20.2 ± 1.5 nm (Figure 4b), (ii) sample B: L_c = 20.2 ± 1.8 nm (Figure 21), and (iii) sample C: L_c = 20 ± 2 nm (Figure 30), were investigated. For sample A and B, though both samples were core-shell initially, the main difference between them was the ratio wüstite to magnetite when the clusters were formed. Both samples were synthesized at the same time (first half of 2014), soft colloidal nanoclusters were formed from sample A in the spring of 2015 when the

wüstite core was still present and the clusters were stored in aqueous media afterwards for 12 months before performing the various characterizations (XRD confirms a 5-10% wüstite core after storage in aqueous media for 12 months, data not shown). Nanoclusters formed starting from sample B (synthesis done in the first half of 2014, Figure 21a) were prepared in summer 2016, when the wüstite core was already fully oxidized to magnetite during the storage at RT—Figure 21b (no wüstite detected by XRD, data not shown).

Given the different nature of the nanocubes at the starting point prior to the cluster formation, the cluster samples obtained behaved differently under an alternating magnetic field, with the main difference reflected on the SAR values and on the trend observed when forming clusters. For sample A and C, the trend was an increase in SAR values for dimers and trimers, while a decrease was observed for sample B.

3.3.1. Core-shell iron oxide nanocubes. Sample A

As mentioned at the end of section 3.2., the nanoclusters synthesis protocol had to be scaled up in order to carry out hyperthermia experiments to measure SAR values. But in the meantime, as several samples of soft colloidal nanoclusters, formed starting from sample A (Figure 4b, a = 20.2 ± 1.5 nm), were already available, they were used for the initial hyperthermia study. The nanoclusters were formed one year before and stored in milli-Q water over that period of time, thus their stability had to be firstly checked. Also, the nanocluster samples belonged to different batches that were later combined only if their hydrodynamic diameters were within a 5% range.

3.3.1.1. Hyperthermia

For the sample formed with a ratio of molecules of polymer/nm^2 of 16.5, only one sample was available (Figure 5a). The sample was concentrated at the magnet and redispersed to a volume of 175 µL, at a concentration of [Fe] = 0.65 g/L, that was still suitable for magnetic hyperthermia measurements. The stability before and after magnet exposure was checked by DLS. The intensity weighted mean hydrodynamic size (Z-average) before bringing the sample at the magnet was 55.4 ± 0.3 nm (PDI 0.2) and after 3 hours at the magnet it was 48.6 ± 0.3 nm (PDI 0.12). A part of the sample was certainly left in solution as the color of the supernatant was slightly yellow. The surprising fact was a decrease both of Z-average and PDI, assuming that the first nanocubes that would migrate towards the 0.3 T magnet would be the bigger NPs and not the smaller ones. But if we take into consideration the fact that for smaller core-shell nanocubes the oxidation of the core occurs faster, then the results can be explained by the faster migration of smaller IONCs with a higher content of magnetite compared to bigger IONCs with a higher content of paramagnetic wüstite core. The SAR value, measured at magnetic field and frequency of 30 mT and 302 kHz, was **213 ± 9 W/g$_{Fe}$**.

There were two samples formed with a ratio of 33 molecules of polymer/nm^2 of particle surface (Figure 5b,E-H). One sample had a d_H of 59.5 ± 0.4 nm (PDI 0.21) and the other one 62 ± 1 nm (PDI 0.07). Besides similar hydrodynamic diameters the samples formed the same type of structures as seen under TEM (data not shown), thus the two samples were merged. The two samples combined had a Z-average of 61.5 ± 0.4 nm (PDI 0.14) before bringing the sample at the magnet and 63.0 ± 0.3 nm (PDI 0.14) after 4 h concentration at the magnet, with a final volume of 150 µL and a

concentration 0.78 g/L of Fe. The SAR value measured at magnetic field amplitude and frequency of 30 mT and 302 kHz was **253 ± 10 W/g_{Fe}**.

A total of 4 samples were available for a ratio of 66 molecules of polymer/nm^2 of particle surface (Figure 5d). Two of them were combined and used to determine SAR, one sample was used to study the stability of nanoclusters under external stimuli like sonication, and a forth one was utilized to study the improvement of SAR value with the oxidation of the wüstite core (see later). The two samples that were combined and concentrated at the magnet had the following characteristics: sample 1—Z-average of 105 ± 2 nm (PDI 0.11), and sample 2—Z-average of 104 ± 1 nm (PDI 0.08). Before magnet exposure, d_H was 101 ± 1 nm (PDI 0.09) and after 45 min at the magnet, Z-average was 105 ± 1 nm (PDI 0.07), for a final volume of 150 µL and a concentration of 0.95 g/L of Fe. The SAR value was **184 ± 8 W/g_{Fe}** at magnetic field and frequency of 30 mT and 302 kHz.

The SAR values were measured at the highest frequency and magnetic field of the instrument (nB Nanoscale Biomagnetics DM100 series) as the Fe concentration of the samples were in the range 0.65 - 0.95 g/L, lower than usual concentrations employed for hyperthermia studies (2 - 4 g/L) that is needed for the macroscopic increase of the temperature of the media. By plotting (Figure 15) the trend observed for the different samples, we saw an increase in SAR for dimers and trimers (33 molecules polymer/nm^2—Figure 5b) compared to both individually coated nanoparticles (16.5 molecules polymer/nm^2—Figure 5a) and soft colloidal clusters with n≥4 (66 molecules polymer/nm^2—Figure 5d), with ‘n’ being the number of particles per cluster. This SAR trend was also nicely reflected by the saturation magnetization M_s values obtained from SQUID measurements (Figure 19, Table 4). Indeed, the

increase in M_s for the dimers and trimers might also explain why such cluster arrangements produced higher heat dissipation (Figure 15) than the corresponding single and more centro-symmetrical clusters.

This observation revealed the fact that by forming anisotropic structures, the so-called 'dimers' (n = 2, two nanocubes side by side) and 'trimers' (n = 3, two nanocubes side by side and a third nanocube close to the side at which the nanocubes are connected) the response to the magnetic field was increased and the SAR value increased too. Indeed, when placing the sample at the magnet only 3 hours were needed for the accumulation of the dimers and trimers compared to 4 hours for the individually coated IONCs—4 hours were not even sufficient as part of the sample was still in solution, as mentioned before.

Meanwhile, in soft colloidal nanoclusters (n ≥ 4) the particle magnetic moments tended to arrange in a so-called demagnetizing configuration as in such centro-symmetrical configuration the overall magnetic moments might have degraded their interaction. More in depth explanations on magnetic characterization of the nanoclusters is given in the next section.

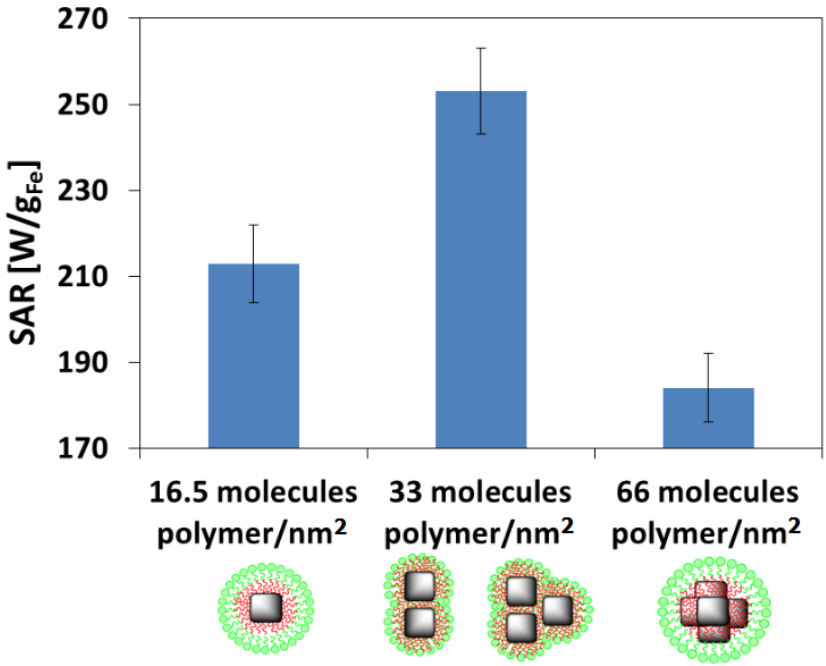

Figure 15: SAR values[§] for soft colloidal nanoclusters formed with ratios of 16.5, 33 and 66 molecules PS*c*MA/nm^2 of particle surface. A higher SAR value was recorder for dimers and trimers compared both to individual IONCs and clusters with n ≥ 4. Clustering the IONCs in centro-symmetrical bead like structures decreased their heating performance.

In the previous chapter it was shown that by oxidizing the paramagnetic wüstite core (antiferromagnetic below Néel temperature T_N of 198 K), the SAR values were increased, as the whole nanoparticle responded to the alternating magnetic field and not only its magnetite shell. A sample of nanoclusters (n ≥ 4) with a Z-average of 117 ± 1 nm (PDI 0.04) was concentrated at the magnet for 10 min. After magnet exposure the sample preserved its hydrodynamic diameter constant as the Z-average was 116 ± 1

[§] Each experimental data point was calculated as the mean value of at least three measurements, with error bars indicating the mean deviation.

nm (PDI 0.05). The annealing—the oxidation of the wüstite core—was done overnight, not by magnetic stimulation under alternating magnetic field, but in an oven at 80 °C, in order to speed up the process. The SAR value measured before annealing was **174 ± 9 W/g_{Fe}** (frequency = 302 kHz, magnetic field = 30 mT), similar to the value obtained for the previous sample of clusters (n ≥ 4), *i.e.* 184 ± 8 W/g_{Fe}. After annealing overnight, the SAR value increased slightly up to **188 ± 6 W/g_{Fe}**. This could be attributed to an ever existing wüstite core in the sample. The XRD pattern (data not shown) showed a value around 5-10 w% wüstite, with magnetite the main crystalline phase. It is important to underline that the sample was stable during the overnight annealing process even when applying for 17 h the annealing treatment, as the Z-average value stayed at 116 ± 1 nm (PDI 0.05). Stability is of utmost importance, as sample aggregation plays a crucial role on hyperthermia experiments—by decreasing the SAR value—this being the reason why sample stability was always checked by DLS and TEM.

Next, the same sample was transferred into glycerol and SAR was measured. By increasing the viscosity of the solution, eventually, the Brownian relaxation process is 'blocked' and hence only the Néel relaxation of atomic moments contribute to magnetization dynamics.[62] The SAR value of **125 ± 3 W/g_{Fe}**, saw a drop of 33.5% compared to the initial value of **188 ± 6 W/g_{Fe}** measured in milli-Q water. Nevertheless, the drop was not as significant as similar nanosystems reported in literature[50], in which a 80% SAR drop was measured in PEG 400, a solvent that has a viscosity ten times lower—90 mPa·s (at 20 °C)—compared to glycerol—1069 mPa·s (at 20 °C). In our case, even if the system was made up of closely bound magnetite 20 nm iron oxide

nanocubes, both Néel and Brownian relaxation processes contributed to magnetization dynamics.

Lastly, one more experiment was carried out to check the stability of the nanoclusters under external stimuli other than temperature or magnetic field. A sample formed with 66 molecules polymer/nm^2, with the following characteristics: Z-average 96 ± 1 nm (PDI 0.08) was subjected to 10 minutes of sonication. The idea behind the experiment was to determine whether the nanoclusters formed were indeed 3D constructs, or if what was observed on TEM grids was a mere drying effect. After sonication, the soft colloidal clusters maintained their size—Z-average 97 ± 1 nm (PDI 0.08)—and shape, as can be seen in the TEM micrographs shown in Figure 16.

The data from the experiments described previously can be found in Table 3, that gives an overview of stability experiments carried out on nanoclusters prepared starting from 20.2 ± 1.5 nm iron oxide nanocubes shown in Figure 4b.

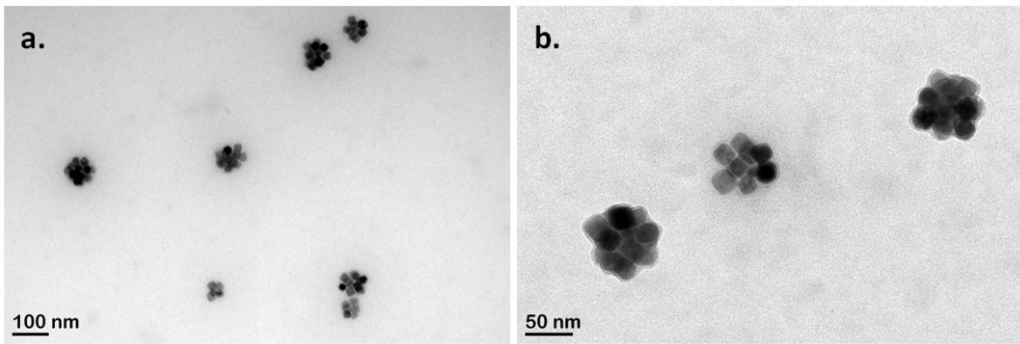

Figure 16: Sonication effect on cluster stability. TEM micrographs of soft colloidal nanoclusters (n ≥ 4) (a) before and (b) after sonication for 10 minutes. No change occurred after sonication indicating a stable polymer-cluster assembly.

Table 3: DLS data and SAR values for the different types of nanoclusters formed with 16.5, 33 or 66 molecules polymer/nm^2 of particle surface

Sample	**Z-average [nm]**		**SAR [W/g_{Fe}]**		**Z-average [nm]**
	before magnet	*after magnet*		*after annealing*	*after annealing*
16.5 molecules/nm^2	55 ± 1 (PDI 0.2)	49 ± 1 (PDI 0.12)	213 ± 9	-	-
33 molecules/nm^2	62 ± 1 (PDI 0.14)	63 ± 1 (PDI 0.14)	253 ± 10	-	-
a. 66 molecules/nm^2	101 ± 1 (PDI 0.09)	105 ± 1 (PDI 0.07)	184 ± 8	-	-
b. 66 molecules/nm^2	117 ± 1 (PDI 0.04)	116 ± 1 (PDI 0.05)	174 ± 9	188 ± 6	116 ± 1 (PDI 0.05)
	before sonication	*after sonication*			
c. 66 molecules/nm^2	96 ± 1 (PDI 0.08)	97 ± 1 (PDI 0.08)	-	-	-

3.3.1.2. Statistics

The size of the soft colloidal nanoclusters was tuned by changing the ratio of amphiphilic polymer to particle surface of the IONCs. Given that the hydrodynamic diameter obtained was an average value, in an attempt to quantify the percentage of individually coated nanoparticles when using the lower ratio of polymer, for example, we applied a statistical image analysis—using ImageJ software. Numerous TEM micrographs were analyzed in order to get a statistical distribution of individually coated nanocubes *vs*. 1D and 2D constructs (dimers and trimers) *vs*. 3D constructs (bigger colloidal nanoclusters, n ≥ 4) for the 3 available samples—samples that were used to calculate SAR values and on which SQUID experiments were carried out.

At least 250 objects were analyzed for each sample (Figure 17). Starting from now on the samples will be called 16.5PS*c*MA, 33PS*c*MA and 66PS*c*MA

corresponding to ratios of 16.5, 33 and 66 molecules of poly(styrene-*co*-maleic anhydride) used for the formation of the clusters. For sample 16.5 PS*c*MA, 255 objects were studied, corresponding to a total of 342 nanocubes, out of which 66% were individually coated, 28% were dimers, 4% were trimers and 2% were bigger clusters (Figure 18). For sample 33PS*c*MA , when doubling the amount of polymer with respect to 16.5PS*c*MA sample, out of 254 objects analyzed (Figure 17)—corresponding to 493 IONCs—70% were 1D and 2D constructs with an equal percentage of dimers and trimers (Figure 18). The 30% remaining objects were 19% individually coated NPs and 11% were 3D arrangements. For sample 66PS*c*MA, when doubling once again the amount of polymer with respect to sample 33PS*c*MA, almost only 3D clusters were obtained, representing 86% (Figure 18) of the 259 objects inspected—corresponding to more than 1 000 NPs (Figure 17). The remaining 14% of sample 66PS*c*MA was equally distributed between single particles (5%), dimers (5%) and trimers (4%). We could then confirm that on the sample where we have measured a higher SAR—33 PS*c*MA—the percentage of dimers and trimers was statistically and significantly more abundant. Individual nanocubes and clusters with $n \geq 4$ were instead the predominant population for the samples 16.5PS*c*MA and 66PS*c*MA, respectively. As already reported by others, also our data suggests that centro-symmetrical clusters significantly reduced the SAR value of the nanocubes (Figure 15).

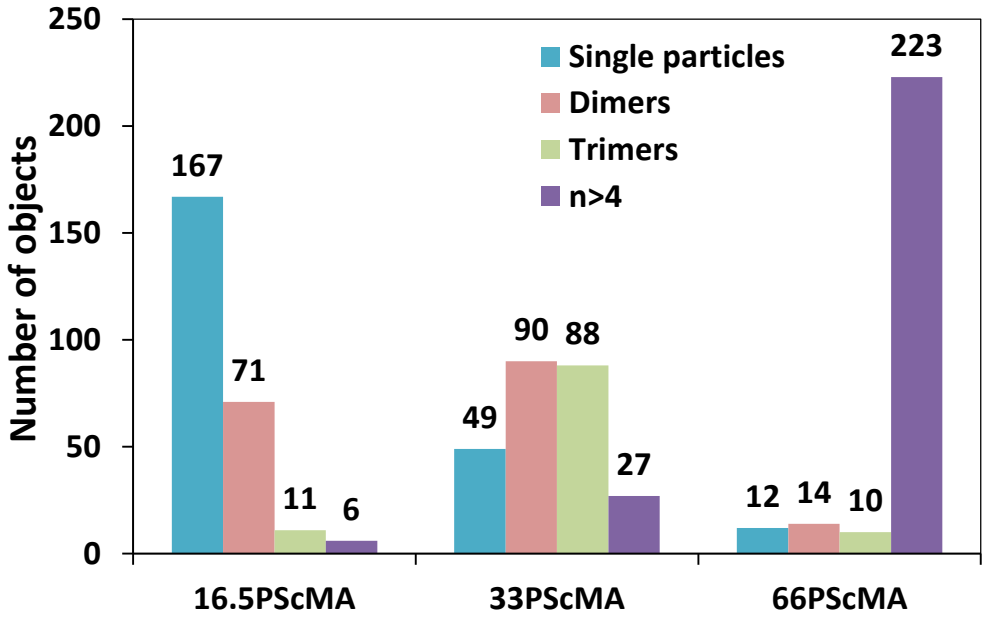

Figure 17: Statistical distributions, by number of objects, for samples 16.5PS*c*MA, 33PS*c*MA and 66PS*c*MA

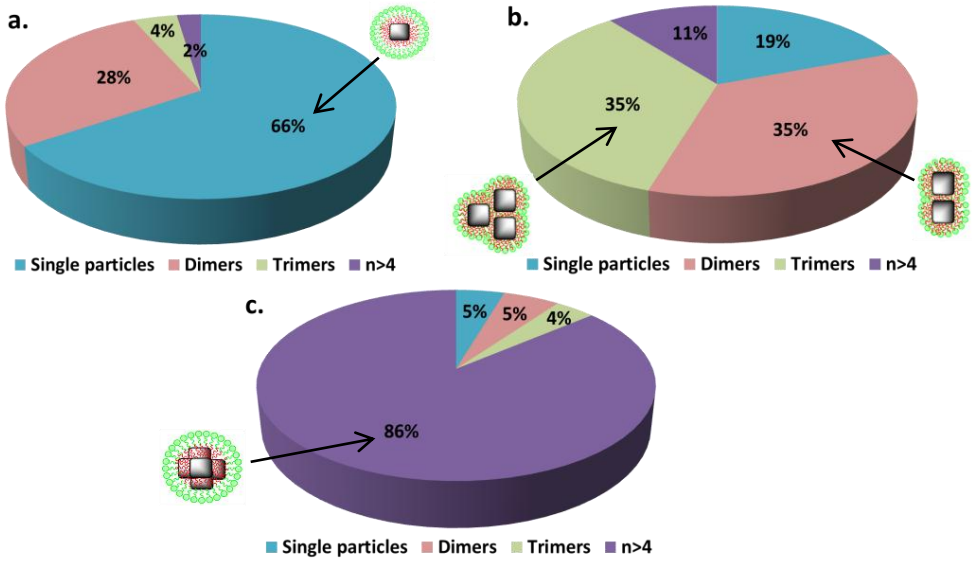

Figure 18: Statistical analysis of size distribution for different cluster preparations. Distributions, by percentage, for samples (a) 16.5PS*c*MA, (b) 33PS*c*MA and (c) 66PS*c*MA indicated the presence of (a) 32% 1D and 2D constructs (28% dimers and 4% trimers) in sample 16.5PS*c*MA, (b) a majority of 70% (35% dimers and 35% trimers) in

sample 33PS*c*MA, and (c) only 10% (5% dimers and 5% trimers) 1D and 2D structures in sample 66PS*c*MA.

3.3.1.3. Magnetization, zero-field-cooled and field-cooled curves

As seen from hyperthermia measurements, soft colloidal nanoclusters of different sizes behaved differently under alternating magnetic fields. The trend consisted of an increase of SAR values for clusters formed of n = 2 or n = 3 IONCs, while increasing the number above 4 the SAR value dropped again (Figure 15). Next we performed SQUID measurements to investigate the trend of magnetic parameters when considering the magnetization *vs*. field and zero-field-cooled field-cooled (ZFC-FC) measurements. Magnetization measurements provided us three important values: saturation magnetization M_s in magnetic fields up to 5570 kA/m, coercive H_c fields (when induced magnetization was zero), and exchange bias H_E fields (shifted hysteresis loop towards field values opposite to the applied magnetic field due to the antiferromagnetic-ferri(o)magnetic (AFM-Fi(o)M) interface coupling). The ZFC-FC measurements probed magnetization as a function of temperature while applying a magnetic field (H ~ 4 kA/m). The maximum of the ZFC curve provided a reasonable estimate of the superparamagnetic blocking temperature T_B, temperature below which the particles were magnetically blocked. All these values are summarized in Table 4.

Table 4: Magnetic properties of sample A[**]

	M_s^{298K} / M_s^{10K} [emu/g_{Fe}][††]	$H_C^{ZFC@298K}$ / $H_C^{ZFC@10K}$ [kA/m] ([mT])	$H_E^{ZFC@298K}$ / $H_E^{ZFC@10K}$ [KA/m] ([mT])	T_B^{5mT} [K]
16.5 PS*c*MA	98/148	5.7 (7.2)/ 22.5 (28.2)	1.4 (1.8)/ 2 (2.5)	346
33 PS*c*MA	109/117	5.7 (7.2)/ 22.4 (28.1)	1.4 (1.8)/ 0.4 (0.5)	355
66 PS*c*MA	84/119	3 (3.8)/ 22.3 (28)	0.6 (0.8)/ 1.3 (1.6)	379

As seen in Figure 19c and Table 4, the saturation magnetization M_s of individual IONCs at RT (16.5PS*c*MA) was 98 emu/g_{Fe}. The magnetization increased up to 109 emu/g_{Fe} for dimers and trimers (33PS*c*MA) and decreased again down to 84 emu/g_{Fe} for clusters in a centro-symmetrical configuration, with n ≥ 4 (66PS*c*MA). This trend was similar to the one of SAR values, where dimers and trimers showed a higher SAR compared to both individual IONCs and bigger clusters. Regarding coercivity (Figure 19d), individually coated IONCs and dimers and trimers had same coercivity H_C of 7.2 mT (Table 4). Due to higher M_s value, dimers and trimers had a higher SAR as the area under the hysteresis was bigger for dimers and trimers compared to individual IONCs. When the number of nanocubes per nanocluster increased further (n ≥ 4), the nanoclusters became 'softer' and behaved as multi domain particles, with lower coercivity (H_C = 3.8 mT) and a ratio between remanent magnetization M_R and M_s < 0.1 (0.06 in our case, with M_R = 5.38 and M_s = 84 emu/g_{Fe}), typical of multi domain particles.[63]

[**] M_s, H_C, H_E and T_B obtained from the analysis of magnetization curves.

[††] M_s values are reported in emu/g_{Fe} as conversion to SI units requires knowing the exact ratios of wüstite and magnetite, which can be only roughly estimated without the Rietveld analysis of X-ray diffraction patterns

The presence of low amounts of wüstite phase was supported by small values of exchange bias ($H_E \leq 2.5$ mT), that were, surprisingly, present even at RT. The antiferromagnetic-ferri(o)magnetic interface coupling is expected to be seen only at temperatures below Néel temperature T_N (T_N = 198 K for wüstite). Magnetization versus magnetic field curves recorded at 10 K (ZFC) showed similar exchange bias fields with values between 0.5 and 2.5 mT.

Lastly, as T_B of individual particles, dimers and trimers, and clusters with n≥ 4, determined from temperature dependent ZFC-FC magnetization measurements (Figure 20), were all above RT, with values of 346, 355 and 379 K, under magnetic fields of 5 mT (Table 4), respectively, we can infer that the clusters were blocked at RT.

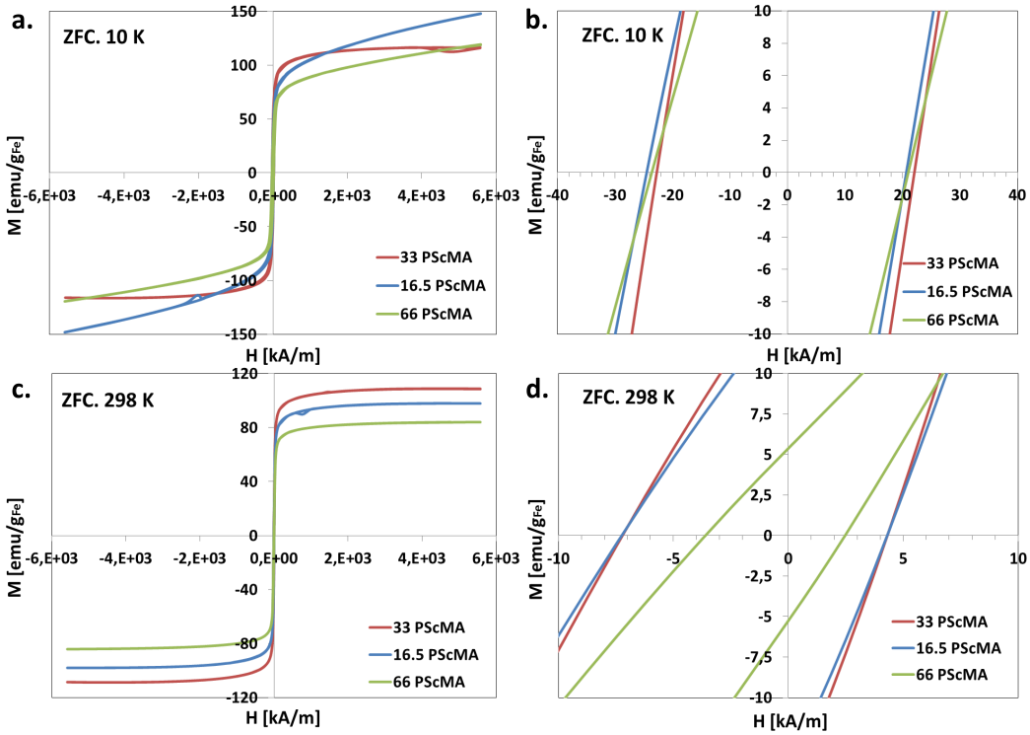

Figure 19: (a) Magnetization *vs.* magnetic field curves recorded at (a) 10 K and (c) 298 K for 16.5PS*c*MA (blue line—individual IONCs), 33PS*c*MA (red line—dimers and

trimers), and 66PS*c*MA (green line—clusters with n ≥ 4); (b) and (d) Zoom of the low magnetic field region to better visualize coercivity H_C.

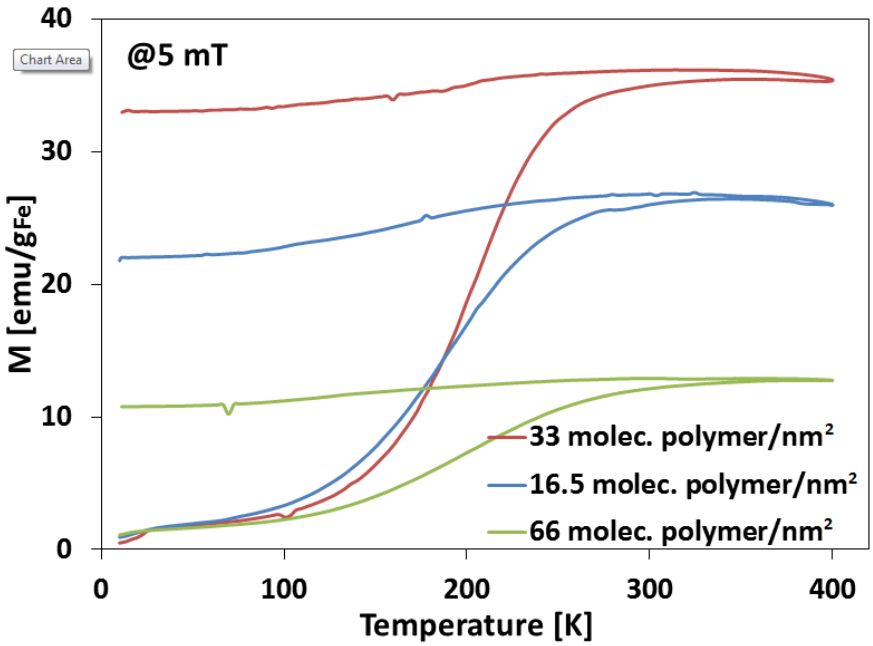

Figure 20: Temperature dependent zero-field-cooled and field-cooled magnetization measurements performed on aqueous suspension of nanoclusters embedded in gypsum matrix recorded at 5 mT magnetic field: 16.5PS*c*MA (blue line—individual IONCs, T_B 346 K), 33PS*c*MA (red line—dimers and trimers, T_B 355 K), and 66PS*c*MA (green line—clusters with n ≥ 4, T_B 379 K).

3.3.2. Core-shell iron oxide nanocubes. Sample B

3.3.2.1. Clustering process and cluster characterization

New samples of clusters were prepared for hyperthermia measurements. The starting sample B used was similar to the previous one, core-shell iron oxide nanocubes, with cube edge length of 20.2 ± 1.8 nm (Figure 21). However, the main difference was that the IONCs were synthesized and stored in chloroform, on the bench, for 2 years before being

used to prepare the clusters. As the wüstite core was oxidized over time, due to its unstable nature under oxygen, the XRD was checked in order to determine if there was any wüstite phase still present. The XRD results (data not shown) showed only magnetite phase present.

In an attempt to prepare more concentrated samples of nanoclusters ([Fe] ≥ 1 g/L), 4 new batches of soft colloidal nanoclusters were prepared. They were:

- two samples prepared by using 18 molecules polymer/nm^2 (V_{Tot} = 10 mL, m_{Fe} = 0.23 mg (Fe concentration 23 ppm), $m_{polymer}$ = 0.875 mg),
- one sample prepared by using the same ratio of 18 molecules polymer/nm^2, but both the Fe and polymer amounts were doubled (V_{Tot} = 10 mL, m_{Fe} = 0.46 mg (Fe concentration 46 ppm), $m_{polymer}$ = 1.75 mg),
- one sample prepared by using the same ratio of 18 molecules polymer/nm^2, but both the Fe and polymer amounts were tripled (V_{Tot} = 10 mL, m_{Fe} = 0.69 mg (Fe concentration 69 ppm), $m_{polymer}$ = 2.625 mg).

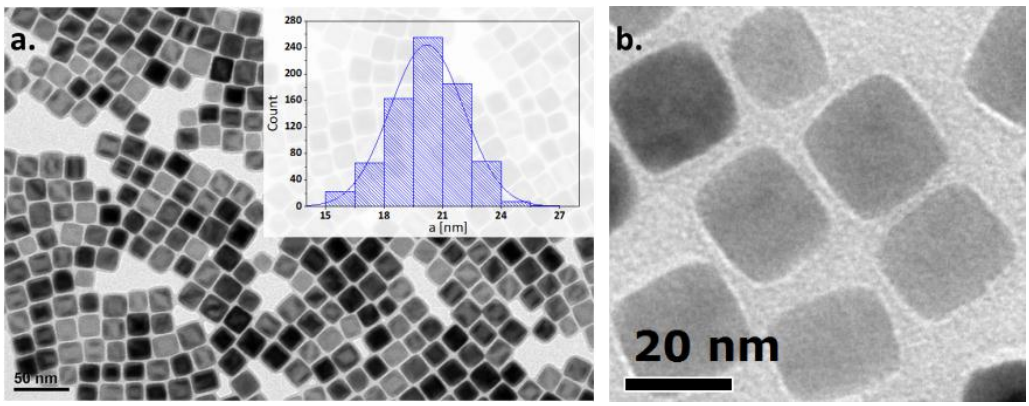

Figure 21: An oxidized sample used for cluster formation. TEM micrograph of (a) as-synthesized core-shell iron oxide nanocubes dispersed in $CHCl_3$ [inset: size histogram, a = 20.2 ± 1.8 nm], and (b) the same IONCs dispersed in $CHCl_3$ 2 years after synthesis.

The two samples prepared with a ratio of 18 molecules of polymer/nm^2 had similar characteristics by DLS: Z-average of 41.5 ± 0.3 nm (PDI 0.13) and Z-average of 39.3 ± 0.1 (PDI 0.16). The samples were combined and concentrated at the magnet for 25 h. After magnet concentration the hydrodynamic diameter was 37.4 ± 0.2 nm (PDI 0.14).

A new parameter emerged from this experiment, as by doubling the initial iron concentration, while keeping the amount of polymer per nm^2 constant, dimers and trimers started forming. This could be explained by a stronger dipole-dipole interaction—a long range order force—due to the increased Fe concentration thus increased number of nanocubes in the same solution volume. The sample formed by using 18 molecules polymer/nm^2, with the initial Fe concentration of 46 ppm, Z-average of 62.0 ± 0.9 nm (PDI 0.18), was concentrated at the magnet for 19 h. The sample was stable as after magnet exposure, Z-average was 57.6 ± 0.6 nm (PDI 0.13).

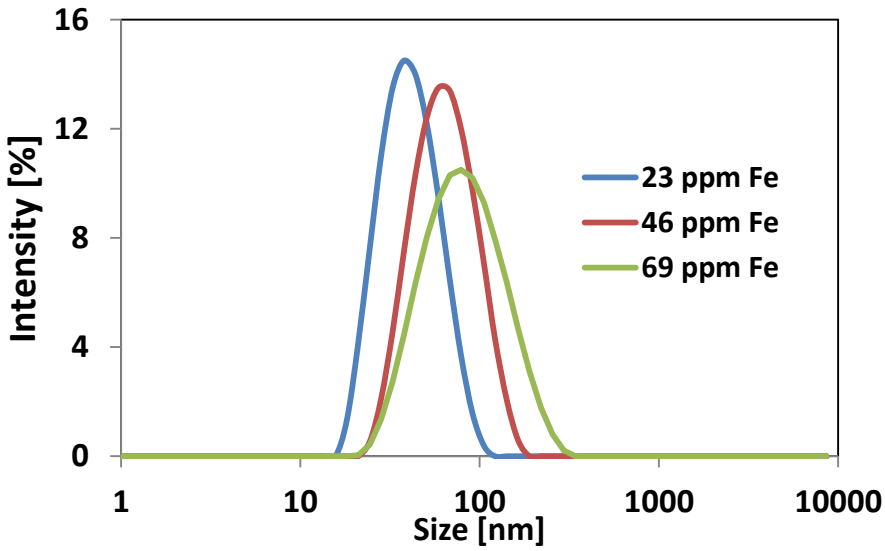

Figure 22: Tuning the mean hydrodynamic diameter by changing the initial [Fe] from 23 to 69 ppm. DLS volume distributions, by intensity, of water transferred IONCs, ratio

of polymer 18 molecules/nm^2, for Fe concentrations of 23 ppm—blue curve, 46 ppm—red curve, and 69 ppm—green curve. It was then possible to tune the hydrodynamic size not only by varying the amount of polymer, but by changing the initial [Fe] as well.

Lastly, the sample formed by using 18 molecules polymer/nm^2, with the initial Fe concentration of 69 ppm, formed more trimers, increasing the Z-average to 74.3 ± 0.3 nm (PDI 0.22). Also this sample was concentrated at the magnet. After 72 h at the magnet, Z-average was 72.4 ± 0.9 nm (PDI 0.23).

If we are to compare the samples by average hydrodynamic size, intensity mean, an increase in size was observed, by doubling and later tripling the initial concentration of iron, from 23 to 69 ppm, 1D and 2D nanoconstructs were formed (Figure 22).

This trend could also be seen on TEM micrographs of samples in water (Figure 23). For an initial Fe concentration of 23 ppm—concentration of the standard clustering procedure—individually coated NPs were obtained. For 46 ppm Fe, dimers and trimers were formed, while for 69 ppm Fe the proportion of dimers and trimers continued to rise. As mentioned earlier, a new parameter emerged for the formation of clusters. If beforehand, the only way of creating bigger clusters was by increasing the amount of amphiphilic polymer, it was then possible to fine tune the size of the clusters (thus the number of nanocubes per cluster).

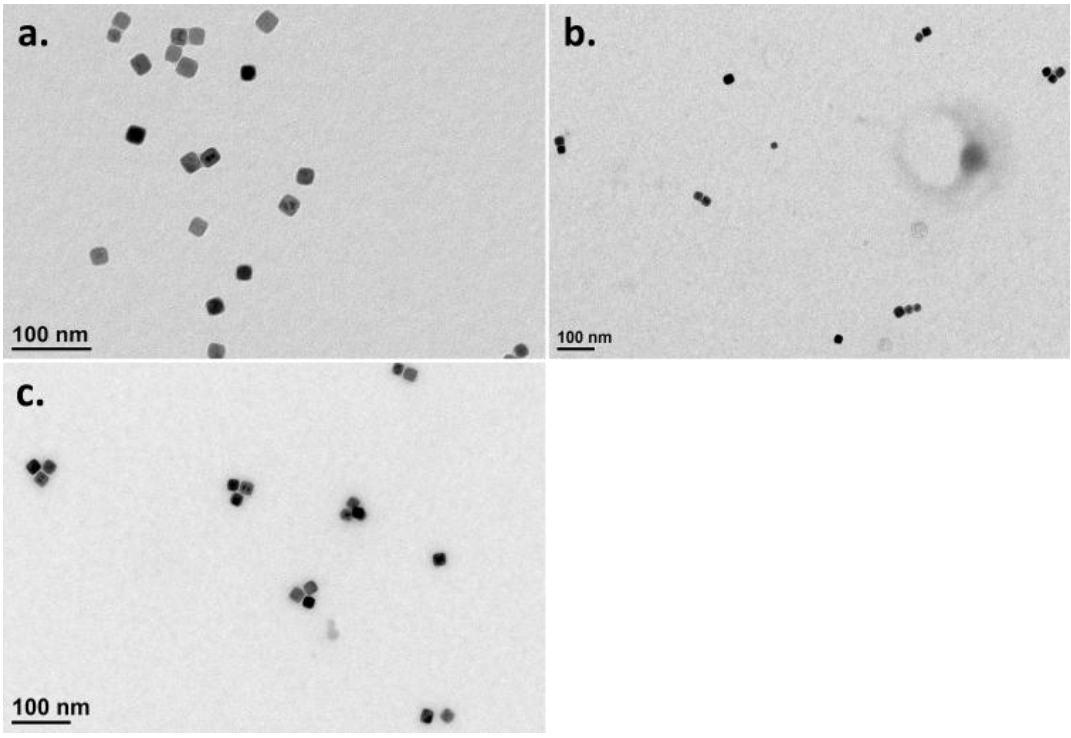

Figure 23: Soft colloidal cluster formation by changing the initial Fe concentration. TEM micrographs of the water transferred IONCs, ratio of polymer 18 molecules/nm^2, while changing the initial Fe concentration: (a) 23, (b) 46, and (c) 69 ppm. By increasing the initial iron concentration, the dipole-dipole interaction—a long range order force—was stronger, thus more dimers and trimers were formed during the water transfer (b,c).

3.3.2.2. Hyperthermia

Next, hyperthermia experiments were carried out in order to determine SAR values of the three cluster samples obtained from sample B. As stated earlier, the idea behind increasing the initial Fe concentration was to have more concentrated samples, that would allow measuring SAR values at different frequencies and fields and would not restrain our study to only one frequency and magnetic field—the highest one available on our instrument—which was the case previously.

The SAR values are summarized in Table 5. These values are also plotted in Figure 24 as a function of frequency applied, varying the frequency from 127.5 kHz to 302 kHz, while keeping the magnetic field amplitude constant at 30 mT (24 kA/m). Only for the sample made up of dimers and trimers—initial Fe concentration of 69 ppm—did the SAR increase linearly with the frequency applied. But what was most striking was the decrease of SAR when forming dimers and trimers, which was not the case beforehand. In an attempt to better understand the relaxation mechanisms dominating the magnetization dynamics when exposed to an AMF, magnetic characterization of the nanoclusters was carried out and the data is presented in section 3.3.2.4.

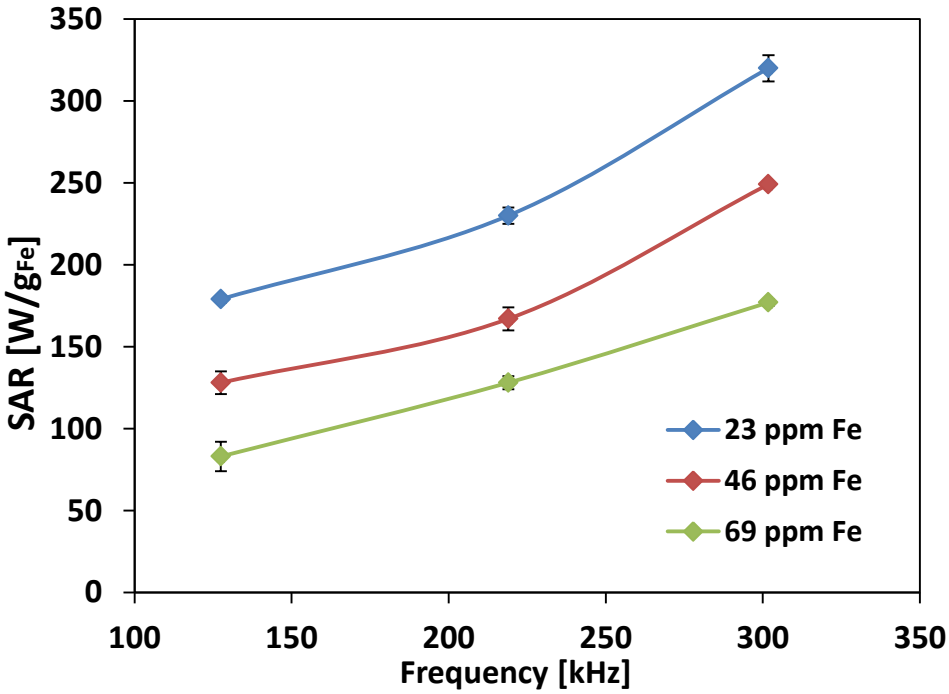

Figure 24: SAR values (with standard deviation) as a function of frequency at the magnetic field amplitude of 24 kA/m for nanoclusters prepared with an initial [Fe] of 23 ppm (blue diamonds—89% individual IONCs: Figure 23a), 46 ppm (red diamonds—

Figure 23b), and 69 ppm (green diamonds—61% dimers and trimers: Figure 23c). A SAR decrease was observed for the formation of dimers and trimers, which was surprising, as it was the inverse case for sample A.

Table 5: SAR values of nanoconstructs @30 mT magnetic field

	23 ppm Fe		46 ppm Fe		69 ppm Fe	
Frequency [kHz]	**SAR [W/g_{Fe}]**	**StdDev. [W/g_{Fe}]**	**SAR [W/g_{Fe}]**	**StdDev. [W/g_{Fe}]**	**SAR [W/g_{Fe}]**	**StdDev. [W/g_{Fe}]**
127.5	179	2	128	7	83	9
219	230	5	167	7	128	4
302	320	8	249	1	177	2

3.3.2.3. Statistics

Also here image analysis was employed for statistical distributions, in order to quantify the percentage of individually coated nanoparticles when using the lower Fe concentration *vs.* the percentage of dimers and trimers formed when tripling the initial Fe concentration. Numerous TEM micrographs were analyzed. At least 235 objects were analyzed for each sample (Figure 25).

Two samples were analyzed out of the three available. In the case of these core-shell iron oxide nanocubes, though the size of the particles (20.2 ± 1.8 nm) was similar to the previous sample (20.2 ± 1.5 nm), due to a different crystallographic structure, the SAR value was halved when forming the 1D and 2D objects, which was not the case previously when a 19% increase was reported (Figure 15).

For the sample of IONCs transferred into water at the lower Fe concentration (23 ppm), 250 objects were studied (Figure 25), corresponding to a total of 274 nanocubes, out of which an overwhelming 89% were individually coated, while 7%, 3%, and 1% were dimers, trimers, and clusters with n ≥ 4, respectively (Figure 26). When tripling the initial Fe concentration

to 69 ppm, out of 236 objects analyzed (Figure 25)—corresponding to 403 IONCs—61% were 1D and 2D constructs, with 34% and 27% corresponding to dimers and trimers (Figure 26). The 39% remaining objects were 36% individually coated IONCs and only 3% were bigger clusters.

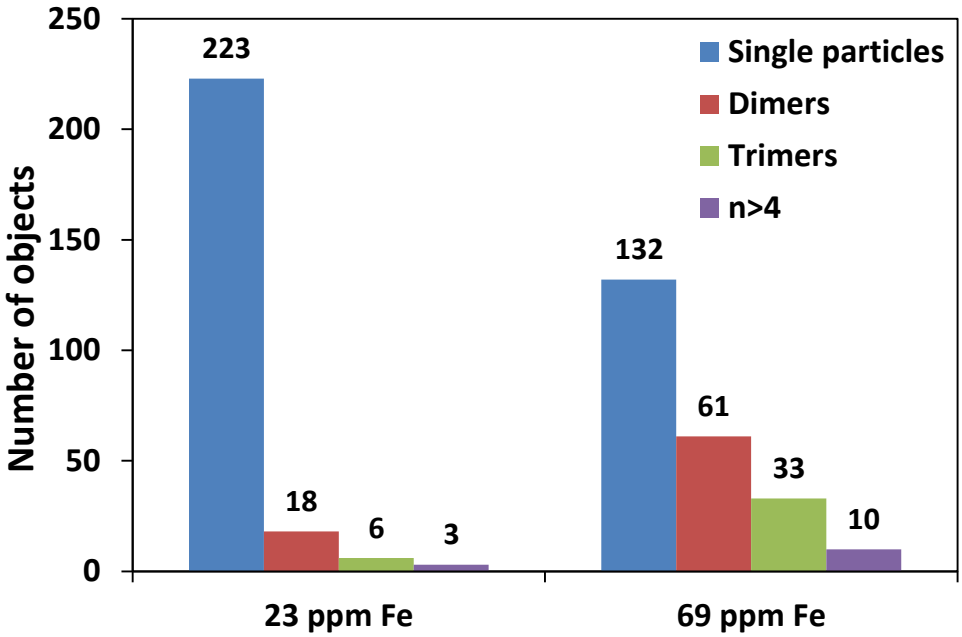

Figure 25: Statistical distributions, by number of objects, for samples prepared with an initial Fe concentration of 23 (individual IONCs) and 69 ppm (dimers and trimers).

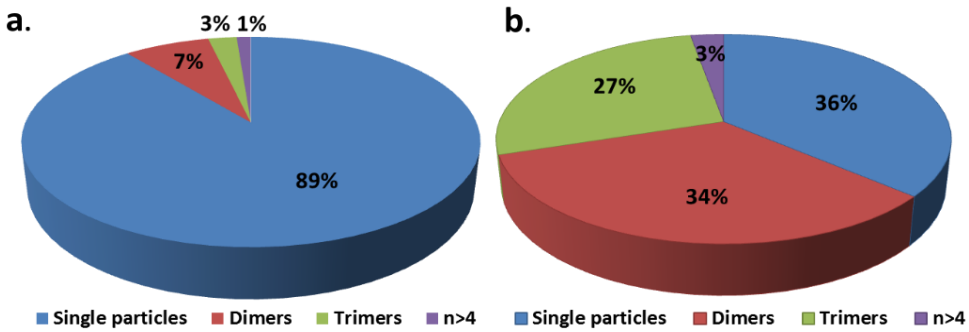

Figure 26: Statistical analysis of size distribution for different cluster preparations. Distributions, by percentage, for samples prepared with an initial [Fe] of (a) 23

(individual IONCs) and (b) 69 ppm (dimers and trimers), indicated that 89% of IONCs were individually coated, 10% were 1D and 2D constructs and 1% were 3D centro-symmetrical clusters for the sample shown in (a), while 36% were individual IONCs, 61% were 1D and 2D constructs (34% dimers and 27% trimers) and 3% were 3D centro-symmetrical clusters for the sample shown in (b).

3.3.2.4. Magnetic characterization

3.3.2.4.1. Magnetization, zero-field-cooled and field-cooled curves

In an earlier section on magnetically induced hyperthermia, we saw that soft colloidal nanoclusters, made from sample B, showed SAR values that decreased for constructs formed of n = 2 or n = 3 IONCs. To better understand if other differences contributed to this trend that is opposite to the one observed for clusters made from sample A, we initially turned to classical SQUID measurements: magnetization *vs*. field and zero-field-cooled field-cooled (ZFC-FC) measurements. These measurements allowed us to determine the following values: M_S, H_C, H_E and T_B. The magnetization curves were recorded both at RT (298 K) and at 10 K (where temperature fluctuation are negligible). All the values are summarized in Table 6.

Magnetization *vs.* field hysteresis loops of individual IONCs *vs.* dimers and trimers are plotted in Figure 27a (at 10 K) and Figure 27c (at 298 K), with the respective zoom of the low magnetic field region to better visualize coercive H_C and exchange bias H_E fields. Both at 10 K and at RT the individual IONCs had smaller M_S values compared to dimers/trimers: 89.5/96.4 (Figure 27a) and 88.4/91.8 emu/g_{Fe} (Figure 27c).

It is worth mentioning that similar to sample A, when forming dimers and trimers: (i) saturation magnetization increased, (ii) coercive fields, at 298 K, were the same for individual IONCs and dimers and trimers (6.9/6.7 mT),

however in comparison to sample 'A', M_S values were smaller (M_S values for sample A were 98 (single IONCs) and 109 (dimers and trimers) emu/g_{Fe} at 298 K).

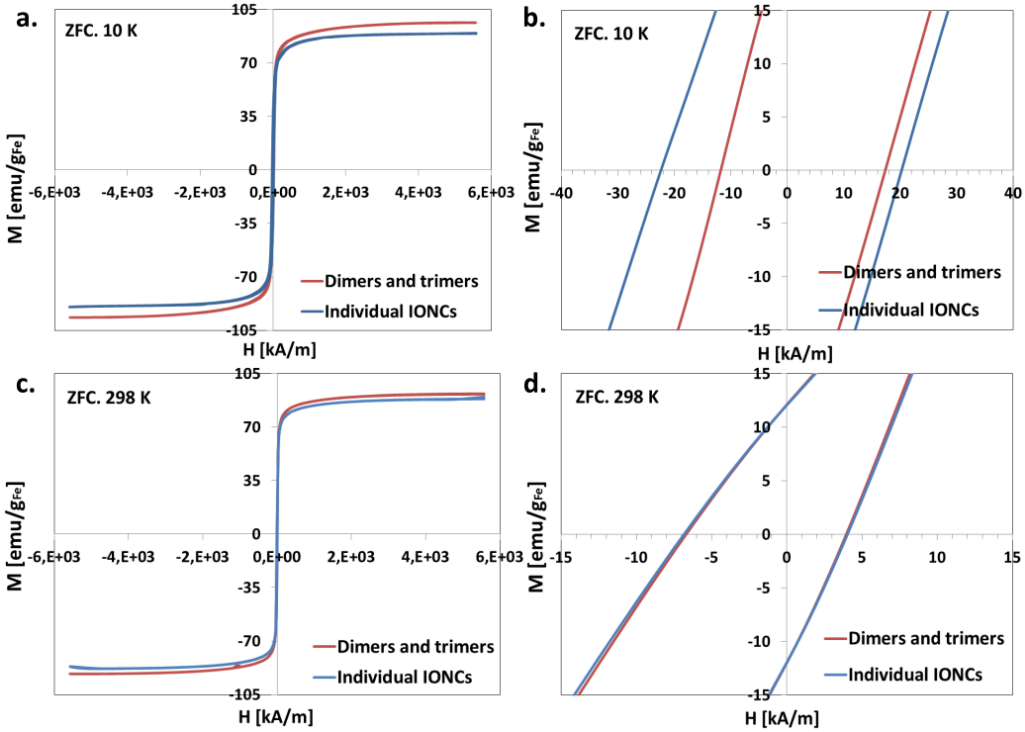

Figure 27: Magnetization *vs.* magnetic field curves recorded at (a) 10 K and (c) 298 K for an initial [Fe] of 69 ppm (dimers and trimers—red line)) and 23 ppm (individual IONCs—blue line); (b,d) Zoom of the low magnetic field region to better visualize coercive H_C fields.

Table 6: Magnetic properties of sample B

	M_s^{298K}/ M_s^{10K} [emu/g_{Fe}]	$H_C^{ZFC@298K}$/ $H_C^{ZFC@10K}$ [kA/m] ([mT])	$H_E^{ZFC@298K}$/ $H_E^{ZFC@10K}$ [KA/m] ([mT])	T_B^{5mT} [K]
23 ppm Fe (individual IONCs)	88.4/89.5	5.5 (6.9)/ 21 (26.3)	1.5 (1.9)/ 1 (1.3)	358
69 ppm Fe (dimers and trimers)	91.8/96.4	5.3 (6.7)/ 14.8 (18.5)	1.35 (1.7)/ 2.8 (3.5)	370

The blocking temperatures T_B of individual particles and dimers and trimers determined from temperature dependent ZFC-FC magnetization measurements (Figure 28), were above RT, with values of 358 and 370 K, under magnetic fields of 5 mT (Table 6). The respective blocking temperatures of clusters formed from sample A were 347 K and 355 K.

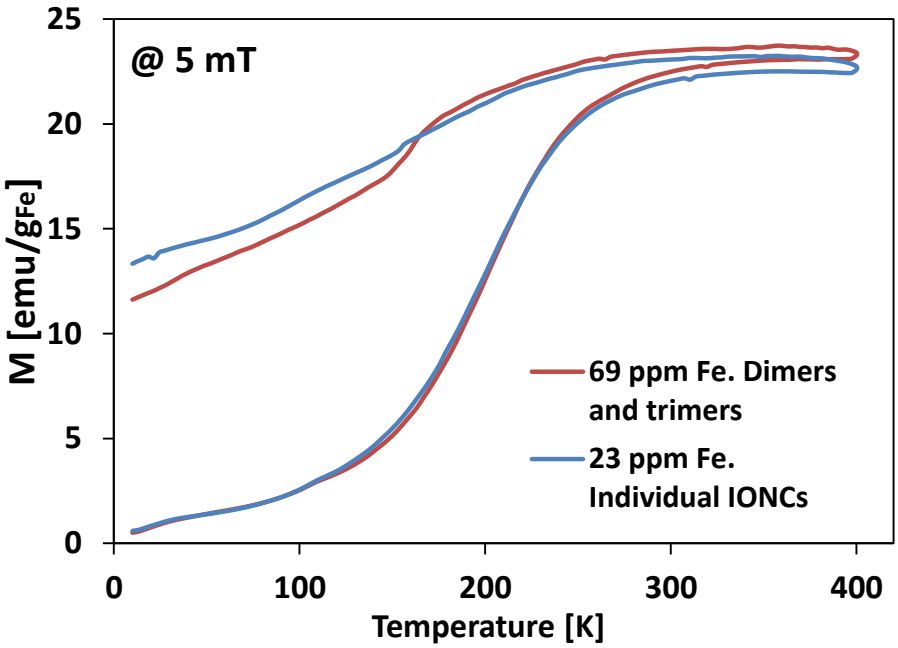

Figure 28: Temperature dependent zero-field-cooled and field-cooled magnetization measurements performed on nanoclusters embedded in gypsum matrix at 5 mT magnetic field for samples prepared with an initial [Fe] of 23 (blue line, T_B 358 K) and 69 ppm (red line, T_B 370 K).

The results obtained from SQUID measurements at room temperature, ZFC, show no significant difference between the two types of constructs: individual or dimers/trimers. Currently, we are trying to advance our understanding of magnetization processes underlying magnetically induced heating in these particular nanosystems. One of the major challenge is that a

typical SQUID measurement time is in the 10-100 s timescale, while magnetization dynamical processes governing hyperthermia are typically in the order of microseconds. This means further magnetic dynamics characterization such as high frequency AC magnetometry had to be exploited as discussed in the next section.

3.3.2.4.2. Dynamic hysteresis loops

High-frequency hysteresis loops were measured using a home-made set-up (with adjustable frequency and intensity) similar to the one described by Connord *et al.*[64] This set-up was kindly provided by our colleague Prof. Francisco Teran (IMDEA group, Madrid). We had the set-up for a month in our laboratory. This system quantifies the inductive magnetic signal[‡‡] of IONC dispersions, which is usually later calibrated by comparing the magnetization values at a given alternating magnetic field (H_{AC}) intensity obtained under H_{AC} and SQUID measurements.[51] By calibrating the system, quantitative information is obtained. But one can use the set-up also for a qualitative analysis, by running the measurements at same Fe concentration and comparing the hysteresis areas under the same experimental conditions. The individually coated IONCs and the sample of dimers/trimers formed from sample B were subjected to dynamic hysteresis loops at frequency of 96 kHz and magnetic field amplitude of 30 mT (24 kA/m), at an [Fe] concentration of 1 g/L. The data plotted in Figure 29a shows a larger hysteresis area for the individual IONCs compared to dimers and trimers. This result supported the SAR trend that showed for sample B a decrease when forming 1D and 2D nanoconstructs like dimers and trimers.

[‡‡] The AC magnetic signal depended on the Fe content. The lowest Fe concentration at which reliable measurements were achieved was [Fe] = 2 g/L.

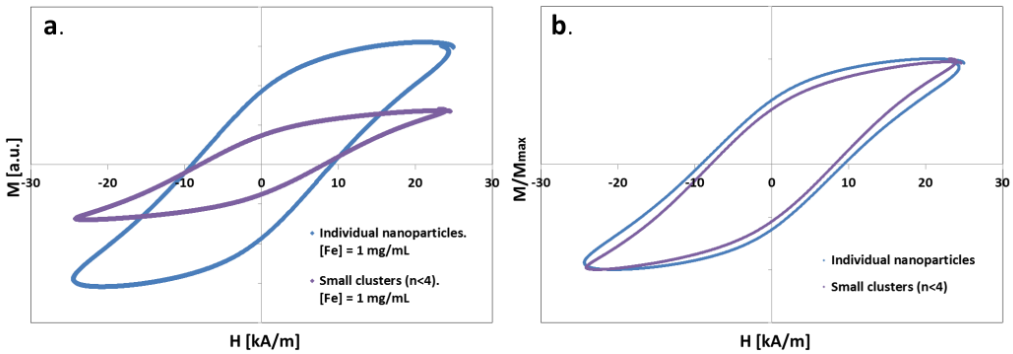

Figure 29: Dynamic hysteresis loops for different samples. (a) AC hysteresis loops for different Fe concentrations, (b) normalized hysteresis loops of individually coated IONCs (blue line) *vs.* dimers and trimers (violet line) under given H_{AC} condition (f = 96 kHz, B = 30 mT). The sample of dimers and trimers exhibited a smaller hysteresis area compared to individual IONCs.

3.3.3. Core-shell iron oxide nanocubes. Sample C

3.3.3.1. Clustering process and cluster characterization

The idea behind the formation of the last set of soft colloidal nanoclusters was to combine the study on the cluster formation with the research on the improvement of SAR values by oxidizing the wüstite core in mild conditions. We were curious to find out whether the clusters, once formed, would be stable during the thermal oxidation and what would be the change in SAR values of individual IONCs *vs.* dimers and trimers and *vs.* bigger soft colloidal clusters (n ≥ 4). Would the SAR trend be similar to sample A or sample B? Due to a lack of time, the oxidation was not done by magnetic stimulation under alternating fields, but by heating in oven at 80°C overnight, several days in a row.

The sample chosen for these new experiments had to be similar to the previous ones and be freshly synthesized. We chose sample C—a sample of core-shell iron oxide nanocubes with cube edge length of 20 ± 2 nm (Figure

30). The IONCs were synthesized 3 months before the cluster preparation and stored in chloroform. XRD data confirmed the presence of wüstite crystallographic phase just before performing the cluster formation (data not shown).

To our surprise, the water transfer for sample C did not work. Several experiments were carried out, but regardless of the amount of polymer used, once THF was evaporated the IONCs were aggregated on the walls of the vials instead of being transferred into water. For the few samples whereby the IONCs did not aggregate during THF evaporation, upon the last step—*i.e*. the addition of $CHCl_3$—the samples went from aqueous phase to organic phase.

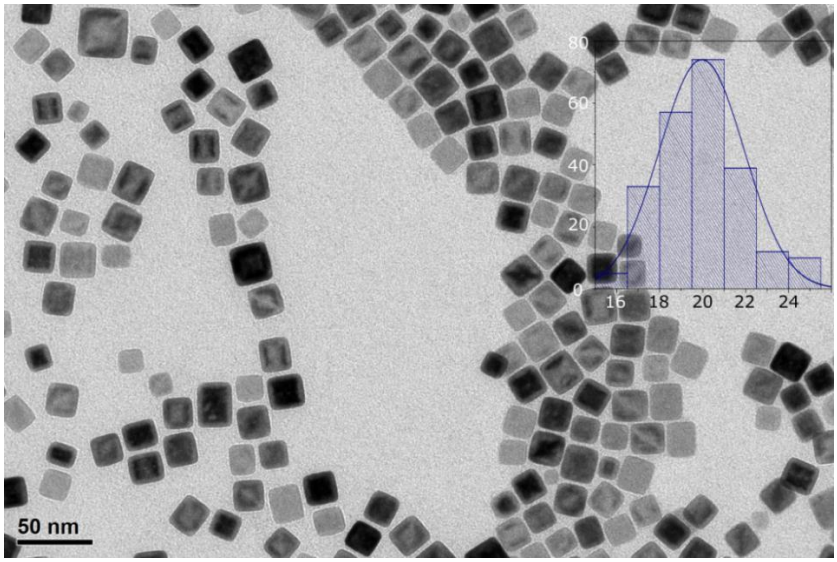

Figure 30: A fresh core-shell sample used for cluster formation. TEM micrograph of as-synthesized core-shell iron oxide nanocubes dispersed in chloroform [inset: size histogram, a = 20 ± 2 nm].

Free oleic acid (OA) in solution—the first step of the clustering procedure when the particles were dispersed in THF/H_2O mixture—played a

key role in cluster formation and it will be explained in detail in section 3.3.3.2. Therefore, it was decided to increase the amount of surfactant, by adding known amounts of OA—from 1 to 25 µL—to the solution of THF/H_2O in which the IONCs were dispersed alongside the amphiphilic polymer. The experimental conditions and the outcome of each experimental trial in terms of success of cluster formations are summarized in Table 7.

Table 7: Experimental conditions for nanocluster formation starting from sample C

Exp. number	Ratio of polymer/ nm^2	Volume of polymer [mL]	Volume of oleic acid [µL]	Fe amount [mg]	% wt. OA compared to Fe amount	Outcome
1	**18**	0.25	**2.5**	0.23	1	✓
2	**18**	0.25	**5**	0.23	2	✓
3	**18**	0.25	**10**	0.23	4	/[††]
4	**18**	0.25	**25**	0.23	10	✗
5	**72**	1	**2.5**	0.23	1	✓
6	**72**	1	**5**	0.23	2	/[§§]
7	**72**	1	**10**	0.23	4	✗
8	**72**	1	**25**	0.23	10	✗
9	**11**	0.15	**1**	0.23	0.4	✓
10	**11**	0.15	**2.5**	0.23	1	✓
11	**11**	0.15	**5**	0.23	2	/[††]
12	**11**	0.15	**7.5**	0.23	3	✗

For all samples, irrespective of the initial amount of polymer, upon addition of small amounts of OA (≤ 5 µL) the cluster formation occurred during water transfer. By further increasing the OA amount the IONCs migrated

[§§] The water transfer worked partially. Not all the IONCs were transferred into aqueous phase. Some of the IONPs stayed in organic phase.

towards organic phase upon the last step of $CHCl_3$ addition. For example, for 18 molecules polymer/nm^2 after addition of 2.5 and 5 µL OA (Figure 31—#1 corresponding to 2.5 µL and #2 corresponding to 5 µL), there was a clear separation between the nanoclusters dispersed in water (top layer of the Eppendorf tube) and the organic phase (bottom of the Eppendorf tube). When adding 10 µL OA (Figure 31, #3) the aqueous phase was cloudy with most of the IONCs found at the interface between organic/water phase. Lastly, upon addition of 25 µL OA (Figure 32, #4) the aqueous phase is transparent, no clusters were obtained. The IONCs were only in organic phase.

The samples for which cluster formation worked—#1, #2, #5, #9, #10—were characterized by DLS and TEM. Unexpectedly, for the ratio of 18 molecules PS*c*MA/nm^2 clusters with hydrodynamic diameters around 100 nm were formed, instead of individually coated IONCs as seen in the previous sections for samples A, B, spherical IONPs, 19 nm IONCs with rounded edges, *etc*. When quadrupling the polymer ratio from 18 to 72 molecules polymer/nm^2 even bigger clusters were formed—Z-average of 190 ± 2 nm with PDI 0.07 (Table 8—entry 3, experiment #5). As expected, by increasing the amount of polymer bigger clusters were formed, but the unpredicted results were:

(i) d_H of the clusters was twice the expected size from previous results (18 molecules PS*c*MA/nm^2 having Z-average of 98-105 nm instead of 49-55 nm[***]),

(ii) the increase of size by increasing the amount of surfactant, while keeping the polymer to particle surface ratio constant.

Regarding the latter result, it is worth mentioning a slight increase in size from 98 ± 1 nm to 105 ± 1 nm when increasing the amount of surfactant

[***] See Table 3, entry 1—16.5 molecules polymer/nm^2.

from 1 to 2 % of polymer volume (experiment #1: 250 µL polymer and 2.5 µL OA, experiment #2: 250 µL polymer and 5 µL OA), while a more pronounced increase happened when increasing the amount of surfactant from 1.5% to 3.75% polymer volume (experiment #9: 150 µL polymer and 1 µL OA, experiment #10: 150 µL polymer and 2.5 µL OA)—Z-average raised from 82 ± 1 nm to 106 ± 1 nm. These facts suggest that the amount of surfactant played an important role not only in the outcome of the water transfer, but it also influences the average size of the clusters, especially for smaller clusters. The DLS data is summarized in Table 8.

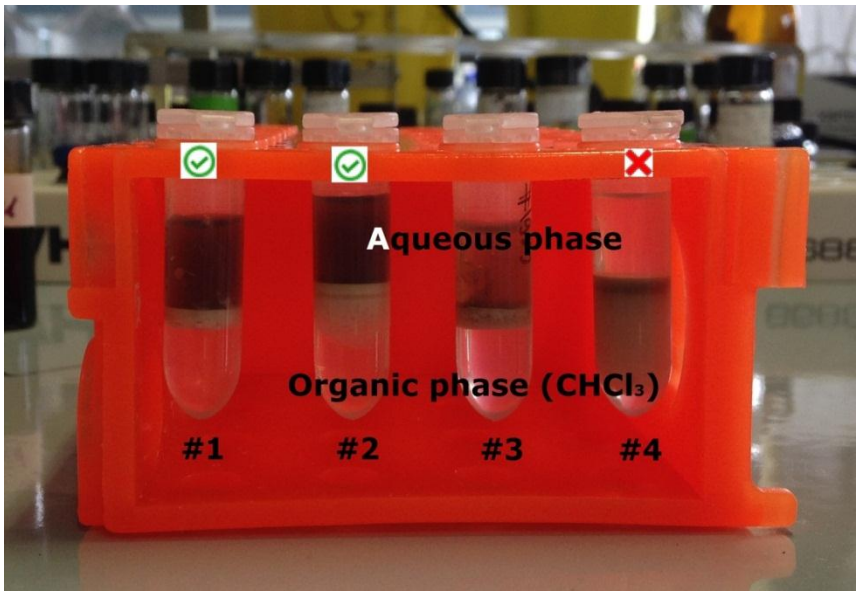

Figure 31: Importance of free surfactant for cluster formation. Eppendorf vials corresponding to experiments #1 to #4, after $CHCl_3$ addition and phase separation (experimental conditions presented in Table 7). When adding small amounts of surfactant (2.5 or 5 µL per 0.23 mg Fe) the soft colloidal clusters were formed. When further increasing the amount of extra surfactant (10 or 25 µL per 0.23 mg Fe) the water transfer did not proceed, as the particles went into organic phase after addition of $CHCl_3$.

Table 8: DLS data for clusters formed with 20 nm IONCs@PS*c*MA (in H_2O)

Experiment number	Z-Ave [nm]	PdI	Intensity mean [nm]	Number mean [nm]	Volume mean [nm]
1	98 ± 1	0.07 ± 0.01	106 ± 1	74 ± 3	90 ± 1
2	105 ± 1	0.07 ± 0.02	114 ± 1	81 ± 2	99 ± 1
5	190 ± 2	0.07 ± 0.01	206 ± 1	168 ± 6	217 ± 1
9	82 ± 1	0.15 ± 0.01	94 ± 1	52 ± 1	70 ± 1
10	106 ± 1	0.10 ± 0.01	119 ± 3	73 ± 3	98 ± 1

The DLS results were supported by transmission electron microscopy images. From the TEM micrographs presented in Figure 32, one could confirm the unpredicted formation of bigger clusters (n > 4) for the ratio of 18 PS*c*MA/nm^2—Figure 32a, with addition of 2.5 µL OA, and Figure 32b, with addition of 5 µL OA during the first step of water transfer. When increasing the ratio of polymer/nm^2 to 72, clusters with d_H around 200 nm were formed (Figure 32c). As our main aim was to construct soft colloidal nanoclusters smaller than 100 nm, the amount of amphiphilic polymer was further reduced to 11 polymer molecules/nm^2 (with addition of 1 µL OA—Table 8: experiment 9). For this ratio, dimers and trimers were formed (Figure 32d). Further decreasing the amount of polymer did not result in individually coated IONCs. The water transfer did not work for 7 PS*c*MA/nm^2. In all the experiments carried out before, the range—in which the cluster size could be tuned from individual IONCs to dimers and trimers and later to bigger clusters—was from 16 to 66 molecules polymer/nm^2. For sample C the range was shrunk and only dimers and trimers and bigger clusters could be obtained for 11 to 18 molecules polymer/nm^2, respectively. In order to better understand the reasons behind these surprising results thermogravimetric analyses of the various samples were performed.

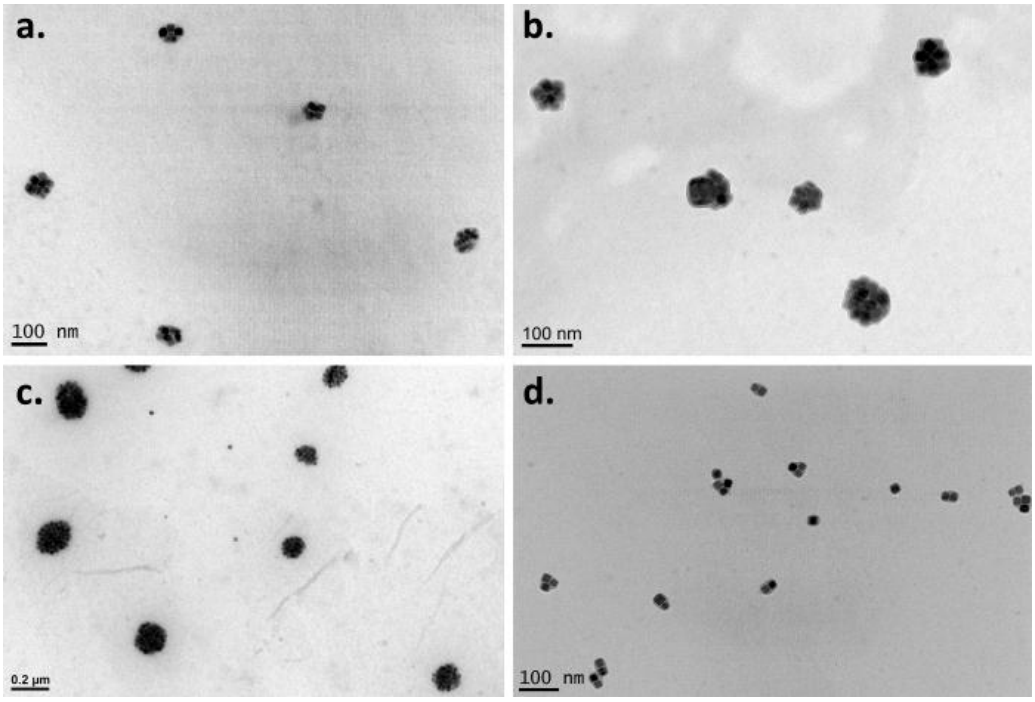

Figure 32: Soft colloidal clusters formed with addition of various amounts of extra polymer. TEM micrographs[†††] of 20 nm IONCs@PS*c*MA (sample C) in H_2O for a ratio of (a) 18 [+2.5 µL OA], (b) 18 [+5 µL OA], (c) 72 [+ 2.5 µL OA] and (d) 11 [+ 1 µL OA] PS*c*MA molecules/nm^2 particle surface.

3.3.3.2. Thermogravimetric analysis

As briefly mentioned earlier, towards the end of our research, we stumbled upon the fact that the amount of surfactant played an important role in cluster formation. When trying to reproduce the clustering process with a new batch of core-shell IONCs, we noticed that even if we were using the same ratio of polymer/nm^2 of particle surface as done previously, the procedure did not result in cluster formation. This fact prompted us to investigate the amount of surfactant present on the surface of the IONCs by

[†††] Different scale bars in TEM micrographs

means of thermogravimetric analysis (TGA) in order to find a possible correlation with the unsuccessful result of cluster formation.

First, we investigated the sample for which the clustering process worked straight away. The thermogravimetric analysis of the sample A in $CHCl_3$ (Figure 33, blue line) showed a first weight loss of 26.4% wt. in the temperature range from 150 to 300 °C and a second weight loss of 31.2% wt. from 300 to 400 °C. In literature, the first transition is usually attributed to unbound or physisorbed OA[65–67], while the second transition is attributed to the oleate molecules chemisorbed to the particle surface[65–67]. The first weight loss for the sample occurred in the same temperature region in which the mass loss of oleic acid was *ca*. 90% wt. (Figure 33, red line), strongly supporting the claim that the first weight loss was due to free oleic acid. The equilibrium between free oleic acid and oleate bound to the surface of the IONCs was a crucial parameter to be controlled in order to obtain soft colloidal clusters as it will be discussed in this section.

Before going any further, it is worth mentioning that the amount of oleic acid chemisorbed to the surface of the IONCs—ligand density (ρ_l)—was much higher than the theoretical 5 ligands/nm^2.[68,69] The calculated ligand density was 27 ligands/nm^2 which implied a multilayer coating of surfactant. The formula used for the calculation of ligand density was the one described by Tong *et al.*[70] :

$$\rho_l = \frac{w_l N_{Av}}{M_{w,l}} \cdot \frac{m_{NP}}{w_{NP} A_{NP}} \quad \text{(Eq. 2)}$$

wherein w_l was the weight fraction of the ligand, N_{Av} was Avogadro's number, $M_{w,l}$ was the molecular weight of the ligand, m_{NP} was the mass of one nanoparticle, w_{NP} was the weight fraction of the iron oxide nanoparticles, and A_{NP} was the surface area of one NP. The cube edge length of one nanocube

was taken as 20 nm for area and volume calculations. For mass calculation the density of bulk magnetite was considered (5.18 g/cm^3). The weight fraction of ligand considered was the one corresponding to the second weight loss as determined by TGA. If we consider the total weight loss of ligand, the organic part that showed a two-step decomposition between 150 and 400 °C, then the ligand density was 50 ligands/nm^2, with a 46% to 54% distribution between free oleic acid and oleate bound to the surface of the NPs. When having these fractions of free oleic acid and oleate bound to NPs the clusters were easily obtained.

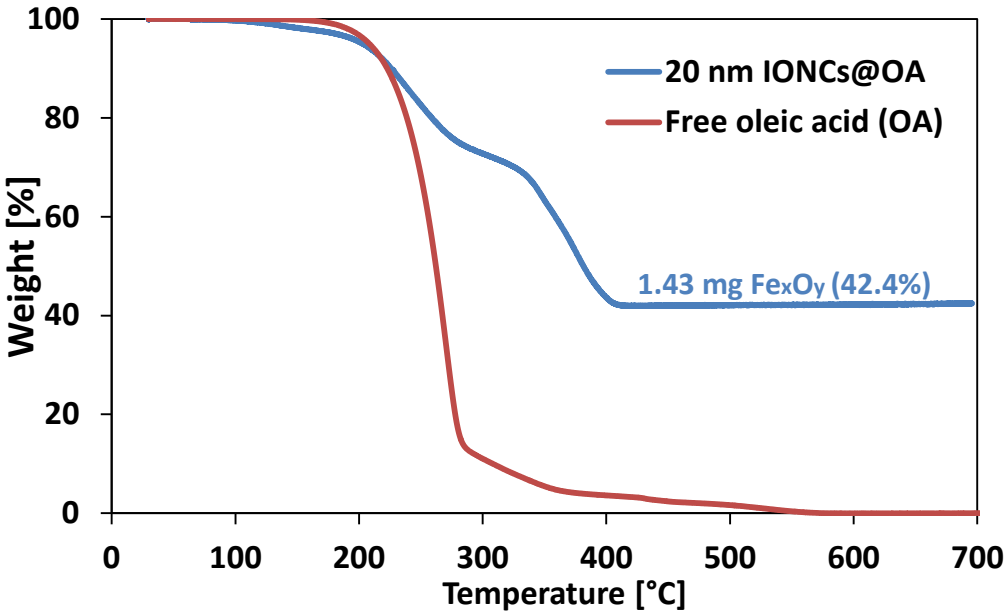

Figure 33: Sample A. TGA degradation profiles of oleic acid capped IONCs (blue curve) and free oleic acid (red curve) performed in air. The first weight loss in the region between 150 and 300 °C corresponded to free oleic acid in solution, while the second weight loss in the region between 300 and 400 °C corresponded to oleate chemisorbed to the surface of the IONCs.

Next, thermogravimetric analyses were carried out on sample C—the sample for which the clustering process didn't work without addition of extra OA. For the as-synthesized sample in $CHCl_3$ (Figure 30), the organic layer accounted for a mass loss of 79.6% wt., with 11.5% wt. (Figure 34—blue curve) corresponding to free oleic acid in solution and 68.1% wt. to chemisorbed surfactant (Figure 35—blue curve). Upon addition of 1 µL OA per 0.23 mg Fe, the overall mass loss increased to 85.2% wt. with 24.6% (Figure 34—violet curve) and 60.6% wt. (Figure 35—violet curve) corresponding to oleic acid physisorbed and chemisorbed to the surface of the IONCs, respectively. Upon the addition of 2.5 µL OA the weight loss was 89.3% wt. with a bigger amount of free surfactant 32.3% wt. (Figure 34—green curve) and a lower amount of chemisorbed OA 57% wt. (Figure 35—green curve) compared to previous samples. These results suggested that it was the decrease in the amount of surfactant tightly bound to the surface of the IONPs, accompanied by an increase in free oleic acid, that facilitated the clustering process and the water transfer. When chemisorbed OA was higher than 61% wt. the polystyrene branches of the amphiphilic PS*c*MA could not intercalate with the surfactant layer, as the surfactant molecules were tightly packed one close to another. As some of the OA molecules were stripped from the external layers—by decreasing the chemisorbed OA amounts to values below 61% wt.—PS braches took the place of OA molecules and the water transfer proceeded as expected.

If we took a closer look at the TGA degradation profiles (Figure 35), we could see that the second mass loss was a multistep process. Also, if we recall Equation 2, the second mass loss of 60.6% (Figure 36—violet curve) corresponded to a calculated ligand density of 150 ligands/nm^2, that is 5.5 times more than the ligand density calculated for sample A—27 ligands/nm^2.

Thus we decided to run a one-hour long isotherm at 320°C—the temperature at which the second loss started.

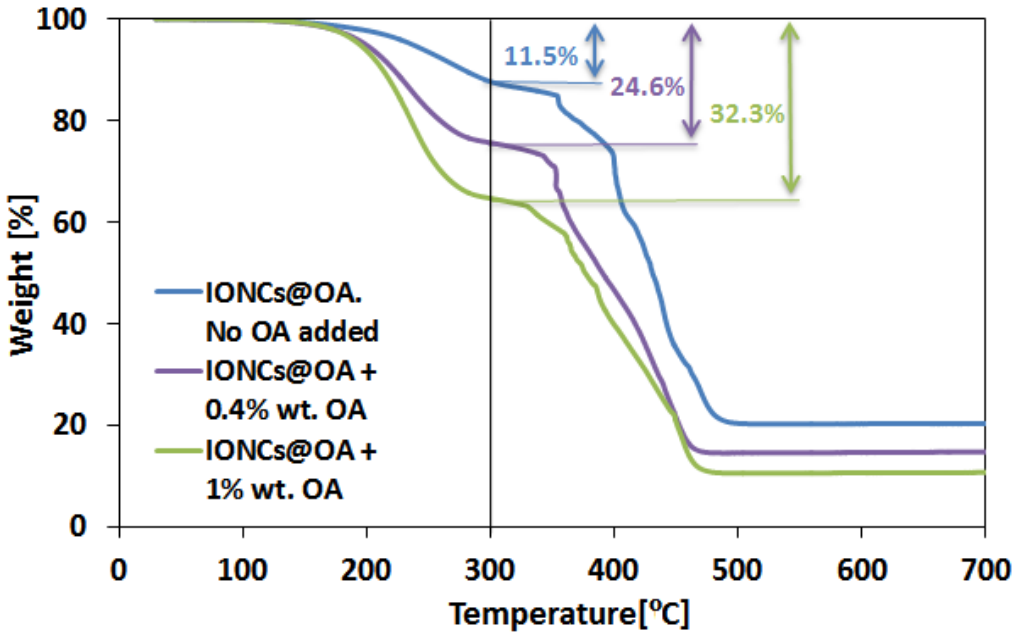

Figure 34: Sample C with different amounts of added free oleic acid. TGA degradation profiles of as-synthesized oleic acid capped IONCs (blue curve), oleic acid capped IONCs with addition of 0.4% wt. OA (violet curve), and oleic acid capped IONCs with addition of 1% wt. OA (green curve), performed in air. By adding extra surfactant, the first weight loss in the region from 150 to 300 °C increased from 11.5% (no extra OA), to 24.6% and 32.3% for addition of 2.5 and 5 µL of surfactant (per 0.23 mg Fe), respectively. This loss corresponded to free oleic acid in solution and physisorbed OA.

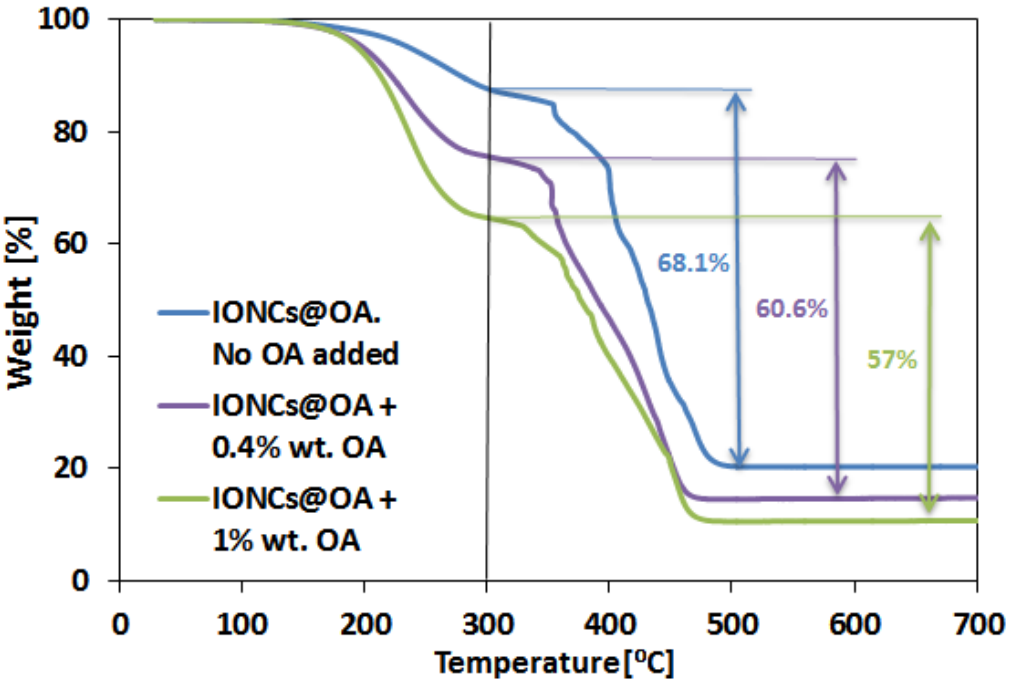

Figure 35: TGA degradation profiles of as-synthesized oleic acid capped IONCs [IONCs@OA] (blue curve), IONCs@OA with addition of 0.4% wt. OA (violet curve), IONCs@OA with addition of 1% wt. OA (green curve), performed in air. By adding extra surfactant, the 2nd weight loss in the region from 300 to 400 °C decreased from 68.1% (no extra OA), to 60.6% and 57% for addition of 2.5 and 5 µL of surfactant (per 0.23 mg Fe), respectively. This loss corresponded to OA chemisorbed to the surface of IONCs.

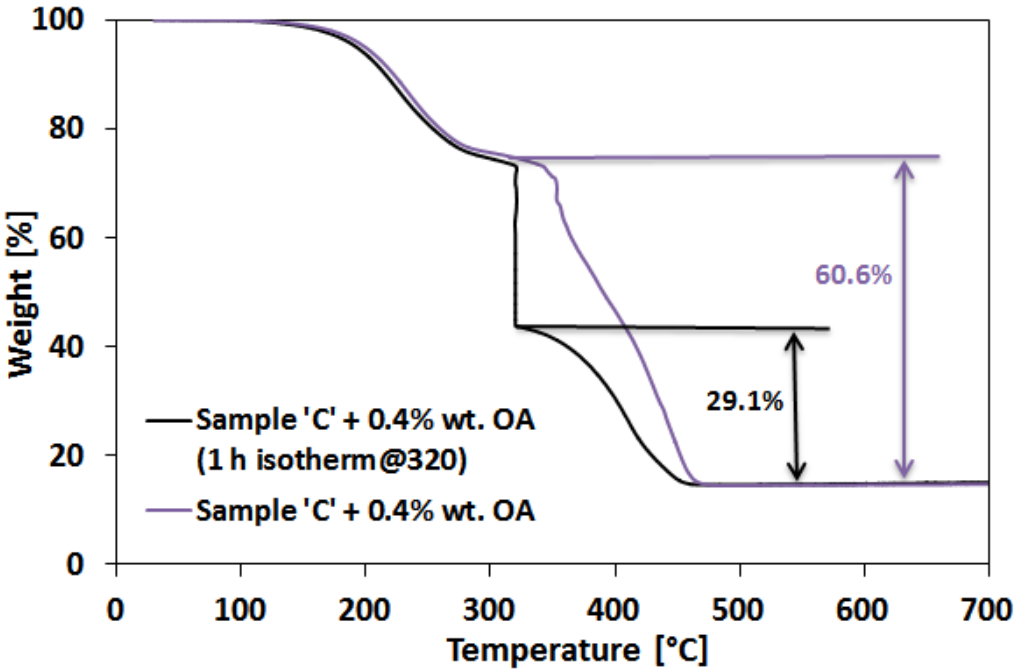

Figure 36: Breakdown of the multistep second weight loss into two steps by applying a one-hour isotherm @320 °C. TGA degradation profiles of sample C with addition of 1 µL OA per 0.23 mg Fe (+ 0.4% wt. OA) without (violet curve) and with (black curve) one-hour isotherm at 320°C, performed in air. By applying the isotherm the amount of oleate bound to the surface dropped from 60.6% down to 29.1%.

When applying the one-hour isotherm, we could better distinguish the 3rd mass loss as a single step process (Figure 36—black curve). The weight loss corresponding to chemisorbed OA decreased from 60.6% to 29.1% (Figure 36), the latter value corresponding to a ligand density of 72 ligands/nm^2. The higher amount of surfactant chemisorbed to the surface of the IONCs could have explained why the clusters obtained with sample C had a bigger d_H compared to clusters obtained with sample A when using the same amount of poly(styrene-*co*-maleic anhydride). Indeed, when the two samples were synthesized, the one parameter that changed was the amount of oleic acid

used—1.6 g for sample A and 2.6 g for sample C. This change in synthesis parameters was reflected in the total amount of surfactant chemisorbed to the surface of the nanoparticles.

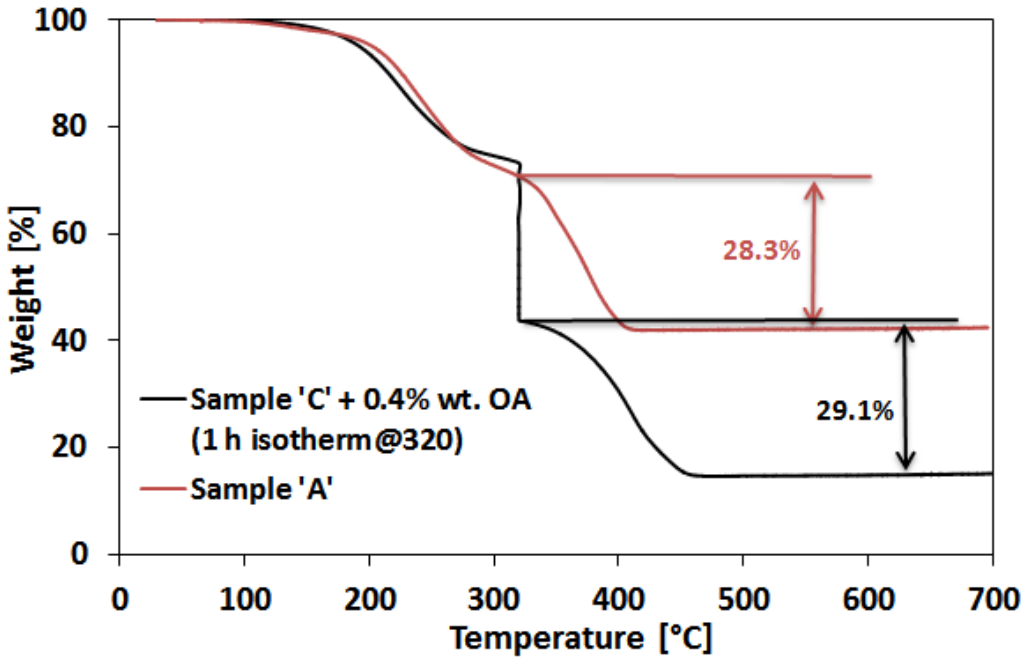

Figure 37: Sample A *vs*. sample C. TGA degradation profiles of sample A as-synthesized (red curve) and sample C with addition of 1 µL OA per 0.23 mg Fe (black curve), performed in air.

3.3.3.3. Hyperthermia (before and after annealing)

For sample C only dimers and trimers and bigger clusters with n ≥ 4 were obtained by the clustering process. In order to have a comparison with individual IONCs as well, a part of sample C was transferred into water by ligand exchange with gallic-PEG (as performed on core-shell IONCs in chapter 2). The DLS data showed an increase in Z-average from 59 ± 1 nm for individual IONCs to 98 ± 1 for clusters with n ≥ 4 (Table 9). Though, by DLS, the characteristics of individual IONCs and the sample of dimers and trimers were

very close by intensity, number and volume weighted hydrodynamic diameters (Table 9), from the TEM micrographs we could clearly see the distinction between single IONCs (Figure 38a) and the dimers and trimers sample (Figure 38b).

Table 9: DLS data for clusters formed with sample 'C', in H_2O, before annealing for 52 hours @80°C

Sample	Z-Ave [nm]	PdI	Intensity mean [nm]	Number mean [nm]	Volume mean [nm]
Individual IONCs@GaPEG	59 ± 1	0.18 ± 0.01	71 ± 2	34 ± 1	46 ± 1
11PS*c*MA (dimers and trimers)	65 ± 1	0.20 ± 0.01	77 ± 2	38 ± 3	47 ± 5
18 PS*c*MA (clusters with n ≥ 4)	98 ± 1	0.07 ± 0.01	106 ± 1	74 ± 3	91 ± 1

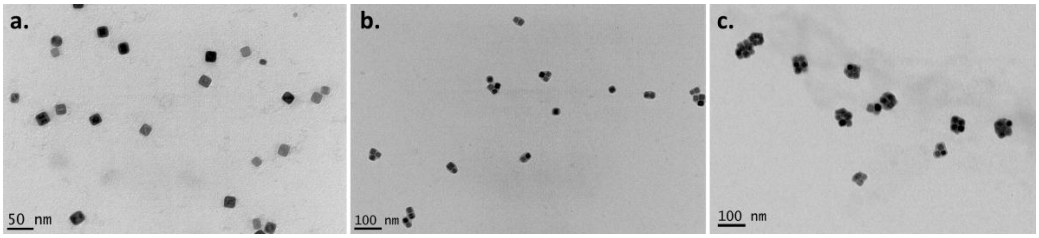

Figure 38: Soft colloidal clusters formed with freshly synthesized 20 nm core-shell IONCs (sample C) plus addition of extra surfactant. TEM micrographs[‡‡‡] of 20 nm (a) IONCs@GaPEG (individual IONCs), (b) 11 [+1 µL OA] (dimers and trimers) and (c) 18 PS*c*MA molecules/nm^2 [+ 2.5 µL OA] (clusters with n ≥ 4), in H_2O.

Once the clusters were obtained, as mentioned at the beginning of section 3.3.3.1., the idea was to oxidize the wüstite core to magnetite, in mild

[‡‡‡] Different scale bars in TEM micrographs

conditions—in an oven at 80°C. Hyperthermia experiments were carried out before the annealing process and after each step of the annealing process, alongside with DLS and TEM characterization in order to check the stability of the clusters. A schematic representation of the idea is depicted in Figure 39. Each step of the annealing process was done overnight, up to a total of 52 hours. After 52 hours, the SAR values did not improve significantly, thus the annealing process was stopped.

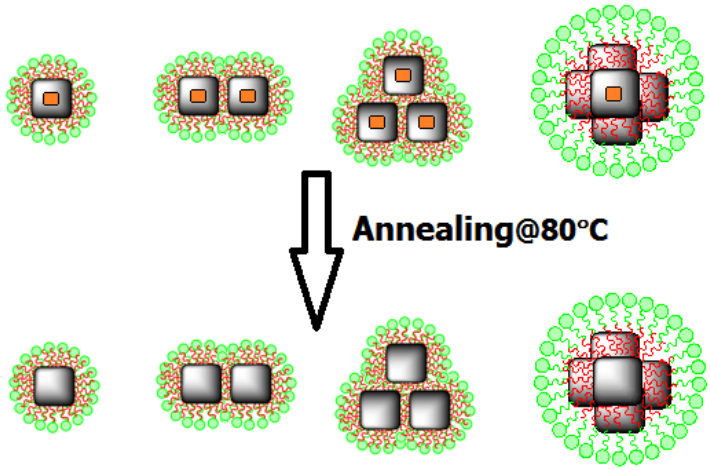

Figure 39: Schematic representation of the oxidation of the wüstite core for clusters of different sizes in an oven at 80 °C.

All the samples were stable during the annealing process as confirmed by DLS measurements (Figure 40). For example, for sample 18 PS*c*MA (bigger clusters with n ≥ 4), the volume weighted hydrodynamic diameter remained unchanged during the whole annealing process, with Z-average of 98 ± 1 nm (PDI 0.07) before annealing and 97 ± 1 (PDI 0.08) after 52 hours annealing.

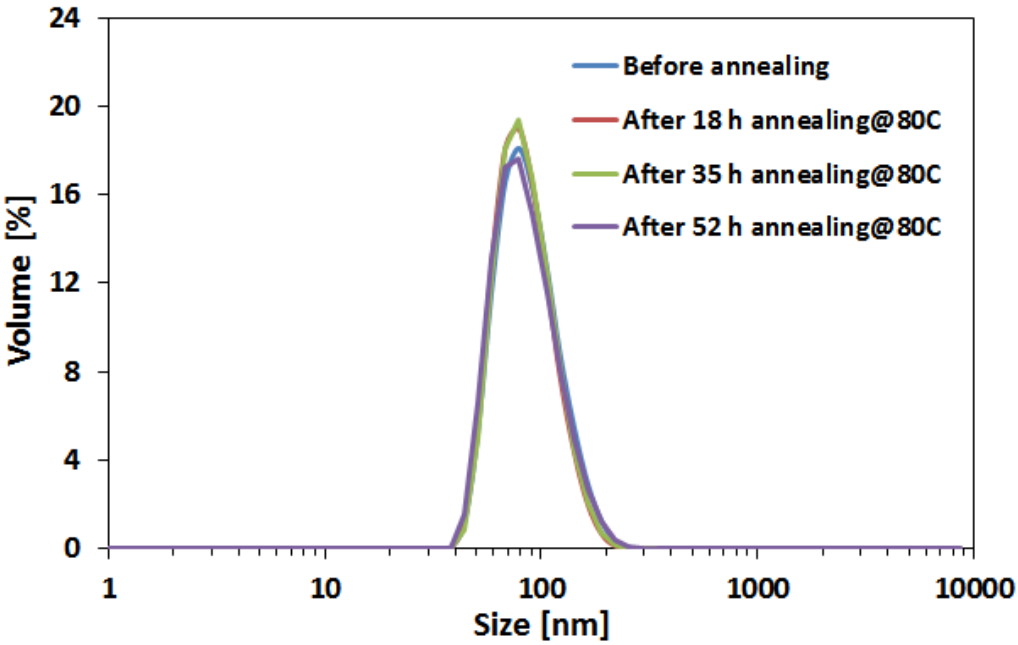

Figure 40: Stability of the mean hydrodynamic diameter during annealing experiments. DLS volume distributions for soft colloidal nanoclusters 18PS*c*MA before annealing (blue line), after 18 hours (red line), 35 hours (green line) and 52 hours (violet line) of annealing at 80 °C. The sample was stable under annealing @80 °C, as no aggregation occured. Z-average before annealing: 98 ± 1 nm (PDI 0.07), after 52 hours of annealing: 97 ± 1 (PDI 0.08).

The SAR values before annealing were below 50 W/g_{Fe} (Figure 41, Table 10), which was expected of core-shell iron oxide nanocubes, due to non-contributing paramagnetic wüstite core. As we started oxidizing the core by heat treatment, the SAR values increased up to 3.7 times to 131 ± 5, 179 ± 1, and 97 ± 4 W/g_{Fe} for individual IONCs, dimers and trimers and bigger clusters, respectively (Table 10). The dimers and trimers sample showed higher SAR values compared to the other two samples after only 18 hours of annealing. The trend was maintained through the whole annealing process, up to 52 hours (Figure 41, Table 10).

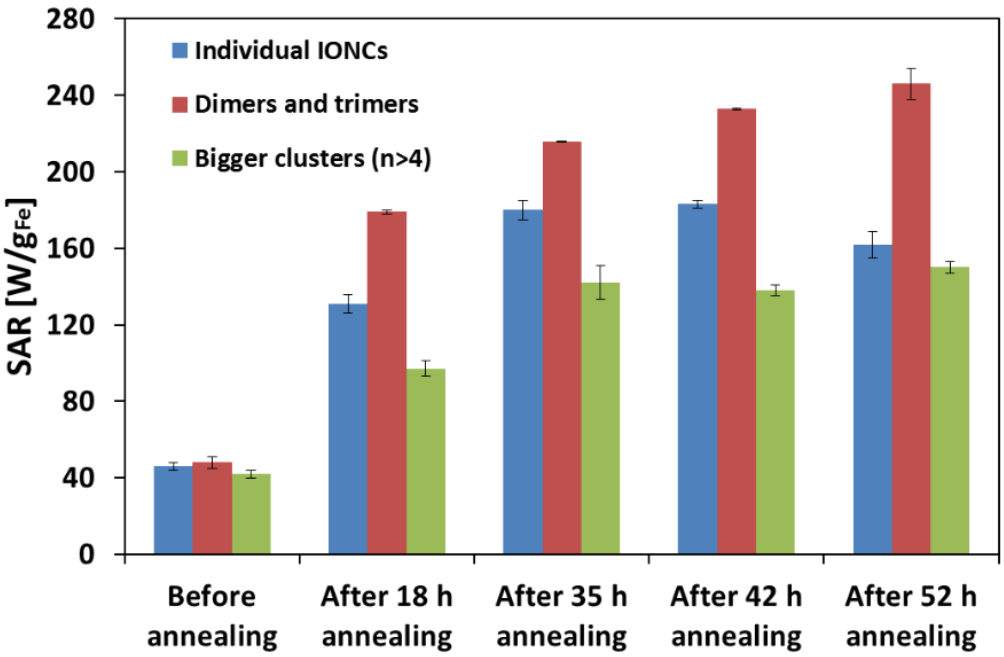

Figure 41: SAR values (with standard deviation) for soft colloidal nanoclusters during the annealing process: IONCs@GaPEG (blue bars—individual IONCs), 11PS*c*MA (red bars—dimers and trimers), and 18PS*c*MA (green bars—clusters with n ≥ 4). Only after 18 hours of annealing the sample of dimers and trimers showed higher SAR values. The trend was maintained up to 52 hours of annealing.

Table 10: SAR values of nanoclusters at 302 kHz frequency and 30 mT magnetic field amplitude

	Individual IONCs@GaPEG	**Dimers and trimers**	**Bigger clusters (n ≥ 4)**
	SAR [W/g_{Fe}]	**SAR [W/g_{Fe}]**	**SAR [W/g_{Fe}]**
Before annealing	46 ± 2	48 ± 3	42 ± 2
After 18 h annealing	131 ± 5	179 ± 1	97 ± 4
After 35 h annealing	180 ± 5	216 ± 1	142 ± 9
After 42 h annealing	183 ± 2	233 ± 1	138 ± 3
After 52 h annealing	162 ± 7	246 ± 8	150 ± 3

3.3.3.4. Magnetic characterization after annealing

As seen, from hyperthermia measurements, soft colloidal nanoclusters of different sizes—annealed for 52 hours at 80 °C—behaved differently under alternating magnetic fields. The trend, same as the one for sample A, consisted of an increase of SAR values for clusters formed of n = 2 or n = 3 IONCs compared to individual IONCs, while increasing n number above 4 the SAR value dropped again (Figure 41). Next, we turned to SQUID measurements to check the trend in M_S and T_B: magnetization *vs*. field and zero-field-cooled field-cooled (ZFC-FC) measurements. The magnetization curves were recorded both at 298 K and 10 K. All the magnetic parameters determined from SQUID experiments—M_S, H_C, H_E and T_B—are summarized in Table 11.

As seen in Figure 42c and Table 11, the saturation magnetization Ms of individual IONCs at RT was 86.5 emu/gFe. The magnetization increased up to 90.1 emu/gFe for dimers and trimers (11 PScMA) and decreased back to 86.1 emu/gFe for centro-symmetrical clusters with n ≥ 4 (18 PScMA). This trend was similar to the one of SAR values (Figure 41), where dimers and trimers showed a higher SAR compared to both individual IONCs and bigger clusters. Regarding coercivity (Figure 42d), dimers and trimers had the highest coercivity HC of 6.9 mT, while individual IONCs and bigger clusters had coercivities HC of 5.0 and 4.1 mT, respectively (Table 11). Lastly, blocking temperature TB of individual particles, dimers and trimers, and clusters with n≥ 4, determined from temperature dependent ZFC-FC magnetization measurements (Figure 43), were all above RT, with values of 400, 370 and 373 K, under magnetic fields of 5 mT (Table 11).

Table 11: Magnetic properties of sample C, after 52 hours of annealing @80 °C

	M_s^{298K} / M_s^{10K} [emu/g_{Fe}]	$H_C^{ZFC@298K}$ / $H_C^{ZFC@10K}$ [kA/m] ([mT])	$H_E^{ZFC@298K}$ / $H_E^{ZFC@10K}$ [KA/m] ([mT])	T_B^{5mT} [K]
Individual IONCs@GaPEG	86.5/93.1	4 (5)/ 27 (33.8)	1 (1.25)/ 1 (1.25)	400
11PS*c*MA (dimers and trimers)	90.1/94.5	5.5 (6.9)/ 26.5 (33.2)	1.5 (1.9)/ 1.5 (1.9)	370
18PS*c*MA (clusters with n≥ 4)	86.1/83.7	3.25 (4.1)/ 25 (31.3)	0.75 (0.9)/ 1.25 (1.6)	373

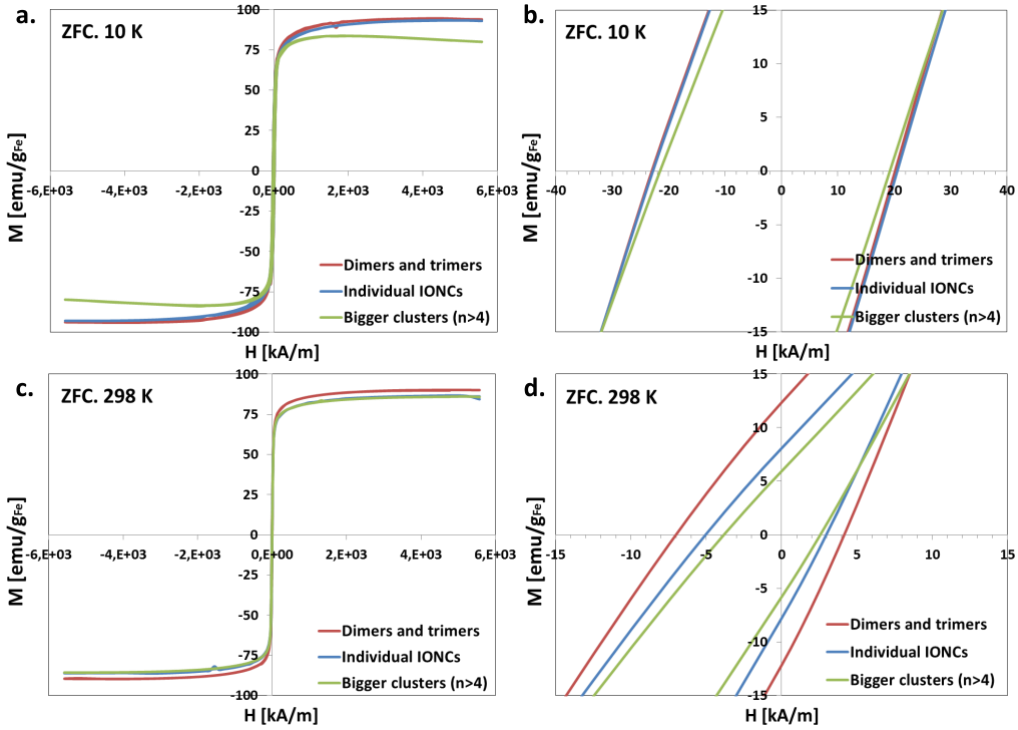

Figure 42: Magnetization *vs*. magnetic field curves recorded at (a) 10 K and (c) 298 K for IONCs@GaPEG (blue line—individual IONCs), 11 PS*c*MA (red line—dimers and trimers), and 18 PS*c*MA (green line—clusters with n ≥ 4); (b) and (d) Zoom of the low magnetic field region to better visualize coercivity H_C.

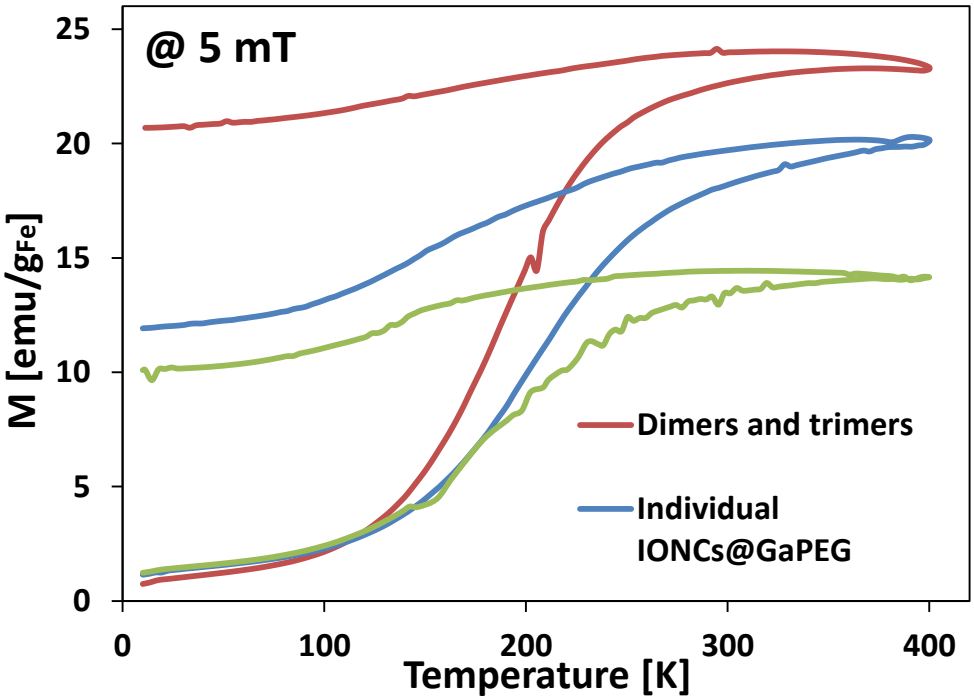

Figure 43: Temperature dependent zero-field-cooled and field-cooled magnetization measurements performed on aqueous suspension of nanoclusters embedded in gypsum matrix recorded at 5 mT magnetic field: IONCs@GaPEG (blue line—individual IONCs), 11 PS*c*MA (red line—dimers and trimers), and 18 PS*c*MA (green line—clusters with n ≥ 4)

3.4. Conclusion

To summarize, a procedure for the water transfer of iron oxide nanoparticles and the formation of soft colloidal nanoclusters during the water transfer have been developed. The polymer used was poly(styrene-*co*-maleic anhydride), cumene terminated (M_n of 1 600 g/mol). Nanoclusters of different sizes were obtained by changing the polymer to nanoparticle surface ratio. The method proved to be versatile as nanoparticles of different shapes, sizes, and types were clustered in a controlled manner. The cluster sizes were confirmed by DLS, TEM, and AC Susceptibility measurements.

After cluster formation, the focus shifted towards correlating specific absorption rate SAR values of nanoclusters made of core-shell IONCs to their size, composition and magnetic features. From the studies on the clustering process, three crucial parameters have emerged:

(i) the amount of polymer, as seen in section 3.2., was the main parameter allowing the clustering process control,

(ii) the initial Fe concentration had the same effect as the amount of amphiphilic polymer used: an increase in [Fe] concentration was accompanied by an increase in the numbers of dimers and trimers formed during water transfer—as seen in section 3.3.2.1.,

(iii) the amount of free surfactant was critical for the water transfer and cluster formation—as seen in section 3.3.3.2.

Regarding SAR values, the three samples presented different trends: sample A and C showed an increase in SAR value when anisotropic structures like dimers and trimers were formed, while sample B showed a decrease. For sample A and C, magnetization measurements *vs.* field gave us an indication about the increase of the response to the magnetic fields accompanied by an

increase in SAR values (for dimers and trimers), while for clusters formed with more than 4 IONCs, particles' magnetic moments tended to arrange in a so-called demagnetizing configuration, degrading the overall magnetic moment and behaving like multi-domain particles. For sample B, SQUID measurements were not enough to deepen our understanding of SAR values, thus we complemented the data with AC hysteresis loops under conditions similar to hyperthermia experiments. Larger area of the AC loops was recorded for those samples whose SAR was higher. For clusters from sample B, the SAR trend was confirmed as, under alternating field conditions, dimers and trimers displayed qualitatively a smaller hysteresis loop compared to individual IONCs.

3.5. Experimental part

CHEMICALS

All reagents were obtained from commercial suppliers and used without further purification. Iron pentacarbonyl $Fe(CO)_5$ (98%), 1-octadecene (1-ODE, 99%), oleic acid (OA, 90%), triethylamine (99%), chloroform ($CHCl_3$), ethanol (EtOH), dichloromethane (DCM), poly(styrene-*co*-maleic anhydride), cumene terminated (M_n = 1 600 g/mol), α,ω-aminopropyl-poly(ethylene glycol) (M_n = 2 000 g/mol), gallic acid, phosphate buffered saline (PBS) (150 mM NaCl, pH 7.4), sodium hydroxide were purchased from Sigma-Aldrich. Sodium oleate (97%) was obtained from TCI. THF was purchased from Carlo Erba Reagents.

CHARACTERIZATION

Dynamic Light scattering (DLS)

Particle size measurements were carried out using a Malvern Zetasizer Nano series instrument, operated in the 173° backscattered mode on diluted aqueous solutions of nanoclusters. The measurements were performed at 25 °C. An equilibration time of 2 minutes was allowed before each measurement and at least three measurements were performed for each sample.

Transmission electron microscopy (TEM)

Conventional TEM images were obtained using JEOL JEM 1011 electron microscope, working at an acceleration voltage of 100 kV and equipped with a W thermionic electron source and a 11Mp Orius CCD Camera (Gatan company, USA). Samples were prepared by placing a drop of sample onto a carbon coated copper grid which was then left to dry before imaging.

Thermogravimetric analysis (TGA)

The weight loss of oleic acid coated nanoparticles was determined using a TA Instruments Hi-Res TGA 2950 thermogravimetric analyzer under air atmosphere (60 cm^3/min). The samples (5-10 mg) of the surfactant coated nanocubes were heated from room temperature to 50 °C and an isotherm was applied for 15 minutes, then heated to 700 °C at a heating rate of 10 °C/minute.

SAR measurements

The calorimetric measurements to determine the specific absorption rate (SAR) value of the iron oxide nanoclusters were carried out using the Nanoscale Biomagnetics instrument (DM100) operating over the range of frequencies from 105 to 302 kHz and fields up to 40 mT and 30 mT, for 105 kHz and 302 kHz, respectively. The SAR values were calculated using the formula:

$$SAR\ (\frac{W}{g}) = \frac{C}{m} \times \frac{dT}{dt}$$

where *C* is the specific heat capacity of dispersing medium (H_2O in most cases) per unit volume (J/K) and m is the concentration (g/L of Fe) of magnetic material in solution. The calorimetric measurements were carried out in quasi-adiabatic conditions and the slope of the curve $\frac{dT}{dt}$ was measured by taking into account only the first 20-25 seconds of measurement.

Magnetic characterization

Field dependent static magnetic measurements were carried out by employing an ever cooled Magnetic Property Measurement System (*MPMS-XL*, Quantum Design) on immobile nanoclusters. The samples were prepared by mixing 50 µL of nanoclusters dispersed in milli-Q water, at an iron concentration of 0.9 g/L, with 60 mg gypsum in the designated polycarbonate capsules and by drying them thoroughly. The zero-field-cooled (ZFC) and field-cooled (FC)

temperature dependent magnetization measurements were performed on samples prepared in the same way in the cooling field of 5 mT. The residual magnetic field in the SQUID magnets was nulled using the designated low field Hall sensor prior to ZFC measurements. All the presented magnetization data are corrected with respect to the diamagnetic and paramagnetic contributions of water and gypsum using the automatic background subtraction routine. The curves were normalized to the iron concentration as obtained from the elemental analysis.

Elemental analysis

Elemental analysis was carried out via Inductively Coupled Plasma Atomic Emission Spectroscopy (ICP-AES) on a ThermoFisher iCAP 6000 series instrument. The samples were prepared by digesting 2.5-10 µL sample in 1 mL aqua regia in a 10 mL volumetric flask, overnight. The next day, the flask was filled up to the graduation mark with milli-Q water and filtered through a 0.45 µm filter membrane prior to the measurement.

SYNTHESIS

Synthesis of nanocubes

Core-shell iron oxide nanocubes were synthesized following a recently published procedure[23] with a slight modification in order to obtain bigger nanoparticles. Briefly, in a typical synthesis[§§§] of 20 nm nanocubes (Figure 4b), oleic acid (1.6 g, 5.7 mmol), sodium oleate (0.939 g, 3 mmol) and 1-octadecene (5 mL) were added to a 50 mL three-necked flask connected to a reflux cooler and pumped to vacuum for 30 min at 90 °C. Afterwards, the solution was cooled down to 60 °C and put under N_2 flux. Then the precursor solution

[§§§] For samples A and B. For sample C, the synthesis parameters that changed were the amount of OA (2.6 g, 9.3 mmol) and the initial volume of 1-octadecene (3 mL).

$Fe(CO)_5$ (0.597 g, 3 mmol, dissolved in 1 mL of 1-ODE) was injected and the mixture heated, in 20 min, to 320 °C. The solution reaction was stirred vigorously at 320 °C and as nucleation started (the solution turned black) it was kept at that temperature for another 1.5 h, then cooled down and exposed to air for 30 min at 130 °C. Next it was left to cool to room temperature. Finally, the IONCs were collected by centrifugation at 8 000 rpm and washed with methanol. The cleaning process was carried out three times and the IONCs were stored in chloroform.

METHODS

Controlled clustering

Briefly, for the formation of soft colloidal nanoclusters with hydrodynamic diameters around 100 nm, in a 20 mL vial, to 9 mL THF solution 1 mL of stock solution[****] of poly(styrene-*co*-maleic anhydride), cumene terminated (M_n = 1 600 g/mol), dissolved in THF ([PS*c*MA] = 2.19 mM) was added, followed by the addition of 35 µL of iron oxide nanocubes solution ([Fe] = 6.09 g/L, 0.33 µM) with a cube edge length of 20 nm. Afterwards, 1 mL H_2O was added dropwise, while sonicating the solution in an ice bath for 2 minutes. Next, the solution was placed on a horizontal shaker rotating at a speed of 125 rotations per minute and it was left overnight to slowly evaporate the THF. The following day, the remaining 0.8 to 1 mL of solution was transferred to a 2 mL Eppendorf and an equivalent volume of $CHCl_3$ was added. The Eppendorf vial was vigorously stirred and the two phases were left to separate for a couple of hours. Once the upper part became clear(/showed no signs of turbidity) the aqueous phase was transferred into a 1 mL HPLC vial.

[****] Corresponding to 66 PS*c*MA molecules/nm^2 for sample A. For 33 PS*c*MA, to 9.5 mL THF 0.5 mL stock solution was added. For 16.5 PS*c*MA, to 9.75 mL THF 0.25 mL stock solution was added.

4. Doxorubicin loading and heat-triggered release from iron oxide nanocubes coated with thermo-responsive polymers

4.1. Introduction

Targeted and triggered drug delivery have become important branches of nanomedicine and pharmacology research focusing on the fabrication of nanoparticle as smart drug delivery systems (DDSs). In particular, for cancer therapy, the administration of high doses of chemotherapy drugs as now required is mainly due (i) to the limited aqueous solubility of the drug molecules; (ii) to the non-specific whole-body drug distribution which generates toxicity not only towards tumor cells but also to healthy cells, alongside (iii) with the potential development of drug resistance.[71,72] As such, there has been significant research activity centered on the design of responsive nano-scale delivery vehicles such as polymer–drug conjugates, liposomes, dendrimers, polymeric micelles and polymer-inorganic nanoparticles hybrid systems. These systems are designed to carry drugs through the circulatory system and release the drug only once they have accumulated at the target site—upon application of a well-defined stimulus.[73] Drug release in this case is triggered by response to internal or external stimuli such as temperature, pH, light, magnetic field, electric field as well as presence of specific targeting biomolecules at the surface of DDSs.[74,75] Upon application of stimulus, changes in polarity, volume, configuration and conformation of the responsive polymer can occur, leading to disaggregation or deformation of the nanostructures hence facilitating the cargo release. Such drug delivery vehicles allow a high local concentration of the drug to be delivered only at the target site leading to highly effective therapy. This offers the advantages of (i)

reduced side effects since the drug is concentrated only at the diseased site and (ii) reduction of drug dosage or administration frequency since high concentrations of drug can be attained at the target site.[72] Among the nano-scaled drug delivery vehicles, hybrid systems incorporating inorganic nanoparticles such as iron oxide nanoparticles (IONPs), gold nanoparticles, quantum dots, and silica with polymers have attracted much attention in recent years as they combine the unique intrinsic features of inorganic nanoparticles with those of responsive polymers affording multi-purpose complex hybrid nanostructures.[76]

Of the aforementioned hybrid systems, much attention has been paid to the preparation of drug delivery vehicles incorporating magnetic nanoparticles (MNPs), typically iron oxide nanoparticles due to their biodegradability and low toxicity.[77] The presence of iron oxide nanoparticles within the nanostructures offers the advantage (i) to image *via* magnetic resonance imaging the drug delivery vehicle, (ii) to target *via* magnetic guidance the nanostructure to the intended site, and (iii) to trigger the drug release through heating generated under application of alternating magnetic field at specific frequencies and fields by magnetic hyperthermia.[78]

For the preparation of magnetic hybrid systems different techniques have been exploited which include: (i) *grafting from* approach which consists of surface initiated polymerization directly at the nanoparticle site,[79–81] (ii) *grafting to* approach that is a post polymerization modification whereby pre-synthesized polymers are attached to the surface of nanoparticles through ligating moieties on the polymers or *via* physical adsorption,[82–86] (iii) *in situ* functionalization whereby nanoparticle synthesis is conducted in the presence

of a polymer resulting in functionalization,[87–89] and (iv) *encapsulation via* self-assembly into micelle type aggregates.[90–95]

In most works cited in literature, the polymerization used for construction of the magnetic hybrid systems is usually achieved *via* conventional free radical polymerization in solution or emulsion. However, conventional free radical polymerization suffers from poor control over molecular weight and molar mass distribution as well as the inability to generate block copolymers. This has led to an increased interest in living radical polymerization (LRP) techniques since their emergence almost two decades ago.[96] Living radical polymerization techniques that have been widely studied include atom transfer radical polymerization (ATRP), nitroxide mediated polymerization (NMP), and reversible addition-fragmentation chain transfer polymerization (RAFT).[97] LRP techniques allow rapid access to well defined functional (*co*)polymers in a variety of different molecular architecture and thus offer good control over the size of hybrid nanostructures when exploited for surface functionalization.[95] The tolerance to a wide variety of functional groups by these techniques enables facile access to a wide range of responsive hybrid systems—smart nanomaterials—at the same time offering the possibility of further functionalization *via* post-polymerization modification at the functional groups on the polymers. For details on LRP polymerization techniques, the reader is referred to several reviews and books.[96–100]

As stated earlier, chemotherapeutic drugs suffer from lack of aqueous solubility, lack of selectivity and possible development of drug resistance. By incorporating these drugs inside polymeric hybrid nanosystems—*e.g.* thermo-responsive systems—both biodistribution and circulation times are improved, alongside an increased concentration of the agent by the enhanced

permeability and retention (EPR) effect. To improve the accumulation of the therapeutic agent, the key appeal of using magnetic nanosystems is the ability to direct and accrue the therapeutic agent in a particular region by magnetic guidance/targeting.[101] Under the influence of an external magnetic field, the superparamagnetic nanoparticles become magnetic and accumulate at the tumor site and once the field is removed they return to a paramagnetic state, making excretion possible.[102]

In this chapter my research will focus on hybrid drug delivery systems integrating iron oxide nanocubes with thermo-responsive polymers for delivery of chemotherapeutic agents through a temperature stimulus. This opens up the perspective of combining hyperthermia treatment with chemotherapy. In this case, the thermo-responsive polymer accommodates the drug and after accumulation at the target site the application of an alternating magnetic field results in heat being generated from the magnetic nanoparticles—'nanoheaters'—which forces the polymer to undergo conformational changes that leads to release of the encapsulated drug.[72] Although the cancer therapy *via* hyperthermia using magnetic nanoparticles alone has been proven to be effective[103], it is however more effective if combined with chemotherapy[104].

Thermo-responsive polymers can undergo reversible changes in conformation and physical properties in response to changes in temperature.[73] Such polymers may exhibit a lower critical solution temperature T_{LC} or an upper critical solution temperature T_{UC}.[105] For polymers that exhibit a lower critical solution temperature, polymer solubility is good in aqueous solution at temperatures below T_{LC} but is observed to decrease above the T_{LC}—transition known as the coil to globule transformation. Thus, when incorporated in

hybrid nanostructures, the response to temperature has the effect of swelling (coil state) and shrinking (globule state) the nanostructure with variations in temperature which can be exploited to trigger release of any entrapped molecules (Figure 1).

Figure 1: Schematic representation of the heat-triggered drug delivery concept

For drug delivery applications, it is desirable to have the transition temperature T_{LC} of the polymer a few degrees above the body temperature as this ensures that drug leakage does not occur during transportation through the circulatory system and at the same time the temperature required for treatment is not too high to cause damage to the patient. It is also important that the polymer employed is biocompatible, water soluble and provides good stability to the hybrid magneto-polymer composite. Most of the thermo-responsive hybrid nanostructures detailed in literature utilize polymers that exhibit T_{LC} behavior with the most widely used polymer being poly(*N-iso*propylacrylamide), T_{LC} of 32 °C. Though the transition temperature of this polymer is below body temperature, the T_{LC} can be easily adjusted by copolymerizing *N-iso*propylacrylamide with hydrophilic monomers to elevate the T_{LC} to above body temperature. Homopolymers such as poly(*N,N*-diethylacrylamide) (PDEAAm), poly(propylene oxide) (PPO), poly(vinyl methyl ether) (PVME), poly[2-(dimethylamino)ethyl methacrylate] (PDMAEMA), and poly(ethylene glycol) (PEG), as well as block copolymers including

poly(ethylene oxide)-poly(propylene oxide)-poly(ethylene oxide) (PEO-PPO-PEO) triblock copolymers have also been employed.[106]

4.2. Thermo-responsive polymers based on poly(*N*-*iso*propylacrylamide)-*co*-poly(ethylene glycol) methyl ether acrylate

Recently, using RAFT polymerization, our group has reported the facile functionalization of strongly interactive iron oxide nanocubes (IONCs) with thermo-responsive (T-responsive) polymers and studied the doxorubicin hydrochloride (doxo) loading and release from this nanosystem under an alternating magnetic field (AMF).[107] We demonstrated, as proof of concept, that the heat-triggered release of doxo from the thermo-responsive polymer functionalized IONCs was possible by applying an AMF under biologically relevant frequency and field conditions, given that—for a safe application of hyperthermia to patients—the product of frequency and magnetic field (H·f) should be smaller than 5 x 10^9 A/m·s.[108] In our case the doxo release was done under the frequency of 105 kHz and the field amplitude of 25 mT (20 kA/m), well below the so-called 'biological limit'.

My contribution to this work was the study of the loading conditions of doxo as a function of initial doxo concentration, incubation time, cleaning method, and loading volume. Initially we used doxo stock solutions prepared weeks or months beforehand. After realizing that doxo is not stable if stored, at 4 °C in the dark, for long periods of time, we started preparing fresh doxo solutions before each loading experiment. The amount of doxo loaded was quantified by UV-Vis spectroscopy, by subtracting from the initial amount the doxo the amount that was left in the supernatant after each cleaning step by magnetic separation. For the preparation of samples for *in vivo* tests

quantification by fluorescence spectroscopy of the doxo released in the supernatant was carried out since fluorescence imaging would have been the imaging modality during the *in vivo* experiments to be used at the animal facility of our partners in Paris. We wondered if doxo quenching effects occurred after loading on the thermo-responsive polymer coated nanocubes. The release studies in water were also compared to the ones done in dimethyl sulfoxide (DMSO). DMSO was indeed a good solvent for the T-responsive polymers which would have helped the extension of the polymer to the coil state, thus releasing in solution the total amount of the drug loaded.

4.2.1. Determining drug loading conditions

The classical loading conditions employed in our lab for doxo loading before I undertook the more in depth study were as follows: iron oxide nanocubes at 50 ppm Fe, 50 ppm initial doxo concentration, solvent—phosphate buffered saline (PBS), incubation time—24 hours, loading volumes of 2 mL for small batches or 20 mL for release studies under AMF, and cleaning of the excess of drug done at the magnet (0.3 T). All these parameters were investigated with the aim of preparing a stable nanocarrier in the shortest time possible, and considering that for a complete *in vivo* study 28 mg of Fe in IONCs was needed overall and out of the total amount 14 mg of T-responsive polymer coated nanocubes had to be loaded with doxo. Per each animal injection 0.7 mg of Fe were needed.

The first parameter investigated was the effect of doxo concentration, that was the amount of doxo that was added to the IONCs solution. In this series of experiments all other conditions were kept constant and only the doxo amount was varied. As can be seen from the results summarized in Table

1, by progressively increasing the amount of starting doxo from 5 µg to 250 µg, the amount of doxo associated per 0.1 mg Fe increases from 0.3 µg to 122 µg, respectively. As the total amount of doxo associated per 0.1 mg Fe increased, the percentage loaded (calculated based on the initial doxo) saw initially a steep increase, from 6 to 40.8% (Figure 2), after which a plateau like behavior was observed with values in the range from 36 to 51% (Table 1, Figure2). Also it is worth mentioning that the number of magnetic cleaning steps needed to completely remove the excess of doxo increases by increasing the amount of initial doxo amount. For instance for 5 µg initial doxo (2.5 ppm doxo) 2 washing steps were enough, for 50 µg doxo (25 ppm doxo) 4 steps were needed, and for 250 µg doxo 7 washing steps were necessary to get rid of the free doxo in solution.

Table 1: Study of the effect of doxo amount added to the IONCs solution for 24 hours incubation on drug loading (%). Solvent: PBS. Cleaning: magnet.

Sample	**Starting m_{DOXO} [µg]**	V_{TOT} [mL]	m_{DOXO} in supernatant [µg]	Loading (%)
1.1. 50 ppm Fe	**5**	2	4.7	6
1.2. 50 ppm Fe	**7.5**	2	6.3	16
1.3. 50 ppm Fe	**10**	2	7.6	24
1.4. 50 ppm Fe	**25**	2	14.8	40.8
1.5. 50 ppm Fe	**50**	2	31.8	36.4
1.6. 50 ppm Fe	**75**	2	46.4	38.1
1.7. 50 ppm Fe	**150**	2	83.8	44.1
1.8. 50 ppm Fe	**250**	2	123	50.8

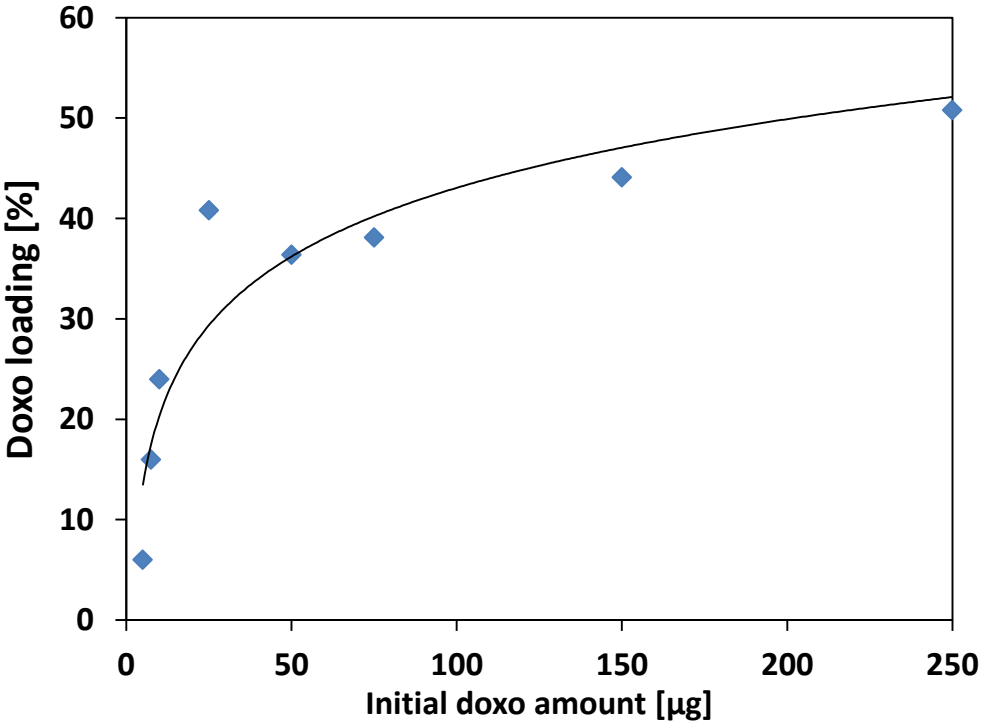

Figure 2: Percentage of doxorubicin loaded inside the T-responsive polymeric shell as a function of the initial amount of drug (before incubation for 24 hours). The overall amount of doxo loaded increased with the increase in starting doxo amount. The loading reached 40% for 25 µg doxo and it seemed to plateau in the range between 35 and 50% loading. The black curve is just an indication for the eye.

Table 2: Study of the effect of drug incubation time on drug loading (%). Volume: 3 mL. Solvent: PBS. Cleaning: magnet.

Sample	Starting m_{DOXO} [µg]	**Time [h]**	m_{DOXO} in supernatant [µg]	Loading (%)
2.1. 50 ppm Fe	50	**6**	36.1	27.8
2.2. 50 ppm Fe	50	**17**	36.3	27.4
2.3. 50 ppm Fe	50	**24**	35.9	28.2

Next, the incubation time that accounts for the time during which the thermo-responsive nanocubes were exposed to doxo, at 25 °C, was studied. Interestingly, the loading was similar for 6, 17 and 24 hours. Already after a couple of hours of incubation the drug was loaded inside the T-responsive polymer corona on the IONCs: 27.8% loading after 6 hours, 27.4% loading after 17 hours, and 28.2% loading after 24 hours of incubation with doxo (Table 2). Longer incubation of the nanocube solution with the chemotherapeutic drug did not yield higher loading. This information was useful for the preparation of big batch loading experiments for *in vivo* studies as the time for the incubation and for the cleaning steps were limiting factors for the production of the big batch.

The third parameter investigated was the cleaning method. Cleaning at the magnet was convenient and fast—within 30 min all the IONCs were accumulated at the magnet (V_{Tot} = 2 mL). But exposure to the magnet was destabilizing the nanocarriers, by possibly inducing a permanent magnetic moment in the iron oxide nanocubes with consequent partial aggregation. The typical 19 nm IONCs used for this study showed very good heating capabilities,[22] but being at the interface between superparamagnetic and ferro(i)magnetic regimes they were difficult to handle and functionalize.[107] Preferably, the exposure to the magnet had to be avoided in order to avoid aggregation due to dipole-dipole interaction. For this reason centrifugation as alternative cleaning strategy to separate unbound doxo from the doxo-loaded nanocubes was also considered. The procedure was as follows: after incubation with the drug for 24 hours, the solution was transferred into Amicon tubes (100 kDa molecular weight cutoff membrane) and centrifuged for 15 min at the speed of 2 000 rotations per minute (rpm). Next the

supernatant was removed and the IONCs left in the Amicon tube were resuspended in fresh buffer. The centrifugation process was repeated three times. Complete removal of the free drug was monitored by UV-Vis spectroscopy as assessed by the disappearance of the absorption peak of doxo at λ_{max} = 485 nm in the solution collected below the Amicon filter. Stability of the doxo-loaded nanocubes was preserved, as assed by dynamic light scattering measurements: the average hydrodynamic diameter d_H by number was 233 ± 6 nm for the centrifuged sample, while the sample prepared in the same conditions and cleaned at the magnet had a hydrodynamic diameter of 301 ± 6 nm (the initial sample had a d_H around 200 nm). Unfortunately, a bigger loss of iron occurred when removing the excess of doxo by centrifugation compared to using magnetic decantation. As measured by ICP, the iron loss was 76%, due to the IONCs that got trapped inside the filter's membrane and could not be resuspended in solution. That was not the case when a magnet was employed and only 6% Fe loss was estimated in the case of magnetic separation. Between the loss of stability and loss of ¾ of the material, a loss of stability and sample aggregation was preferred.

Lastly the volume of the solution during loading was briefly studied. When increasing the total volume from 2 to 3 mL, while keeping the other parameters constant, including Fe concentration (50 ppm), doxo concentration (25 ppm), and loading time (24 hours), a drop in loading capacity was observed. By reducing the solution volume, a higher loading was observed (with a corresponding loading percentage of 36.4% of doxo loaded for 2 mL *vs.* 28.2% of doxo for 3 mL). In another experiment, when further increasing the volume, from 2 mL to 20 mL, the amount of doxo loaded decreased from 23.1% to 17.6%, respectively.

Overall, in order to have a compromise between the stability of the sample, doxo loading efficiency, yield of the doxo loaded nanocube material and a reasonable time for the whole loading and cleaning procedure the following doxo loading conditions were set: 50 ppm Fe, 25 ppm doxo, 3 cleaning steps in 2 or 20 mL solution volumes using PBS as solvent, and incubation done overnight (*ca.* 17 hours). For the magnetic cleaning the small 2 mL batches were kept at the magnet 3 times for 30 minutes, while the big 20 mL batches were kept at the magnet 3 times for 60 minutes, due to a slower magnet accumulation.

4.2.2. Drug loading quantification: UV-Vis spectroscopy

It is known from literature that aqueous doxorubicin solutions photodegrade upon UV excitation.[109] In order to avoid light exposure we kept all our solutions covered in aluminum foil inside a fridge at 4 °C. Nevertheless, a curious fact was noticed during the numerous loading experiments: even if the stock doxorubicin hydrochloride solution (1 mg/mL) was kept in the dark at 4 °C, after a couple of weeks the molar extinction coefficient decreased up to 25% of the value that was obtained the day when the solution was prepared.

The absorption spectra of doxo at concentration of 5, 10, 15, 25, 50, and 100 µg/mL—measured on the day the stock solution was prepared—are plotted in Figure 3a. These solutions were kept as described earlier and measured 3 weeks later. The corresponding spectra are plotted in Figure 3c. One can clearly see that the absorption values recorded were much lower compared to the values determined 3 weeks prior. As for the molar extinction coefficient the value dropped from 10 448 $Lmol^{-1}cm^{-1}$ to 7 999 $Lmol^{-1}cm^{-1}$. For all following experiments fresh stock doxo solutions were prepared before each loading experiment. But the preparations for the *in vivo* tests were

already in full swing by the time we realized that, therefore in Table 3 it will be mentioned if the stock doxo solution used was a fresh or an old one. As we will see, this fact influences the loading capacity and it will be explained later.

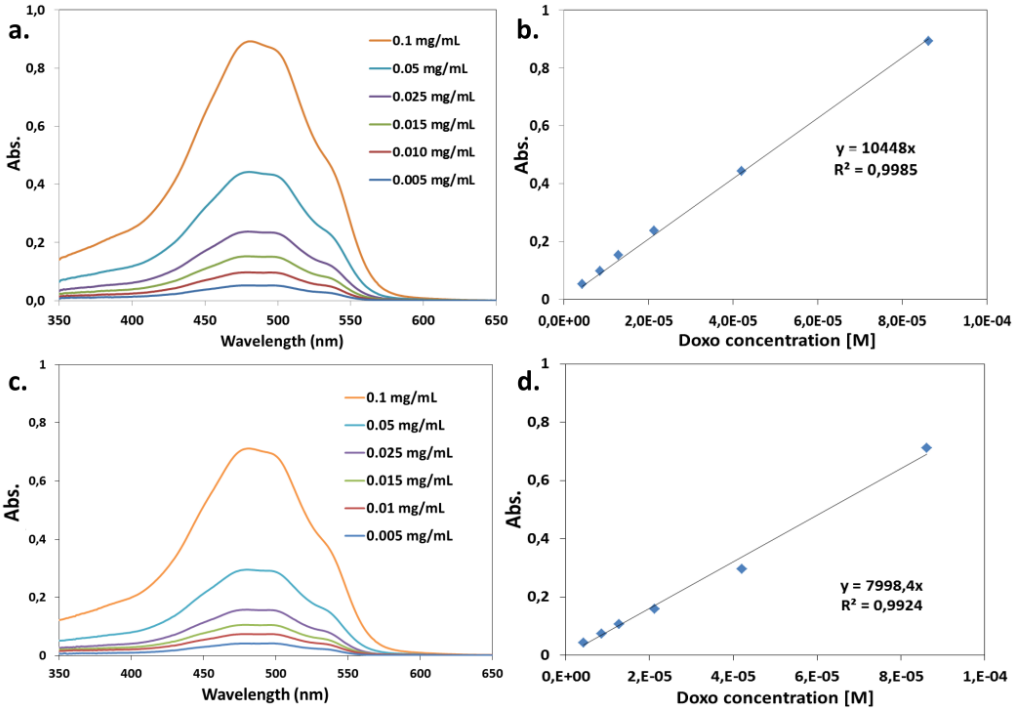

Figure 3: Doxorubicin hydrochloride instability over time. (a,c) Absorption spectra of doxo in phosphate buffered saline at different drug concentrations and (b,d) the corresponding calibration curves. The slope is the molar extinction coefficient—the length of the light path being 1 cm. The same solution was measured (a) on the day it was prepared or (c) three weeks later (while kept in the dark at 4 °C). The extinction coefficient value dropped from (b) 10 448 $Lmol^{-1}cm^{-1}$ to (d) 7 999 $Lmol^{-1}cm^{-1}$.

4.2.3. Sample preparation for *in vivo* studies

The procedure for doxo loading was slightly modified in order to introduce a sterilization step. After addition of the IONCs to PBS, the solution was left under UV light for one hour. All the rest of the loading conditions were kept the same, only with the addition of a 3 minute sonication step at the end of the loading procedure in order to disperse the IONCs.

The aim of the first experiment was to see the difference in loading in small batch *vs*. big batch. Once again a drop in loading was observed, with 47.5% loading for 2 mL batch and 44.9% loading for 20 mL batch (Table 3), consistent with previous results. Next, as we realized the importance of using fresh doxo stock solutions, we compared two solutions: one using an old doxo solution and the other one using a fresh one. The difference in loading percentage was significant: 19.6% loading for the fresh solution and 40.9% for the old solution (Table 3). A possible explanation to the drop of loading efficiency could be related to the aggregation state of doxo when kept longer in solution as already reported[110]. During magnet cleaning the doxo aggregates could also have sedimented at the bottom of the vial although not trapped inside the polymeric corona. For the remaining experiments only fresh doxo solutions were used and the loading efficiency decreased, with maximum 27% loading achieved for the sample that was to be used for *in vivo* experiments. Unfortunately, despite the high loading—94 µg doxorubicin hydrochloride per 0.7 mg Fe—the sample did not heat under alternating magnetic field: the maximum T reached, by 50 µL sample of doxo loaded thermo-responsive IONCs at an Fe concentration of 14 g/L, was 32 °C under frequency and field amplitude of 110 kHz and 25 mT, while the lower critical solution temperature of this batch was 35 °C, given that the body temperature of mice is *ca*. 31 °C.

Table 3: Loading conditions and loading values (%) for various samples prepared with the scope of preparing for the *in vivo* experiments. Incubation: overnight. Cleaning: magnet.

Sample	m_{Fe} [mg]	Starting m_{DOXO} [µg] (doxo solution used)	Volume [mL] (solvent)	Loading determined by UV-Vis [%]
1.1. 50 ppm Fe (small batch)	0.1	25 (old)	2 (milliQ-H_2O)	47.5
1.2. 50 ppm Fe (big batch)	1	250 (old)	20 (milliQ-H_2O)	44.9
2.1. 50 ppm Fe (small batch)	0.1	25 (fresh)	2 (PBS)	19.6
2.2. 50 ppm Fe (small batch)	0.1	25 (old)	2 (PBS)	40.9 (26.9)[††††]
3.1. 25 ppm Fe (small batch)	0.05	50 (fresh)	2 (PBS)	23.1
3.2. 25 ppm Fe (big batch)	0.5	500 (fresh)	20 (PBS)	17.6
4.1. 25 ppm Fe (big batch)	0.5	500 (fresh)	20 (PBS)	14.2
4.2. 50 ppm Fe (big batch)	1	500 (fresh)	20 (PBS)	21
5. The samples for *in vivo* experiments [Paris] (x 10 vials of 20 mL)	1	500 (fresh)	20 (PBS)	27 (9.3)[‡‡‡‡]

[††††] Loading as determined by fluorescence spectroscopy after release in DMSO:PBS (90:10) mixture.
[‡‡‡‡] Loading as determined by fluorescence spectroscopy after release in DMSO:PBS (90:10) mixture.

By performing additional TEM characterization (Figure 4) on this sample, the nanocubes obtained with RAFT living polymerization were highly polydispersed. On the TEM micrographs some individual IONCs and a majority of aggregates were observed, aggregates that hampered the IONCs heating performance both *in vitro* and, of course, *in vivo*. It is important to underline that under given AMF conditions for the 19 nm particles the Brownian relaxation mechanism was not negligible. By aggregating the particles in a controlled[50] or a non-controlled manner a decrease of their heating capacity was observed. However the same individually coated nanocubes stabilized by poly(ethylene glycol), having a gallic acid moiety as anchoring unit, were suitable nanoheaters and were capable to produce "tumor destructuration" *in vivo*.[104] Therefore, the next goal of the polymer chemists in our group was to obtain nanocubes functionalized with thermo-responsive polymers that (i) would be individually coated by the thermo-responsive shell, (ii) that would be stable and (iii) that would not aggregate during the polymerization or the cleaning steps, thus providing comparable specific absorption rate (SAR) values for further *in vivo* studies.

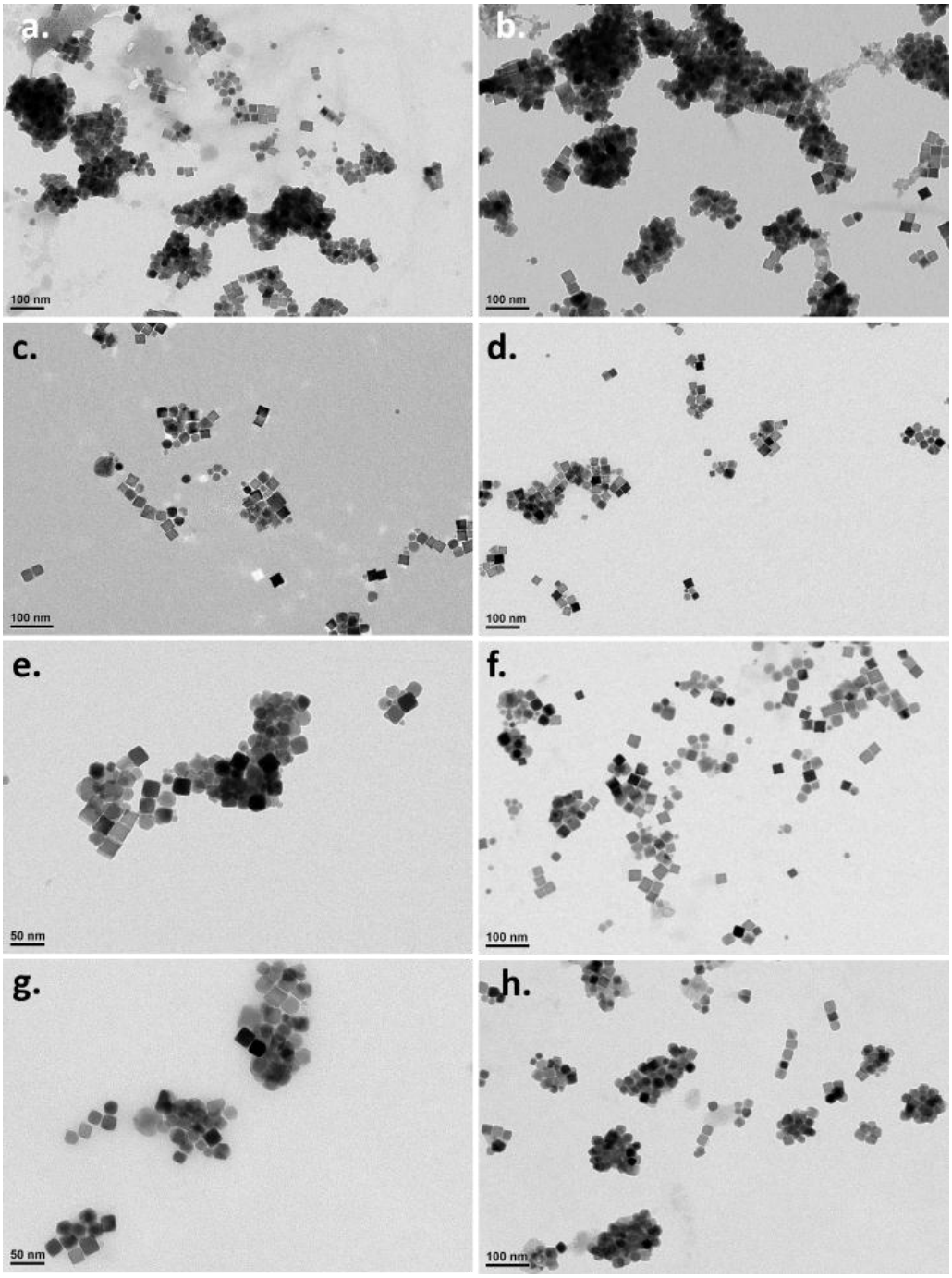

Figure 4: Representative TEM micrographs of samples (a,b) 1, (c,d) 2, (e,f) 3, and (g,h) 4 prepared for *in vivo* studies. (a,c,e,g) IONCs coated with T-responsive polymers in PBS before doxo loading. (b,d,f,h) After doxo loading inside T-responsive polymer

corona of IONCs. The doxo loading procedure did not impact the agglomeration state of the sample. If the starting sample was forming bead like structures before loading (a), the 3D agglomerates were observed after loading as well (b). From batch to batch the stability of the IONCs was varying, with some forming mainly 2D nanoconstructs on the TEM grid (c,d) while others were composed of both individual nanocubes and bead like agglomerates (f,h).

4.3. Thermo-responsive polymers based on poly(diethylene glycol methyl ether methacrylate-*co*-oligo ethylene glycol methyl ether methacrylate)

With the aim of obtaining individually coated thermo-responsive nanoparticles for *in vivo* application, in the last three years another PhD student from our group has set up a new polymerization procedure that has guaranteed such an achievement (patent pending). Also the monomer composition of the thermo-responsive polymers was changed. Instead of using poly(*N*-*iso*propylacrylamide)-*co*-poly(ethylene glycol) methyl ether acrylate (PNIPAM-*co*-PEGA), poly(diethylene glycol methyl ether methacrylate-*co*-oligo ethylene glycol methyl ether methacrylate) (P(DEGMEMA-*co*-OEGMEMA)) was used due to its sustained biocompatibility. In addition, the LCST of this PEG-based polymer could be easily tuned to reach a desirable value by varying the monomer compositions, as described previously for PNIPAM.

4.3.1. Drug loading with previously determined loading conditions

Doxo loading experiments were carried out on the newly synthesized T-responsive polymers, P(DEGMEMA-*co*-OEGMEMA) IONCs. Initially, similar loading conditions were employed for drug loading, as the goal was still the same: having a stable nanocarriers for *in vivo* studies. The experimental conditions for sample SIM404 are summarized in Table 4. To small batches of 2

mL with Fe concentration of 50 ppm, 50 and 100 µg doxo were added for incubation overnight.

For sample SIM404 the average hydrodynamic size was not checked before drug loading, but it was done for all the subsequent experiments. After doxo loading, the sample to which 50 µg doxo was added had a number weighted d_H of 57 ± 1 nm, the d_H of the sample with the double amount of doxo added was 63 ± 5 nm (Table 5). This new polymerization method (patent pending) provided samples that were extremely stable and that would take hours or even days to accumulate at the 0.3 T magnet, while with the old RAFT polymerization the sample were attracted to the magnet within minutes—usually one cleaning step lasted only 30 min. Therefore the magnetic accumulation step for the new batches lasted 24 to 48 hours per each cleaning, depending on the sample. The whole cleaning process lasted 5 to 7 days. After 5 days exposure to the magnet, although the average hydrodynamic diameters increased to above 150 nm and the PDI indicated a slightly larger polydispersity (PDI increased from 0.34 to 0.5, Table 5) no aggregation was observed on the TEM micrographs (Figure 5). The IONCs formed chain like structures due to dipole-dipole interaction, but no 3D aggregation was present, like it was the case with PNIPAM-*co*-PEGA coated IONCs (Figure 4a,b,e,h).

Table 4: Doxo loading conditions for sample SIM404

Sample	m_{Fe} [mg]	m_{DOXO} [mg]	V_{TOT} [mL]
1. control	0	0.05	2
2. control	0	0.1	2
3. 50 ppm Fe 25 ppm doxo	0.1	0.05	2
4. 50 ppm Fe 50 ppm doxo	0.1	0.1	2

Table 5: DLS data for sample SIM 404

Sample	Z-average [nm]	PDI	Number mean [nm]
3. after doxo loading before magnet	122 ± 5	0.35 ± 0.01	57 ± 1
3. after doxo loading after cleaning@magnet	213 ± 7	0.34 ± 0.04	148 ± 14
4. after doxo loading before magnet	493 ± 84	0.7 ± 0.1	63 ± 5
4. after doxo loading after cleaning@magnet	421 ± 34	0.50 ± 0.07	206 ± 42

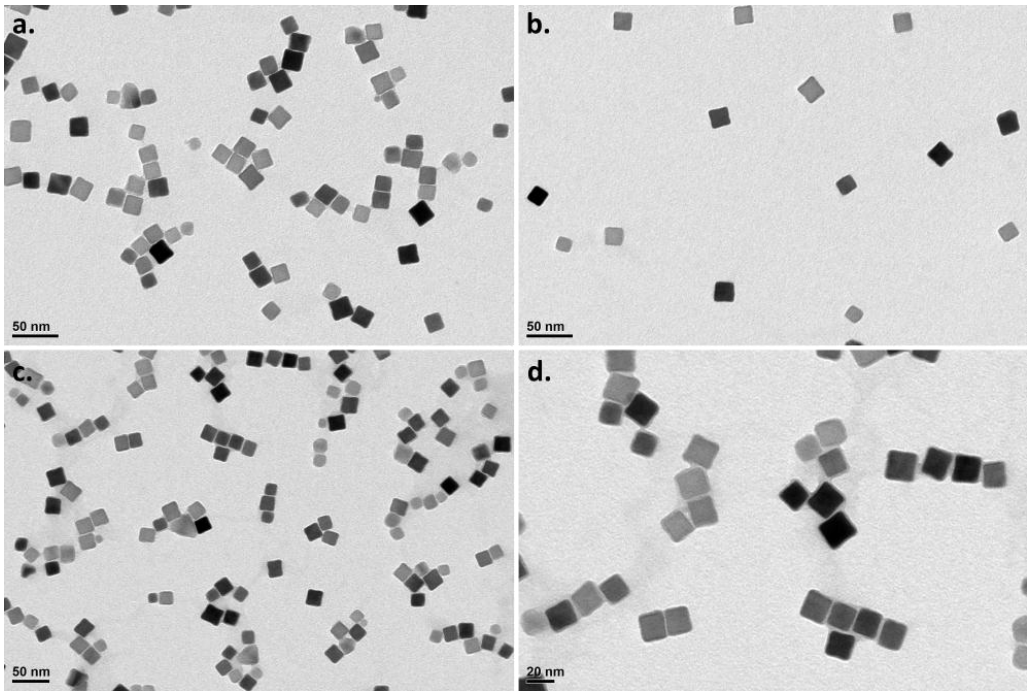

Figure 5: Doxo loaded IONCs@P(DEGMEMA-*co*-OEGMEMA). TEM micrographs of doxo loaded IONCs for initial conditions of (a,b) 50 ppm Fe, 25 ppm doxo and (c,d) 50 ppm Fe, 50 ppm doxo. The samples were stable after 5 days exposure to the magnet as no 3D aggregates were observed. Due to dipole-dipole interaction the IONCs formed chain like structures (a,c,d), but also individual IONCs could be observed on the TEM grid (b).

The loading was calculated by carrying out UV-Vis spectroscopy measurements and by subtracting the amount of doxo left in the supernatant after the loading from the initial doxo amount. The loading capacity of the 50 ppm Fe, 25 ppm doxo sample was 64% (32 µg doxo per 0.1 mg Fe) and for the 50 ppm Fe, 50 ppm doxo sample 69% of the initial drug was loaded inside the polymeric corona (69 µg doxo per 0.1 mg Fe). These first tests were performed with a doxorubicin hydrochloride solution which was an old batch, and therefore these loading efficiencies might be overestimated. In the following experiments, fresh doxo solutions were prepared before each loading.

Next, we found out how SAR values changed (i) for the different batches of IONCs (influence of the starting magnetic material), (ii) the same starting material but different batches of polymerization (influence of the polymeric shell), and (iii) as a function of Fe concentration and thus number of nanocubes in solution.

We first measured the SAR values of different iron oxide nanocubes of similar core size to verify the batch to batch reproducibility (16.6 ± 2.5 nm cube-edge length for sample SIM404 and 17.7 ± 2.4 nm for sample SIM406). As we can see from Table 6, the SAR value of sample SIM404 was 167 ± 3 W/g_{Fe}, 18% lower compared to sample SIM406-0. The factors that influenced SAR where the size of the sample and the sample polydispersity. A monodispersed sample with a cube edge length of 19 nm was the ideal candidate, but not always achieved. A SAR value of *ca*. 170 W/g_{Fe} was still a good value, as previously under magnetic field amplitude of 25 mT and frequency of 105 kHz the SAR value of IONCs@PNIPAM-*co*-PEGA was *ca*. 40 W/g_{Fe}.

Afterwards, the influence of the polymeric corona was checked. From the same starting batch SIM406, 5 polymerizations were carried out in

parrallel. The SAR values ranged from 181 ± 1 W/g_{Fe} to 236 ± 6 W/g_{Fe} (Table 6). The factors influencing the batch to batch reproducibility were mainly the polymer thickness and the amount of free polymer in solution after polymerization (that depended on sample cleaning done by ultracentrifugation).

Lastly, the influence of the iron concentration was studied. The most concentrated sample, SIM406-4, whose Fe concentration was 8.1 g/L was diluted to 3.7 g/L and later to 2 g/L and SAR values were measured for these 3 different concentrations. For the lowest Fe concentration the SAR value was 181 ± 2 W/g_{Fe}, then it increased to 200 ± 2 W/g_{Fe} for the middle Fe concentration and dropped once again to 181 ± 2 W/g_{Fe} for 8.1 g/L Fe. Reports in literature are very controversial: some groups report a decrease of SAR with Fe concentration, other observe an increase in SAR, while others observe yet another trend: an increase in SAR followed by a decrease[52], with the optimal Fe concentration range being between 1.5 and 3 g/L. Even if we observed a 10% variation in SAR values as a function of Fe concentration, *in vivo* the Fe concentration would be 14 g/L so we considered the value for higher Fe concentrations.

Table 6: Specific absorption rate values for different samples of IONCs@P(DEGMEMA-co-OEGMEMA) measured under magnetic field amplitude of 25 mT and frequency of 105 kHz
(DM1 NanoScale Biomagnetics device)

Sample	Volume [mL]	Fe concentration [g/L]	SAR [W/g_{Fe}]
SIM404	1	2.9	167 ± 3
SIM406-0	1	2.0	205 ± 3
SIM406-1	1	2.8	236 ± 6
SIM406-2	1	3.0	-[§§§§]
SIM406-3	1.1	2.9	194 ± 4
SIM406-4	0.5	8.1	181 ± 1
SIM406-4	0.5	3.7	200 ± 2
SIM406-4	0.5	2.0	181 ± 2

As sample SIM406-4 was the most concentrated one it was used to carry out doxo loading experiments. The loading conditions were: 50 ppm Fe, 25 ppm doxo (initial m_{doxo} = 50 µg), V_{Total} = 2 mL. The stability of the sample, assessed by DLS and TEM, was monitored during the loading process. The average hydrodynamic size by number was 65 ± 2 nm (PDI 0.16) before doxo loading and it increased to 83 ± 5 nm (PDI 0.19) after incubation with the drug overnight and up to 271 ± 20 nm (PDI 0.4) after 5 days of cleaning at the magnet (Table 7). The DLS results were once again in contradiction with what was observed by TEM (Figure 7): sample presented no aggregation and both chain like structures were observed at the end of the loading process (Figure 7c) and individual IONCs (Figure 7d). The chain-like structure might account for the larger DLS sizes measured.

[§§§§]Sample precipitated during hyperthermia experiments. SAR value could not be determined.

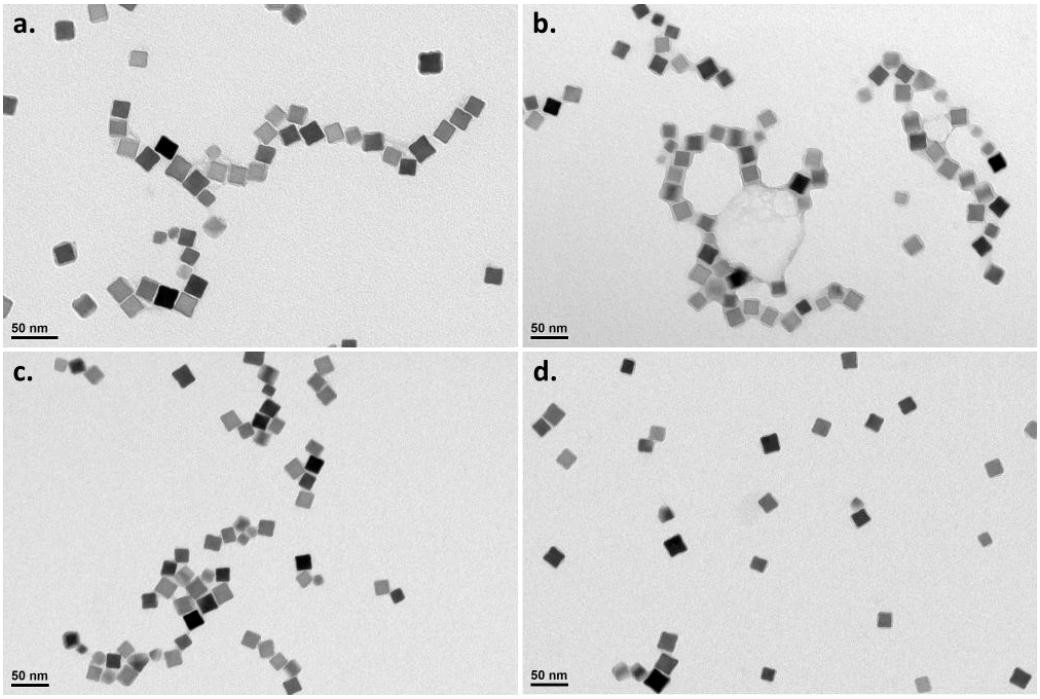

Figure 6: Representative TEM micrographs of IONCs coated with T-responsive polymers (a) before doxo loading, (b) after doxo loading overnight before magnet exposure, and (c,d) after doxo loading and after cleaning at the magnet for 5 days. One could observe that no aggregation of the sample took place. After doxo loading and before magnet exposure, the polymer shell was ticker, which could be an indication of the drug loaded inside the corona. After cleaning the sample by exposing it to a 0.3 T magnet the sample formed chain like structures due to dipole-dipole interactions (c) as seen for non-loaded sample as well (a), but also individual IONCs could be observed on the TEM grid (d), that contradicted the high hydrodynamic diameters d_H determined by DLS.

Table 7: DLS data for sample SIM406-4

Sample	Z-average [nm]	PDI	Number mean [nm]	Intensity mean [nm]	Volume mean [nm]
before doxo loading	106 ± 1	0.16 ± 0.01	65 ± 2	126 ± 2	100 ± 1
after doxo loading before magnet	144 ± 3	0.19 ± 0.02	83 ± 5	173 ± 9	173 ± 16
after doxo loading after cleaning @magnet	313 ± 14	0.4 ± 0.1	271 ± 20	518 ± 137	547 ± 174

The loading achieved with a fresh sample of doxo was 43% (21.5 µg doxo per 0.1 mg Fe), lower compared to loading with the old doxo sample—32 µg doxo per 0.1 mg Fe, consistent with previous results. Once we knew that we could load doxo inside the new thermo-responsive polymer, P(DEGMEMA-*co*-OEGMEMA), the next goal was to investigate the release under AMF.

For the samples prepared with RAFT polymerization, only a few *in vitro* release tests under AMF were carried out. The release experiment under AMF described in the work by Kakwere *et al.*[107] was done on 800 µL of sample at an Fe concentration of 3.8 g/L. We observed a release of 22% of the loaded doxo after 240 minutes of hyperthermia under alternating magnetic field amplitude of 25 mT and frequency of 220 kHz. It should be underlined that in these conditions, the maximal temperature reached was 87 °C, a temperature 35 °C above the LCST of the polymer (52 °C for that batch of T-responsive polymers). But release from smaller volumes, *e.g*. 50 µL, was not studied. Also, the heating performance of big volumes (150 µL) *vs.* small volumes (50 µL) of T-responsive polymer coated IONCs had to be assessed in both hyperthermia devices that we had: (i) NanoScale Biomagnetics that allowed a more precise

SAR value calculation as the heat losses due to heat exchange with the environment were minimized (on which all of the SAR measurements so far were carried out) and (ii) Nanotherics device in which heat losses were more significant and the magnetic field amplitude was homogeneous only in the middle of the coil, thus the position of the sample vial influenced the SAR value measured. But this was the instrument being used for *in vivo* experiments.

4.3.2. Studies to prepare for *in vivo* experiments

4.3.2.1. Volume influence on specific absorption rate value and hyperthermia

Firstly, we looked into the influence of volume on both SAR values and the maximum temperature reached during 30 minute hyperthermia experiments. The SAR value was measured before hyperthermia experiments. For 150 µL sample volume at 2.5 g/L Fe concentration, SAR was 220 ± 5 W/g_{Fe} (B = 25 mT, f = 105 kHz). The SAR value for 50 µL sample at the same Fe concentration and under same frequency and field amplitude condition was 266 ± 5 W/g_{Fe}.

Next, the temperature profile as a function of time was recorded for both samples at Fe concentration of 2.5 g/L. We opted for a lower Fe concentration as we were aiming for temperatures a few degrees above the LCST of the polymer that was usually *ca.* 40 °C. The three hyperthermia experiments were run with 30 minute break in between and no sample sonication during the rest time. We were trying to mimic the *in vivo* conditions and see the effect of sample aggregation on heating performance.

The temperature profile for the sample with a 150 µL volume is plotted in Figure 7. One could observe a slow temperature increase for the first hyperthermia treatment, while in the consecutive runs the increase was

steeper. This was due to sample aggregation during heating and thus to a higher local Fe concentration at the bottom of the vial where the temperature probe was placed. Despite aggregation, the maximum temperature reached during the second run was 55 °C, the same as for the first run. This led us to believe that even if sample aggregated after reaching its LCST, the particles still heated despite aggregation.

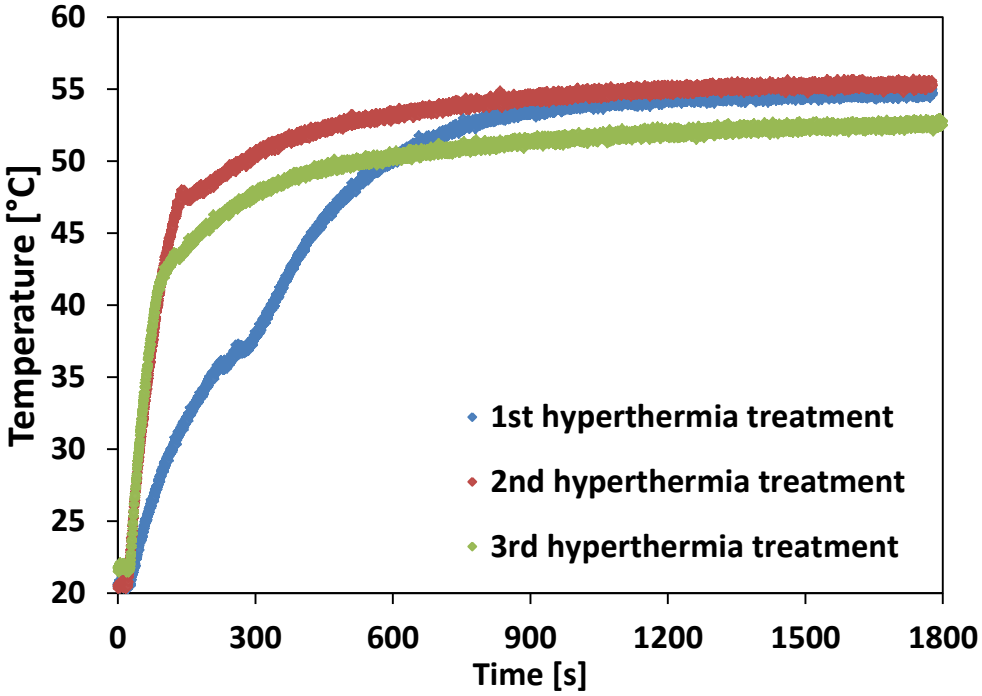

Figure 7: Three consecutive 30 minute long hyperthermia treatments under frequency and field conditions of 105 kHz and 25 mT (*NanoScale Biomagnetics instrument*) for a volume of 150 µL IONCs—at an Fe concentration of 2.5 g/L—coated with T-responsive polymers: blue line—first hyperthermia experiment, red line—second hyperthermia experiment, and green line—third hyperthermia experiment. The maximum temperature reached during 30 minute exposure to AMF was 55 °C. Once the temperature reached the LCST in the first run, the sample precipitated, thus the

heating curve for 2nd and 3rd run was steeper as locally (at the bottom of the vial) the concentration of the IONCs was much higher.

For the sample with a 50 µL volume (Figure 8), the maximum temperature reached was only 43.5 °C, but still above the LCST of the polymer. This sample aggregated as well after the 1st run, but similar to the previous sample aggregation did not have a significant impact on heating performance.

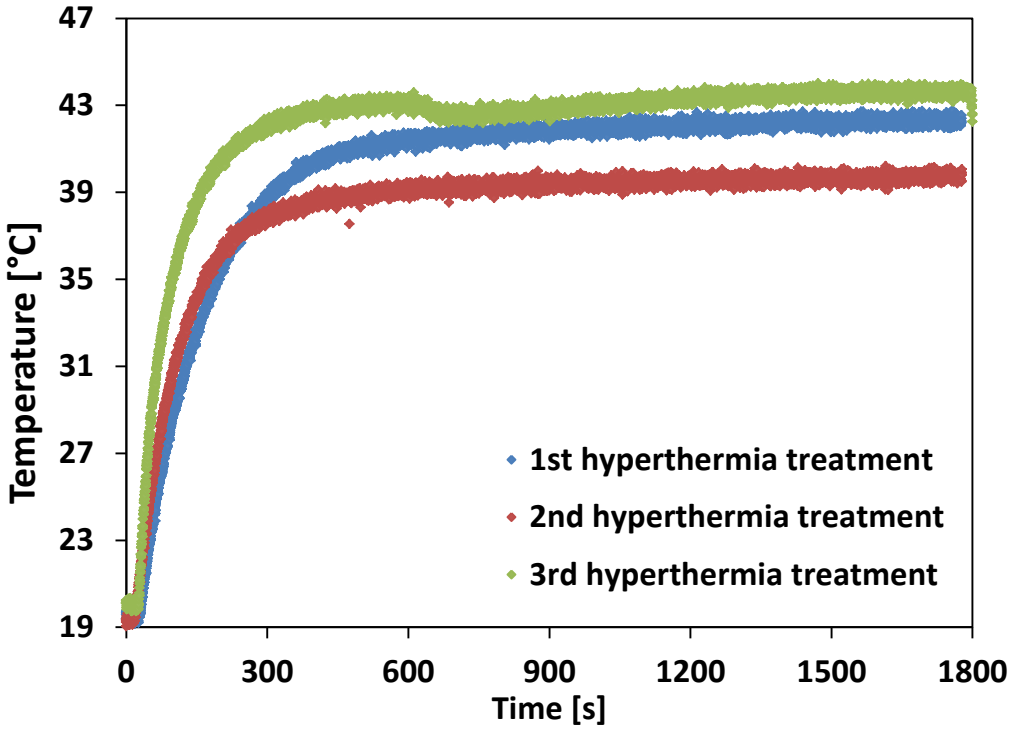

Figure 8: Three consecutive 30 minute long hyperthermia treatments under frequency and field conditions of 105 kHz and 25 mT (*NanoScale Biomagnetics instrument*) for a volume of 50 µL IONCs—at an Fe concentration of 2.5 g/L—coated with T-responsive polymers: blue line—first hyperthermia experiment, red line—second hyperthermia experiment, and green line—third hyperthermia experiment. The maximum temperature reached during 30 minute exposure to AMF was 43.5 °C, 11.5 °C lower compared to the 150 µL sample, for the same Fe concentration. Even if the maximum

temperature was lower than before it was still situated in the range from 40 to 45 °C, that corresponded to mild hyperthermia treatments. Similar to previous sample, the sample aggregated after the first run.

4.3.2.2. Doxorubicin loading and release under AMF study

Following the study of the volume influence on SAR and maximum temperature reached carried out with the NanoScale Biomagnetics hyperthermia device, the next goal was to compare the two hyperthermia instruments in terms of SAR and maximum temperature reached for samples of 50 µL: with and without loaded drug. A new doxo loading experiment was carried out on 2 mL and 20 mL of sample. The experimental conditions are summarized in Table 8.

The average hydrodynamic diameter by number was 52 ± 20 nm (PDI 0.19) before doxo loading. It increased to 86 ± 6 nm (PDI 0.19) and 78 ± 8 nm (PDI 0.2) after incubation with the drug overnight for 2 mL and 20 mL samples, and further to 93 ± 52 nm (PDI 0.7) and to 88 ± 23 nm (PDI 0.65) after 7 days of cleaning at the magnet for 2 mL and 20 mL samples, respectively (Table 9). The TEM images revealed only chain like arrangements (3D aggregates could be excluded) on the TEM grids for all the samples: before loading, after loading and after cleaning at the magnet for one week (Figure 9).

Table 8: Doxo loading conditions for sample SIM408

Sample	m_{Fe} [mg]	m_{DOXO} [mg]	V_{TOT} [mL]
1. 50 ppm Fe 25 ppm doxo	0.1	0.05	2
2. control	0	0.05	2
3. 50 ppm Fe 25 ppm doxo	1	0.5	20
4. control	0	0.5	20

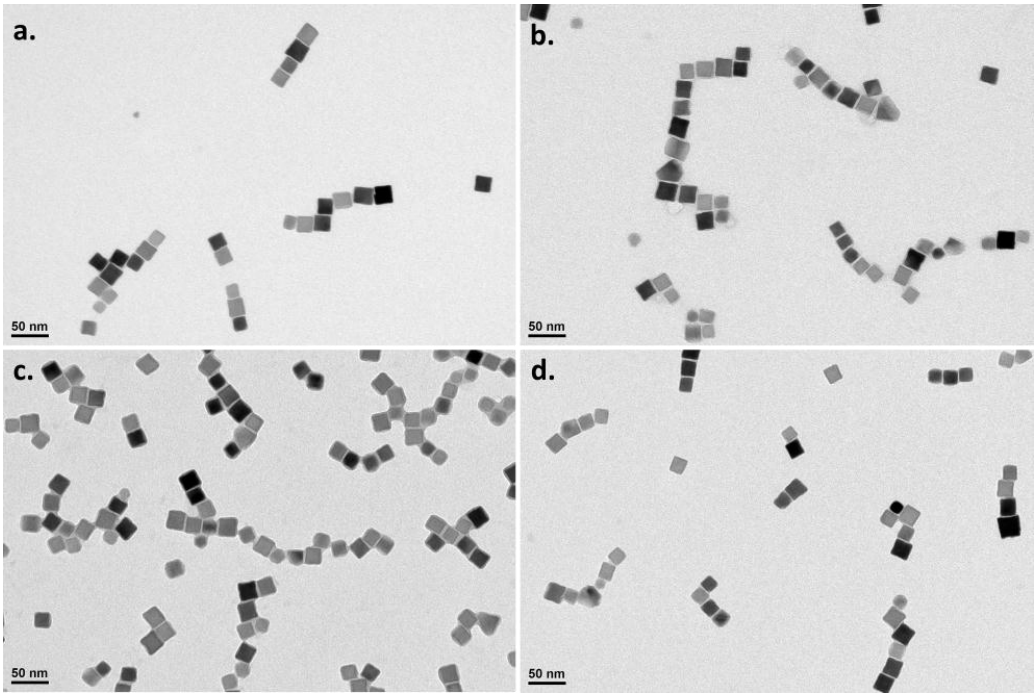

Figure 9: Representative TEM micrographs of IONCs coated with T-responsive polymers (a) before doxo loading, (b) after doxo loading overnight before magnet exposure, and (c,d) after doxo loading and after cleaning at the magnet for 7 days: (c) V_{Tot} = 2 mL and (d) V_{Tot} = 20 mL. The IONCs were well dispersed in solution, no aggregation occured. Due to dipole-dipole interactions the IONCs formed chain like structures on all four TEM grids.

Table 9: DLS data for sample SIM408

Sample	Z-average [nm]	PDI	Number mean [nm]	Intensity mean [nm]	Volume mean [nm]
SIM408 before doxo loading	118 ± 1	0.19 ± 0.01	52 ± 20	145 ± 3	106 ± 9
1. after doxo loading before magnet	148 ± 2	0.19 ± 0.02	86 ± 6	179 ± 6	165 ± 8
1. after doxo loading after cleaning@magnet	469 ± 18	0.70 ± 0.16	93 ± 52	950 ± 5	2168 ± 14
3. after doxo loading before magnet	149 ± 2	0.20 ± 0.02	78 ± 8	204 ± 26	173 ± 5
3. after doxo loading after cleaning@magnet	490 ± 20	0.65 ± 0.08	88 ± 23	1090 ± 4	2899 ± 83

The loading efficiency measured by UV-Vis spectroscopy was 34% for the small batch of 2 mL (17 µg doxo per 0.1 mg Fe) and 23% for the 20 mL batch (115 µg doxo per 1 mg Fe), consistent with previous results when a decrease in loading efficiency was observed by increasing the volume.

Before running the 30 minute long hyperthermia treatments on doxo loaded samples, the SAR of this batch was measured on a non-loaded sample. For the 50 µL sample at 3.95 g/L Fe concentration measured with the NanoScale Biomagnetic instrument, SAR was 223 ± 1 W/g_{Fe} (B = 25 mT, f = 105 kHz). The SAR value of the same 50 µL sample at the same Fe concentration, measured with the NanoTherics device was 149 ± 8 W/g_{Fe} (B = 25 mT, f = 110 kHz), as expected, lower compared to the one measured with the NanoScale Biomagnetics device. As earlier explained the NanoTherics device has more heat losses given that the sample holder is less isolated than the NanoScale device.

Next, the temperature profile as a function of time was recorded for the non-loaded nanocube solution at Fe concentration of 3.95 g/L in the

NanoTherics device (Figure 10). Similar to the 150 µL sample measured with the NanoScale Biomagnetics device (Figure 7), a slow temperature increase for the first hyperthermia treatment could be observed, while the increase was steeper in consecutive runs (at least 15 minutes needed to reach the plateau temperature in the first run *vs*. *ca*. 5 minutes for the 2nd and 3rd treatment, Figure 10). The maximum temperature reached in the first run was 48 °C, after which the sample aggregated. After aggregation the sample reached lower maximum temperatures of 45 and 46 °C, but these temperatures were still suitable for mild hyperthermia treatments.

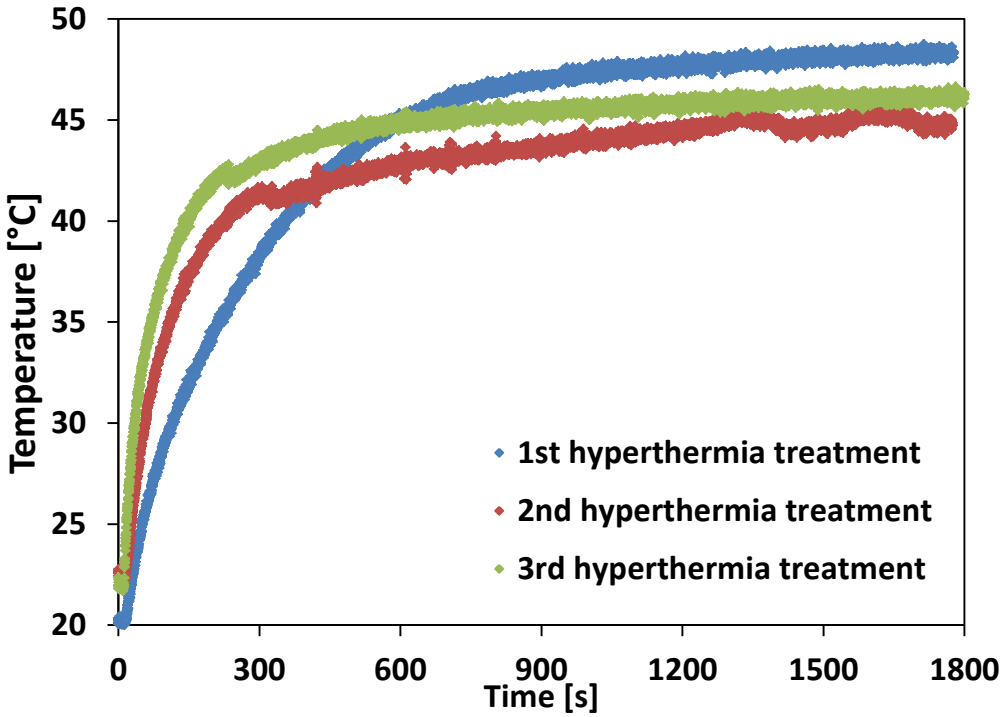

Figure 10: Three consecutive 30 minute long hyperthermia treatments under frequency and field conditions of 110 kHz and 25 mT (*NanoTherics instrument*) for a volume of 50 µL IONCs—at an Fe concentration of 3.95 g/L—coated with T-responsive polymers: blue line—first hyperthermia experiment, red line—second hyperthermia experiment, and green line—third hyperthermia experiment. The maximum

temperature reached during 30 minute exposure was 48 °C. Sample aggregated after 1st hyperthermia run, and though temperature difference ΔT decreased from 28 °C (for the 1st run) to 22 °C (for the 2nd run), the maximum temperature reached was above 44 °C, thus suitable for hyperthermia experiments.

After checking the temperature profile for 50 µL of non-loaded nanocube solution in both devices, the next step was to check the same temperature profile on drug loaded nanocube solution (in both devices). The sample SIM408 that was loaded previously, with 23% drug loading efficiency, was used for these experiments. In Figure 11 and Figure 12 the temperature profiles of the doxo loaded T-responsive IONCs solutions are plotted, with the first one corresponding to a 50 µL solution (Fe concentration of 3.2 g/L) measured in the NanoScale Biomagnetics device and the second one to a 50 µL solution (Fe concentration of 3.5 g/L) measured in the Nanotherics device. A slightly higher Fe concentration was used for the Nanotherics device in order to compensate for heat losses. However, we underestimated the Fe concentration needed to reach the LCST of the polymer, and unfortunately the maximum temperature reached was only 39.5 °C, thus the LCST temperature was not overcome for the sample analyzed with the NanoTherics device (Figure 12).

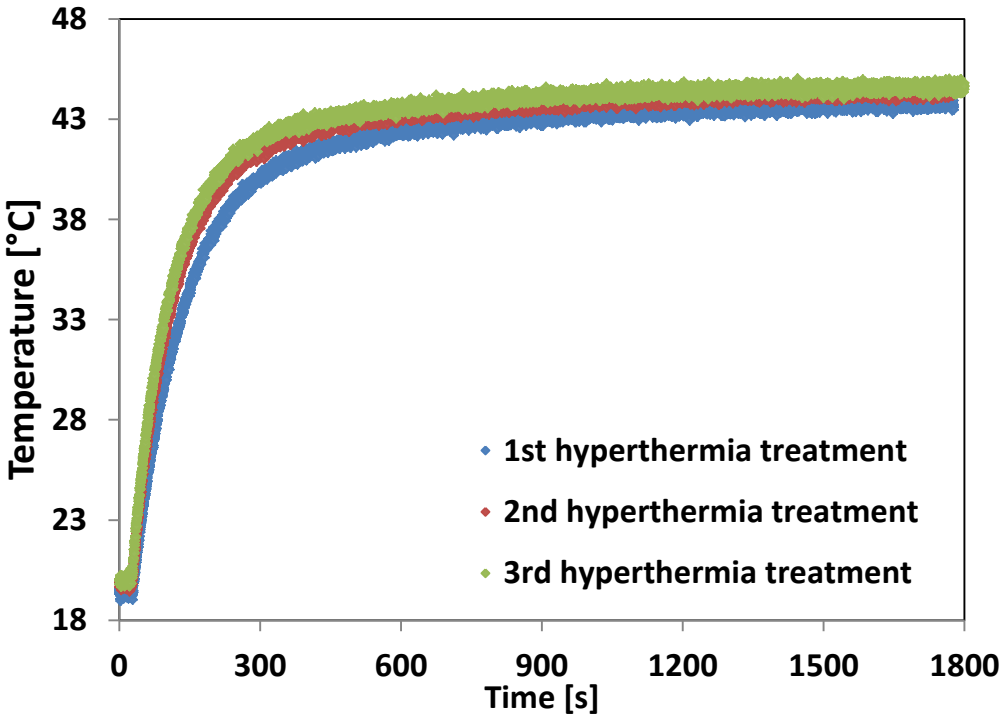

Figure 11: Three consecutive 30 minute long hyperthermia treatments under frequency and field conditions of 105 kHz and 25 mT (*NanoScale Biomagnetics instrument*) for a volume of 50 µL IONCs—at an Fe concentration of 3.2 g/L—coated with T-responsive polymers and loaded with doxorubicin hydrochloride: blue line—first treatment, red line—second treatment, and green line—third hyperthermia treatment.

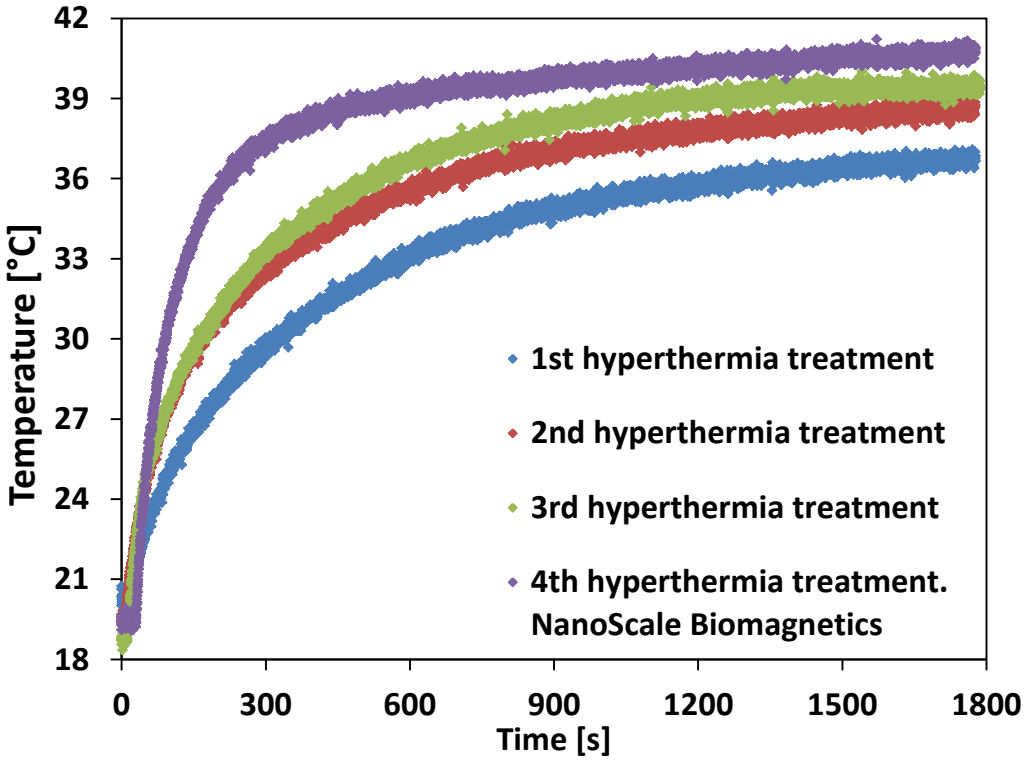

Figure 12: Three consecutive 30 minute long hyperthermia treatments under frequency and field conditions of 110 kHz and 25 mT (*NanoTherics instrument*) and a fourth treatment under frequency and field conditions of 105 kHz and 25 mT (*NanoScale Biomagnetics device*) for a volume of 50 µL IONCs—at an Fe concentration of 3.5 g/L—coated with T-responsive polymers and loaded with doxorubicin hydrochloride: blue line—first hyperthermia experiment, red line—second hyperthermia experiment, green line—third hyperthermia experiment, and violet line—fourth hyperthermia experiment. The maximum temperature reached during 30 minute exposure to AMF with the NanoTherics instrument was 39.5 °C, the maximum temperature increasing to 41 °C during the 4th run carried out with NanoScale Biomagnetics device.

The same sample, after 3 hyperthermia treatments in the NanoTherics device, was exposed to an alternating magnetic field inside the NanoScale Biomagnetics device in order to see if the maximum temperature reached (39.5 °C) was due to the doxo loaded inside the polymer that decreased the heating performance of the sample (as the same non-loaded sample reached 48 °C at a slightly higher Fe concentration of 3.95 g/L) or if it was due to the device. In the 4th run, the maximum temperature increased to 40.8 °C (Figure 12), thus not significantly higher than the value reached on the NanoTherics device.

Also, if we compare the maximum temperature of 44.5 °C reached with the NanoScale device (50 µL at Fe concentration of 3.2 g/L) for the doxo loaded sample to a similar[*****] non-loaded sample at a lower Fe concentration (50 µL at Fe concentration of 2.5 g/L), but that reached a T_{max} of 42.5 °C (Figure 8), the data suggests that the drug loaded nanocubes had lower heating performance.

Lastly, given that we needed more material for one final study, yet another sample was prepared for doxo release studies under AMF: SIM407. The loading conditions were: 50 ppm Fe, 50 ppm doxo, V_{Total} = 20 mL. The DLS data is summarized in Table 10 and the TEM images of the samples after doxo loading can be seen in Figure 13.

[*****] Batch to batch variability must be taken into consideration. I am comparing batch SIM408 and batch SIM406, with same cube edge length of a = 17.7 ± 2.4 nm.

Table 10: DLS data for sample SIM407

Sample	Z-average [nm]	PDI	Number mean [nm]	Intensity mean [nm]	Volume mean [nm]
before doxo loading	114 ± 2	0.19 ± 0.02	72 ± 10	140 ± 3	98 ± 8
after doxo loading before magnet	126 ± 1	0.21 ± 0.01	83 ± 5	151 ± 3	129 ± 1
after doxo loading after cleaning @magnet	129 ± 1	0.16 ± 0.01	98 ± 1	152 ± 2	138 ± 2

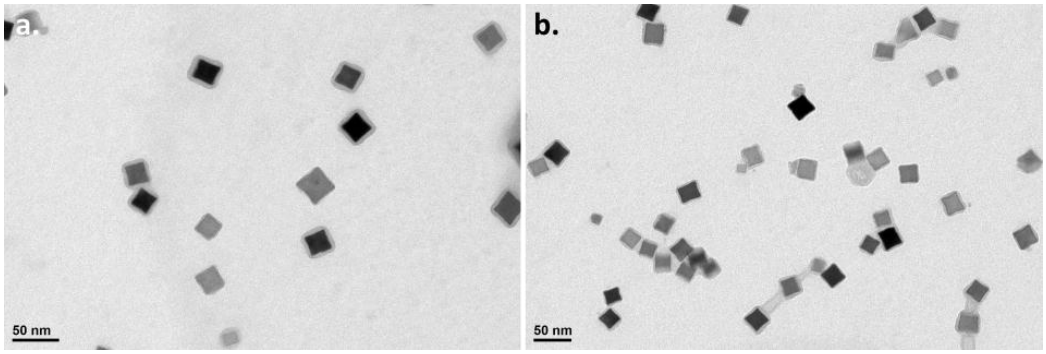

Figure 13: Representative TEM micrographs of IONCs coated with T-responsive polymers after doxo loading overnight and before magnet exposure. The IONCs are well dispersed in solution, no aggregation occured. The chain like structures were no longer observed and this correlated to Z-average of 126 ± 1 nm with a low PDI of 0.21. The light grey polymer shell could be well observed on the TEM micrographs (a).

Interestingly, despite having a cube edge length of 18.7 ± 3.3 nm, this sample did not form chain like structure on the TEM grid (Figure 13), alongside having PDI values ≤ 0.21: before doxo loading (0.19 ± 0.02), after doxo loading and before magnet cleaning (0.21 ± 0.01) and after one week magnetic cleaning (0.16 ± 0.01) (Table 10). In the previous loading experiments the PDI values after magnet exposure were usually ≥ 0.4: 0.4 ± 0.1 for sample SIM406-4 (Table 7), 0.70 ± 0.16 for sample SIM408 small batch, and 0.65 ± 0.08 nm for

sample SIM408 big batch (Table 9). Correspondingly, the Z-average increased from 114 ± 2 nm before doxo loading to 129 ± 1 nm at the end of the drug loading and cleaning procedure. The increase could be attributed to the drug incorporation. By UV-Vis spectroscopy the loading efficiency was determined to be 43% (430 µg doxo per 1 mg Fe).

The drug loaded sample SIM407 was used for release experiments under alternating magnetic fields. The Fe concentration chosen was 4 g/L in order to reach temperatures above the LCST of the polymer (41 °C). The volume was kept at 50 µL to mimic *in vivo* experiments conditions, but NanoScale Biomagnetics was the device used for this experiment in order to minimize heat losses. This was only a trial run to determine the total amount of doxo released after 3 cycles of hyperthermia treatment.

The temperature profiles of the three hyperthermia cycles on doxo loaded 50 µL nanocube solution at an Fe concentration of 4 g/L are plotted in Figure 14. The maximum temperature reached in the first run was 48.9 °C, followed by two cycles reaching 49.1 °C. These high temperatures were above the LCST of the polymer, therefore they should have insured a heat triggered release of the drug. Indeed, the absorption spectrum of the supernatant after 90 minutes exposure to AMF and magnetic separation of the IONCs overnight (diluted twice due to small volumes and a minimum of 50 µL needed for UV-Vis spectroscopy measurements), the characteristic peak of doxo at 485 nm could be observed (Figure 15). Unfortunately, the exact amount could not be quantified due to interference of the Fe absorption band. Also, pinkish color (characteristic doxorubicin solution color) was observed on the walls of the plastic vial, suggesting that doxo tended to stick to polymeric materials and

was not well solubilized in solution, as reported in literature and observed by us on numerous occasions.

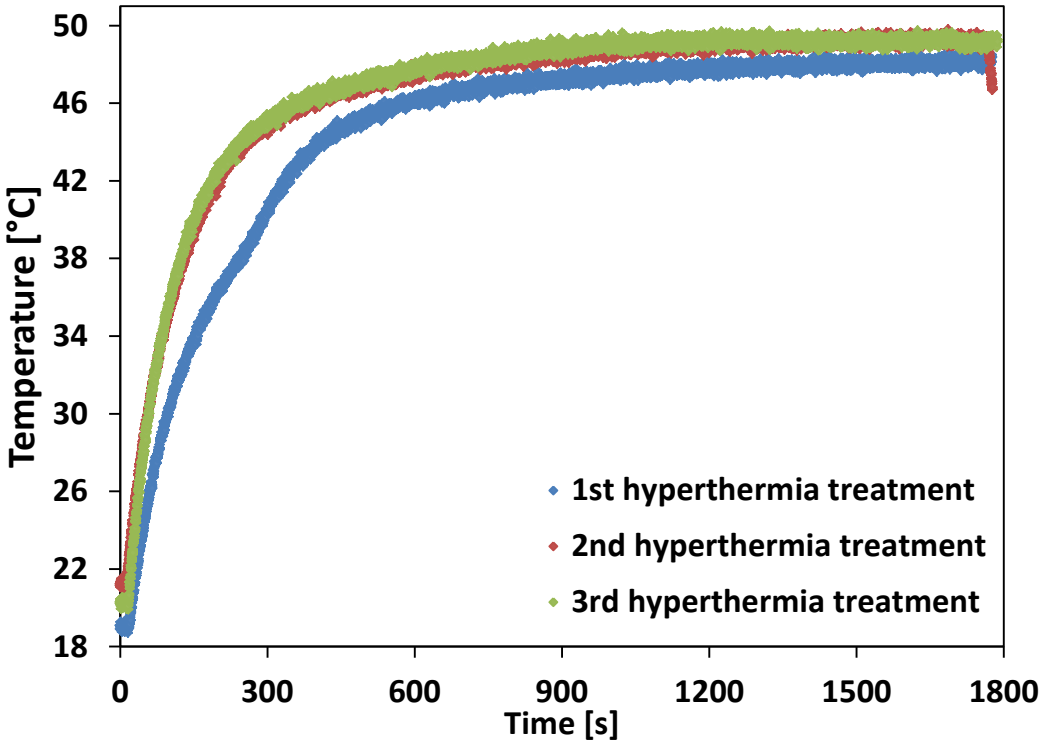

Figure 14: Three consecutive 30 minute long hyperthermia treatments under frequency and field conditions of 110 kHz and 25 mT (*NanoTherics instrument*) for a volume of 50 µL IONCs—at an Fe concentration of 4 g/L—coated with T-responsive polymers and loaded with doxorubicin hydrochloride: blue line—first hyperthermia experiment, red line—second hyperthermia experiment, and green line—third hyperthermia experiment. The maximum temperature reached during 30 min exposure to AMF with the NanoTherics instrument was 49 °C.

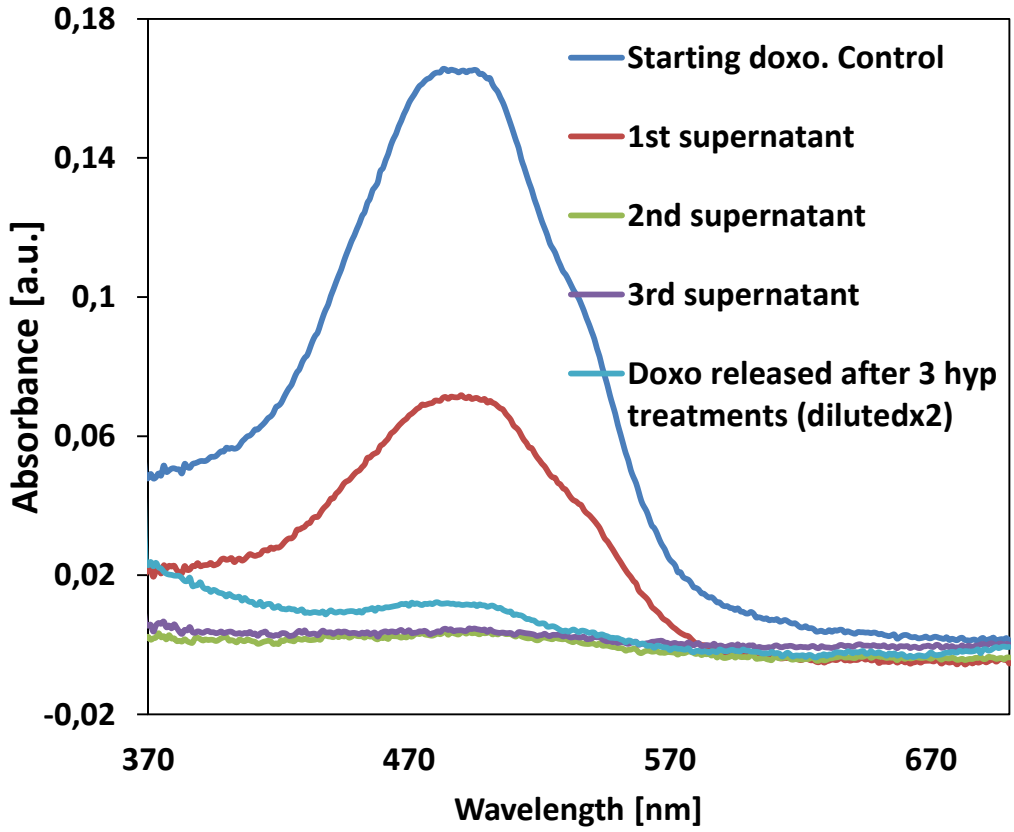

Figure 15: Heat-triggered doxo release under alternating magnetic field for a volume of 50 µL at Fe concentration of 4 g/L. Absorption spectra of the initial doxorubicin hydrochloride solution in PBS (blue line), 1st cleaning step (red line), 2nd cleaning step (green line), 3rd cleaning step (violet line), and 25 µ L of supernatant (+25 µL of PBS) after 90 minutes of AMF (3 hyperthermia cycles for 30 minutes with 24 hours break in between the hyperthermia treatments). The doxo characteristic peak could be observed in the supernatant solution, confirming the heat-triggered drug release.

4.4. Conclusions

In this chapter, two nanosystems designed for heat-triggered chemotherapeutic drug release were investigated. In a first instance, the doxo loading conditions as a function of initial doxo concentration, incubation time, cleaning method, and loading volume were studied on thermo-responsive polymers grown from the surface of the IONCs by reversible addition-fragmentation chain transfer polymerization. The thermo-responsive polymer of choice was poly(*N*-*iso*propylacrylamide)-*co*-poly(ethylene glycol) methyl ether acrylate, whose lower critical solution temperatures values could be tuned from 32 °C (the LCST of PNIPAM) to values above body temperature (42 - 52 °C).

In the second part, the study was focused on better characterizing and predicting sample performance for *in vivo* use. The polymerization method (patent pending) and the thermo-responsive polymer were changed in order to obtain individually coated iron oxide nanocubes with high specific absorption values. The polymer of choice was poly(diethylene glycol methyl ether methacrylate-*co*-oligo ethylene glycol methyl ether methacrylate) due to its biocompatibility and ease of LCST tuning to values in the range 39 - 42 °C, correlated to polymer composition. The heating performance of thermo-responsive polymer coated iron oxide nanocubes, in terms of specific absorption rate and maximum temperature reached during 30 minute hyperthermia treatment, was assessed in small volumes of 50 µL at Fe concentrations ranging from 2.5 to 4 g/L. Lastly, the heat-triggered doxorubicin release under alternating magnetic fields at biologically relevant frequency and field conditions was qualitatively, but not quantitatively proven.

4.5. Experimental part

CHEMICALS

Doxorubicin hydrochloride and all other solvents were purchased from Sigma Aldrich at the highest purity available and used as received. Iron oxide nanocubes (IONCs) were prepared as previously reported.[22,111] Thermo-responsive polymers were grown from the surface of the IONCs by RAFT copolymerization of *N-iso*propylacrylamide and poly(ethylene glycol) methyl ether acrylate as previously reported.[107]

CHARACTERIZATION

Dynamic Light Scattering (DLS)

Particle size measurements were carried out using a Malvern Zetasizer Nano series instrument, operated in the 173° backscattered mode on diluted aqueous solutions of nanoclusters. The measurements were performed at 25 °C. An equilibration time of 2 minutes was allowed before each measurement and at least three measurements were performed for each sample.

Transmission Electron Microscopy (TEM)

Conventional TEM images were obtained using JEOL JEM 1011 electron microscope, working with an acceleration voltage of 100 kV and equipped with a W thermionic electron source and a 11Mp Orius CCD Camera (Gatan company, USA). Samples were prepared by placing a drop of sample onto a carbon coated copper grid which was then left to dry before imaging.

Specific absorption rate (SAR) measurements

The calorimetric measurements to determine the specific absorption rate value of the iron oxide nanoclusters were carried out using either the Nanoscale Biomagnetics instrument (DM100), operating under frequency and

field conditions of 105 kHz and 25 mT (20 kA/m), or NanoTherics instrument operating under frequency and field conditions of 110 kHz and 25 mT (20 kA/m). The SAR value was calculated using the formula:

$$SAR\ (\frac{W}{g}) = \frac{C}{m} \times \frac{dT}{dt}$$

where *C* is the specific heat capacity of dispersing medium (H_2O in most cases) per unit volume (J/K) and m is the concentration (g/L of Fe) of magnetic material in solution. The calorimetric measurements were carried out in quasi-adiabatic conditions and the slope of the curve $\frac{dT}{dt}$ was measured by taking into account only the first 20-25 seconds of measurement.

Elemental analysis

Elemental analysis was carried out via Inductively Coupled Plasma Atomic Emission Spectroscopy (ICP-AES) on a ThermoFisher iCAP 6000 series instrument. The samples were prepared by digesting 2.5-10 µL sample in 1 mL of aqua regia in a 10 mL volumetric flask, overnight. The next day, the flask was filled up to the graduation mark with milli-Q water and filtered through a 0.45 µm membrane prior to the measurement.

Spectroscopy

UV-visible absorption spectra were recorded on a Varian Cary 300 UV-Vis spectrophotometer. Photoluminescence (PL) spectra were recorded using a Cary Eclipse spectrophotometer.

METHODS

Doxorubicin hydrochloride loading. Example procedure.

To thermo-responsive polymer functionalized iron oxide nanocubes (2 mL, 50 ppm of Fe) in PBS buffer (pH 7.4) was added doxorubicin hydrochloride (50 µg). The solution was placed on an orbital shaker overnight—set at the speed of 1 000 rpm—to load the drug within the polymer layer. The unloaded drug was removed by placing the solution on a magnet whereupon the loaded nanoparticles went to the magnet and the free drug remained in solution and was taken out using a micropipette. Fresh PBS buffer was then added to the vial with the nanoparticles in order to re-suspend them and more unloaded drug was then removed as previously described. The process was repeated (usually three times) until no absorption signal due to doxorubicin in the supernatant was observed via UV-Vis spectroscopy (λ_{max} = 485 nm). The amount of doxo loaded was evaluated by using a calibration curve of doxo in PBS. The doxo concentrations used for the calibration curve were 5, 10, 15, 25, 50, and 100 µg/mL. The absorption spectra of the standard solutions and the calibration curve are shown in Figure 17a and 17b, respectively.

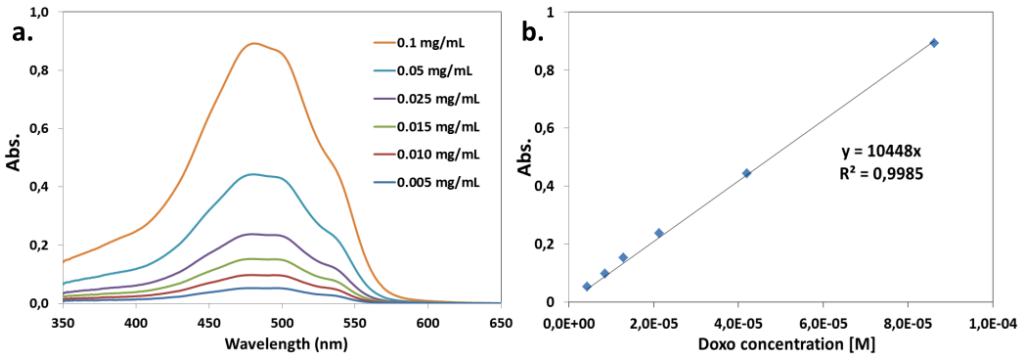

Figure 17: Doxorubicin hydrochloride calibration curve. (a) Absorption spectra of doxo in PBS at different drug concentrations, and (b) the corresponding calibration curve.

Doxorubicin hydrochloride release in dimethyl sulfoxide

Briefly, 10 µL of doxorubicin hydrochloride loaded thermo-responsive IONCs in PBS ([Fe] = 2.5 g/L) were diluted with 90 µL of DMSO in a 250 µL Eppendorf tube. The supernatant was collected by magnetic decantation and subjected to fluorescence spectroscopy measurements. The amount of doxo released was evaluated by using a calibration curve of doxo in DMSO:PBS (90:10) mixture. The doxo concentrations used for the calibration curve were 1.6, 2, 3.25, 6.25, 12.5, and 25 µg/mL. The absorption spectra of the standard solutions and the calibration curve are shown in Figure 18a and 18b, respectively.

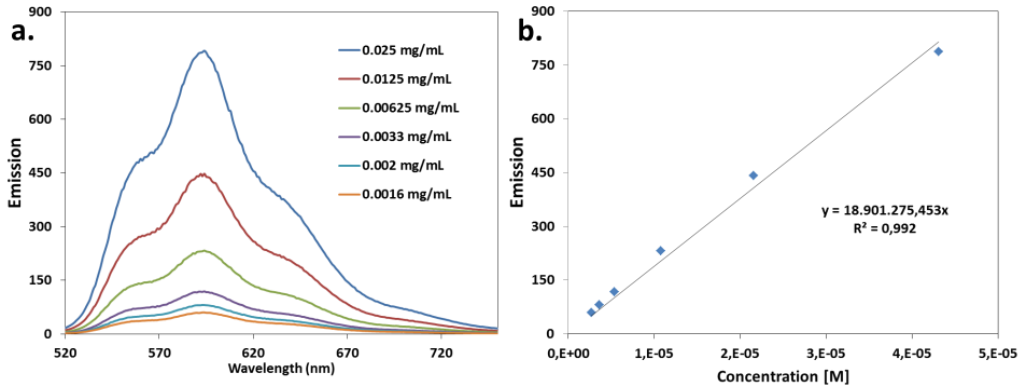

Figure 18: Doxorubicin hydrochloride calibration curve. (a) Fluorescence spectra of doxo in DMSO:PBS (90:10) mixture at different drug concentrations, and (b) the corresponding calibration curve.

Doxorubicin hydrochloride release under alternating magnetic field

Two samples of iron oxide nanocubes coated with thermo-responsive polymers and loaded with doxorubicin, with an iron concentration of 2 g/L (100 µL) in conical glass vials were placed on magnets (0.3 T) to remove any traces of unbound/leaked doxorubicin. The collected nanoparticles were resuspended in 50 µL of fresh PBS buffer (pH 7.4) and then one sample was placed centrally in the magnetic coil of the

hyperthermia instrument followed by application of an alternating magnetic field while the other sample was left at room temperature. The AMF was initially applied for 30 minutes (110 kHz, 25 mT) with the temperature measuring probe dipped in solution. After letting for 30 minutes the solution to cool down, another AMF cycle was applied. This was repeated one more time, after which the sample was taken out of the instrument and placed on the magnet for a couple of hours to collect the nanoparticles at the bottom of the vial. The amount of drug released was measured by UV-Vis spectroscopy. An aliquot of the doxo loaded sample was kept at room temperature and treated in the same way, but not subjected to an AMF, for comparison. No unspecific release was measured on this sample.

5. Overall conclusions

Three main projects were conducted during my thesis that was focused on the study of nanosystems based on iron oxide nanocubes for magnetic hyperthermia.

The novel use of MH set-up for the mild oxidization of $Fe_{1-x}O/Fe_{3-\delta}O_4$ core-shell nanocubes to single Fe_3O_4 phase was demonstrated. As specific absorption rate values of wüstite/magnetite core-shell nanocubes were lower compared to magnetite IONCs of similar cube edge length, the FeO core was oxidized by MH stimulation. After several MH treatments, the SAR values increased twice, while colloidal stability, size distribution and shape remained unaffected. The magnetically stimulated IONCs showed higher saturation magnetization, reflecting structural and compositional changes, as confirmed by electron microscopy and superconductive quantum interference device studies. The mild MH treatment also opened up the possibility of attaching biologically relevant molecules to the surface of nanocubes and preserving their activity while improving the IONCs heat performance.

The SAR values of core-shell IONCs were also enhanced by clustering the nanocubes in chain like structures. Initially, the controlled clustering of the IONCs during their water transfer was developed, enabling the formation of clusters with mean hydrodynamic sizes between 30 and 100 nm. The hyperthermia response of individual nanocubes *vs.* soft colloidal nanoclusters of different sizes was evaluated. The so called “dimers” and “trimers”—2D structures formed with two and three IONCs—showed higher SAR values.

Drug loading on two nanosystems designed for heat-triggered chemotherapeutic drug release was achieved. Both systems were based on magnetite IONCs coated with thermo-responsive polymers loaded with doxorubicin. The goal was to have stable nanocarriers at body temperature that would release the cargo exclusively upon the application of an alternating magnetic field. Once individually thermo-responsive polymer coated IONCs with high SAR values were obtained, the heat-triggered doxorubicin release under AMF—at biologically relevant field conditions—was qualitatively, but not quantitatively proven.

Annex: Nano-iron oxide-catalyzed oxidation of benzyl alcohol

Introduction

Nanoparticle based catalysis is considered nowadays the bridge between heterogeneous and homogeneous catalysis. In the latter, catalysts are present in the same phase as reactants and products, offering high selectivity and the possibility of mechanistic studies through kinetic investigations. On the other hand, the main advantage of heterogeneous catalysts is their recyclability and superior thermal stability, features not associated with homogeneous catalysis.[112] By employing magnetic nanoparticles as catalysts the recovery and reuse is easily implemented by magnetic decantation.

Iron oxides are widespread in nature and play an important role in many biological processes. Availability, low-toxicity and price are three of the main advantages of using iron-based catalysts over other transition metals. The group of Prof. Matthias Beller was one of the first that investigated iron oxide nanoparticle (IONP) based catalytic processes under mild reaction conditions, using hydrogen peroxide as the oxidant. In their first communication[113], that was one year later followed by an article in the *Journal of Molecular Catalysis A: Chemical*[114], they showed that, by tuning the size of the nanoparticles, catalyst activity and selectivity was controlled in the oxidation of alcohol and olefins. In their research they employed two types of γ-Fe_2O_3 nanoparticles: 3 - 5 nm uniform NPs and 20 - 50 nm commercially available NPs. The small IONPs showed high activity, but low selectivity and the inverse was true for the bigger polydispersed NPs: lower activity, but very high selectivity. The high activity and low selectivity of 3 - 5 nm IONPs was close to

that of Fe salts, where Fe^{3+} was the catalyst. The authors hypothesized that by downsizing the particle size to a few nanometers catalytic activity and selectivity values could approach those of Fe^{3+} single-site homogeneous catalysis. By increasing the size, better selectivity was obtained and the activity, though lower compared to the 3-5 nm NPs, was more than six times higher than the values obtained for bulk γ-Fe_2O_3 (particle size > 100 nm).

Thus, I set out to study the nano-iron oxide-catalyzed oxidation of benzyl alcohol under mild conditions. In particular, I wanted to answer two questions: (i) does the use of monodispersed 22 nm spherical IONPs (Figure 1a) influence the catalytic activity, as the surface area would be considerably increased compared to a polydispersed 20 - 50 nm sample and (ii) how does the change in the shape of the catalyst from spherical to cubic (Figure 1b), while maintaining the same total surface area per nanoparticle, impact the catalytic activity and selectivity.

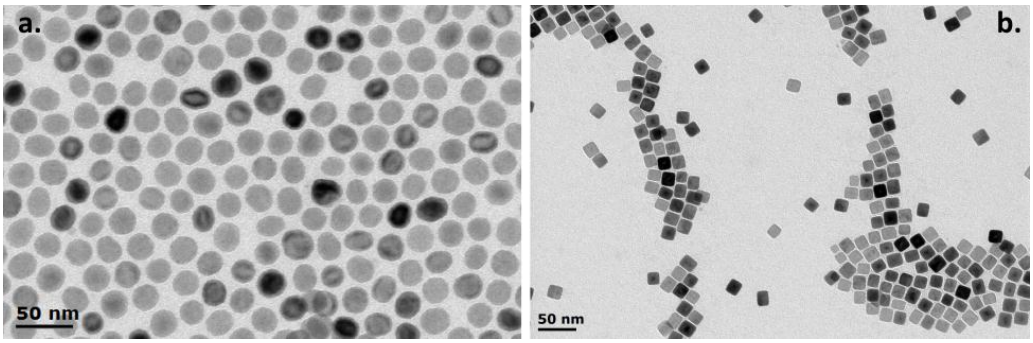

Figure 1: Shape influence on catalytic activity. Representative TEM micrographs of (a) spherical γ-Fe_2O_3 and (b) cubic $Fe_{1-x}O/Fe_3O_4$ NPs in $CHCl_3$.

First trials

The chosen model reaction was the oxidation of benzyl alcohol into benzaldehyde that is a typical benchmark reaction for liquid phase oxidation.[113]

The general procedure for the oxidation of benzyl alcohol was the following (Scheme 1): to a glass vial (10 mL), benzyl alcohol (1 mL, 10.0 mmol) and 0.5 mol% of iron oxide nanoparticles (8.0 mg) were added. The reaction mixture was vigorously stirred (1 000 - 1 250 rpm) at 75 °C. H_2O_2 (30 wt. % in water, 1.0 mL, 10.0 mmol) was added continuously with a syringe pump in 12 hours. The mixture was then cooled to room temperature and the remaining reactant and product were extracted three times with 3 mL of dichloromethane. After removing the excess of solvent under reduced pressure, 2-methoxynaphthalene (55.4 mg, 0.35 mmol) was added as an internal standard for quantitative analysis by gas chromatography-flame ionization detector (GC-FID). All GC-FID experiments were run three times and the average value is reported.

The nanoparticles remained in the organic phase in that case. As the oxidant was an aqueous solution, another reaction was run in which the nanoparticles were first transferred into aqueous media by ligand exchange with caffeic acid, by slightly modifying a previously published method.[115] In two 20 ml vials, to 16 mL of tetrahydrofuran (THF) 825 µL of 22 nm NPs ([Fe]= 6.8 g/L, [IONPs] = 0.58 µM) in chloroform ($CHCl_3$) and 11.2 mg of caffeic acid were added, respectively. The ratio of ligand/nm^2 of IONPs was 80 - 85. The vials were then stirred in a rotary evaporator (P = 1 atmosphere) at 55 °C for 3 hours. After the addition of 2 ml H_2O and 120 µL NaOH 2.5 M, IONPs and the sodium caffeate started precipitating. To remove the excess of caffeic acid the

samples were centrifuged three times at 2 500 rpm for 10 min. Each time, the supernatant was discarded and milliQ-water was added. Lastly, bubbling with nitrogen was performed in order to remove traces of tetrahydrofuran and 35 µL hydrochloric acid 12 M were added to neutralize the base added in an earlier step.

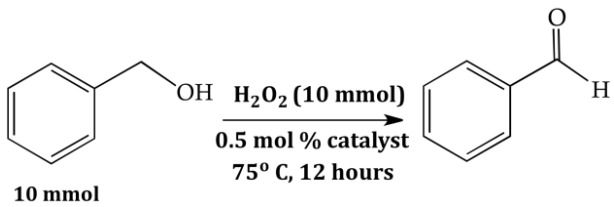

Scheme 1: Reaction conditions for the selective oxidation of benzyl alcohol to benzaldehyde, 0.5 mol% catalyst.

Table 1: Oxidation of benzyl alcohol to benzaldehyde in solvent-free conditions

Entry	Type of catalyst	Conversion [%]	Yield [%]
1	22 nm γ-Fe_2O_3@oleic acid	53.4	23.3
2	16 nm $Fe_{1-x}O/Fe_3O_4$@oleic acid	51.6	24
3	22 nm γ-Fe_2O_3@caffeic acid	58.2	26.2
4	No catalyst	36.7	7.5

The results are presented in Table 1. For 0.5 mol% catalyst, used as-synthesized, the conversions and yields are very similar for the 22 nm spherical IONPs (entry 1) and the 16 nm cube edge length core-shell iron oxide nanocubes (entry 2). The shape of the nanoparticles does not seem to have an influence under solvent-free conditions. The limiting factor is most probably the total surface area and, taking into consideration the fact that the total surface area is comparable for the two samples, that assumption was corroborated by the results. Once the catalyst was coated with caffeic acid, which made it dispersible in aqueous phase, the conversion and yield increased by *ca*. 10% (entry 3). Although the catalyst shows high activity, the

selectivity is low, with 44%, 46% and 45% for entries 1, 2 and 3, respectively. A control experiment in the absence of catalyst, showed a 36.7% conversion (entry 4), with 80% of the products being side-products that cannot be detected by GC-FID. These results point towards non-selective radical side-reactions, typical for Fenton-type reactions.

The enquiry into the change from non-selective radical to selective non-radical reactions, for iron-dependent oxidation reactions, was reported by Shi and co-workers[116]. The conclusions drawn by the authors involved the dependence between the absolute proton concentration and the change of pH value during the reaction *vs.* the catalytic activity: lowering the pH increased the conversion and the smaller the pH deviation, the higher was the selectivity. The use of the acidic buffer of pH 1 and the control of ΔpH below 0.05 suppressed unwanted radical reactions. The best conversion value obtained was 92%, with 87% selectivity towards benzaldehyde and benzoic acid (86:14 ratio of CHO to CO_2H) for 2 mol% catalyst loading, 1.5 H_2O_2 equivalents and 5 mL buffer solution.

In an attempt to increase both conversion and selectivity for the monodispersed 22 nm spherical IONPs and the core-shell cubic IONPS, the experiments previously carried out were repeated, this time with 5 mL acidic buffer, based on $KHSO_4$. The results shown in Table 2 confirmed a rise in conversion and yield when using a buffer, alongside a decrease in side-reactions. In the control experiment conversion dropped to 23.8% for the Fe-free reaction (entry 4), a 35% decrease compared to solvent-free conditions. The side-reactions were not fully suppressed as the variation of pH was controlled at 0.07 at best, but not down to 0.01 as in the literature reference[116]. Nevertheless, the results were encouraging as with only 0.5 mol%

catalyst loading, the 16 nm core-shell iron oxide nanocubes coated with caffeic acid gave 89% conversion with 67.7% selectivity (entry 3). In these cases, no traces of benzoic acid were detected by GC-FID. Given that the best results were obtained for the cubic nanoparticles coated with a small hydrophilic molecule, further studies focused on that type of catalyst. Two parameters were probed: reaction time and catalyst loading.

Table 2: Oxidation of benzyl alcohol to benzaldehyde in acidic buffer conditions

Entry	Type of catalyst	Conversion [%]	Yield [%]	Selectivity [%]
1	22 nm γ-Fe_2O_3@caffeic acid	85.7	56	65.3
2	22 nm γ-Fe_2O_3@oleic acid	82.6	52.7	63.8
3	16 nm $Fe_{1-x}O/Fe_3O_4$@caffeic acid	89.1	60.4	67.8
4	No catalyst	23.8	1.5	n/a

Optimization of catalysis parameters

Reaction time

In an effort to optimize reaction conditions, the reaction time parameter was investigated. Shorter reaction times are favorable as more reactions can be carried out in the same period of time. 16 nm core-shell iron oxide nanocubes ($Fe_{1-x}O/Fe_3O_4$@caffeic acid) were used as catalyst, with a 0.5 mol% loading. The reaction times considered were t = 1, 3, 6 and 15 hours. As can be observed from Figure 2, increasing the time from 1 to 15 hours, both conversion and yield steadily increased from 54% to 89% conversion of benzyl alcohol and from 18% to 60% benzaldehyde yield. Interestingly, the difference between 6 and 15 hours was a modest 7% increase in conversion and 11% in yield. This fact was used in the follow up study, when the catalyst loading was doubled from 0.5 to 1 mol% and both times were considered.

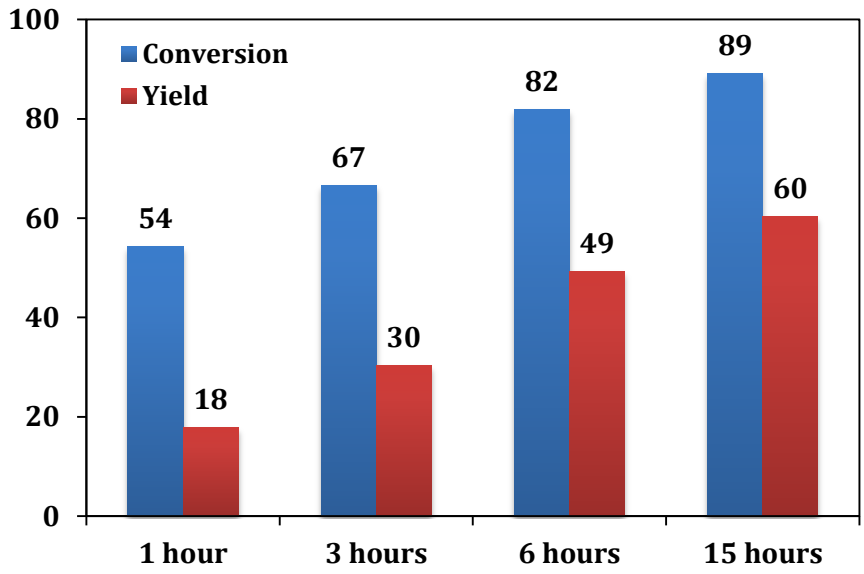

Figure 2: Reaction time study. Conversion and yield of $Fe_{1-x}O/Fe_3O_4$-catalyzed oxidation of benzyl alcohol as a function of reaction time.

Catalyst amount

Next parameter examined was the catalyst loading. By increasing the catalyst loading conversion and yield are expected to rise for a given reaction time. In the experiments carried out, the amount of catalyst was doubled to 1 mol% and the reactions were run for 6 and 15 hours. The results plotted in Figure 3 showed a more pronounced increase in conversion and yield for the six-hour reaction when the catalyst loading was doubled, while the 15-hour runs showed no improvement in benzyl alcohol conversion and a meager 9% increase in yield. It is worth pointing out the fact that for the 1 mol% catalyst loading, both conversion and yield were slightly better for a six-hour reaction compared to the 15-hour reaction. A possible explanation of this fact was a plateauing of conversion and yield values, as seen previously for 0.5 mol% catalyst loading.

Recyclability studies

Lastly, a recyclability study was performed. As mentioned before, the main advantage of heterogeneous catalysis over homogeneous catalysis is the possibility of isolating and reusing the catalyst. For 1 mol% catalyst loading, t = 6 hours, 5 cycles were run. As seen from Figure 4, benzaldehyde yield dropped faster compared to conversion, which remained around 89%. The decrease in yield was accompanied by the emergence of benzoic acid as side-product at the 4th run and its increase from 4th to 5th cycle. Selectivity also dropped from 78% for the 1st run to 65.5% for the 5th run.

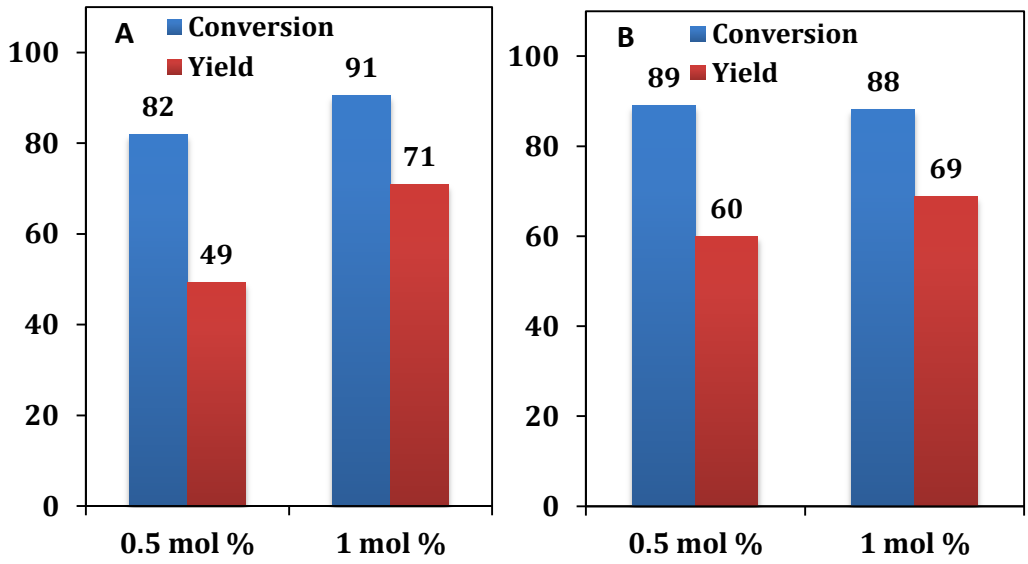

Figure 3: Catalyst amount comparison. Conversion and yield of $Fe_{1-x}O/Fe_3O_4$-catalyzed oxidation of benzyl alcohol for 0.5 and 1 mol% catalyst loading for (A) t = 6 hours and (B) t = 15 hours.

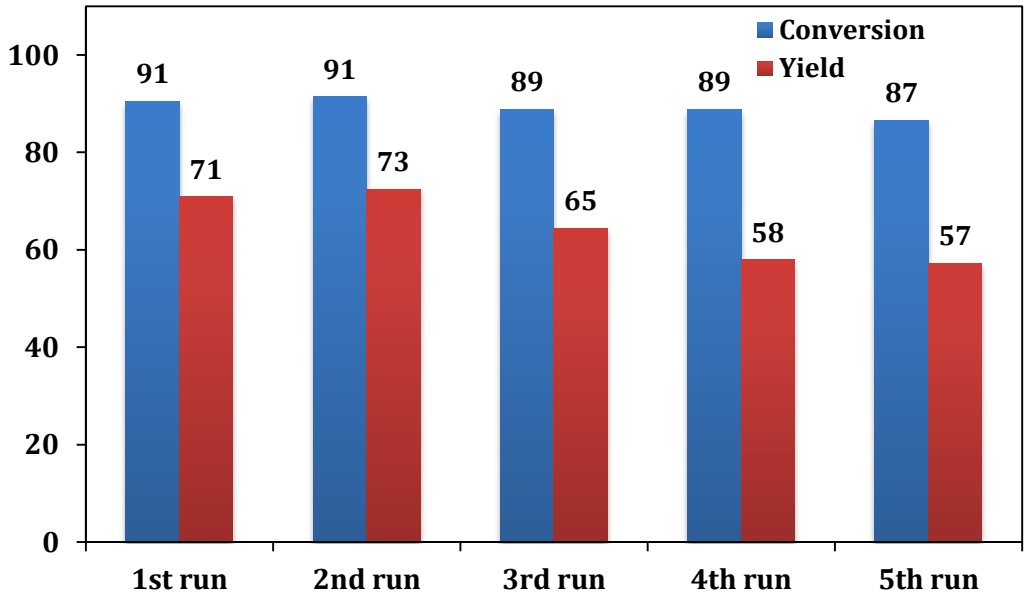

Figure 4: Recyclability studies. Conversion and yield of $Fe_{1-x}O/Fe_3O_4$-catalyzed oxidation of benzyl alcohol for 1 mol% catalyst loading, t = 6 hours.

Conclusions

At ICIQ, during my ten-month mobility stay, I have investigated two nanosystems made up of iron oxide nanoparticles: (i) 22 nm spherical iron oxide nanoparticles and (ii) 16 nm cube edge length core-shell iron oxide nanocubes ($Fe_{1-x}O/Fe_3O_4$), either as-synthesized, thus stabilized in organic solvents by oleic acid, or coated with caffeic acid, a small molecules that imparted the IONPs hydrophilicity. The main focus was the study of the suitability of the IONPs as catalysts in mild reaction conditions. The reaction investigated was the selective oxidation of benzyl alcohol, using hydrogen peroxide as an oxidant. The optimized parameters were the reaction time, the amount and the type of catalyst. Lastly, recyclability studies were carried out for the best reaction conditions.

Bibliography

(1) Q. A. Pankhurst; Connolly, J.; S. K. Jones; Dobson, J. *J. Phys. D Appl. Phys.* **2003**, *36*, R167–R181.

(2) Bogart, L. K.; Pourroy, G.; Murphy, C. J.; Puntes, V.; Pellegrino, T.; Al, B. E. T. *ACS Nano* **2014**, *8*, 3107–3122.

(3) Lagendijk, J. J. W. *Phys. Med. Biol.* **2000**, *45*, R61–R76.

(4) Rosensweig, R. E. *J. Magn. Magn. Mater.* **2002**, *252*, 370–374.

(5) Laurent, S.; Dutz, S.; Häfeli, U. O.; Mahmoudi, M. *Adv. Colloid Interface Sci.* **2011**, *166*, 8–23.

(6) Fortin, J.-P.; Wilhelm, C.; Servais, J.; Ménager, C.; Bacri, J.-C.; Gazeau, F. *J. Am. Chem. Soc.* **2007**, *129*, 2628–2635.

(7) Mehdaoui, B.; Meffre, A.; Carrey, J.; Lachaize, S.; Lacroix, L.-M.; Gougeon, M.; Chaudret, B.; Respaud, M. *Adv. Funct. Mater.* **2011**, *21*, 4573–4581.

(8) Meffre, A.; Mehdaoui, B.; Kelsen, V.; Fazzini, P. F.; Carrey, J.; Lachaize, S.; Respaud, M.; Chaudret, B. *Nano Lett.* **2012**, *12*, 4722–4728.

(9) Martinez-Boubeta, C.; Simeonidis, K.; Makridis, A.; Angelakeris, M.; Iglesias, O.; Guardia, P.; Cabot, A.; Yedra, L.; Estradé, S.; Peiró, F.; Saghi, Z.; Midgley, P. a; Conde-Leborán, I.; Serantes, D.; Baldomir, D. *Sci. Rep.* **2013**, *3*, 1652.

(10) Guardia, P.; Riedinger, A.; Nitti, S.; Pugliese, G.; Marras, S.; Genovese, A.; Materia, M. E.; Lefevre, C.; Manna, L.; Pellegrino, T. *J. Mater. Chem. B* **2014**, *2*, 4426.

(11) Sun, S. H.; Zeng, H. *J. Am. Chem. Soc.* **2002**, *124*, 8204–8205.

(12) Kovalenko, M. V.; Bodnarchuk, M. I.; Lechner, R. T.; Hesser, G.; Schäffler, F.; Heiss, W. *J. Am. Chem. Soc.* **2007**, *129*, 6352–6353.

(13) Shavel, A.; Rodríguez-González, B.; Spasova, M.; Farle, M.; Liz-Marzán, L. M. *Adv. Funct. Mater.* **2007**, *17*, 3870–3876.

(14) Corrias, A.; Mountjoy, G.; Loche, D.; Puntes, V.; Falqui, A.; Zanella, M.; Parak, W. J.; Casula, M. F. *J. Phys. Chem. C* **2009**, *113*, 18667–18675.

(15) Redl, F. X.; Black, C. T.; Papaefthymiou, G. C.; Sandstrom, R. L.; Yin, M.; Zeng, H.; Murray, C. B.; O'Brien, S. P. *J. Am. Chem. Soc.* **2004**, *126*, 14583–14599.

(16) Bronstein, L.; Huang, X.; Retrum, J.; Schmucker, A.; Pink, M.; Stein, B. D.; Dragnea, B. *Chem. Mater.* **2007**, *19*, 3624–3632.

(17) Hai, H. T.; Yang, H. T.; Kura, H.; Hasegawa, D.; Ogata, Y.; Takahashi, M.; Ogawa, T. *J. Colloid Interface Sci.* **2010**, *346*, 37–42.

(18) Lak, A.; Kraken, M.; Ludwig, F.; Kornowski, A.; Eberbeck, D.; Sievers, S.; Litterst, F. J.; Weller, H.; Schilling, M. *Nanoscale* **2013**, *5*, 12286–12295.

(19) Estrader, M.; López-Ortega, A.; Estradé, S.; Golosovsky, I. V.; Salazar-Alvarez, G.; Vasilakaki, M.; Trohidou, K. N.; Varela, M.; Stanley, D. C.; Sinko, M.; Pechan, M. J.; Keavney, D. J.; Peiró, F.; Suriñach, S.; Baró, M. D.; Nogués, J. *Nat. Commun.* **2013**, *4*, 2960.

(20) Pichon, B. P.; Gerber, O.; Lefevre, C.; Florea, I.; Fleutot, S.; Baaziz, W.; Pauly, M.; Ohlmann, M.; Ulhaq, C.; Ersen, O.; Panissod, P.; Drillon, M.; Begin-Colin, S. *Chem. Mater.* **2011**, *23*, 2886–2900.

(21) Wetterskog, E.; Tai, C.; Grins, J.; Bergstrom, L.; Salazar-Alvarez, G. *ACSNano* **2013**, *7*, 7132–7144.

(22) Guardia, P.; Di Corato, R.; Lartigue, L.; Wilhelm, C.; Espinosa, A.; Garcia-Hernandez, M.; Gazeau, F.; Manna, L.; Pellegrino, T. *ACS Nano* **2012**, *6*, 3080–3091.

(23) Lak, A.; Niculaes, D.; Anyfantis, G. C.; Bertoni, G.; Barthel, M. J.; Marras, S.; Cassani, M.; Nitti, S.; Athanassiou, A.; Giannini, C.; Pellegrino, T. *Sci. Rep.* **2016**, *6*, 33295.

(24) Amstad, E.; Gillich, T.; Bilecka, I.; Textor, M.; Reimhult, E. *Nano Lett.* **2009**, *9*, 4042–4048.

(25) Cheng, K.; Peng, S.; Xu, C.; Sun, S. *J. Am. Chem. Soc.* **2009**, *131*, 10637–10644.

(26) Ling, D.; Park, W.; Park, Y. Il; Lee, N.; Li, F.; Song, C.; Yang, S.-G.; Choi, S. H.; Na, K.; Hyeon, T. *Angew. Chem. Int. Ed. Engl.* **2011**, *50*, 11360–11365.

(27) Wang, W.; Ji, X.; Na, H. Bin; Sa, M.; Smith, A.; Palui, G.; Perez, J. M.; Mattoussi, H. *Langmuir* **2014**, 6197–6208.

(28) Pellegrino, T.; Manna, L.; Kudera, S.; Liedl, T.; Koktysh, D.; Rogach, A. L.; Keller, S.; Ra, J.; Natile, G.; Parak, W. J. *Nano Lett.* **2004**, *4*, 703–707.

(29) Kim, B.-S.; Qiu, J.-M.; Wang, J.-P.; Taton, T. A. *Nano Lett.* **2005**, *5*, 1987–1991.

(30) Yu, W. W.; Chang, E.; Falkner, J. C.; Zhang, J.; Al-Somali, A. M.; Sayes, C. M.; Johns, J.; Drezek, R.; Colvin, V. L. *J. Am. Chem. Soc.* **2007**, *129*, 2871–2879.

(31) Tromsdorf, U. I.; Bigall, N. C.; Kaul, M. G.; Bruns, O. T.; Nikolic, M. S.; Mollwitz, B.; Sperling, R. A.; Reimer, R.; Hohenberg, H.; Parak, W. J.; Fo, S.; Beisiegel, U.; Adam, G.; Weller, H. *Nano Lett.* **2007**, *7*, 2422–2427.

(32) Riedinger, A.; Guardia, P.; Curcio, A.; Garcia, M. a; Cingolani, R.; Manna, L.; Pellegrino, T. *Nano Lett.* **2013**, *13*, 2399–2406.

(33) Dias, J. T.; Moros, M.; Del Pino, P.; Rivera, S.; Grazú, V.; De La Fuente, J. M. *Angew. Chemie - Int. Ed.* **2013**, *52*, 11526–11529.

(34) Levy, M.; Quarta, A.; Espinosa, A.; Figuerola, A.; Wilhelm, C.; García-Hernandez, M.; Genovese, A.; Falqui, A.; Alloyeau, D.; Cozzoli, P. D.; García, M. A.; Gazeau, F.; Pellegrino, T. *Chem. Mater.* **2011**, *23*, 4170–4180.

(35) Guibert, C.; Dupuis, V.; Peyre, V.; Fresnais, J. *J. Phys. Chem. C* **2015**, *119*, 28148–28154.

(36) Hytch, M. J.; Snoeck, E.; Kilaas, R. *Ultramicroscopy* **1998**, *74*, 131–146.

(37) Batlle, X.; Pérez, N.; Guardia, P.; Iglesias, O.; Labarta, A.; Bartolomé, F.; Garca, L. M.; Bartolomé, J.; Roca, A. G.; Morales, M. P.; Serna, C. J. *J. Appl. Phys.* **2011**, *109*, 1–7.

(38) Sun, X.; Frey Huls, N.; Sigdel, A.; Sun, S. *Nano Lett.* **2012**, *12*, 246–251.

(39) Fitzsimmons, M. R.; Yashar, P.; Leighton, C.; Schuller, I. K.; Majkrzak, C. F.; Dura, J. A. *Phys. Rev. Lett.* **2000**, *84*, 3986–3989.

(40) Margulies, D. T.; Parker, F. T.; Rudee, M. L.; Spada, F. E.; Chapman, J. N.; Aitchison, P. R.; Berkowitz, a E. *Phys. Rev. Lett.* **1997**, *79*, 5162–5165.

(41) Parkinson, G. S.; Manz, T. A.; Novotný, Z.; Sprunger, P. T.; Kurtz, R. L.; Schmid, M.; Sholl, D. S.; Diebold, U. *Phys. Rev. B - Condens. Matter Mater. Phys.* **2012**, *85*, 1–7.

(42) Bobo, J. F.; Basso, D.; Snoeck, E.; Gatel, C.; Hrabovsky, D.; Gauffier, J. L.; Ressier, L.; Mamy, R.; Visnovsky, S.; Hamrle, J.; Teillet, J.; Fert, A. R. *Eur. Phys. J. B* **2001**, *24*, 43–49.

(43) Walter, A.; Billotey, C.; Garofalo, A.; Ulhaq-Bouillet, C.; Lefèvre, C.; Taleb, J.; Laurent, S.; Vander Elst, L.; Muller, R. N.; Lartigue, L.; Gazeau, F.; Felder-Flesch, D.; Begin-Colin, S. *Chem. Mater.* **2014**, *26*, 5252–5264.

(44) Guardia, P.; Labarta, A.; Batlle, X. *J. Phys. Chem. C* **2011**, *115*, 390–396.

(45) Tai, C. W.; Lereah, Y. *Appl. Phys. Lett.* **2009**, *94*, 51908.

(46) Figuerola, A.; Di Corato, R.; Manna, L.; Pellegrino, T. *Pharmacol. Res.* **2010**, *62*, 126–143.

(47) Pollert, E.; Goglio, G.; Mornet, S.; Duguet, E. *Nanomaterials: A Danger or a Promise?*; Brayner, R.; Fiévet, F.; Coradin, T., Eds.; Springer London: London, 2013.

(48) Pellegrino, T.; Manna, L.; Kudera, S.; Liedl, T.; Koktysh, D.; Rogach, A. L.; Keller, S.; Natile, G.; Parak, W. J.; München, M. U. .

(49) Lin, C.-A. J.; Sperling, R. a; Li, J. K.; Yang, T.-Y.; Li, P.-Y.; Zanella, M.; Chang, W. H.; Parak, W. J. *Small* **2008**, *4*, 334–341.

(50) Materia, M. E.; Guardia, P.; Sathya, A.; Pernia Leal, M.; Marotta, R.; Di Corato, R.; Pellegrino, T. *Langmuir* **2015**, *31*, 808–816.

(51) Ovejero, J. G.; Cabrera, D.; Carrey, J.; Valdivielso, T.; Salas, G.; Teran, F. J. *Phys. Chem. Chem. Phys.* **2016**, *18*, 10954–10963.

(52) Coral, D. F.; Mendoza Zélis, P.; Marciello, M.; Morales, M. D. P.; Craievich, A.; Sánchez, F. H.; Fernández Van Raap, M. B. *Langmuir* **2016**, *32*, 1201–1213.

(53) Serantes, D.; Simeonidis, K.; Angelakeris, M.; Chubykalo-Fesenko, O.; Marciello, M.; Del Puerto Morales, M.; Baldomir, D.; Martinez-Boubeta, C. *J. Phys. Chem. C* **2014**, *118*, 5927–5934.

(54) Medeiros, S. F.; Santos, a M.; Fessi, H.; Elaissari, A. *Int. J. Pharm.* **2011**, *403*, 139–161.

(55) Xiong, F.; Chen, Y.; Chen, J.; Yang, B.; Zhang, Y.; Gao, H.; Hua, Z.; Gu, N. *J. Control. Release* **2013**, *172*, 993–1001.

(56) Ai, H.; Flask, C.; Weinberg, B.; Shuai, X.; Pagel, M. D.; Farrell, D.; Duerk, J.; Gao, J. *Adv. Mater.* **2005**, *17*, 1949–1952.

(57) Berret, J.-F.; Schonbeck, N.; Gazeau, F.; El Kharrat, D.; Sandre, O.; Vacher, A.; Airiau, M. *J. Am. Chem. Soc.* **2006**, *128*, 1755–1761.

(58) Pothayee, N.; Balasubramaniam, S.; Pothayee, N.; Jain, N.; Hu, N.; Lin, Y.; Davis, R. M.; Sriranganathan, N.; Koretsky, A. P.; Riffle, J. S. *J. Mater. Chem. B. Mater. Biol. Med.* **2013**, *1*, 1142–1149.

(59) Yang, J.; Lee, C. H.; Ko, H. J.; Suh, J. S.; Yoon, H. G.; Lee, K.; Huh, Y. M.; Haam, S. *Angew. Chemie - Int. Ed.* **2007**, *46*, 8836–8839.

(60) Pöselt, E.; Kloust, H.; Tromsdorf, U.; Janschel, M.; Hahn, C.; Maßlo, C.; Weller, H. *ACS Nano* **2012**, *6*, 1619–1624.

(61) Zoppellaro, G.; Kolokithas-Ntoukas, A.; Polakova, K.; Tucek, J.; Zboril, R.; Loudos, G.; Fragogeorgi, E.; Diwoky, C.; Tomankova, K.; Avgoustakis, K.; Kouzoudis, D.; Bakandritsos, A. *Chem. Mater.* **2014**, *26*, 2062–2074.

(62) Soukup, D.; Moise, S.; Cespedes, E.; Dobson, J.; Telling, N. D. *ACS Nano* **2015**, *9*, 231–240.

(63) Argyle, K. S.; Dunlop, D. J. *J. Geophys. Res. Solid Earth* **1990**, *95*, 7069–7082.

(64) Connord, V.; Mehdaoui, B.; Tan, R. P.; Carrey, J.; Respaud, M. *Rev. Sci. Instrum.* **2014**, *85*, 93904.

(65) Mahdavi, M.; Ahmad, M. Bin; Haron, M. J.; Namvar, F.; Nadi, B.; Ab Rahman, M. Z.; Amin, J. *Molecules* **2013**, *18*, 7533–7548.

(66) Jadhav, N. V.; Prasad, A. I.; Kumar, A.; Mishra, R.; Dhara, S.; Babu, K. R.; Prajapat, C. L.; Misra, N. L.; Ningthoujam, R. S.; Pandey, B. N.; Vatsa, R. K. *Colloids Surfaces B Biointerfaces* **2013**, *108*, 158–168.

(67) Marín, T.; Montoya, P.; Arnache, O.; Calderón, J. *J. Phys. Chem. B* **2016**, *120*, 6634–6645.

(68) Hauser, H.; Darke, A.; Phillips, M. C. *Eur. J. Biochem.* **1976**, 335–344.

(69) Lueth, H.; Nyburg, S. C.; Robinson, P. M.; Scott, H. G. *Mol. Cryst. Liq. Cryst.* **1974**, 337–357.

(70) Tong, L.; Lu, E.; Pichaandi, J.; Cao, P.; Nitz, M.; Winnik, M. a. *Chem. Mater.* **2015**, *27*, 4899–4910.

(71) Lee, J.-H.; Chen, K.-J.; Noh, S.-H.; Garcia, M. A.; Wang, H.; Lin, W.-Y.; Jeong, H.; Kong, B. J.; Stout, D. B.; Cheon, J.; Tseng, H.-R. *Angew. Chemie Int. Ed.* **2013**, *52*, 4384–4388.

(72) May, J. P. .; Li, S.-D. *Expert Opin. Drug Deliv.* **2013**, *10*, 511–527.

(73) Nakayama, M.; Okano, T. *React. Funct. Polym.* **2011**, *71*, 235–244.

(74) Stuart, M. A. C.; Huck, W. T. S.; Genzer, J.; Muller, M.; Ober, C.; Stamm, M.; Sukhorukov, G. B.; Szleifer, I.; Tsukruk, V. V; Urban, M.; Winnik, F.; Zauscher, S.; Luzinov, I.; Minko, S. *Nat. Mater.* **2010**, *9*, 101–113.

(75) Yang, L.; Liu, H. *Powder Technol.* **2013**, *240*, 54–65.

(76) Guo, Y.; Harirchian-Saei, S.; Izumi, C. M. S.; Moffitt, M. G. *ACS Nano* **2011**, *5*, 3309–3318.

(77) Oh, J. K.; Park, J. M. *Prog. Polym. Sci.* **2011**, *36*, 168–189.

(78) Kumar, C. S. S. R.; Mohammad, F. *Adv. Drug Deliv. Rev.* **2011**, *63*, 789–808.

(79) Zhou, L.; Yuan, J.; Yuan, W.; Sui, X.; Wu, S.; Li, Z.; Shen, D. *J. Magn. Magn. Mater.* **2009**, *321*, 2799–2804.

(80) Barick, K. C.; Singh, S.; Jadhav, N. V.; Bahadur, D.; Pandey, B. N.; Hassan, P. a. *Adv. Funct. Mater.* **2012**, *22*, 4975–4984.

(81) Marcelo, G.; Muñoz-Bonilla, A.; Rodríguez-Hernández, J.; Fernández-García, M. *Polym. Chem.* **2013**, *4*, 558–567.

(82) Banerjee, S. S.; Chen, D.-H. *Nanotechnology* **2008**, *19*, 505104–505111.

(83) Nigam, S.; Chandra, S.; Newgreen, D. F.; Bahadur, D.; Chen, Q. *Langmuir* **2014**, *30*, 1004–1011.

(84) Guo, M.; Yan, Y.; Liu, X.; Yan, H.; Liu, K.; Zhang, H.; Cao, Y. *Nanoscale* **2010**, *2*, 434–441.

(85) Yu, S.; Wu, G.; Gu, X.; Wang, J.; Wang, Y.; Gao, H.; Ma, J. *Colloids Surf. B. Biointerfaces* **2013**, *103*, 15–22.

(86) Wang, B.; Xu, C.; Xie, J.; Yang, Z.; Sun, S. *J. Am. Chem. Soc.* **2008**, *130*, 14436–14437.

(87) Bilalis, P.; Chatzipavlidis, A.; Tziveleka, L.-A.; Boukos, N.; Kordas, G. *J. Mater. Chem.* **2012**, *22*, 13451–13454.

(88) Guo, M.; Yan, Y.; Zhang, H.; Yan, H.; Cao, Y.; Liu, K.; Wan, S.; Huang, J.; Yue, W. *J. Mater. Chem.* **2008**, *18*, 5104–5112.

(89) Guo, M.; Que, C.; Wang, C.; Liu, X.; Yan, H.; Liu, K. *Biomaterials* **2011**, *32*, 185–194.

(90) Omer, M.; Haider, S.; Park, S.-Y. *Polymer (Guildf).* **2011**, *52*, 91–97.

(91) Zhu, S.; Zhou, Z.; Zhang, D.; Jin, C.; Li, Z. *Microporous Mesoporous Mater.* **2007**, *106*, 56–61.

(92) Du, B.; Mei, A.; Tao, P.; Zhao, B.; Cao, Z.; Nie, J.; Xu, J.; Fan, Z. *J. Phys. Chem. C* **2009**, *113*, 10090–10096.

(93) Yuan, Q.; Venkatasubramanian, R.; Hein, S.; Misra, R. D. K. *Acta Biomater.* **2008**, *4*, 1024–1037.

(94) Zhang, J.; Misra, R. D. K. *Acta Biomater.* **2007**, *3*, 838–850.

(95) Beija, M.; Marty, J.-D.; Destarac, M. *Prog. Polym. Sci.* **2011**, *36*, 845–886.

(96) Matyjaszewski, K.; Davis, T. P. Handbook of Radical Polymerization, 2002.

(97) Perrier, S.; Takolpuckdee, P. *J. Polym. Sci. Part A Polym. Chem.* **2005**, *43*, 5347–5393.

(98) Wang, J.-S.; Matyjaszewski, K. *J. Am. Chem. Soc.* **1995**, *117*, 5614–5615.

(99) Hawker, C. J.; Bosman, A. W.; Harth, E. *Chem. Rev.* **2001**, *101*, 3661–3688.

(100) Chiefari, J.; Chong, Y. K.; Ercole, F.; Krstina, J.; Jeffery, J.; Le, T. P. T.; Mayadunne, R. T. A.; Meijs, G. F.; Moad, C. L.; Moad, G.; Rizzardo, E.; Thang, S. H. *Macromolecules* **1998**, *31*, 5559–5562.

(101) Yang, X.; Chen, Y.; Yuan, R.; Chen, G.; Blanco, E.; Gao, J.; Shuai, X. *Polymer (Guildf).* **2008**, *49*, 3477–3485.

(102) Mody, V. V.; Cox, A.; Shah, S.; Singh, A.; Bevins, W.; Parihar, H. *Appl. Nanosci.* **2013**.

(103) Maier-Hauff, K.; Ulrich, F.; Nestler, D.; Niehoff, H.; Wust, P.; Thiesen, B.; Orawa, H.; Budach, V.; Jordan, A. *J. Neurooncol.* **2011**, *103*, 317–324.

(104) Kolosnjaj-Tabi, J.; Di Corato, R.; Lartigue, L.; Marangon, I.; Guardia, P.; Silva, A. K. A.; Luciani, N.; Clément, O.; Flaud, P.; Singh, J. V.; Decuzzi, P.; Pellegrino, T.; Wilhelm, C.; Gazeau, F. *ACS Nano* **2014**, *8*, 4268–4283.

(105) Aseyev, V.; Tenhu, H.; Winnik, F. In *Self Organized Nanostructures of Amphiphilic Block Copolymers II*; Müller, A. H. E.; Borisov, O., Eds.; Springer Berlin Heidelberg, 2011; Vol. 242, pp. 29–89.

(106) Liu, T.-Y.; Hu, S.-H.; Liu, D.-M.; Chen, S.-Y.; Chen, I. W. *Nano Today* **2009**, *4*, 52–65.

(107) Kakwere, H.; Leal, M. P.; Materia, M. E.; Curcio, A.; Guardia, P.; Niculaes, D.; Marotta, R.; Falqui, A.; Pellegrino, T. *ACS Appl. Mater. Interfaces* **2015**, *7*, 10132–10145.

(108) Hergt, R.; Dutz, S. *J. Magn. Magn. Mater.* **2007**, *311*, 187–192.

(109) Nawara, K.; Krysinski, P.; Blanchard, G. J. *J. Phys. Chem. A* **2012**, *116*, 4330–4337.

(110) Fülöp, Z.; Gref, R.; Loftsson, T. *Int. J. Pharm.* **2013**, *454*, 559–561.

(111) Guardia, P.; Riedinger, A.; Nitti, S.; Pugliese, G.; Marras, S.; Genovese, A.; Materia, M. E.; Lefevre, C.; Manna, L.; Pellegrino, T. *J. Mater. Chem. B* **2014**, *2*, 4426.

(112) Wang, D.; Astruc, D. *Chem. Rev.* **2014**, 6949–6985.

(113) Shi, F.; Tse, M. K.; Pohl, M. M.; Brückner, A.; Zhang, S.; Beller, M. *Angew. Chemie - Int. Ed.* **2007**, *46*, 8866–8868.

(114) Shi, F.; Tse, M. K.; Pohl, M. M.; Radnik, J.; Brückner, A.; Zhang, S.; Beller, M. *J. Mol. Catal. A Chem.* **2008**, *292*, 28–35.

(115) Liu, Y.; Chen, T.; Wu, C.; Qiu, L.; Hu, R.; Li, J.; Cansiz, S.; Zhang, L.; Cui, C.; Zhu, G.; You, M.; Zhang, T.; Tan, W. *J. Am. Chem. Soc.* **2014**, *136*, 12552–12555.

(116) Shi, F.; Tse, M. K.; Li, Z.; Beller, M. *Chem. - A Eur. J.* **2008**, *14*, 8793–8797.

Appendix: List of publications and communications at conferences

Scientific publications

Original publications in ISI Journals:

1. Lak, A.; Niculaes, D.; Anyfantis, G. C.; Bertoni, G.; Barthel, M. J.; Marras, S.; Cassani, M.; Nitti, S.; Athanassiou, A.; Giannini, C.; Pellegrino, T.; Facile transformation of FeO/Fe_3O_4 core-shell nanocubes to Fe_3O_4 via magnetic stimulation, *Sci. Rep.*, **2016,** 6**,** 33295–33306

2. Kakwere, H.; Pernia Leal, M.; Materia, M. E.; Curcio, A.; Guardia, P.; Niculaes, D.; Marotta, R.; Falqui, A.; Pellegrino, T.; Functionalization of strongly interacting magnetic nanocubes with (thermo)responsive coating and their application in hyperthermia and heat-triggered drug delivery, *ACS Applied Materials & Interfaces,* **2015,** 7 (19)**,** 10132–10145

Communications at conferences

Oral communications:

1. 10 minute presentation on '*Controlled (multi)functionalization of magnetic nanoparticles for application in biology and catalysis*' at the mid-term review meeting of the Mag(net)icFun network. Place: IIT, Genoa (Italy). Date: 03.06.2014
2. 15 minute presentation on '*Monodisperse iron oxide nanocubes with a core-shell structure*' at the 4th workshop of the Mag(net)icFun network. Place: University of Regensburg, Regensburg (Germany). Date: 27.10.2014
3. 10 minute oral presentation on '*Soft colloidal (nano)clusters of iron oxide nanoparticles'* at the 5th workshop of the Mag(net)icFun network. Place: University of Keele, Stoke-on-Trent (United Kingdom). Date: 24.04.2015
4. 20 minute presentation on '*Iron oxide nanocubes coated with thermo-responsive polymers for magnetically induced hyperthermia and drug delivery*´ at the 2015 International Chemical Congress of Pacific Basin Societies. Place: Honolulu (United States). Date: 19.12.2015
5. 20 minute presentation on 'Updates on the project: *Soft colloidal (nano)clusters of iron oxide nanoparticles*' at the 6th workshop of the Mag(net)icFun network. Place: Trinity College Dublin, Dublin (Ireland). Date: 04.03.2016
6. 30 minute presentation on '(*Core-shell) Iron oxide nanocubes for magnetically induced hyperthermia*' at the final review meeting of the Mag(net)icFun network. Place: University of Regensburg, Regensburg (Germany). Date: 21.11.2016

Acknowledgements

None of this would have been possible without the help of so many people to whom I am grateful for their time, support, encouragement, and advice given—formally or informally—over a cup of caffè macchiato.

First of all, I would like to thank my supervisor, Dr. Teresa Pellegrino, and the co-supervisors, Professors Renata Riva and Miquel A. Pericàs, for their support during my doctoral training. Their continuous guidance steered my research, alongside insightful comments and suggestions that contributed to my technical training and encouraged me to deepen my understanding of various aspects of the field. I would also like to thank Dr. Liberato Manna for offering me the possibility of carrying out my doctoral research in his laboratory.

Secondly, I would like to thank the Initial Training Network Mag(net)icFun, both for providing the funding that allowed me to undertake this research—through funds secured from the European Commission Marie Skłodowska-Curie Actions—and for giving me the opportunity to attend conferences and workshops where I got to meet so many outstanding people.

After having spent three years at IIT, I am in great debt to many colleagues from the Nanochemistry group. I would like to thank the following people in no particular order: Giammarino Pugliese, Simone Nitti, Filippo Drago, Gabriele la Rosa, Dr. Rosaria Brescia, Alice Scarpellini, Simone

Lauciello, Tiziano Catelani, Doriana Debellis, Thanh Binh Mai, Dr. Mirko Prato, Dr. Milena Arciniegas, Maria Elena Materia, and Anatolii Polovitsin. I would particularly like to thank Filippo Drago for his patience with my ICP samples that may have been late 'once or twice'. Many thanks to my colleagues from Nanomaterials for biomedicine group for their useful suggestions during our weekly meetings.

During my mobility stay at ICIQ, I had the opportunity to discover another lab organization, as well as to envision how cross-disciplinary studies can contribute to the different research fields involved. I would like to thank all the group members for welcoming me to the team, with special thanks to Marta Rodriguez Rodriguez, Francesca Besostri, and Dr. Carles Rodriguez.

Above all, I would like to thank those who have given substantial contribution to the results presented in this doctoral thesis: Dr. George C. Anyfantis and Simone Nitti for the synthesis of multiple samples of iron oxide nanocubes, Dr. Aidin Lak for all the magnetic measurements, Sergio Maras for performing XRD measurements, Giammarino Pugliese for carrying out TGA experiments, Dalibor Soukup (from Keele University) for carrying out AC Susceptibility measurements, Marco Cassani for help with the dot blot assays, Dr. Giovanni Bertoni for performing HRTEM/STEM and the GPA analysis alongside Dr. Aidin Lak, Dr. Hamilton Kakwere and Thanh Binh Mai for the synthesis of thermo-responsive polymers.

Additionally, I would like to thank my supervisor, Dr. Teresa Pellegrino, and Dr. Aidin Lak for proofreading this manuscript.

A double degree between two countries—with four parties involved—entails a lot of bureaucracy, alongside possible miscommunication. The co-tutelle agreement between Università degli Studi di Genova and Universitat Rovira I Virgili would have never been signed not for the determination with which Iulia Manolache fought to get things done. I would like to thank Iulia for her dedication to see things through, for not giving up in front of a challenge and for her friendship all these years.

Completing this work would have been all the more difficult were it not for the friendship and support provided by fellow PhD students and researchers from the various Robotics departments of IIT. I am indebted to them for their friendship and the incredible memories we created together. They provided the much needed escape from my work, they helped me keep things in perspective during bad times and celebrated my successes no matter how small.

Finally, I would like to thank my family for always being there—one phone call away, for not nagging me about working all through last Christmas break, for being my number one cheerleader(s) and for gently pushing me to aim higher—each and every day.

UNIVERSITAT ROVIRA I VIRGILI
AVANCES EN SISTEMAS INTERACTIVOS PARA PERSONAS CON PARÁLISIS CEREBRAL
Dina Niculaes

UNIVERSITÀ DEGLI STUDI
DI GENOVA

UNIVERSITAT
ROVIRA i VIRGILI

ISTITUTO ITALIANO
DI TECNOLOGIA
NANOCHEMISTRY

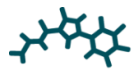

Institut
Català
d'Investigació
Química